RÉPUBLIQUE FRANÇAISE
Liberté Égalité Fraternité

Doctorat de l'Université de Toulouse

délivré par l'ENAC

Positionnement GNSS Précis: une Analyse d'Architectures de Graphes de Facteurs et de Différences Temporelles de Phase de Porteuse

---

Thèse présentée et soutenue, le 10 décembre 2025 par

Hakim CHERFI

École doctorale
EDMITT - Ecole Doctorale Mathématiques, Informatique et Télécommunications de Toulouse

Spécialité
Informatique et Télécommunications

Unité de recherche
ENAC-LAB - Laboratoire de Recherche ENAC

Thèse dirigée par
Paul THEVENON et Joan SOLÀ

Composition du jury
Mme Valérie RENAUDIN, Rapporteure, Université Gustave-Eiffel
Mme Sandra VERHAGEN, Rapporteure, Technical University of Delft
M. Patrick DANèS, Examinateur, LAAS-CNRS
M. MOHAMMED ELMUSRATI, Examinateur, School of Technology and Innovations University of Vaasa
M. Paul THEVENON, Directeur de thèse, Ecole Nationale de l'Aviation Civile
M. Joan SOLÀ, Co-directeur de thèse, Institut de Robotica i Informatica Industrial

Membres invités
M. Julien Lesouple, co-encadrant, Ecole Nationale de l'Aviation Civile

Tine, sachant à quel point ce livre t'apportera bonheur et apaisement, je te le dédie.

Remerciements

Tout d'abord, je tiens à remercier l'ensemble de l'encadrement de ma thèse. Paul, Julien, Joan, merci d'avoir choisi de travailler avec moi, pour votre accueil à l'ENAC, ainsi que pour votre soutien. Vous avez fait preuve de mesure, de raison, de flexibilité, d'ouverture d'esprit, de bonne humeur et d'aide inconditionnelle pendant toute ma période à l'ENAC. Votre encadrement attentif et exigeant a largement contribué à mon évolution scientifique et humaine tout au long de cette thèse.

La soutenance orale fut un agréable moment, merci à tous les membres du jury pour leur temps et leur énergie consacrés à l'évaluation de ce travail, particulièrement Patrick Danès pour ta bienveillance, tes conseils, ainsi que ton suivi régulier de l'avancement de cette thèse. Dans la même lignée, je tiens à remercier Karim Dahia pour sa présence lors de comités de suivi individuels.

Je remercie l'ensemble des membres permanents de l'équipe TELECOM, composée de l'axe SIGNAV (Christophe, Anaïs, Axel, Carl, Jérémy, Anne-Christine, Antoine), de l'axe EMA (Alexandre, Rémi, Christophe, Lucille, Zeina, Hélène, Théo, mention spéciale pour Matthieu le El, tu as au moins dix fois ma maturité et pourtant tu es plus jeune que moi, snif ...) ainsi que les quelques collègues de l'axe RESCO que j'ai pu côtoyer (Alain, Guthemberg).

Bien sûr, un doctorant se rassure en discutant avec ... des doctorants. Un grand merci à l'ensemble des doctorants (Gabriel, Robin, Alexandre, Mathias & Antoine, content que vous ayez débarqué ! Ibrahim, Paul, Valencia, Audric, Anne-Laure, Bisma, Camille Xinyi, Evelyn, Alexandra, Soad, Tassany, Jiyai, mention *très* spéciale pour Clémence, ta présence à moins de 5 mètres 8 heures par jour est rassurante, même si je n'ai toujours pas compris l'effet Doppler ... Victor & Alice, c'est grâce à vous que je me suis senti chez moi en **F011** dès le premier jour de thèse) avec lesquels j'ai pu échanger pendant ces trois années.

Merci à l'ensemble des stagiaires passés par le labo (Kenza & Maria, Sofia & Aiswarya, Sarah & Alice, Koxe & Arthur, Hercule, Maël, Loan, Leiticia, Serigne, Ai-Chi, shout-out to Shang-Ping, without your dedication, the results in this thesis would be MUCH weaker, you nailed it, good luck with your PhD) et qui m'ont permis d'avancer dans mes travaux.

Réfléchir, en mettant de côté l'aspect utilitariste de l'exercice, est apaisant. Merci à Florence, Johan, Stéphane ainsi qu'à l'ensemble des participants du groupe de travail centré sur l'étude des groupes de Lie[1], au sein duquel j'ai énormément appris.

[1]Marius Sophus Lie, 1842 – 1899.

This document may not be reproduced, modified, adapted, published, translated in any way, in whole or in part, nor disclosed to a third party without the prior written consent of ENAC. © 2025, ENAC

Merci pour la décompression hebdomadaire (version civilisée) grâce aux potes du foot, avec le big boss des big boss coach Philippe, Pipo Inzaghi, Lulu Pedri, Samih Cech, Roman Mudrik, Simon, Arnold, Thomas, Nico & Allan, Amine la Rue & Alex Mazin Greenwood, Akilesh, Flo le vrai, Sam président, Poulain & Olivier, Julio, Steph la défense (je dors bien grâce à toi), Julien César, Romain, Dr. Mehdi, et tous ceux qui m'ont fait de bonnes passes.

Et la décompression dominicale (version sauvage) avec Yassine Gatlato, Ryad, tonton Farid, la Sincérité, Hamza & Hamza, Mohamed Barça, Youssef, Nourdine Benzema, Charaf Ronaldinho, Smaïl el Gigante, Brahim, Farès BEIN, Houwari, Rachid & Kader, Fayçal Neuer, Mohamed Ramos, et tous ceux que j'oublie mais qui comptent pour moi.

Merci à Alex Lazo, Vincent Tevenaz & Théo Quiros, j'en reviens pas que vous soyez venus à la soutenance, Étienne le randonneur vertical qui aime engouffrer ses amis dans ses péripéties, Benja, Ibis & Nuno, les anciens du IDIM, je me suis tapé de bonnes barres avec vous, Redouane & Mathis, vous me manquez les gars, ça fait longtemps.

Chez les Cherfi, merci à tonton Mokrane, Karima, Danyl & Célina, Jedha, Momo & Loan, Naïma, Le Chach (fier de ce que tu fais le couz), Tine (je n'ai pas eu de prof qui a autant aimé m'aider, merci), une pensée pour Zina, Amzer & Gamze, Nagzer & Lucia, Farid, Halim Djundi & Toufik, Brahim & Zizir Smaïl, Seddik, Délina & Dania.

Côté Jabri, merci à Shera & Bilouuuu, Fatifa ma deuxième mère, Nounouya, Eden & Camila, Lisa de Nabil, Lisa de Jamel, Sabah & Yasin, Ninou & Watitoo, Kassimou & Naïmouuu, Guigui & Victor, Zaza, Selmounet & Jaja, Sofiane, Hamid & Mohamed-Said, Mamie Mouma & Kamal.

Merci à Guy (le véritable poumon de ma chef) & Kika ainsi que les enfants (Florian, Quentin, Miss Ophélia), Ahmed de Karavan.

Durant cette thèse, j'ai eu la chance de rencontrer des personnes avec lesquelles se sont construits des liens forts, sincères et durables, que je considère aujourd'hui comme une véritable famille. Je les remercie ici, sans ordre particulier.

Émile la Ghizz, merci pour ton sérieux et ta déconne, ton accueil très chaleureux, tu es ma Roue Libre, ma bouée de sauvetage lors de la préparation des TD, mon fabricant de schéma-blocs, mon "débrieffeur" des ESSI, j'ai beaucoup appris de toi. Bon courage pour la suite de tes aventures dans la recherche.

Mathieu le Heuss, le papillon de nuit, le big boss des doctorants, même ChatGPT en sait moins que toi, celui qui sait concilier des disciplines et recoller des morceaux, qui sait faire rentrer un carré dans un cercle et un cercle dans un carré. Je suis honoré d'avoir croisé ta route, et te souhaite bon vent dans tes aventures aéronautiques.

Mon frère Renaud le logicien, tu m'as foudroyé en me présentant Gödel[2] et l'axiomatique récursive, le principe d'explosion, le miracle de la linguistique et d'autres encore, me permettant ainsi de me poser de vraies questions épistémologiques, sur la valeur de la science, et de me sentir un peu plus humain. Et dans cet océan de questions philosophiques

[2]Kurt Gödel, 1906 – 1978.

profondes, tu as humblement pris le temps de m'écouter et de m'éclairer sur mes "petits" problèmes de recherche. Immense respect.

Nicolas l'asocial, soulagé par ton départ du bureau, mais quel manque ! Merci de m'avoir présenté au Cald (qui est devenu un père spirituel !) et à Mathadultes, de m'avoir proposé plusieurs définitions de la *recherche*, d'avoir initié les *Maths Meeting*, d'avoir transformé le **F011** en PMU de la science, et finalement pour ton courage de dire ce que tu penses. Tu vas me manquer fréro.

Mention spéciale pour Loïc Shi-Garrier aka "la Shig", la rigueur, la curiosité, l'humilité, je suis très content d'avoir pu échanger avec toi, aux maths meeting ou au restaurant, je compte sur toi, jeune padawan, pour boucler ce programme dont vous parlez régulièrement avec l'asocial.

Mehdi, il est évidemment impossible de résumer en quelques lignes tout ce que je te dois ... Merci de m'avoir présenté à Anthony Soprano, qui m'a ensuite conduit à Christopher Moltisanti, de m'avoir accompagné dans la rédaction de ce manuscrit, lequel, lors de la compilation, affiche fièrement exactement zéro warnings LaTeX, de m'avoir épargné certaines questions dérisoires et d'avoir su orienter mon énergie vers des aspects bien plus essentiels. Je pourrais encore écrire une dizaine de pages à ton sujet. Je ferai preuve de retenue et m'arrêterai ici.

Et puis finalement, il y a ceux du quotidien, ou presque.

Mes deux frères d'une autre mère Pilolette et Coudeur 31, vous savez. Il y a aussi Toulie, Joe Dalton et Vito Corleone (moi aussi j'écris des livres).

This document may not be reproduced, modified, adapted, published, translated in any way, in whole or in part, nor disclosed to a third party without the prior written consent of ENAC. © 2025, ENAC

Résumé

Le positionnement GNSS (Global Navigation Satellite Systems) est aujourd'hui essentiel dans de nombreuses applications, allant de la navigation sur smartphone à la géodésie de haute précision. Si les récepteurs GNSS sont désormais largement accessibles, en particulier dans les appareils grand public à faible coût, atteindre une précision de positionnement élevée reste un défi majeur. Des facteurs tels que les multitrajets, les perturbations atmosphériques et les obstructions de signaux en environnement urbain limitent les performances des méthodes GNSS classiques.

Cette thèse s'intéresse à ces limitations en explorant des techniques avancées de fusion de données et d'optimisation pour améliorer la précision du positionnement GNSS, notamment dans le cas de récepteurs mono-constellation et mono-fréquence. L'approche repose sur l'optimisation par graphe de facteurs (FGO), un cadre puissant qui modélise le problème d'estimation sous forme d'un graphe composé de variables (positions, vitesses, biais) et de facteurs (mesures capteurs). Contrairement aux méthodes classiques comme les moindres carrés pondérés ou le filtre de Kalman étendu, FGO permet d'intégrer dans une unique optimisation les observations passées, présentes et futures, améliorant ainsi la cohérence et la précision.

Un accent particulier est mis sur l'utilisation des observations de phase différenciées dans le temps (TDCP), qui permettent une précision centimétrique sans nécessiter de résolution d'ambiguïté entière, ce qui est un défi majeur des techniques à base de phase. Toutefois, le TDCP présente également des difficultés, notamment la présence de sauts de cycle (causés par des pertes ou distorsions du signal). Pour y remédier, une méthode innovante basée sur FGO est développée pour détecter et exclure ces sauts de cycle, assurant ainsi la fiabilité du TDCP.

La thèse analyse aussi les approximations courantes du modèle TDCP et leur impact sur la précision du positionnement, ainsi que les corrélations souvent négligées entre observations TDCP. Ces corrélations, dues à la structure même des observations (différences de phases successives), peuvent nuire aux performances dans certains cas. Des analyses théoriques et expérimentales identifient les situations où ces simplifications sont acceptables ou non.

L'évaluation est menée à l'aide de données synthétiques (scénarios contrôlés) et de données réelles issues des stations de référence du réseau IGS (International GNSS Service), permettant une validation réaliste sans altération excessive du signal. Bien que le temps réel ne soit pas l'objectif ici, les méthodes développées peuvent être étendues à des applications embarquées, et la question de leur évolutivité est discutée en fin de manuscrit.

This document may not be reproduced, modified, adapted, published, translated in any way, in whole or in part, nor disclosed to a third party without the prior written consent of ENAC. © 2025, ENAC

En résumé, cette thèse apporte un algorithme FGO de détection et d'exclusion des sauts de cycle adapté au TDCP, une évaluation critique des approximations du modèle TDCP, et une étude des corrélations TDCP et de leur impact sur la précision.

Abstract

Global Navigation Satellite System (GNSS) positioning is at the heart of many applications today, from smartphone navigation to high-precision geodesy. While GNSS receivers provide wide accessibility, especially in low-cost consumer devices, achieving high positioning accuracy remains a significant challenge. Factors such as multipath effects, atmospheric disturbances, and signal blockages in urban environments impair the performance of standard GNSS methods.

This thesis addresses these limitations by exploring advanced sensor fusion and optimization techniques to improve GNSS positioning accuracy, particularly for single-frequency, single-constellation receivers. The approach focuses on Factor Graph Optimization (FGO), a powerful framework that models the estimation problem as a graph composed of variables (e.g., positions, velocities) and factors (e.g., sensor measurements). Unlike traditional methods like Weighted Least Squares or the Extended Kalman Filter (EKF), FGO integrates observations from the past, present, and future within a unified optimization problem, improving robustness and precision.

The thesis particularly emphasizes the use of Time-Differenced Carrier Phase (TDCP) observations, which provide centimeter-level accuracy without the need for integer ambiguity resolution, a major challenge in carrier-phase-based positioning. However, TDCP comes with its own difficulties, notably the presence of Cycle Slips (sudden changes in the carrier-phase due to signal loss or distortion). To address this, a novel FGO-based method for detecting and excluding cycle slips is developed, ensuring TDCP reliability.

Furthermore, the thesis examines the approximations commonly applied to TDCP models, analyzing their impact on positioning accuracy. It also investigates the neglected correlations in TDCP observations, which result from their construction as differences of consecutive carrier-phases. While often ignored in the literature, this correlation can degrade performance under certain conditions. The work provides theoretical and experimental insights into when such simplifications are acceptable.

The study employs both synthetic data—to evaluate algorithmic performance in controlled scenarios—and real-world GNSS data from International GNSS Service (IGS) stations, ensuring the realism of results without excessive signal degradation. Although real-time performance is not the focus, the methods are designed with future applications in mind, and the thesis concludes with a discussion on scalability and applicability to consumer-grade devices.

Overall, this thesis contributes to an FGO-based cycle slip detection and exclusion algo-

This document may not be reproduced, modified, adapted, published, translated in any way, in whole or in part, nor disclosed to a third party without the prior written consent of ENAC. © 2025, ENAC

rithm tailored for TDCP, a critical evaluation of TDCP approximations and their effects on positioning, and an analysis of TDCP correlation and its relevance in high-precision applications.

Contents

Introduction **25**

1 Context . . . 25
2 Objectives . . . 26
3 Contributions . . . 30
4 Outline . . . 30

1 GNSS Principles **33**

1.1 GNSS Constellations and Positioning Principle . . . 33
1.1.1 GNSS Constellations . . . 33
1.1.2 Positioning Principle . . . 35
1.2 Observation Models . . . 39
1.2.1 Code Pseudorange . . . 40
1.2.2 Carrier-Phase . . . 41
1.2.3 TDCP . . . 43
1.2.4 Doppler . . . 44
1.2.5 Terms in Observation Models . . . 45
1.3 Positioning Algorithms . . . 52
1.3.1 Single Point Positioning . . . 53
1.3.2 PPP . . . 58
1.3.3 RTK . . . 60
1.4 Low-Level GNSS Signal Processing . . . 62
1.4.1 GPS Signal Structure . . . 62
1.4.2 Acquisition . . . 63
1.4.3 Tracking . . . 64
1.4.4 Observations from Low-Level Estimates . . . 65
1.5 Conclusion . . . 66

2 Factor Graph Optimization **69**

2.1 Background and Definitions . . . 69
2.1.1 Applications of Factor Graph Optimization . . . 69

2.1.2 Definitions . . . 71
2.2 Linear Case . . . 76
2.2.1 Estimator and Moments . . . 76
2.2.2 Orthogonal Projections . . . 76
2.2.3 Computation of the Solution . . . 78
2.3 Nonlinear Case . . . 81
2.3.1 Equations . . . 81
2.3.2 Solvers . . . 82
2.4 Transformations of FGO . . . 83
2.4.1 Linear Combinations of Observations . . . 83
2.4.2 Restriction of the Observation Model . . . 84
2.4.3 Transformation of the Parameter Vector . . . 84
2.4.4 Difference of Two Graphs and Differential Positioning . . . 85
2.4.5 Common Bias and Random Affine Bias . . . 86
2.5 Kalman Filter Update as an FGO . . . 87
2.5.1 Equations of the Kalman Filter . . . 87
2.5.2 Representation of the Update with an FGO . . . 90
2.6 Conclusion . . . 91

3 FGO-Based Cycle Slip Detection and Identification 93
3.1 FGO-Based Fault Detection . . . 94
3.1.1 Statement of the Problem . . . 94
3.1.2 Linear Case, Random Vector, Likelihood and Residual . . . 94
3.1.3 Cochran's Theorem . . . 96
3.1.4 Misspecified Likelihood . . . 97
3.1.5 Corollary of Cochran's Theorem . . . 98
3.1.6 Binary Hypothesis Testing . . . 99
3.1.7 Neyman-Pearson Lemma . . . 100
3.1.8 Application of the Neyman-Pearson Lemma . . . 101
3.1.9 Noncentrality Parameter Set of Values for Discrete Single Fault . . . 103
3.1.10 Extension to Nonlinear Models . . . 106
3.2 FGO-Based Fault Identification . . . 108
3.2.1 Statement of the Problem . . . 108
3.2.2 Multiple Hypothesis Testing . . . 109
3.2.3 Maximum Likelihood Rule for Model Selection Among Observations 109
3.2.4 Sub-graphs for Single Fault . . . 110
3.2.5 Law of Faulty FGO and Fault-Free FGO . . . 110
3.3 Application: TDCP & FGO-Based Single CS Detection . . . 112
3.3.1 Observations and Corrections . . . 112

3.3.2 First GNSS Receiver & Dataset Characterization . . . 114
3.3.3 Second GNSS Receiver & Dataset Characterization . . . 118
3.4 Cycle Slip Detection . . . 129
3.4.1 Statement of the Problem . . . 130
3.4.2 Factor Graph Representation . . . 131
3.4.3 Construction of the TDCP . . . 132
3.4.4 Positioning Error Analysis Using FGO . . . 134
3.4.5 Cycle Slip Detection Using FGO Residuals . . . 138
3.4.6 Cycle Slip Identification Using FGO Residuals . . . 140
3.5 FGO-based Multiple Cycle Slip Detection and Identification . . . 144
3.6 Conclusion . . . 145

4 Uncertainty Quantifiation of TDCP Factor for Displacement Estimation in an FGO 147
4.1 Review of TDCP Models . . . 148
4.2 Temporal Difference of Carrier-Phase Observations . . . 149
4.3 Restriction of the TDCP Model . . . 151
4.3.1 Correct TDCP Model . . . 152
4.3.2 Assumed TDCP Model . . . 153
4.3.3 Difference Between Correct and Assumed TDCP Models . . . 154
4.4 Uncertainty Quantification of the Position in the TDCP Model . . . 155
4.4.1 TDCP Model Error . . . 155
4.4.2 Receiver Displacement Estimation Error . . . 159
4.5 Conclusion . . . 166

5 Impact of TDCP Correlations on Positioning 169
5.1 FGO-Based GNSS Positioning with Code and Carrier-Phase . . . 169
5.2 FGO Architectures . . . 171
5.2.1 Architecture 1: Code Pseudorange Only . . . 172
5.2.2 Architecture 2: Code and Correlated TDCP . . . 173
5.2.3 Architecture 3: Code and Uncorrelated TDCP . . . 176
5.3 Experiments . . . 177
5.3.1 Context . . . 178
5.3.2 Impact of Omitted Correlations . . . 178
5.3.3 Impact of Time Window Length . . . 182
5.4 Conclusion . . . 185

Conclusion and Future Works 187
1 Conclusion . . . 187
2 Future Works . . . 190

This document may not be reproduced, modified, adapted, published, translated in any way, in whole or in part, nor disclosed to a third party without the prior written consent of ENAC. © 2025, ENAC

Acronyms **193**

Bibliography **202**

A Maximum Likelihood Estimation **203**

A.1 Definitions 203

B Analytical Solution of the Linear Gaussian Factor Graph Optimization Problem **205**

B.1 Definitions 205

B.2 Generalized Inverse 205

C Kalman Filter Update Equations **209**

D Geometry of the TDCP Model **211**

D.1 Direction of Null and Extremum Model Error 211

D.2 TDCP Model Error Along the Worst Direction 212

E Horizontal and Vertical Impact of TDCP Correlations **215**

E.1 Horizontal Positioning Error 215

E.2 Vertical Positioning Error 215

List of Figures

1.1 Principle of Multilateration with Ranges 36
1.2 Principle of Multilateration with Pseudoranges 39
1.3 Ionospheric Effect 48
1.4 Sagnac Effect 50
1.5 Multipath and Occlusion 51
1.6 Dilution of Precision 57

2.1 Example of Deterministic Factor Graph 72
2.2 Example of Stochastic Factor Graph 74
2.3 Single Point Positioning as a Factor Graph 75
2.4 Observation Space, Orthogonal Projections, Maximum Likelihood Estimator and Residual 78
2.5 Kalman Filter Update as a Factor Graph 90

3.1 Well-Specified Factor Graph 95
3.2 Misspecified Factor Graph 97
3.3 Neyman-Pearson for Chi-Squared Densities 103
3.4 Cumulative Distribution Functions of Noncentral Chi-Squared 104
3.5 Evaluation of Cumulative Distribution Functions of Noncentral Chi-Squared 105
3.6 Probability of Detection with respect to Noncentrality Parameter 105
3.7 Fault Identification with Factor Graphs 110
3.8 TLSE Receiver's Antenna 114
3.9 TLSE: Code Pseudorange Residuals 117
3.10 TLSE: Carrier-Phase Residuals 118
3.11 TLSG Receiver's Antenna 119
3.12 Single Difference of Code Pseudorange Residuals 123

3.13 Mean of Single Difference of Code Pseudorange Residuals with respect to Elevation . . . 124
3.14 Standard Deviation of Single Difference of Code Pseudorange Residuals with respect to Elevation . . . 125
3.15 Single Difference of Carrier-Phase Residuals . . . 126
3.16 Mean of Single Difference of Carrier-Phase Residuals with respect to Elevation 127
3.17 Standard Deviation of Single Difference of Carrier-Phase Residuals with respect to Elevation . . . 128
3.18 Factor Graph with Code Pseudorange and Carrier-Phase Observations . . . 131
3.19 Factor Graph with Code Pseudorange and TDCP Observations . . . 134
3.20 Histogram of Global Positioning Error, Synthetic Observations . . . 135
3.21 Histograms of Horizontal and Vertical Positioning Errors, Synthetic Observations . . . 136
3.22 Horizontal Positioning Errors, Synthetic Observations . . . 136
3.23 Histogram of Global Positioning Error, Real Observations . . . 137
3.24 Histograms of Horizontal and Vertical Positioning Error, Real Observations 137
3.25 Horizontal Positioning Errors, Real Observations . . . 138
3.26 Confusion Matrix for Cycle Slip Identification, Synthetic Observations . . . 140
3.27 Correct Identification Rate per PRN, Synthetic Observations . . . 141
3.28 Confusion Matrix for Cycle Slip Identification, Real Observations . . . 142
3.29 Correct Identification Rate per PRN, Real Observations . . . 143
3.30 Skyplot of Satellites G18 and G26 from 15:00 to Midnight . . . 143
3.31 Elevation for Satellites G18 and G26 . . . 144

4.1 Two Positions TDCP Factor Graph . . . 152
4.2 Correct TDCP Displacement Factor Graph . . . 153
4.3 Assumed TDCP Displacement Factor Graph . . . 154
4.4 TDCP Model Error, Sphere, Small Position Error . . . 156
4.5 TDCP Model Error, Plane, Small Position Error . . . 156
4.6 TDCP Model Error, Plane, Large Position Error . . . 157
4.7 TDCP Model Error in the Worst Direction . . . 158
4.8 Skyplot at TLSE, January 1, 2024, 12:30 UTC . . . 160
4.9 Displacement Estimation, Small Error . . . 160
4.10 Displacement Estimation Error, Large Position Error . . . 161

4.11 Horizontal Displacement Estimation Error 162
4.12 Vertical Displacement Estimation Error 162
4.13 Displacement Estimation Error, Variable Position Error 163
4.14 Displacement Estimation Error, Variable Time Interval 164
4.15 TLSE Satellite Visibility 165

5.1 First FGO Architecture 173
5.2 Second FGO Architecture 176
5.3 Third FGO Architecture 177
5.4 Impact of Temporal Window, Synthetic Observations 183
5.5 Impact of Temporal Window, Real Observations 184

E.1 Horizontal Impact of Temporal Window, Synthetic Observations 217
E.2 Horizontal Impact of Temporal Window, Real Observations 218
E.3 Vertical Impact of Temporal Window, Synthetic Observations 220
E.4 Vertical Impact of Temporal Window, Real Observations 221

This document may not be reproduced, modified, adapted, published, translated in any way, in whole or in part, nor disclosed to a third party without the prior written consent of ENAC. © 2025, ENAC

List of Tables

1.1 GNSS Constellations Characteristics 34
1.2 Errors in Code Pseudorange Observations 41
1.3 Errors in Carrier-Phase Observations 43

3.1 Binary Confusion Matrix 100
3.2 Multiclass Confusion Matrix 109
3.3 Cycle Slip Detection Confusion Matrix for Synthetic Observations 139
3.4 Cycle Slip Detection Confusion Matrix for Real Observations 139

4.1 Maximum TDCP Model Error 159
4.2 Maximum Displacement Estimation Error 165
4.3 Maximum Horizontal Displacement Estimation Error 165
4.4 Maximum Vertical Displacement Estimation Error 166

5.1 Summary of FGO Architectures 177
5.2 Distribution of Positioning Errors, Synthetic Data 179
5.3 Distribution of Positioning Errors, Real Data 180
5.4 Positioning Statistics, Synthetic Data 180
5.5 Positioning Statistics, Real Data 181

E.1 Distribution of Horizontal Positioning Errors, Synthetic Data 216
E.2 Distribution of Horizontal Positioning Errors, Real Data 216
E.3 Distribution of Vertical Positioning Errors, Synthetic Data 219
E.4 Distributions of Vertical Positioning Errors, Real Data 219

This document may not be reproduced, modified, adapted, published, translated in any way, in whole or in part, nor disclosed to a third party without the prior written consent of ENAC. © 2025, ENAC

List of Algorithms

2.1 Construction of a Factor Graph Representation 71
2.2 Gauss-Newton 82

This document may not be reproduced, modified, adapted, published, translated in any way, in whole or in part, nor disclosed to a third party without the prior written consent of ENAC. © 2025, ENAC

Introduction

1 Context

Global Navigation Satellite System (GNSS) positioning is a fundamental technology in a large number of applications. Whether for consumer applications on smartphones, terrestrial, maritime, or aerial navigation, fleet tracking or precision agriculture, GNSS receivers are now of upmost importance. Their ability to provide real-time global positioning has revolutionized many industries and continues to generate significant interest in research and development.

However, GNSS positioning accuracy remains a major challenge. Various factors, such as atmospheric modeling, multipath effects and dense urban environments, can affect positioning results. Reducing these errors is crucial in order to improve the reliability and accuracy of navigation systems, particularly for critical applications such as autonomous driving, aviation, and geodesy.

In recent years, there has been a growing trend to enhance the positioning accuracy of standalone low-cost GNSS receivers, such as those found in smartphones, by means of data fusion techniques. By integrating GNSS data with measurements from other sensors, such as Inertial Measurement Unit (IMU), barometers, and visual odometry, engineers aim to compensate for GNSS limitations and to improve positioning results. These multi-sensor fusion approaches leverage advanced filtering and machine learning algorithms to refine location estimates, making precise positioning more accessible for a wider range of applications.

In this context, since the year 2021, Google has been running the Google Smartphone Decimeter Challenge (GSDC) [1, 2, 3], a competition aimed at improving smartphone positioning accuracy by leveraging raw GNSS data along with measurements from other onboard sensors. This challenge provides datasets collected from various smartphones in complex environments, allowing researchers and engineers to develop and test advanced signal processing and data fusion algorithms. The goal of GSDC is to achieve decimeter-level positioning accuracy using only a smartphone's sensors, which presents a significant challenge due to hardware limitations and signal disruptions affecting GNSS data.

The winning solutions of the 2021 and 2022 editions of the GSDC [4, 5, 6], as well as the second place of the 2023 edition [7] rely on a specific information fusion algorithm known as Factor Graph Optimization (FGO). It is an advanced framework that represents an

This document may not be reproduced, modified, adapted, published, translated in any way, in whole or in part, nor disclosed to a third party without the prior written consent of ENAC. © 2025, ENAC

estimation problem as a bipartite graph, where the first type of nodes correspond to unknown state variables (such as position, velocity, and sensor biases) that are estimated, and the second type of nodes correspond to what are called factors. A factor is a function, and this function is linked to the variables it depends on. In the context of estimation, a factor generally corresponds to a likelihood function, based on a sample of a random variable. An important assumption is that the random variables underlying the observations associated with each factor are mutually independent. From an optimization point of view, a factor can be seen as soft constraints derived from sensor measurements. By jointly optimizing all variables in the graph, FGO enables a more robust and consistent estimation of the user's trajectory compared to traditional estimation methods like the Weighted Least Squares (WLS) or Extended Kalman Filter (EKF).

FGO is particularly well-suited for data fusion, as it incorporates all available data into a single optimization framework. Unlike traditional filtering methods, such as the EKF, which processes data sequentially, that is usable only if specific assumptions regarding the random process of observations and dynamics are satisfied, and is not able to take into account future observations for a present estimation problem, FGO maintains a global view of the entire trajectory, and can be used with a larger spectrum of random process hypotheses, allowing a more consistent and accurate state estimation. This ability to jointly optimize past, present and future states results in smoother and more precise trajectory reconstruction, which is especially effective in cases where many dependencies between variables exists.

The FGO framework has been widely used in the field of robotics for many years, where it is a standard tool for system trajectory estimation in unknown environment, a problem known as Simultaneous Localization And Mapping (SLAM). However, within the GNSS community, its application was still relatively new at the beginning of this thesis in 2022: few studies had explored its potential for precise GNSS positioning but since then, it has gained significant attention and is now increasingly adopted for GNSS-based localization, particularly in challenging environments where traditional methods struggle to deliver high accuracy.

For example, in the context of the GSDC, high-ranking teams successfully employ FGO to fuse raw GNSS observations, IMU data, motion information, and others. This approach helps mitigating GNSS signal degradations in challenging environments, such as urban canyons, leading to significantly improved positioning accuracy. These results highlight the growing importance of graph-based optimization techniques in high-precision positioning applications, especially when working with low-cost, consumer-grade GNSS receivers.

2 Objectives

The Single Point Positioning (SPP) method typically provides a snapshot position fix at each instant, but its accuracy is highly sensitive to the quality of the current GNSS signals,

which may fluctuate due to signal interference, multipath effects, or satellite visibility. Additionally, SPP does not account for previous measurements or the dynamics of the receiver's movement, which can limit its performance in challenging environments. On the other hand, an EKF would still benefit from previous observations to estimate a current position, but future observations would not play a role in that goal, and its use requires strong assumptions on considered random processes to be satisfied.

For these reasons, this thesis proposes a more comprehensive approach by combining multiple sources of information to achieve a trajectory estimate over time. By taking into account data from several instants, this thesis aims to develop a more robust positioning framework that combines the information of all observations. By using FGO, observations from multiple time steps are used as well as constraints that link consecutive as well as non-consecutive instants, leading to a more consistent and accurate trajectory estimation. Each state variable is instant-specific, and the relationships between them are represented by factors. This structure enables the fusion of various data sources in a rigorous way, allowing for error smoothing and improved positioning robustness. By leveraging the temporal coherence of movement, FGO ensures that each estimated position is influenced not only by the current observations, but also by past and future observations, significantly enhancing the accuracy and stability of the positioning solution.

In GNSS, it is common to combine a GNSS receiver observations with observations from a known reference station by a technique known as Differential GNSS (DGNSS). It is used in [4] to compute absolute positions. By incorporating a reference station, the solution applies DGNSS techniques to correct positioning errors caused by common biases in available observations. Essentially, the measurement performed by a reference station can be used as a correction information if the reference station position is known. This approach is necessary because the raw GNSS data collected from poor quality receivers are too degraded to achieve high-precision absolute positioning. This strategy significantly improves positioning accuracy by reducing the impact of common biases in the receiver observations and in the reference station observations, as well as a larger spectrum of random variables that are specified with more details in this thesis. The trade-off is that all independent terms add-up, i.e., a better modeling of the observations is provided, but with an increase of additional noise. For these reasons, the DGNSS techniques are applied when necessary.

The GNSS is made of multiple satellite constellations, including Global Positioning System (GPS), Galileo, GLONASS, and BeiDou, each providing independent signals for global positioning. Additionally, these satellites transmit signals on multiple frequency bands, which help mitigate some errors such as ionospheric delays and enable improved positioning accuracy. Modern smartphones are now equipped with multi-constellation, multi-frequency GNSS receivers, allowing them to process a large amount of information, leading to enhanced accuracy, availability, and robustness in challenging environments. However, in this thesis, the questions and algorithms studied are considered in the single-constellation, single-frequency case. While the methodologies developed can easily be extended to multi-constellation and multi-frequency scenarios, restricting the

This document may not be reproduced, modified, adapted, published, translated in any way, in whole or in part, nor disclosed to a third party without the prior written consent of ENAC. © 2025, ENAC

analysis to a simpler setting allows for a more controlled study of the fundamental challenges and solutions in GNSS positioning. The insights gained from the single-frequency, single-constellation framework remain relevant, as the underlying principles generalize to multi-frequency and/or multi-constellation configurations.

In GNSS positioning, code pseudorange measurements are the most commonly used method for determining the receiver's location. These measurements are based on pseudoranges. A pseudorange represents the time it takes for a signal to travel from a satellite to the receiver, plus an additional receiver clock offset with respect to the considered constellation time. The pseudorange is computed by measuring the time delay between the emission and reception of the signal. This method, however, is limited by the synchronization properties of the signal and the presence of various sources of error, such as ionospheric and tropospheric delays, multipath effects, and others. As a result, code measurements generally provide positioning accuracy at the meter level.

In contrast, the carrier-phase of a GNSS signal can be measured and used to achieve far more precise positioning. The phase measurements provide better accuracy because the carrier wavelength are much shorter than the code patterns, known as Pseudo Random Noise (PRN) chips. The challenge, however, lies in resolving the integer ambiguity, i.e., determining how many cycles of the carrier wave have occurred between the satellite and the receiver. Once this ambiguity is correctly resolved, carrier phase measurements can provide centimeter-level accuracy.

The Time-Differenced Carrier Phase (TDCP) works by using carrier-phase at multiple instants. Combining TDCP and code pseudoranges from multiple satellites is a way to achieve high-precision positioning. The TDCP technique works by computing the difference between the carrier-phase of a signal from a satellite at two instants. This TDCP leads to more accurate positioning because it is much more precise than code measurements. Also, TDCP can significantly reduce errors caused by ionospheric and tropospheric delays since these error terms are highly correlated with respect to time, so for short time intervals, the TDCP is not much impacted by these errors, while code observations are.

Also, with TDCP, there is no need to estimate the ambiguities (the unknown number of cycles of the carrier signal between the satellite and the receiver) in the traditional sense, as is required in standard carrier phase-based positioning. The key assumption in TDCP is that the ambiguity for each satellite remains constant over time. However, this assumption may not always hold true in real-world conditions. External factors, such as signal interruptions, multipath errors, or receiver tracking problems, can cause the phase to jump unexpectedly, resulting in an event called Cycle Slip (CS). A CS can significantly impact the positioning accuracy, as it alters the phase measurements and introduce unknown biases in TDCP observations, which are then used for positioning.

Since these CS can happen without direct observation or notification by the receiver, they must be detected and corrected to prevent errors from propagating. In this context, the

detection of CS becomes critical to maintaining the accuracy of the positioning solution. The challenge lies in identifying these faults accurately.

Once corrected, the TDCP factors establish connections between variables at different time steps, as it is based on linear combinations of carrier phase observations across different epochs. In the constructed graphs, these TDCP factors provide constraints linking variables at different time steps, helping in trajectory smoothing and positioning accuracy.

Finally, the construction of a set of TDCP measurements from a linear combination of carrier phase observations typically leads to a set of highly correlated observations. For example, these correlations arise because each TDCP measurement is formed by differencing carrier phase observations between consecutive epochs, meaning that adjacent TDCP observations share a common carrier phase term. As a result, the noises affecting these measurements are not independent but exhibit strong statistical dependencies. Despite this, in most of the existing literature, these correlations are neglected. However, ignoring these correlations may lead to suboptimal estimation performance in certain scenarios. Therefore, a study of the impact of these correlations is necessary. An analysis of their influence on positioning accuracy, and determining under what conditions they can be safely ignored is done. The goal of this analysis is to provide insights into whether existing simplifications remain valid or if a more rigorous treatment of TDCP correlations is necessary for high-precision GNSS applications.

In terms of practical application, since the focus is on precise positioning applications over multiple instants, the number of considered instants is studied so that conclusions can be made regarding this parameter and its impact on the quality of estimated positions.

All the algorithms and methods developed are evaluated using both synthetic data and real-world data. Running the algorithms on synthetic data with controlled noise terms allows to test them under ideal conditions, where the exact trajectory and error sources are perfectly known and controlled. This provides a baseline for assessing the theoretical performance of each method. However, since real-world GNSS data is subject to unmodeled errors, the same algorithms are tested on real GNSS data. This allows to observe how these errors impact positioning accuracy and analyze the differences between idealized and practical performance. This dual approach ensures that the proposed methods are not only theoretical but also applicable to real-world navigation challenges. To ensure that the real-world data used is still of high quality and not excessively degraded, the observations are taken from International GNSS Service (IGS) stations. The IGS network consists of a global set of well-maintained, high-precision GNSS reference stations that provide high-quality measurements with minimal multipath effects. By using data from these stations, the proposed algorithms are evaluated in realistic yet controlled conditions, avoiding extreme signal degradations such as those found in dense urban environments. This approach allows to focus on analyzing algorithmic performance without being overly influenced by poor data quality, while still capturing the natural errors and variations

This document may not be reproduced, modified, adapted, published, translated in any way, in whole or in part, nor disclosed to a third party without the prior written consent of ENAC. © 2025, ENAC

present in real GNSS measurements. These IGS stations are fixed, but this information is not used, so the developed algorithms apply to a moving receiver as well.

3 Contributions

- To address the challenge of CS, an FGO-based CS detection and exclusion algorithm is provided. The aim is to develop a tool that can effectively detect when a cycle slip occurs, identify it, and then flag it as a fault. Once all excluded, the positions can be recomputed using the available valid data. By accurately detecting and handling CS, the system can maintain continuous and precise positioning, even in challenging conditions where signal interruptions or tracking issues may arise. This process ensures that the TDCP-based approach remains reliable and effective for high-precision GNSS applications. This work is supported by a peer-reviewed conference paper

  [8] H. Cherfi, J. Lesouple, J. Solà, and P. Thevenon, "Single Frequency GNSS Carrier Phase Cycle Slip Detection and Identification Using a Factor Graph Approach," in *Proc. ION Pacific PNT 2024*, (Honolulu, HI, USA), pp. 344 – 355, Apr. 2024.

- In the TDCP literature, several approximations of the TDCP model are proposed to simplify its usage, for example by writing it as a function of a GNSS receiver's displacement, or as a linear function. These approximations often involve restrictions of the correct TDCP model by assumptions on parameters. While these simplifications can make TDCP easier to integrate into practical positioning algorithms, their actual validity has never been rigorously assessed. There is limited research evaluating how these approximations impact positioning accuracy. Therefore, an analysis of these approximations is carried, assessing their impact on positioning performance, and determining under which conditions they remain valid. This study helps to clarify in which scenario approximate TDCP formulations can be used, or if more precise models are needed for high-accuracy applications. This work is supported by an article

  - H. Cherfi, J. Lesouple, J. Solà, and P. Thevenon, "Uncertainty Quantification of First Fix in a Time-Differenced Carrier Phase Observation Model," *Sensors*, vol. 25, May 2025.

4 Outline

- Chapter 1 is dedicated to the fundamentals of GNSS, providing a comprehensive introduction to the system. It covers the GPS signal structure, detailing how satellites transmit signals and how receivers process them to compute a position. It also discusses the different segments of the GNSS system, including the space segment (satellite constellations) and the user segment (GNSS receivers and their applications). Also, it introduces the observation models used in GNSS positioning, describing the mathematical formulations of pseudorange and carrier-phase measurements, along with the

various error sources that affect positioning accuracy. In a last section, traditional positioning algorithms are reviewed. This chapter provides the necessary background for understanding the more advanced algorithms and positioning techniques explored in later parts of this thesis.

- Chapter 2 is dedicated to FGO, providing a detailed exploration of its mathematical foundations. First, the case of expected values that are linear functions of the parameter vector of interest is studied, allowing for straightforward optimization formulations. Then, it extends to the nonlinear case, which is more representative of real-world GNSS problems and requires iterative optimization techniques. Additionally, the chapter introduces equivalences between different estimation methods, including the Kalman Filter (KF), the SPP with its WLS method, and FGO, highlighting how these approaches relate to each other in terms of state estimation. Finally, a section covers the composition of FGO with linear applications, exploring how different graph structures can be obtained, and which one are of interest.

- Chapter 3 covers the CS issue and provides an FGO-based single fault detection and exclusion algorithm. Since TDCP relies on the assumption that the carrier phase ambiguity remains constant over time, undetected CS in carrier-phase measurements can introduce significant errors, making TDCP unreliable. The approach exploits the integer nature of a CS, and by construction of a statistic, a decision test is provided that detects CS. Theoretical considerations are given regarding probabilities of false alarm, or of missed CS detection. In the case of detected CS, multiple graphs are built in order to identify and exclude the CS. By developing a robust method for handling cycle slips, this chapter aims to ensure that TDCP measurements can be used reliably and accurately, improving the overall performance of GNSS positioning solutions.

- Chapter 4 focuses on quantifying the error introduced by approximations of the TDCP model and determining under which conditions these approximations remain valid. In the literature, various simplifications of the TDCP formulation are commonly used. However, their impact on positioning accuracy has not been rigorously evaluated. This chapter provides an analysis of these approximations, comparing them against the TDCP model to measure the errors they introduce. By conducting both theoretical derivations and practical implementations, scenarios are identified where these approximations hold and situations where they lead to significant errors. This study provides guidelines regarding TDCP model approximations depending on the application, ensuring that errors remain within acceptable limits.

- Chapter 5 focuses on quantifying the impact of TDCP correlation and identifying cases where these correlations can be safely ignored. Since TDCP observations are derived from consecutive carrier-phase observations, they exhibit strong statistical dependencies, which are often neglected in the literature. This chapter analyzes how these correlations influence positioning accuracy, comparing models that account for correla-

This document may not be reproduced, modified, adapted, published, translated in any way, in whole or in part, nor disclosed to a third party without the prior written consent of ENAC. © 2025, ENAC

tion with those that assume independent TDCP measurements. Using both theoretical derivations and experimental evaluations, it is assessed whether ignoring correlations leads to significantly degraded performance. The findings from this chapter helps to determine when it is necessary to explicitly model TDCP correlations and when it is reasonable to omit them without compromising accuracy.

Chapter 1

GNSS Principles

This chapter is structured into several sections. It begins by generalities on Global Navigation Satellite System (GNSS) constellations and positioning principles. Next are introduced the observation models commonly used, including code pseudorange, carrier-phase, Doppler, and Time-Differenced Carrier Phase (TDCP) observations, including all phenomena that affect these observations. The main classes of positioning algorithms are presented, covering Single Point Positioning (SPP), Precise Point Positioning (PPP), and Real-Time Kinematic (RTK), which leverage GNSS observations in different ways to enhance positioning accuracy. Finally, the low-level aspects of a GNSS receiver are introduced, detailing the structure of a Global Positioning System (GPS) satellite signal and the process of converting received signals at an antenna into usable observations.

1.1 GNSS Constellations and Positioning Principle

1.1.1 GNSS Constellations

The GNSS encompasses multiple satellite constellations that provide Position, Velocity and Time (PVT) estimates on a global scale. It has become an essential tool for various applications, ranging from automotive and aviation to high-precision geodesy and autonomous systems. Different constellations, such as GPS (United States), Galileo (Europe), GLONASS (Russia), and BeiDou (China), offer positioning services with specific characteristics.

The GNSS architecture is generally divided into three main segments: the space segment, the control (or ground) segment, and the user segment.

The space segment comprises the constellation of GNSS satellites orbiting around the Earth. They transmit signals containing information necessary for positioning and timing. These satellites are arranged to ensure global coverage of Earth. They are equipped with highly accurate atomic clocks and signal transmitters.

The user segment includes all GNSS receivers, which can range from handheld devices

This document may not be reproduced, modified, adapted, published, translated in any way, in whole or in part, nor disclosed to a third party without the prior written consent of ENAC. © 2025, ENAC

Table 1.1: GNSS constellations characteristics [9, 10, 11, 12].

Constellation	GPS	Galileo	Glonass
Satellites	24 to 32	30	24
Orbital planes	6	3	3
Orbital altitude	20 100 km	23 222 km	19 100 km
Inclination	55°	56°	64.8°
Orbital period	11 h and 58 min	14 h and 5 min	11 h and 15 min

and smartphones to complex systems used in aircraft and surveying equipment. These receivers use the signals from multiple satellites to compute PVT.

The ground segment refers to the network of Earth-based stations and control centers responsible for monitoring, controlling, and maintaining the overall health and accuracy of the satellite constellation. Its primary functions include tracking satellite orbits, synchronizing satellite clocks, uploading updated navigation data, and managing satellite operations. Typically, the ground segment consists of a master control station, a network of monitoring stations spread around the globe, and uplink stations that transmit data to the satellites. The monitoring stations continuously observe the GNSS signals and send their observations to the master control station, which processes the data to detect anomalies and compute corrections. These corrections are then uploaded to the satellites to ensure they broadcast accurate ephemeris and clock information.

Together, these segments interact to provide reliable and accurate navigation services across the globe.

In Table 1.1 are visible characteristics of GPS, GLONASS and Galileo constellations. The BeiDou Navigation Satellite System (BDS) was initially developed as a regional navigation system, primarily serving the Asia-Pacific region. With the launch of BeiDou-3, it has evolved into a global system capable of providing positioning, navigation, and timing services worldwide. Unlike GPS, GLONASS, and Galileo, which rely solely on Medium Earth orbit (MEO) satellites arranged in uniform orbital planes, BeiDou employs a hybrid constellation composed of MEO and Geostationary Earth Orbit (GEO) satellites. This unique architecture introduces distinct orbital characteristics that complicate direct comparison with other GNSS constellations. For this reason, BeiDou's parameters are not detailed in the present table, which focuses on systems with more homogeneous MEO-based configurations.

Although multiple GNSS constellations are currently operational, this thesis focuses on the GPS constellation. This choice is motivated by the need to reduce complexity and enhance the readability and accessibility of the theoretical developments and experimental analyses. By narrowing the scope to a single, well-established constellation, the aim is to

clearly expose fundamental principles of satellite-based positioning, without the additional overhead introduced by system-specific parameters or combined processing strategies.

Naturally, this simplification has an impact on the experimental results, particularly in terms of positioning accuracy and satellite availability, which would likely improve with the inclusion of multiple constellations. However, it is important to emphasize that the methods, algorithms, and questions addressed throughout this work are not specific to GPS alone. On the contrary, they are applicable to any GNSS constellation, and can even be extended to multi-constellation scenarios, which are increasingly common in modern receivers. As such, the insights gained and solutions proposed here retain their relevance in broader, more realistic operational contexts involving diverse and heterogeneous GNSS infrastructures.

Although GNSS is widely recognized for its role in positioning and navigation, its applications extend beyond this application. For instance, in scientific research, it supports atmospheric studies through techniques such as reflectometry. In this thesis, however, the focus is on achieving precise positioning. The following section introduces the fundamental principles underlying GNSS-based positioning.

1.1.2 Positioning Principle

1.1.2.1 Multilateration with Ranges

Satellite-based positioning relies on the principle of multilateration, a technique used to determine the location of an object by measuring the distance (or range) between this object and multiple reference objects.

In $\mathbb{R}^3$, given a point of unknown coordinates $\boldsymbol{r} \in \mathbb{R}^3$ (the receiver) and a set of points of known coordinates $\{\boldsymbol{s}_1, \dots, \boldsymbol{s}_m\}$ (called references), if the distances between the receiver and these references are $\{\rho_r^{s_1}, \dots, \rho_r^{s_m}\}$, then the multilateration consists in finding the solution set of the system

$$\begin{cases} \|\boldsymbol{s}_1 - \boldsymbol{r}\| = \rho_r^{s_1} \\ \quad \vdots \\ \|\boldsymbol{s}_m - \boldsymbol{r}\| = \rho_r^{s_m}. \end{cases} \tag{1.1}$$

Each line of Equation (1.1) represents a sphere centered on the reference $\boldsymbol{s}_i$ and of radius $\rho_r^{s_i}$. The multilateration actually works by finding the intersection of these spheres. Depending on the set of references, the solution set can be infinite, finite, or empty. If there are more than one solution, adding references reduces the number of solutions. The multilateration works if the intersection reduces to a singleton, i.e., the object's coordinates satisfying Equation (1.1) are unique.

Multilateration is a fundamental technique employed in a wider range of domains, such as wireless communications, navigation systems, and surveillance applications, due to its ability to estimate positions based on distance measurements.

In the context of GNSS-based positioning, the object is a GNSS receiver and the references

This document may not be reproduced, modified, adapted, published, translated in any way, in whole or in part, nor disclosed to a third party without the prior written consent of ENAC. © 2025, ENAC

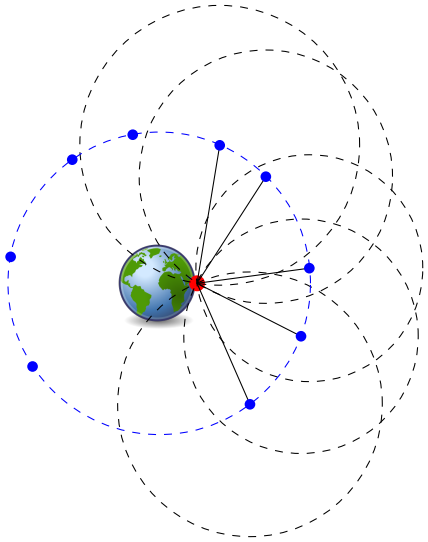

Figure 1.1: Representation (in 2D) of the multilateration principle. The blue points are GNSS satellites, the red point is a GNSS receiver. For each visible satellite, the distance between the receiver and the satellite defines a sphere centered on the satellite, with a radius equal to that distance. The receiver's location corresponds to the intersection of these spheres.

are GNSS satellites. In order to work, it is necessary (but not sufficient) to use three references.

The principle of multilateration is visible in Figure 1.1.

The ranges ρ_r^{si} are not measured directly. Instead, signals are emitted by the GNSS satellites and are received by a GNSS receiver. The distance is computed by measuring a propagation duration of this signal. Unfortunately, this process introduces additional complexity, making the GNSS-positioning more challenging than what is presented here.

1.1.2.2 Multilateration with Pseudoranges

In the context of GNSS, the distances between the receiver and the satellites are not directly measured. Instead, each GNSS satellite sends a signal that is received by a GNSS receiver. This receiver computes the propagation duration for each received signal. Since these electromagnetic waves travel (in first approximation) at the speed of light c, the range between the receiver and a satellite i is known thanks to the propagation duration Δt_i and the relation

$$\rho_r^{si} = c \cdot \Delta t_i, \tag{1.2}$$

where the propagation duration Δt_i is obtained by computing the difference between the instant of reception and the instant of emission of the considered signal.

Since GNSS satellites operate in MEO, typically around 20 000 km, they do not maintain a fixed position relative to the Earth's surface like geostationary satellites. One consequence of this is that not all GNSS satellites are able to reach a given GNSS receiver, as the Earth's

surface blocks their signals. This means that the number of visible satellites changes over time.

Another important aspect is related to the measurement of propagation duration. The *time* exists, but its measure is always relative (i.e., never absolute). Instead, durations, i.e., an instant with respect to a time coordinates system, can be measured. For example, in everyday life, when someone says that it is 5 o'clock, it is actually a measure of the duration between midnight and the current time, with midnight serving as the time reference. The same applies to the date or year.

As mentioned, in GNSS positioning, propagation duration must be measured. This has to be done within a single time coordinates system to ensure valid measurements. Otherwise, if different time coordinates system are used, discrepancies in the measured duration can occur, as shown in the following: suppose that two events happen, with a duration between them of $x > 0$ seconds. If $t_{\text{event } i}^{\text{coord } j}$ denotes the instant of the event i expressed in the time system coordinates j and if two time coordinates system are considered that do not drift with respect to each other, then the duration between the two events is

$$t_{\text{event } 2}^{\text{coord } 1} - t_{\text{event } 1}^{\text{coord } 1} = t_{\text{event } 2}^{\text{coord } 2} - t_{\text{event } 1}^{\text{coord } 2} = x \text{ s}. \tag{1.3}$$

Since the two considered time system coordinates do not drift, it comes

$$t_{\text{event } 2}^{\text{coord } 2} - t_{\text{event } 2}^{\text{coord } 1} = t_{\text{event } 1}^{\text{coord } 2} - t_{\text{event } 1}^{\text{coord } 1}. \tag{1.4}$$

Assuming that the reference of these two time coordinates systems is not the same, i.e.,

$$t_{\text{event } 2}^{\text{coord } 2} - t_{\text{event } 2}^{\text{coord } 1} = t_{\text{event } 1}^{\text{coord } 2} - t_{\text{event } 1}^{\text{coord } 1} = y \text{ s} \tag{1.5}$$

where $y \in \mathbb{R}$, then

$$t_{\text{event } 2}^{\text{coord } 2} - t_{\text{event } 1}^{\text{coord } 1} = x + y \text{ s} \neq x \text{ s}. \tag{1.6}$$

Although measuring a duration, it is possible that $x + y < 0\,\text{s}$. This highlights the importance to measure a duration between two events in the same time coordinates system.

In practice, each GNSS satellite sends signals that are received by a GNSS receiver, along with information about the transmission instant, expressed in the satellite's time coordinates system, and information regarding its position.

All the satellite time coordinates system are different. This is due to the fact that all GNSS satellites carry their own onboard clock. Although of high quality, these clocks are not perfect, which translates to the introduction of satellite specific time coordinates system. In the GNSS literature, these quantities are called the *satellite clock bias*.

Fortunately, thanks to the ground segment, the offset between each satellite time coordinates system and a global time coordinates system (usually an arbitrary constellation-specific time coordinates system) is computed by the ground segment and sent to the GNSS satellites, and then sent by each satellite to the receiver. The choice of global time

This document may not be reproduced, modified, adapted, published, translated in any way, in whole or in part, nor disclosed to a third party without the prior written consent of ENAC. © 2025, ENAC

coordinates system is arbitrary and does not affect the measurement of durations, as time is invariant under Galilean transformations, in first approximation.

Thanks to these corrections, at this point, a receiver has at his disposal a set of instants of emission of signals by visible satellites, all expressed in a common time coordinates system. Thanks to the receiver internal clock, the instants of reception of these signals by the receiver are known. Unfortunately, these instants of reception are expressed in the receiver time coordinates system. The receiver time coordinates system is not the same as the constellation time coordinates system. For this reason, an additional unknown is introduced in the multilateration: the offset between the receiver time coordinates system and the constellation time coordinates system. In the GNSS literature, this quantity is called the *receiver clock bias*. This aspect is important when considering positioning applications, because although modern GNSS receivers such as the ones available in smartphones are connected to the internet and are synchronized, even a very small clock bias leads to very large errors of range measurements. For example, a receiver clock bias of 1 µs leads to an error of $c \cdot 1\,\mu s \approx 300\,m$.

The range measurement that incorporates the receiver and satellite clock bias is referred to the *pseudorange*.

Because of the introduction of this unknown clock bias, Equation (1.1) does not apply anymore. Instead, a modification of it is introduced to account for this unknown clock bias.

In $\mathbb{R}^3$, given a point of unknown coordinates $\boldsymbol{r} \in \mathbb{R}^3$ (the receiver), $dt_r \in \mathbb{R}$ the unknown receiver clock bias, and a set of points of known coordinates $\{\boldsymbol{s}_1, \ldots, \boldsymbol{s}_m\}$ (called references), if the satellite clock bias corrected pseudoranges between the receiver and these references are $\{\tilde{p}_r^{s_1}, \ldots, \tilde{p}_r^{s_m}\}$, then the multilateration consists in finding the solution set of the system

$$\begin{cases} \|\boldsymbol{s}_1 - \boldsymbol{r}\| = \tilde{p}_r^{s_1} - c \cdot dt_r \\ \quad \vdots \\ \|\boldsymbol{s}_m - \boldsymbol{r}\| = \tilde{p}_r^{s_m} - c \cdot dt_r \end{cases} \tag{1.7}$$

with c the propagation velocity of the emitted signals, its value being the speed of light.

The principle of multilateration with pseudoranges is visible in Figure 1.2.

In this case, it is necessary (but not sufficient) to use **four** reference points.

The four unknowns (the receiver's 3D position $\boldsymbol{r}$ and clock bias dt_r) are the usual unknowns in basic GNSS positioning. In practice, the actual observations are not from abstract static points sending signals through vacuum, but from a much more complex phenomenon. So now that the geometric principles of GNSS positioning have been explained qualitatively, the available observations will be introduced, with models that captures all these imperfections. Then, quantitative approaches are proposed to actually compute a receiver position.

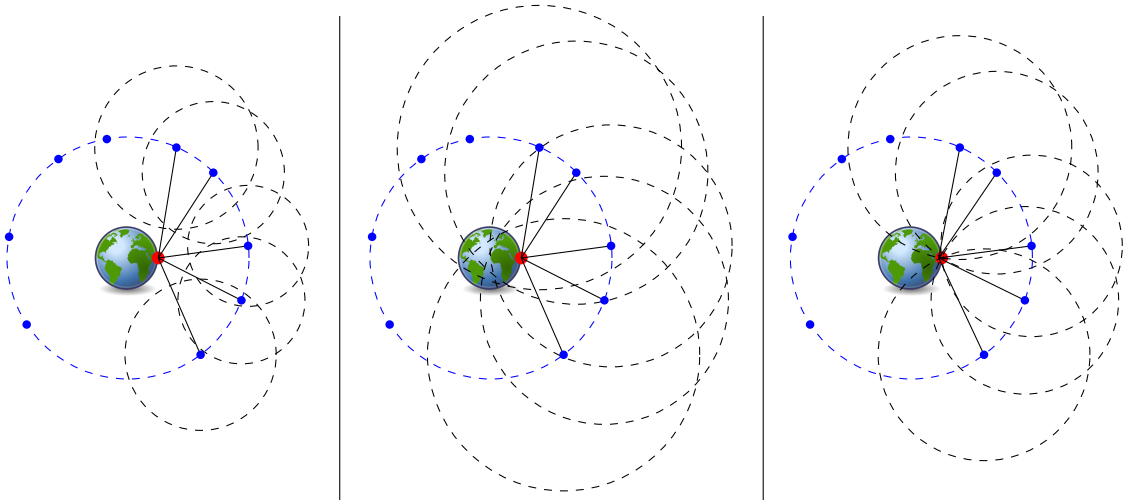

Figure 1.2: Representation (in 2D) of the multilateration principle. The blue points are GNSS satellites, the red point is a GNSS receiver. For each satellite is represented a sphere centered on the satellite, with a radius equal to the pseudorange minus the distance due to the receiver clock bias. The receiver's location corresponds to the intersection of these spheres. Left: the considered receiver clock offset is larger than reality, the intersection is empty. Center: the considered receiver clock offset is smaller than reality, the intersection is empty. Right: the considered receiver clock offset corresponds to the true receiver clock offset, the intersection is a singleton.

1.2 Observation Models

The previous section introduced the fundamental geometric principle underlying GNSS positioning: multilateration. This concept is based on the idea that the position of a GNSS receiver can be determined by measuring the pseudoranges between the receiver and a set of satellites with known positions. Both the receiver's position and clock bias are obtained by solving a system of equations. While this geometric framework provides an essential foundation for understanding GNSS positioning, it is inherently idealized and assumes error-free access to deterministic measurements, which is not the case in practical implementations.

In this section, the shift is on the actual measurements available in real-world GNSS systems. These measurements, which are the basis for all positioning computations, are introduced formally and expressed using observation models. The different types of GNSS measurements are first presented in a general way, laying out the structure of each without yet explaining in details every individual term. This approach allows for a broad understanding of the measurement principles while setting the stage for a more in-depth exploration of the various error sources and biases that influence them.

In practice, the three basic GNSS observations available to the receiver are code pseudoranges, carrier-phase measurements, and Doppler frequency shifts. In positioning applications, these three types of measurements serve distinct purposes: code observations provide direct information on the distance between the satellite and the receiver, but are

This document may not be reproduced, modified, adapted, published, translated in any way, in whole or in part, nor disclosed to a third party without the prior written consent of ENAC. © 2025, ENAC

relatively noisy. Carrier-phase observations offer much higher precision and are essential for high-accuracy techniques, though they are ambiguous due to the integer number of carrier cycles. Doppler observations provide information on the pseudorange rate.

A fourth type of observation, the TDCP, can be constructed, at the receiver level, from the difference between consecutive carrier-phase measurements. It combines the high precision of phase data with the advantage of canceling many constant and slowly-varying biases, making it especially useful for accurate positioning.

Each of these observation types are examined in a dedicated section to understand their characteristics.

Following this initial overview, a last section is organized into a series of dedicated subsections, each addressing a specific component of the observation models. These components include satellite clock errors, atmospheric delays (ionospheric and tropospheric), hardware biases, multipath effects, and measurement noise, among others. For each of these, the physical origin of the effect is discussed along with a mathematical model. The objective is to provide a clear and intuitive understanding of the phenomena involved, without delving into overly complex physical modeling or highly detailed analysis. This level of detail is chosen deliberately: while a solid understanding of the key error sources and their impact on positioning accuracy is necessary, the core objective of this thesis is not to advance physical modeling techniques, but rather to develop and improve positioning algorithms that can work effectively in real environments.

As such, the treatment of the observation models and their components is oriented toward their practical implications for positioning. Emphasis is placed on how each term influences the measurements, how these influences can be modeled or mitigated, and what level of accuracy can be reasonably expected. This modeling framework serves as the foundation for the algorithmic developments that follow in following chapters, where the focus shifts to estimation techniques.

1.2.1 Code Pseudorange

The first type of observations are *code pseudoranges*. The reasons behind this name are detailed in Section 1.4. Given a receiver of coordinates $\boldsymbol{r} \in \mathbb{R}^3$ at the instant of reception and a GNSS satellite i of coordinates $\boldsymbol{s}_i \in \mathbb{R}^3$ at the instant of transmission, the code pseudorange observation can be modeled as [13, Chapter 19]

$$P_r^{s_i} = \rho_r^{s_i} + c \cdot (dt_r - dt^{s_i} + \delta t^{\mathrm{rel},s_i}) + I_r^{s_i} + T_r^{s_i} + \mathrm{sag}_r^{s_i} + d_r - d^{s_i} + \xi_r^{s_i} + \varepsilon_P^{s_i}, \tag{1.8}$$

where the terms are defined as follows (all quantities are expressed in meters unless stated otherwise)

- $P_r^{s_i}$ is the measured code pseudorange,
- $\rho_r^{s_i} = \|\boldsymbol{r} - \boldsymbol{s}_i\|$ is the range between the receiver and the emitting satellite,

Table 1.2: Typical values of errors in code pseudorange observations [14].

Term	Amplitude
Satellite clock bias	100 km
Relativistic effects	13 m
Ionosphere	2 m to 30 m
Troposphere	2 m to 30 m
Sagnac effect	30 m
Hardware delays	2 m
Hardware delay variation	receiver and satellite specific
Multipath and/or occlusion	case-by-case
Receiver error	3 m

- dt_r and dt^{s_i} refer to respectively receiver and satellite clock biases (with respect to the constellation time coordinates system), in seconds,
- $\delta t^{\text{rel},s_i}$ refers to relativistic effects, in seconds,
- $I_r^{s_i}$ refers to the ionospheric delay,
- $T_r^{s_i}$ refers to the tropospheric delay,
- $\text{sag}_r^{s_i}$ refers to the Sagnac effect delay,
- d_r and d^{s_i} refer respectively to the receiver and satellite hardware delays,
- $\xi_r^{s_i}$ refers to hardware delay variations,
- $\varepsilon_P^{s_i}$ refers to multipath and receiver error.

The typical values of each of these terms are summarized in Table 1.2. Note that while some terms are given in seconds in Equation (1.8), they appear in meters in Table 1.2 because they are multiplied by the speed of light c.

1.2.2 Carrier-Phase

The second type of observations are *carrier-phase*. The reasons behind this name are also detailed in Section 1.4. Given a receiver of coordinates $\boldsymbol{r} \in \mathbb{R}^3$ at the instant of reception and a GNSS satellite i of coordinates $\boldsymbol{s}_i \in \mathbb{R}^3$ at the instant of transmission, the carrier-phase observation can be modeled as [13, Chapter 19]

$$\Phi_r^{s_i} = \rho_r^{s_i} + c\cdot(dt_r - dt^{s_i} + \delta t^{\text{rel},s_i}) - I_r^{s_i} + T_r^{s_i} + \text{sag}_r^{s_i} + \lambda\cdot(N_r^{s_i} + \omega_r^{s_i}) + \delta_r - \delta^{s_i} + \zeta_r^{s_i} + \varepsilon_\Phi^{s_i}, \quad (1.9)$$

This document may not be reproduced, modified, adapted, published, translated in any way, in whole or in part, nor disclosed to a third party without the prior written consent of ENAC. © 2025, ENAC

where the terms are defined as follows (all quantities are expressed in meters unless stated otherwise)

- $\Phi_r^{s_i}$ is the measured carrier-phase,
- $\rho_r^{s_i} = \|\boldsymbol{r} - \boldsymbol{s}_i\|$ is the range between the receiver and the emitting satellite,
- dt_r and dt^{s_i} refer respectively to the receiver and satellite clock bias (with respect to the constellation time coordinates system), in seconds,
- $\delta t^{\text{rel},s_i}$ refers to the relativistic effects, in seconds,
- $I_r^{s_i}$ refers to the ionospheric delay,
- $T_r^{s_i}$ refers to the tropospheric delay,
- $\text{sag}_r^{s_i}$ refers to the Sagnac effect delay,
- λ refers to the carrier's wavelength,
- $N_r^{s_i}$ refers to the integer number of cycles between the receiver and the satellite and is unitless,
- $\omega_r^{s_i}$ refers to the phase wind-up, which takes into account orientations of the receiver and satellite antennas, in radians,
- δ_r and δ^{s_i} refer respectively to the receiver and satellite hardware delay,
- $\zeta_r^{s_i}$ refers to hardware delays variation,
- $\varepsilon_\Phi^{s_i}$ refers to multipath and receiver error.

The typical values of each of these terms are summarized in Table 1.3. Note that while some terms are given in seconds in Equation (1.9), they appear in meters in Table 1.3 because they are multiplied by the speed of light c.

It can be noticed that multiple terms are common to the code pseudorange and the carrier-phase. The terms $\rho_r^{s_i}$, dt_r, dt^{s_i} and δ^{rel} appearing in Equation (1.9) are the same in Equation (1.8). In first approximation, the ionospheric effect $I_r^{s_i}$ is the same in both equations, although a minus appears in the carrier-phase equation, leading to an advance instead of a delay. Reasons behind this phenomenon are explained in Section 1.2.5. The tropospheric effects $T_r^{s_i}$ are also considered equal. The carrier-phase observation is also affected by receiver and satellite hardware biases, hardware delay variations, multipath and receiver error. The values of these terms differ from the ones that are present in the code pseudorange Equation (1.8), hence a different notation. Two terms have appeared in Equation (1.9): $\omega_r^{s_i}$ which accounts for a change in the measured phase in case of rotations of the antennas, and an unknown integer number $N_r^{s_i}$ that is multiplied by the wavelength λ of the considered carrier frequency.

Table 1.3: Typical values of errors in carrier-phase observations [14].

Term	Amplitude
Satellite clock bias	100 km
Relativistic effects	13 m
Ionosphere	2 m to 30 m
Troposphere	2 m to 30 m
Sagnac effect	30 m
Hardware delays	2 m
Hardware delay variation	receiver and satellite specific
Multipath and/or occlusion	case-by-case
Receiver error	carrier and C/N0 specific

1.2.3 TDCP

The TDCP observations are obtained by computing the difference between two carrier-phase observations at two different instants, from the same satellite. Formally, given two instants t and t', the TDCP observation for the satellite i is

$$\Delta\Phi_r^{s_i} = \Phi_r^{s_i}(t') - \Phi_r^{s_i}(t) \tag{1.10}$$

where $\Phi_r^{s_i}(t)$ denotes the carrier-phase observation at instant t. This differencing operation eliminates several constant and slowly varying biases, such as the integer ambiguity $N_r^{s_i}$ and the hardware delays δ_r, δ^{s_i}, as long as these do not vary significantly between epochs. The resulting observable provides a highly precise measurement of the receiver coordinates at the two epochs.

The full model for the TDCP observation is derived by differencing Equation (1.9) across two instants,

$$\begin{aligned}\Delta\Phi_r^{s_i} = \Delta\rho_r^{s_i} + c\cdot\left(\Delta dt_r - \Delta dt^{s_i} + \Delta\delta t^{\mathrm{rel},s_i}\right) - \Delta I_r^{s_i} + \Delta T_r^{s_i} \\ + \Delta\mathrm{sag}_r^{s_i} + \lambda\cdot(\Delta N_r^{s_i} + \Delta\omega_r^{s_i}) + \Delta\delta_r - \Delta\delta^{s_i} + \Delta\zeta_r^{s_i} + \Delta\varepsilon_\Phi^{s_i}\end{aligned} \tag{1.11}$$

where Δ indicates the difference of a term at two instants. In this model,

- $\Delta\rho_r^{s_i}$ reflects the change in distance due to the relative motion between satellite and receiver,
- Δdt_r and Δdt^{s_i} exist since the clocks drift, (although satellite are equipped with high-end clocks),
- unless a Cycle Slip (CS) happens, the term $\Delta N_r^{s_i}$ is null, which removes one of the main difficulties of standard carrier-phase processing,

This document may not be reproduced, modified, adapted, published, translated in any way, in whole or in part, nor disclosed to a third party without the prior written consent of ENAC. © 2025, ENAC

- the atmospheric effects being relatively slowly varying, they contribute minimally over short time intervals,
- the hardware delays being constant, their difference cancels
- the receiver errors are considered independent Gaussian random variables, so their variance add-up,
- the Sagnac and relativistic effects as well as phase wind-up remain in the TDCP model.

Because many of the slowly varying error sources cancel out in the differencing, TDCP measurements are notably more precise than absolute carrier-phase or code pseudorange observations.
The study of TDCP is dedicated to Chapter 4.

1.2.4 Doppler

The Doppler observations correspond to the frequency shift of a wave, in relation to an observer that is moving, relatively to the source of the wave.
Considering Galilean Doppler (i.e., omitting relativistic effects) of a signal emitted by a GNSS satellite and received by a GNSS receiver, its formula is given by [13, Chapter 19]

$$D_r^{s_i} = f_r - f^{s_i} \tag{1.12}$$

with

$$\frac{f_r}{f^{s_i}} = \frac{1 + \frac{\boldsymbol{\rho}_r^{s_i\mathsf{T}} \boldsymbol{v}_r}{\rho_r^{s_i} c}}{1 + \frac{\boldsymbol{\rho}_r^{s_i\mathsf{T}} \boldsymbol{v}^{s_i}}{\rho_r^{s_i} c}} \tag{1.13}$$

where

- $D_r^{s_i}$ corresponds to the Doppler observation, in Hz,
- f_r corresponds to the carrier frequency as received by the receiver,
- f^{s_i} corresponds to the carrier frequency as emitted by the emitter,
- $\boldsymbol{\rho}_r^{s_i}$ corresponds to the receiver to satellite vector, $\rho_r^{s_i}$ corresponds to its norm,
- c is the speed of light,
- $\boldsymbol{v}_r$ and $\boldsymbol{v}^{s_i}$ are respectively the receiver and satellite velocity vectors.

The frequencies f_r and f^{s_i} differ from the nominal carrier frequency due to the motion of the receiver and the satellite. Therefore, the Doppler observations provide mainly information on the receiver velocity along the Line-Of-Sight (LOS).

Considering $\boldsymbol{v}_r$ and $\boldsymbol{v}^{s_i}$ are both very small compared to c, at first order, it can be shown that

$$D_r^{s_i} \approx \frac{1}{\lambda}\left(\frac{\boldsymbol{v}^{s_i}}{c} - \frac{\boldsymbol{\rho}_r^{s_i}}{\rho_r^{s_i}}\right)^{\mathsf{T}} (\boldsymbol{v}^{s_i} - \boldsymbol{v}_r) \tag{1.14}$$

with λ the carrier wavelength.

As with the other observables, the raw Doppler measurement also includes contributions from satellite and receiver clock drifts, as well as relativistic effects, which must be modeled or estimated for accurate velocity computation.

This observable can be multiplied by the wavelength λ in order to obtain the relative velocity of the receiver with respect to the satellite velocity, along the LOS.

1.2.5 Terms in Observation Models

Now that the three fundamental GNSS observations (code pseudorange, carrier-phase, and Doppler) have been introduced, this section delves deeper into the components of these observations. The goal is to develop a clearer understanding of the underlying physical principles of GNSS, which is essential for effectively interpreting and processing the raw observations.

1.2.5.1 Range

The term $\rho_r^{s_i} = \|\boldsymbol{r} - \boldsymbol{s}_i\|$ represents the geometric range between the receiver and the satellite. It is computed as the Euclidean distance between the satellite's position $\boldsymbol{s}_i \in \mathbb{R}^3$ at the instant of transmission and the receiver's position $\boldsymbol{r} \in \mathbb{R}^3$ at the instant of reception. In practice, the satellite position $\boldsymbol{s}_i$ is obtained from the ephemerides (orbital parameters) broadcast in the navigation message (Section 1.4), or through precise orbit products, depending on the application and targeted level of precision.

1.2.5.2 Clock Biases

As explained when introducing pseudoranges, GNSS relies on precise timing. Each satellite carries highly stable atomic clocks, but even these exhibit small drifts with respect to the constellation time coordinates. Similarly, the receiver's internal clock is not synchronous with the constellation time coordinates. dt^{s_i} and dt_r are respectively the satellite and receiver clock biases relative to the constellation system time.

Since time errors translate into distance through the speed of light c, a 1 µs error leads to an error of $c \cdot 1\,\mu s \approx 300\,m$ range error. The receiver clock bias is usually treated as unknown in the positioning equations and is estimated along with the receiver's position, as explained in Section 1.1.2.2. Satellite clock corrections are broadcast in the navigation message and consist of a reference epoch and drift coefficients, often modeled as a second-order polynomial [10, Chapter 7].

This document may not be reproduced, modified, adapted, published, translated in any way, in whole or in part, nor disclosed to a third party without the prior written consent of ENAC. © 2025, ENAC

1.2.5.3 Relativistic Effects

Relativistic effects, represented by $\delta t^{\text{rel},s_i}$, are due to both special relativity [15] and general relativity [16].

Two identical clocks (one aboard a satellite and the other on Earth's surface) tick at different rates due to the combined effects of gravitational potential differences (as described by general relativity) and their relative motion (as described by special relativity). The special relativity indicates that because satellites move at speeds of about $3.9\,\text{kms}^{-1}$, their clocks appear to run faster ($38\,\mu\text{s}$ per day) from the Earth's frame of reference [14]. Since the GNSS satellites orbit at around $20\,000\,\text{km}$ of altitude, the general relativity indicates that they are in a zone where the gravitational potential is weaker. Consequently, time flows faster for satellite clocks relative to those on Earth's surface.

A commonly used relativistic clock correction model is [14]

$$\delta t^{\text{rel},s_i} = -\frac{2}{c^2}\boldsymbol{v}_{s_i}^{\mathsf{T}}\boldsymbol{s}_i \tag{1.15}$$

where $\boldsymbol{v}_{s_i} \in \mathbb{R}^3$ is the satellite's velocity and $\boldsymbol{s}_i \in \mathbb{R}^3$ is its position vector, both in an Earth-Centered Inertial (ECI) frame. The amplitude of the relativistic effect ranges up to $13\,\text{m}$ [14].

A secondary relativistic effect introduces a correction to the geometric range due to space-time curvature, known as the Shapiro signal propagation delay. Its impact on the measured pseudorange is lower than $2\,\text{cm}$ [14], so it can generally be neglected (excepted in applications requiring extremely high positioning accuracy).

The understanding of the proposed clock correction and of the Shapiro effect would lead to the introduction of the Lorentz transform and the Einstein tensor, which is out of the scope of this work. Readers interested in comprehension of the impact of both special and general relativity on GNSS can refer to [17].

1.2.5.4 Ionosphere

The ionosphere is the region of Earth's atmosphere extending from approximately $60\,\text{km}$ to over $2000\,\text{km}$ in altitude. It consists of a partially ionized medium formed by solar radiation and by the influx of charged particles. The propagation speed of electromagnetic waves through the ionosphere depends on its electron density, which varies based on two key processes. During the day, solar radiation ionizes atoms, creating free electrons and ions. At night, recombination dominates, resulting in a decrease in electron density.

The ionosphere is a dispersive layer [18], i.e., it behaves like a frequency-dependent medium. For this reason, two distinct refractive indices are studied: one associated with the phase and the other with the group, both derived respectively from the phase velocity and the group velocity of a wave, i.e.,

$$n_\phi = \frac{c}{v_\phi} \tag{1.16}$$

and

$$n_g = \frac{c}{v_g} \tag{1.17}$$

where v_ϕ and v_g are respectively the phase and group velocity, n_ϕ and n_g are respectively the phase and group refractive indices, and c is the speed of light.

In the ionosphere, the phase refractive index can be expressed as a series expansion, and similarly, the group refractive index follows the same approach [19]

$$n_\phi = 1 + \frac{c_2}{f^2} + \frac{c_3}{f^3} + \frac{c_4}{f^4} + \dots \tag{1.18}$$

and

$$n_g = 1 - \frac{c_2}{f^2} - \frac{2c_3}{f^3} - \frac{3c_4}{f^4} - \dots \tag{1.19}$$

where c_2, c_3 and c_4 are coefficients that depend on the local density of electrons, and f is the wave frequency.

The series are typically truncated at the first order to yield practical expressions for the phase and group refractive indices

$$n_\phi \approx 1 + \frac{c_2}{f^2} \tag{1.20}$$

and

$$n_g \approx 1 - \frac{c_2}{f^2} \tag{1.21}$$

where $c_2 \approx -40.3 \cdot n_e$ (in s^{-2}), with n_e being the local density of electrons.

Substituting these first-order approximations into the definitions of phase and group velocities (i.e., Equation (1.20) into Equation (1.16) and Equation (1.21) into Equation (1.17)) leads to

$$v_\phi \approx \frac{c}{1 - \frac{40.3 \cdot n_e}{f^2}} \tag{1.22}$$

and

$$v_g \approx \frac{c}{1 + \frac{40.3 \cdot n_e}{f^2}}. \tag{1.23}$$

From these expressions, the local phase and group velocities are obtained. The expressions reflect the fact that the ionosphere slows down the group velocity of the signal (causing a delay), while the phase velocity can exceed the speed of light (leading to an advance).

With the local phase and group velocities determined, one can compute the corresponding propagation advance or delay. Generally, the refractive index profiles (dependent on altitude due to variations in electron density) are integrated along the vertical path to obtain the vertical delay. This is done by integrating the difference between the refractive index profile and a unity refractive indice (the refractive indice of vacuum), along the propagation path, leading to a propagation advance or delay respectively for the phase and group.

This document may not be reproduced, modified, adapted, published, translated in any way, in whole or in part, nor disclosed to a third party without the prior written consent of ENAC. © 2025, ENAC

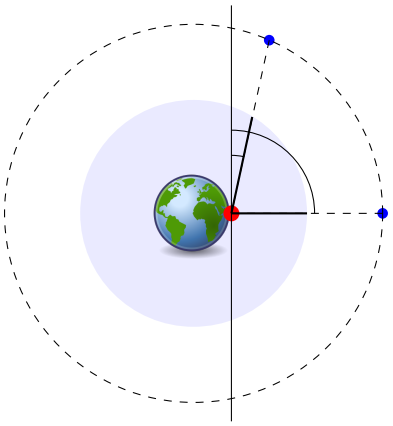

Figure 1.3: Representation (in 2D) of the ionosphere. The blue area represents the ionosphere, and the blue dots indicate the positions of two satellites. The angles represent the elevation angles of the satellites as observed by the receiver (indicated by the red dot). The satellite at higher elevation has a shorter path through the ionosphere, resulting in less ionospheric impact compared to the satellite at lower elevation.

A consequence of this computation is that the obtained group delay corresponds exactly to the obtained phase advance, since $n_\phi - 1 \approx -(n_g - 1)$.

This vertical advance or delay is then extended to account for slant (non-vertical) signal paths. This is done by the use of mapping functions that correct for the increased propagation path length through the ionosphere. In practice, the lower the satellite elevation, the longer the signal path through the ionosphere, as illustrated in Figure 1.3.

Single frequency receivers have to apply an ionospheric correction, as this group delay can reach 30 m [14]. In practice, correction models exist such as Klobuchar [20] and NeQuick [21].

Other approaches are possible to cancel ionospheric effects: dual-frequency receivers can eliminate the first-order ionospheric group delay by forming an ionosphere-free linear combination of signals at two different frequencies (e.g., GPS L1 and L2 frequencies). Refer to Section 1.3.2.1 for an application of this technique.

In reality, higher-order ionospheric effects still remain and may require advanced modeling for high-precision applications [22].

1.2.5.5 Troposphere

The troposphere is the lowest layer of the atmosphere, extending from the Earth's surface up to around 50 km of altitude. In contrast with the ionosphere, it is non-dispersive for GNSS frequencies. As a consequence, group and phase velocity are equal, leading to code and carrier observations that are delayed equally.

The tropospheric delay is often split into two components:

- Dry delay: it accounts for 90 % of the total delay, and is relatively stable since it arises from the dry air,

- Wet delay: caused by water vapor content, it is highly variable and harder to model.

Typical Tropospheric Zenith Path Delay (ZTD) is about 2 m at sea level. The delay increases with lower satellite elevation angles due to the longer path through the atmosphere (as it is the case with the ionosphere), typically to 25 m for a satellite at an elevation of 5°.

As it is the case with the ionosphere, empirical models such as the Saastamoinen model or UNB3 [23] are used to estimate a delay for a satellite at the zenith, which is then mapped to the actual satellite elevation angle using a mapping function.

Both dry and wet delays vary with time. The wet delay is subject to significant daily and seasonal changes, which can affect its variability throughout the year. The dry delay is more constant, but it can still vary slightly with atmospheric pressure changes.

1.2.5.6 Sagnac Effect

The Sagnac effect arises due to the Earth's rotation during the time the GNSS signal propagates from satellite to receiver. Because the Earth rotates, the receiver moves (in an ECI frame) between the instant when the signal is transmitted and the instant when it is received. This causes a path length difference.

The principle of the Sagnac effect is visible in Figure 1.4.

A common approach to correct for the Sagnac effect is to eliminate it by using an ECI frame for satellite and user position calculations. The ECI frame can be conveniently derived by freezing the Earth-Centered Earth-Fixed (ECEF) frame [9]. Another approach consists in applying a rotation to the satellites that depends on the propagation duration [13]. The Sagnac effect can also be corrected with [13, Chapter 19]

$$\mathrm{sag}_r^{s_i} = \frac{1}{c} \left(\boldsymbol{s}_i \times \boldsymbol{r} \right)^\mathsf{T} \boldsymbol{\omega}_E \tag{1.24}$$

where $\boldsymbol{\omega}_E \in \mathbb{R}^3$ is the Earth's rotation vector and $\times$ is the cross product application in $\mathbb{R}^3$.

Its impact on measured pseudoranges can reach 30 m [24].

1.2.5.7 Hardware Delays

Hardware delays (d_r, d^{s_i}, δ_r and δ^{s_i}) arise from processing within the receiver and satellite hardware chains. These include cable, antenna, filter or analog-to-digital conversion latency.

Satellite hardware delays are often corrected through values provided in the navigation message or through differential techniques. Receiver hardware delays must be calibrated or estimated.

As these delays depend on the observation type, on the carrier frequency, on the receiver and on the satellite, they are not further developed.

This document may not be reproduced, modified, adapted, published, translated in any way, in whole or in part, nor disclosed to a third party without the prior written consent of ENAC. © 2025, ENAC

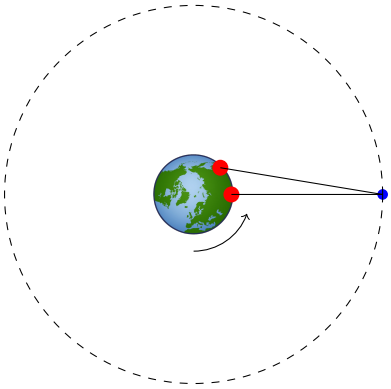

Figure 1.4: Illustration (in 2D) of the Sagnac effect. The receiver's location in the ECEF frame remains constant between the instants of emission and of reception of the GNSS signal. However, due to the Earth's rotation, the receiver's distance to the satellite, at the instant of emission, changes.

1.2.5.8 Code and Carrier-Phase Hardware Delay Variations

These variable code pseudorange delays $\xi_r^{s_i}$ and carrier-phase delays $\zeta_r^{s_i}$ arise from the radiation characteristics of both the transmitting and receiving antennas. Consequently, they are dependent on the direction of signal transmission or reception, as well as on the signal frequency.

In the literature, the code pseudorange delay introduced by these phenomena are often referred to as group-delay variations [25].

1.2.5.9 Multipath and Occlusion

Multipath occurs when a GNSS signal reaches the receiver via the LOS, as well as from Non-Line-Of-Sight (NLOS), typically reflected paths from buildings, ground, water, etc. These delayed replicas interfere with the direct signal and distort the correlation process used to determine code or carrier phase.

The principle of multipath is visible in Figure 1.5.

Multipath is site-dependent and varies with the environment, satellite geometry, and antenna characteristics. For this reason, multipath modeling is a complex problem. Current research focuses on mitigating these effects using a combination of hardware solutions (such as multi-frequency and choke ring antennas designed to suppress reflected signals) and software techniques, including signal processing methods and robust estimation algorithms that can detect and reduce the influence of multipath-contaminated measurements on position solutions [26].

Signal occlusion occurs when the LOS is blocked by obstacles such as buildings, vegetation, etc. In such cases, the receiver may only receive signals that have been reflected or diffracted, often with significant delay and attenuation. These NLOS signals can severely degrade positioning accuracy, as they do not represent the true geometric path between the satellite and receiver.

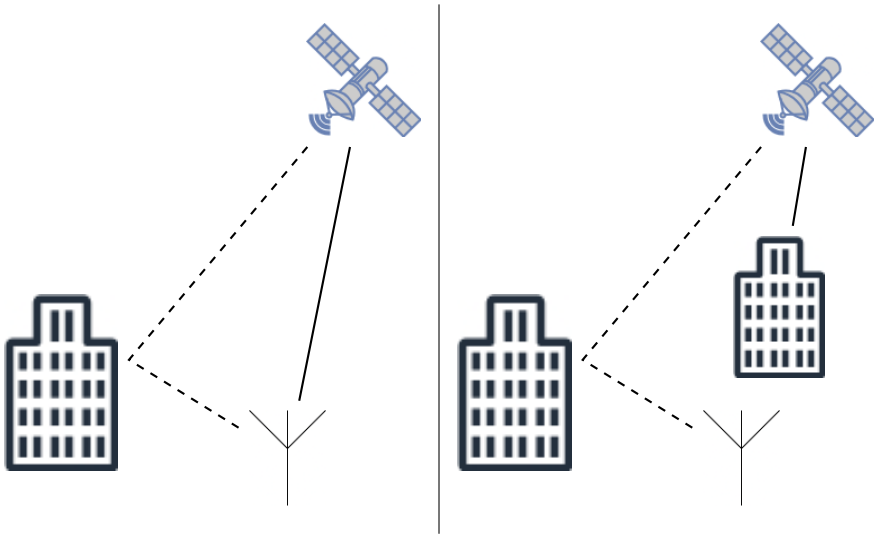

Figure 1.5: Illustration (in 2D) of two GNSS signal propagation scenarios. On the left, a multipath effect occurs where the satellite signal reaches the GNSS antenna via both the LOS (solid line) and a NLOS (dashed line) off a nearby building. On the right, an occlusion scenario is shown where the LOS between the antenna and the satellite is blocked by a building, therefore only the reflected signal is received.

The principle of occlusion is visible in Figure 1.5.

Like multipath, occlusion is highly site-dependent and varies with the physical environment and satellite-receiver geometry. However, unlike typical multipath scenarios where both direct and reflected signals are present, occlusion situations involve only indirect signals, making it even more difficult to distinguish valid measurements. Mitigation strategies [27] involve both hardware approaches, such as the use of directional antennas, and software techniques, including elevation masks, NLOS detection and exclusion algorithms, robust estimation frameworks designed to handle biased or unreliable measurements or machine learning models trained to identify signal anomalies [28].

Multipath errors can significantly impact GNSS code measurements, often introducing biases of several meters, while carrier-phase measurements are generally less affected but can still suffer from sub-centimeter-level errors that may degrade high-precision applications.

1.2.5.10 Receiver Error

Receiver noise in GNSS observations originates from two primary sources. First, electrical components of the signal processing chain within the receiver (amplifiers, filters, and converters) introduce internal noise. Second, the antenna collects external noise from its surrounding environment, which can come from both natural sources (cosmic radiation, lightning, etc.) and artificial sources (electronic devices, radio transmissions, etc.).

This noise introduces random errors in all GNSS observations. The impact of this noise can be assessed by comparing the power of the received satellite signal and the power of the background noise.

This document may not be reproduced, modified, adapted, published, translated in any way, in whole or in part, nor disclosed to a third party without the prior written consent of ENAC. © 2025, ENAC

A commonly used metric for signal quality is the Carrier-to-noise Density Ratio (C/N0), which represents the ratio between the power of the carrier signal and the noise power density in a 1 Hz bandwidth. A high C/N0 indicates either a strong received signal or a low ambient noise floor, both of which result in more reliable GNSS measurements.

The measurement noise introduced by a receiver's tracking loops is directly influenced by the C/N0 of the received signal.

For Binary Phase Shift Keying (BPSK) modulated signals with C/N0 $> 35\,\mathrm{dB\,Hz}$, the standard deviation σ_{DLL} of the introduced noise within a Delay Lock Loop (DLL) with an early-minus-late correlator follows the relation [13, Chapter 19]

$$\sigma_{\mathrm{DLL}} \propto \frac{1}{\sqrt{C/N0}}. \tag{1.25}$$

Assuming a high C/N0, the noise standard deviation σ_{PLL} of a Phase Lock Loop (PLL) follows

$$\sigma_{\mathrm{PLL}} \propto \frac{1}{\sqrt{C/N0}}. \tag{1.26}$$

Equations (1.25) and (1.26) show that the noises in code pseudorange and carrier-phase observations decrease as C/N0 increases.

Modern GNSS receivers, particularly those tracking high-rate modernized signals, can achieve low values of code pseudorange noise standard deviations under favorable signal conditions.

With all GNSS observations now described, they can be used to determine a user's position. The following section introduces three different positioning algorithms used for this purpose.

1.3 Positioning Algorithms

In Section 1.2, a comprehensive modeling framework for the various types of GNSS observations is presented. These observation models account for a wide range of physical phenomena that affect the propagation of GNSS signals and the measurements derived from them. Each phenomenon contributes a specific term to the observation equations, and each term can vary significantly in its mathematical complexity and physical interpretation. They are treated with varying levels of detail and accompanied by references for readers interested in a deeper exploration of individual terms. Examples include atmospheric delays, relativistic effects, and multipath interference, among others.

While it is possible (and often necessary in specialized studies) to examine each of these terms in isolation and develop sophisticated models for their correction, such an approach is not the focus of this work. Instead, the philosophy adopted in this thesis is to treat the observation models in an abstracted manner. That is, many of the individual error sources are corrected or mitigated by external software tools or correction services. This allows

to concentrate on simplified observation models and their use in positioning algorithms, without requiring a deep understanding or modeling of each physical phenomenon.

The use of these corrections depends on the considered application at hand. Indeed, GNSS observations are used in a variety of domains, including but not limited to positioning, timing, remote sensing or reflectometry. Each of these applications has different objectives and requirements, in terms of accuracy, robustness, and computational complexity. In the context of this thesis, the focus is on positioning applications. Depending on the precision required by the application, different positioning strategies can be employed.

In practice, most methods rely on the assumption that the majority of error sources are corrected, at least partially. This enables the formation of a simplified model, where only a subset of terms remain to be estimated. The accuracy of this simplified model, and hence of the final positioning solution, depends on the quality of the corrections applied. Therefore, the selection of an appropriate positioning algorithm must take into account not only the desired level of precision but also the availability and reliability of correction data.

This section introduces a series of positioning techniques that are commonly used in GNSS applications. It starts with SPP, a method characterized by its simplicity and minimal computational requirements. SPP can be implemented with limited infrastructure and is suitable for applications where meter accuracy is sufficient. However, its precision is limited by the presence of uncorrected or imperfectly corrected errors.

To achieve higher levels of accuracy, more advanced techniques are required. PPP and RTK positioning are two such methods. PPP relies on precise satellite orbit and clock products and can achieve decimeter to centimeter accuracy without the need for nearby reference stations, but requires a convergence time. RTK, on the other hand, uses differential techniques and requires a base stations to provide real-time corrections, enabling rapid convergence to centimeter-level accuracy. Both methods involve a higher degree of algorithmic complexity and require more sophisticated correction data.

Each of these techniques presents specific advantages and limitations, and their suitability depends on the constraints and goals of the intended application. The following subsections provide a detailed overview of these positioning methods, examining their theoretical foundations, practical implementation, and expected performance in various use cases.

1.3.1 Single Point Positioning

1.3.1.1 Observations and Estimated Variables

In the context of SPP, the goal is to estimate the receiver's three-dimensional position $\boldsymbol{r}$ along with its clock bias dt_r, using only code pseudorange measurements from visible GNSS satellites. This technique represents the most basic form of GNSS positioning and does not rely on any external correction services or reference stations.

In its formulation, only a single instant (or *epoch*) is considered: the epoch at which the

This document may not be reproduced, modified, adapted, published, translated in any way, in whole or in part, nor disclosed to a third party without the prior written consent of ENAC. © 2025, ENAC

position is to be estimated. There is no temporal correlation considered between epochs, and thus, no need for time-specific notation or dynamic modeling. Each epoch is treated independently.

All relevant physical phenomena affecting the code pseudorange have been described in the previous section. In the case of SPP positioning, the focus is on applying available models and corrections to compute adjusted code pseudorange observations, typically using broadcast ephemerides and correction models available in the navigation message. These corrections, while essential, are not perfect. Thus, residuals errors are left within corrected observations. These residual errors are modeled as mutually independent Gaussian random variables. This assumption allows their variances to be summed, resulting in a simplified observation model characterized by a single additive Gaussian noise term. With all satellite coordinates computed at the correct transmission time and all measurements time-synchronized, the system is properly set up for PVT estimation.

1.3.1.2 Estimation of Receiver Coordinates and Clock Bias

At that point, multilateration with observations containing random variables is introduced. This requires basic knowledge of probabilities and estimation theory. More particularly, the Maximum Likelihood Estimator (MLE) is used throughout all chapters of this thesis. If necessary, refer to Appendix A for details on the construction of the MLE.

The corrected pseudorange measurement from satellite i can be modeled as

$$\tilde{P}_r^{s_i} = \rho_r^{s_i} + c \cdot dt_r + \tilde{\varepsilon}_P^{s_i} \tag{1.27}$$

where

- $\tilde{P}_r^{s_i}$ is the corrected pseudorange measurement to satellite i,
- $\rho_r^{s_i} = \|\boldsymbol{s}_i - \boldsymbol{r}\|$ with $\boldsymbol{r} \in \mathbb{R}^3$ is the unknown receiver position vector, $\boldsymbol{s}_i \in \mathbb{R}^3$ is the known satellite position vector,
- c is the speed of light,
- dt_r is the unknown receiver clock bias,
- $\tilde{\varepsilon}_P^{s_i}$ is a Gaussian random variable that corresponds to the sum of $\varepsilon_P^{s_i}$ and of all correction residuals (i.e., the residual error), so $\tilde{\varepsilon}_P^{s_i} \sim \mathcal{N}(0, \sigma_i^2)$ with σ_i depending on the signal quality and on residual of applied corrections.

The corrected code pseudorange $\tilde{P}_r^{s_i}$ is a random variable. The notation $x \sim \mathcal{N}(\mu, \sigma^2)$ indicates that the random variable x follows a Gaussian distribution, with mean value μ and standard deviation σ.

Assuming that m satellites are visible by the receiver, then m code pseudorange equations

are available

$$\begin{cases} \tilde{P}_r^{s_1} \sim \mathcal{N}\left(\rho_r^{s_1} + c \cdot dt_r, \sigma_1^2\right) \\ \quad \vdots \\ \tilde{P}_r^{s_m} \sim \mathcal{N}\left(\rho_r^{s_m} + c \cdot dt_r, \sigma_m^2\right). \end{cases} \tag{1.28}$$

Usually, the m random variables are assumed independent, i.e., $(\tilde{\varepsilon}_P^{s_i})_{i\in\{1,\dots,m\}}$ are independent.

Now that random variables are introduced in the multilateration problem Equation (1.28), the geometrical approach proposed previously is not applicable.

Instead, given the statistical model defined in Equation (1.28) and the assumption that the corrected pseudorange measurements $\tilde{P}_r^{s_i}$ are independent Gaussian random variables, the estimation of the receiver's position $\boldsymbol{r}$ and clock bias dt_r can be obtained by means of the MLE.

Practically, the receiver has at his disposal a sample of each of these corrected code pseudorange random variables. Let $\tilde{p}_r^{s_i}$ be the observed value (i.e., the sample) of the random variable $\tilde{P}_r^{s_i}$.

In that case, the likelihood function $\mathcal{L}\left(\tilde{p}_r^{s_1}, \dots, \tilde{p}_r^{s_m}\right) : \mathbb{R}^3 \times \mathbb{R} \to \mathbb{R}^+$ is the likelihood of the receiver coordinates and clock bias, given the set of corrected code pseudorange observations $\{\tilde{p}_r^{s_1}, \dots, \tilde{p}_r^{s_m}\}$. As explained in Chapter 2, since the corrected code pseudorange observations are assumed to be samples of mutually independent Gaussian random variables, the likelihood function is the product of each code pseudorange likelihood function, i.e.,

$$\mathcal{L}\left(\tilde{p}_r^{s_1}, \dots, \tilde{p}_r^{s_m}\right) : (\boldsymbol{r}, dt_r) \mapsto \prod_{i=1}^{m} \frac{1}{\sqrt{2\pi\sigma_i^2}} \exp\left(-\frac{1}{2}\frac{\left(\tilde{p}_r^{s_i} - \rho_r^{s_i} - c \cdot dt_r\right)^2}{\sigma_i^2}\right). \tag{1.29}$$

If this function admits a unique maximizer, the MLE is defined as

$$\widehat{\boldsymbol{r}}, \widehat{dt}_r = \arg\max \mathcal{L}\left(\tilde{p}_r^{s_1}, \dots, \tilde{p}_r^{s_m}\right). \tag{1.30}$$

Maximizing the likelihood function Equation (1.29) is equivalent to minimizing the negative log-likelihood, as the log is a monotonic function. This yields a nonlinear Weighted Least Squares (WLS) problem

$$\widehat{\boldsymbol{r}}, \widehat{dt}_r = \arg\min \left((\boldsymbol{r}, dt_r) \mapsto \sum_{i=1}^{m} \left(\frac{\tilde{p}_r^{s_i} - \rho_r^{s_i} - c.dt_r}{\sigma_i}\right)^2\right) \tag{1.31}$$

Now that Equation (1.31) is written qualitatively, the GNSS receiver has to solve it quantitatively, i.e., finding the minimum of the function.

Indeed, the corrected code pseudorange Equation (1.27) is linear with respect to the variable dt_r. On the other hand, the Euclidean distance term $\rho_r^{s_i}$ is not linear with respect to the variable $\boldsymbol{r}$. Therefore, this optimization problem cannot be solved analytically. Instead, it is approached iteratively by linearizing the observation equations around an

This document may not be reproduced, modified, adapted, published, translated in any way, in whole or in part, nor disclosed to a third party without the prior written consent of ENAC. © 2025, ENAC

initial guess, and solving a sequence of linearized WLS problems. Readers can refer to the Gauss-Newton algorithm presented in Chapter 2.

The final output of this process is an estimate of the receiver position and time offset that minimizes the difference between the observed and modeled code pseudoranges.

1.3.1.3 Geometry - Variance of Estimated Position

In the case of multilateration Equation (1.7), the observations are deterministic and error-free. On the other hand, in Equation (1.28) are introduced random variables. The presence of these random variables introduces variance in the obtained receiver positions and clock biases, by definition of an estimator.

Indeed, this variance depends on the random variables contained in the observations. An important aspect is that this variance also depends on the geometric configuration of the satellites relative to the receiver.

To quantify the influence of the geometrical configuration on the estimator, the concept of Dilution Of Precision (DOP) is introduced. The DOP indicators are real numbers that summarize how the geometry amplifies the effect of observations variance in the estimator variance. Stated another way, it quantifies how the deterministic part of the observations relates the random part of the observations to the estimator variance.

In practice, the DOP is computed by assuming that the observations are independent Gaussian random variables with unit variance. From this assumption, if doable, the estimator's variance is derived analytically.

In the case of SPP, the receiver coordinates and its clock bias are estimated. Consequently, the Geometric Dilution Of Precision (GDOP) is defined, representing the DOP related to both the coordinates and clock bias, the Position Dilution Of Precision (PDOP) that corresponds to the DOP related to the coordinates, while the Time Dilution Of Precision (TDOP) relates to the clock bias DOP. Other DOP variants (e.g., Horizontal Dilution Of Precision (HDOP), Vertical Dilution Of Precision (VDOP)) refer to specific components of the position.

As explained in Chapter 2, since the observations of SPP are not linear with respect to the receiver coordinates, an iterative approach is used to construct the MLE. Therefore, no straightforward closed form of the MLE variance is computable analytically. On the other hand, the nonlinear equations can be linearized around an estimate (that is close to the true coordinates). Although using an approximation, this permits the computation of an approximation of the estimator variance.

In that case, when the m code pseudorange measurement noise is assumed to be independent and identically distributed for all satellites, if $\boldsymbol{H} \in \mathcal{M}_{m,4}(\mathbb{R})$ represents the Jacobian matrix of the concatenated code pseudoranges with respect to $\boldsymbol{r}$ and dt_r at this estimate, the covariance of the MLE is given by the matrix $\left(\boldsymbol{H}^\intercal \boldsymbol{H}\right)^{-1}$. From this covariance matrix, computations can be done to express mentioned specific DOP values.

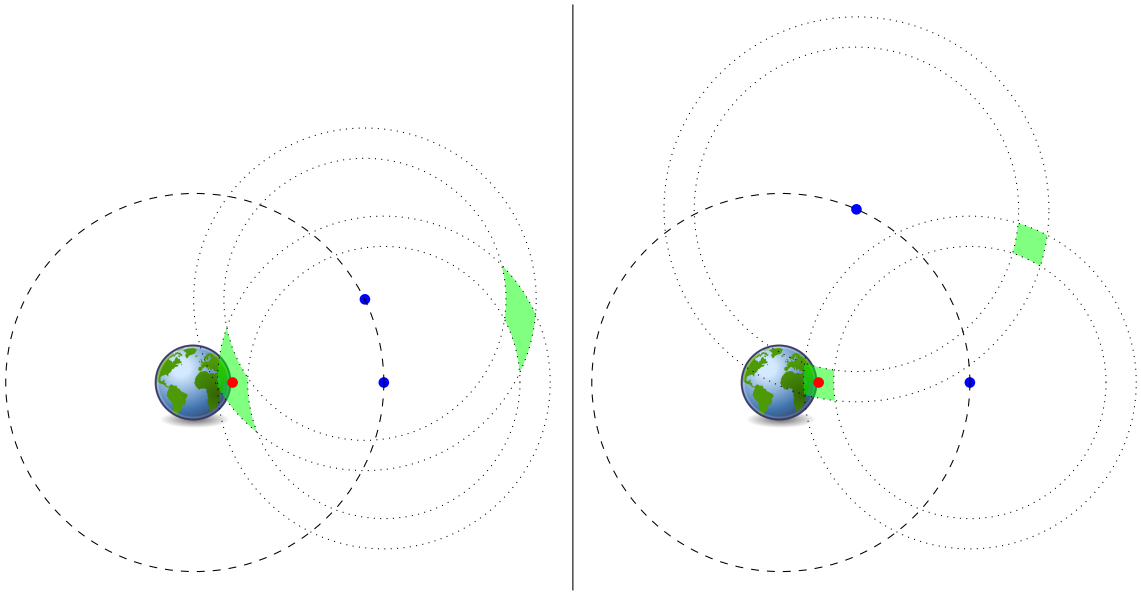

Figure 1.6: Illustration (in 2D) of the DOP, for two different geometries. The receiver is the red dot, the satellites are the blue dots. Ignoring the receiver clock bias, the dotted circles define rings that correspond to the true range with a confidence interval of $\pm k \cdot \sigma_i$, with $\sigma_i = 1\,\text{m}$. The DOP corresponds to the intersection of the rings (in green). Left: the area in green surrounding the receiver indicates a large DOP value, suggesting poor satellite geometry. Right: the smaller green area around the receiver indicates a low DOP, representing a favorable satellite geometry for accurate positioning.

Intuitively, when satellites are clustered in a narrow portion of the sky, errors in the pseudorange measurements lead to large errors in the estimated position. In contrast, a well-distributed satellite constellation, spanning a wide range of azimuth and elevation angles, provides a better geometry and reduces this effect.

The principle of DOP is visible in Figure 1.6.

In summary, even though SPP treats each epoch independently and assumes corrected observations with uncorrelated noise, the geometry of the satellite-receiver configuration plays a central role in determining the statistical quality of the solution. Thus, monitoring DOP values is essential in applications where the reliability and precision of the position estimate are critical.

1.3.1.4 Correction of the Observations

A final aspect of SPP is related to the correction of the code pseudorange observations. In the code pseudorange observations Equation (1.8), many of the terms involved, such as atmospheric delays or Sagnac effect delay depend on the receiver's position. This creates a particular challenge in GNSS positioning: to compute the corrections required for these terms, the receiver's position must be known. However, determining the receiver's position itself relies on applying these corrections. This creates a chicken-and-egg problem, where neither the position nor the corrections can be precisely computed without knowing the

This document may not be reproduced, modified, adapted, published, translated in any way, in whole or in part, nor disclosed to a third party without the prior written consent of ENAC. © 2025, ENAC

other first. To solve this, a common approach involves an initial simplification: these receiver position-dependent terms are ignored or approximated in a first step, allowing for the computation of a coarse receiver position. Once this initial estimate is available, it can be used to evaluate the necessary corrections more accurately. These refined corrections are then reintroduced into the observation model, enabling a more precise position estimate through iterative refinement.

Although SPP does not offer the high precision achievable with more advanced techniques such as PPP or RTK, it provides a practical method for positioning at a decent level of precision. Furthermore, it serves as a foundational algorithm for understanding and implementing more sophisticated GNSS positioning strategies.

1.3.2 PPP

In an idealistic world where code pseudorange observations are perfectly modeled as a Gaussian random vector, with a mean vector that is a perfectly known function of the receiver coordinates and clock bias, SPP would be a very good positioning strategy.

In practice, due to the complexity of the overall GNSS system and of the propagation of GNSS signals between a satellite and a receiver, the actual observations that a GNSS receiver has at his disposal do not follow exactly the equations presented in the SPP section. Therefore, other positioning strategies are developed. The main objective is to reduce the impact of wrong modeling of available observations. Although higher positioning precision is achievable, more complexity is introduced.

As PPP is not the core focus of this thesis, this section describes it very briefly. The core principle of PPP lies in the precise modeling of GNSS observations. For that purpose, it requires the use of accurate satellite coordinates and clock biases from external products. Code pseudorange as well as carrier phase observations, at multiple frequencies, are used. Temporal dependency is introduced in the parameters to be estimated. These parameters include the receiver coordinates and clock bias, but also the ZTD and the carrier-phase ambiguities [13].

1.3.2.1 Ionospheric-Free Combination

Since the ionosphere is a dispersive medium, the delay or advance that it introduces is frequency dependent. For this reason, two code pseudorange and two carrier-phase observations at two frequencies f_a and f_b are considered. From these observations, the ionosphere-free code pseudorange and carrier-phase combinations are built.

Defining the coefficients

$$\begin{cases} \gamma_a = \frac{f_a^2}{f_a^2 - f_b^2} \\ \gamma_b = \frac{f_b^2}{f_a^2 - f_b^2} \end{cases} \tag{1.32}$$

the following linear combination of code pseudorange and carrier-phase combinations are

built

$$\begin{cases} P^{s_i}_{r,IF} = \gamma_a P^{s_i}_{r,f_a} - \gamma_b P^{s_i}_{r,f_b} \\ \Phi^{s_i}_{r,IF} = \gamma_a \Phi^{s_i}_{r,f_a} - \gamma_b \Phi^{s_i}_{r,f_b} \end{cases} \tag{1.33}$$

where $P^{s_i}_{r,f_a}$ indicates the code pseudorange between the receiver and satellite i with a carrier frequency f_a.

The ionospheric delay (or advance) is, in first approximation, inversely proportional to the squared carrier frequency. Since $\frac{\gamma_a}{f_a^2} - \frac{\gamma_b}{f_b^2} = 0$, both linear combinations of code pseudorange and carrier-phase observations Equation (1.33) are not subject to ionospheric delay or advance.

Since $\gamma_a - \gamma_b = 1$, all common terms in the original code pseudoranges $P^{s_i}_{r,f_a}$ and $P^{s_i}_{r,f_b}$ (or in the original carrier-phase $\Phi^{s_i}_{r,f_a}$ and $\Phi^{s_i}_{r,f_b}$) remain in the ionosphere-free combination.

The terms present in the original code pseudoranges $P^{s_i}_{r,f_a}$ and $P^{s_i}_{r,f_b}$ (or in the original carrier-phase $\Phi^{s_i}_{r,f_a}$ and $\Phi^{s_i}_{r,f_b}$) that are modeled as independent Gaussian random variables remain in the resulting expression. Since these terms are independent, their variances add up according to the combination coefficients γ_a and γ_b, i.e., if $\sigma^2_{f_a}$ is the variance of a random variable present in $P^{s_i}_{r,f_a}$ and $\sigma^2_{f_b}$ is the variance of a random variable present in $P^{s_i}_{r,f_b}$, the variance of the random variable present in the ionosphere-free combination σ^2_{IF} is

$$\sigma^2_{IF} = \gamma_a^2 \sigma^2_{f_a} + \gamma_b^2 \sigma^2_{f_b}. \tag{1.34}$$

The same applies to random variables present in $\Phi^{s_i}_{r,f_a}$ and $\Phi^{s_i}_{r,f_b}$. This trade-off (eliminating ionosphere delays and advances at the cost of increased measurement noise) is central to PPP design.

Another aspect is related to the integer ambiguities present in the carrier-phase observations. Since a non-integer linear combination of the ambiguity terms is computed, the ionosphere-free carrier phase observation still includes a number by which is multiplied the effective ionosphere-free wavelength, but this number is not an integer anymore.

1.3.2.2 Estimation of Parameters in PPP

PPP is a GNSS-based positioning application, so the GNSS receiver coordinates are estimated, as well as its clock bias.

Since a ionosphere-free combination of carrier-phase observations is built, the integer ambiguity number present in the carrier-phase observations are combined, leading to real ambiguity terms (one ambiguity term per visible satellite). In the PPP framework, these ambiguity terms are estimated. The reason why these ambiguities are estimated is that additional information is available on them: throughout time, they are supposed to remain constant. Unfortunately, sometimes a CS happens. The use of multiple frequencies increases the risk of CS. Therefore, a strong CS detector is advised prior to positioning, as well as residual monitoring. Chapter 3 is dedicated to proper CS detection and exclusion.

The last variable that is part of the estimated parameters is the ZTD. It corresponds to a

This document may not be reproduced, modified, adapted, published, translated in any way, in whole or in part, nor disclosed to a third party without the prior written consent of ENAC. © 2025, ENAC

real number, and by means of a mapping function to account for slant, it is projected onto the LOS of each visible satellite. This zenithal atmospheric delay due to the troposphere is varying slowly throughout time.

The temporal dependency of the ambiguity numbers and of the ZTD is taken into account. This is handled by means of a state transition model within an Extended Kalman Filter (EKF). For example, the ambiguities can be considered as constant throughout time while the ZTD can be modeled as a random walk.

Also, in this EKF, additional information regarding temporal evolution of the receiver coordinates or clock bias can be incorporated.

The observations used to apply the update within the EKF correspond to the ionospheric free code pseudorange and carrier-phase observations. In this context, precise satellite coordinates and clock corrections are sourced from external organizations such as the International GNSS Service (IGS), which provides post-processed products with high accuracy.

The Kalman Filter (KF) equations are described in more details in Section 2.5.

Overall, PPP combines precise modeling, multi-frequency GNSS data, and advanced estimation techniques to achieve high-precision positioning from a single receiver, making it a different technique than SPP. For readers interested in a deeper understanding of the modeling techniques, estimation strategies, and practical implementations of PPP, comprehensive treatment can be found in [13].

1.3.3 RTK

RTK (Real-Time Kinematic) is a differential positioning technique that significantly improves the accuracy of GNSS-based positioning by relying on real-time corrections from a reference station (also known as a base station). While SPP and even PPP rely only on information derived from satellite-referenced data, RTK operates in a relative framework, exploiting the spatial correlation between two nearby receivers: a static, well-surveyed reference station and a moving receiver, commonly referred to as the rover.

1.3.3.1 Differential Positioning

RTK relies on the assumption that two receivers located sufficiently close to each other observe nearly the same satellite signals and experience similar propagation delays. Therefore, by differencing the observations from the rover and the base station, common errors cancel out.

Let $P_r^{s_i}$ and $P_b^{s_i}$ denote the code pseudorange observations from the rover and base, respectively, to satellite i, and similarly for the carrier-phase observations $\Phi_r^{s_i}$ and $\Phi_b^{s_i}$. The Single Difference (SD) of code pseudorange and carrier-phase between the rover and the base for satellite i are

$$\begin{cases} \Delta P_{r,b}^{s_i} = P_r^{s_i} - P_b^{s_i}, \\ \Delta \Phi_{r,b}^{s_i} = \Phi_r^{s_i} - \Phi_b^{s_i}. \end{cases} \tag{1.35}$$

Trivially, these differences remove terms that are common to both observations. For example, the satellite clock bias is removed from the equations. The advantage of differential positioning is that all common terms that are not very well modeled in the observation models cancel out. Therefore, the baseline length (i.e., the distance between the base and the rover) must be short to ensure removal of correlated atmospheric effects.

In a second step, a reference satellite is chosen. Usually, the satellite at highest elevation is considered as the reference. Then, the difference between SD observations is computed, leading to Double Difference (DD) observations: given two satellites i and j, the DD of code pseudoranges and carrier-phase are

$$\begin{cases} \nabla\Delta P_{r,b}^{s_i,s_j} = \Delta P_{r,b}^{s_i} - \Delta P_{r,b}^{s_j}, \\ \nabla\Delta \Phi_{r,b}^{s_i,s_j} = \Delta \Phi_{r,b}^{s_i} - \Delta \Phi_{r,b}^{s_j}. \end{cases} \tag{1.36}$$

Similarly to what happens to the SD, these differences remove terms that are common to both SD observations. For example, the receiver clock bias is removed from the equations. Also, all common terms that are not very well modeled in the SD cancel out.

After these differencing operations, the remaining terms include the relative geometry between the two receivers and satellite pair, the differential atmospheric effects (minimal if the baseline is short), and the DD integer ambiguities in the DD carrier-phase observations.

1.3.3.2 Integer Ambiguity Resolution and Baseline Estimation

Unlike PPP, where ambiguities in the ionospheric-free combinations become real-valued and are estimated as such, RTK exploits the fact that DD ambiguities, present in the carrier-phase observations, are integers. They can be resolved as such.

The DD carrier-phase observation model can be expressed as

$$\nabla\Delta \Phi_{r,b}^{s_i,s_j} = \nabla\Delta \rho_{r,b}^{s_i,s_j} + \lambda \cdot \nabla\Delta N_{r,b}^{s_i,s_j} + \nabla\Delta \varepsilon_{r,b}^{s_i,s_j} \tag{1.37}$$

where λ denotes the carrier-phase wavelength, $\nabla\Delta\rho_{r,b}^{s_i,s_j}$ is the DD geometric range, $\nabla\Delta N_{r,b}^{s_i,s_j} \in \mathbb{Z}$ is the DD integer ambiguity and $\Delta\varepsilon_{r,b}^{s_i,s_j}$ denotes the DD of noise and of unmodeled terms.

Typically, the estimation of the baseline vector is performed jointly with the resolution of the integer ambiguities. Similarly to the PPP framework, this is typically done by means of an EKF, followed by an Integer Least Squares (ILS) ambiguity resolution algorithm, such as the Least Squares Ambiguity Decorrelation Adjustment (LAMBDA) method [29]. Once the ambiguities are successfully fixed, high precision positioning is achieved.

Within the EKF, the transition model assumes a kinematic model for the rover coordinates, with small process noise, while ambiguities are considered constant over time. The problem of CS is still present, so a proper CS detector is necessary.

Finally, in order to work properly, the base station coordinates must be well-known, in order to compute the rover coordinates.

This document may not be reproduced, modified, adapted, published, translated in any way, in whole or in part, nor disclosed to a third party without the prior written consent of ENAC. © 2025, ENAC

Readers interested in a deeper exploration of RTK algorithms can refer to [13].

With the main positioning algorithms now described, a high-level user is equipped to compute a position. However, the observations used in these algorithms are not directly available from the satellite signals. In practice, a GNSS receiver processes incoming signals to extract the code pseudorange, carrier-phase, and Doppler measurements. The following section introduces some low-level aspects of a GNSS receiver to provide a clearer understanding of how these observations are generated in practice.

1.4 Low-Level GNSS Signal Processing

In the previous sections, the various GNSS observables are introduced. However, it is important to emphasize that these measurements are not directly accessible to a receiver. Instead, a GNSS receiver must first process the radio signals captured by its antenna in order to extract code pseudoranges, carrier-phase and Doppler observations. This section provides an overview of how these measurements are derived from the received signals, specifically focusing on the GPS L1 C/A signal.

Although not central to the positioning and navigation methods explored in this thesis, understanding this signal processing step offers valuable context for how the measurements are formed. For the sake of brevity, the techniques presented here are simplified and may not reflect the most advanced approaches currently used in modern receivers. Nonetheless, they are sufficient for grasping the fundamental concepts. Readers interested in a more comprehensive treatment of these low-level processes are encouraged to consult [30].

1.4.1 GPS Signal Structure

A GNSS receiver typically consists of two main components: a GNSS antenna, which captures the Radio Frequency (RF) signals transmitted by satellites, and a processing unit. The processing unit can be either a dedicated hardware chip, or a computer running a Software Defined Radio (SDR). In the SDR approach, signal processing steps that are detailed next, such as acquisition, tracking and decoding, are implemented in software, offering flexibility and transparency in understanding the receiver's behavior.

The GPS L1 C/A signal is one of the simplest and most widely used GNSS signals. When emitted by a GPS satellite, this signal has the following form

$$s(t) = Ad(t)c(t)\exp\left(i\left(2\pi f_0 t + \phi\right)\right) \tag{1.38}$$

where

- t indicates the time variable,
- s is the emitted signal,
- A is the signal amplitude,

- d is the navigation data,
- c is the satellite-specific Pseudo Random Noise (PRN) code, that is 1 ms periodic, with each period made of 1023 bits (or chips),
- f_0 is the carrier frequency,
- ϕ is the initial carrier-phase.

In conventional GNSS, the navigation data d plays a central role, as it contains in particular ephemeris information, allowing the computation of satellite coordinates. For this reason, actual positioning may take tens of seconds due to navigation data decoding.

Assisted GNSS (A-GNSS) [31] mitigates this delay by using external data (e.g., from cellular networks) to obtain this information. Nowadays, most GNSS receivers are connected, so A-GNSS is applicable. For this reason, the navigation data is not detailed here.

The PRN code c plays a central role in enabling Direct Sequence Spread Spectrum (DSSS) modulation. It serves multiple purposes. First, it spreads the narrowband navigation data d over a much wider frequency band, which enhances the signal's robustness against interference. Second, it enables Code Division Multiple Access (CDMA) by allowing multiple satellites to transmit simultaneously on the same carrier frequency without significant mutual interference. Each satellite uses a unique PRN code, effectively acting as its identifier. The ability to separate these signals at the receiver relies on the specific design of the PRN codes, which have excellent autocorrelation properties (allowing precise code alignment) and low cross-correlation with other codes (minimizing interference between satellites). These properties are essential for correctly identifying and isolating signals from different satellites.

Considering perfect propagation, the signal that reaches the receiver is delayed and Doppler-shifted due to the satellite and receiver motion

$$r(t) = Ad(t-\tau)c(t-\tau)\exp\left(i\left(2\pi(f_0+f_d)(t-\tau)+\phi\right)\right) \tag{1.39}$$

where

- τ is the propagation delay, typically around 70 ms,
- f_d is the Doppler shift, typically up to ± 7 kHz.

1.4.2 Acquisition

The objective of the acquisition process is to identify visible satellites by testing different PRN codes, and to coarsely estimate the associated code delay τ and Doppler frequency f_d for each. The estimates of these two parameters are denoted $\widehat{\tau}$ and $\widehat{f_d}$.

To do so, the receiver generates replicas of a considered PRN code and a carrier at various delays and frequencies. To estimate $\hat{\tau}$ and $\hat{f}_d$, the received signal must be synchronized

This document may not be reproduced, modified, adapted, published, translated in any way, in whole or in part, nor disclosed to a third party without the prior written consent of ENAC. © 2025, ENAC

in time and frequency with locally generated replicas. These code and carrier signals generated are multiplied with the incoming signal. The obtained product is integrated. This leads to a correlation coefficient. A correlation (or acquisition) matrix is built by testing all combinations of delays and frequencies. Then, the receiver searches for a peak in this correlation matrix. If a peak is detected, then it indicates the presence of a signal emitted by a GPS satellite with corresponding PRN code, and provides estimates of $\hat{\tau}$ and $\hat{f}_d$.

The computation of this correlation matrix can become very long, depending on the number of delays and frequencies that are considered.

To improve efficiency, modern SDR use fast convolution methods, involving direct and inverse Fourier Transforms to compute correlations.

Given two functions f and g, defining their cross-correlation

$$R_{f,g} : \tau \mapsto \int_{-\infty}^{+\infty} f(t)\overline{g(t-\tau)}\mathrm{d}t \tag{1.40}$$

where $\overline{z}$ denotes the complex conjugate of z, and their convolution product

$$f \star g : \tau \mapsto \int_{-\infty}^{+\infty} f(t)g(\tau - t)\mathrm{d}t, \tag{1.41}$$

thanks to properties of the Fourier transform applied to a convolution product, it can be shown that

$$R_{f,g} : \tau \mapsto \mathcal{F}^{-1}\left(\mathcal{F}\left(f\right)\mathcal{F}\left(\overline{g_{-1}}\right)\right)(\tau) \tag{1.42}$$

where $\mathcal{F}(f)$ denotes the Fourier transform of the function f and $g_{-1} : t \mapsto g(-t)$.

Equation (1.42) can be applied, with one of the functions being the received signal and the other being a local replica of a PRN code c. This way, the acquisition matrix is built. Thanks to the Fast Fourier Transform (FFT) algorithms, these computations are faster than computing values of the acquisition matrix independently.

Finally, the presence of a signal is determined by an acquisition metric. Often, it is defined as the ratio between the highest and second-highest correlation values. A threshold is used to decide if a satellite is visible. In practice, the higher is the C/N0, the more likely a satellite is considered visible.

The acquisition stage gives coarse estimates $\widehat{\tau}$ and $\widehat{f_d}$. To refine these estimates, the tracking stage starts when the acquisition is done. Also, this stage is necessary to compute the code pseudorange, carrier-phase and Doppler observations.

1.4.3 Tracking

Once the signal is acquired, tracking loops refine the initial estimates $\widehat{\tau}$ and $\widehat{f_d}$ to maintain alignment with the incoming signal, with a reduced computational load compared to the

acquisition process. This is necessary for decoding navigation data, as well as for obtaining better estimates of τ and f_d.

To generate a replica of the carrier, a third variable is introduced: the initial phase ϕ of the generated carrier. The estimated initial carrier-phase is denoted $\widehat{\phi}$.

In practice, two feedback loops are used

- the DLL, that estimates the delay,
- the PLL, that estimates the carrier-phase and frequency.

In a first step, each loop uses discriminators to compute errors. Then, these errors are provided to filters, whose aim is to generate PRN and carrier that correspond to the incoming signal, reducing the errors.

The tracking stage provides accurate estimates $\widehat{\tau}$, $\widehat{f_d}$ and $\widehat{\phi}$.

Understanding the principles of the PLL and DLL would require knowledge related to Automatic and dynamic systems, which is out of the scope of this thesis. For a better understanding, refer to [13, Chapter 14].

Using these estimates, the receiver can compute the actual code pseudorange, carrier-phase, and Doppler observations, an aspect explored in the following section.

1.4.4 Observations from Low-Level Estimates

From the tracked signal, the code pseudorange, carrier-phase and Doppler shift can be computed, leading to these three observations that can be used for positioning applications.

1.4.4.1 Code Pseudorange

The actual signal propagation duration from satellite to receiver is typically around 70 ms, corresponding to a distance of roughly 20 000 km. Since a PRN code lasts 1 ms and is received periodically at that same rate, it cannot be used alone to obtain the propagation duration. This is where navigation data decoding and time synchronization come into play. Acquisition and tracking give an estimate of $\widehat{\tau} \in [0, 1)$ms and $\widehat{f_d}$.

The receiver decodes the navigation message, which includes a Time Of Week (TOW) timestamp for each satellite. Using the known structure of the navigation message, the location of the TOW and the receiver's local clock, the receiver can determine the instant when the satellite transmitted the signal, with a millisecond resolution. By using the transmission instant (from the TOW) with the receiver's reception instant and the estimate $\widehat{\tau}$, the receiver recovers the full signal propagation duration Δt_i (in the range of 70 ms).

Finally, multiplying this total propagation duration by the speed of light gives the code pseudorange, which represent the apparent distance between a satellite and the receiver, i.e.,

$$P_r^{s_i} = c \cdot \Delta t_i \tag{1.43}$$

This document may not be reproduced, modified, adapted, published, translated in any way, in whole or in part, nor disclosed to a third party without the prior written consent of ENAC. © 2025, ENAC

where c is the speed of light and $P_r^{s_i}$ is the code pseudorange as in Equation (1.8).
In practice, this measurement includes various biases and delays that are detailed in Section 1.2.

1.4.4.2 Carrier-Phase

The initial carrier phase estimated during tracking gives access to the carrier-phase observation. It provides a more precise observable than code pseudorange, although additional complexity is present due to the integer ambiguity

$$\Phi_r^{s_i} = \frac{\lambda}{2\pi}\widehat{\phi}_i = \rho_r^{s_i} + \lambda \cdot N_r^{s_i} \tag{1.44}$$

where

- $\Phi_r^{s_i}$ is the carrier-phase observation as in Equation (1.9),
- $\rho_r^{s_i}$ is the receiver to satellite range,
- $\widehat{\phi}_i$ is the tracked carrier phase,
- λ is the carrier wavelength,
- $N_r^{s_i}$ is an unknown integer, the phase ambiguity.

Between two epochs, if the distance between the GNSS receiver and the satellite changes by more than one wavelength (which is often the case), the PLL is able to account for it. Therefore, unless a CS happens, the carrier-phase provides a continuous measurement.
In practice, this measurement also includes various biases and delays that are detailed in Section 1.2.

1.4.4.3 Doppler

The frequency shift can be related to the radial LOS velocity between the satellite and the receiver. The Doppler observation $D_r^{s_i}$ introduced in Section 1.2.4 is obtained by

$$D_r^{s_i} = \widehat{f}_d \tag{1.45}$$

A positive Doppler shift (i.e., $\widehat{f}_d \geq 0$) indicates that the satellite is approaching the receiver.
In practice, this measurement also includes various biases and delays.

1.5 Conclusion

This chapter provides the foundational concepts necessary to understand GNSS and positioning. It begins with an overview of GNSS constellations and explains the multilateration principle with pseudoranges used to determine a receiver's position and clock bias.

The main types of GNSS observations (code pseudorange, carrier-phase, Doppler) are introduced, as well as TDCP, along with detailed models that capture the various physical phenomena affecting their accuracy. These include clock biases, atmospheric delays, relativistic effects, hardware imperfections, and signal propagation issues such as multipath and occlusion. The chapter then presents the main positioning algorithms: SPP, PPP and RTK, each offering different levels of complexity and accuracy, depending on the application requirements and available corrections. Finally, it introduces low-level receiver operations to explain how raw satellite signals are converted into usable observations. Together, these elements establish a comprehensive framework for the positioning methods developed in the following chapters, paving the way for the use of Factor Graph Optimization (FGO), which provides a rigorous and flexible framework for fusing GNSS observations into positioning problems.

This document may not be reproduced, modified, adapted, published, translated in any way, in whole or in part, nor disclosed to a third party without the prior written consent of ENAC. © 2025, ENAC

Chapter 2

Factor Graph Optimization

This chapter introduces the Factor Graph Optimization (FGO) framework. Essentially, the FGO is a representation of a Maximum Likelihood Estimator (MLE)[1]. It starts by a general presentation, defining terms that are used throughout the whole chapter and providing examples. Then, restrictions are introduced regarding the type of factors and variables studied in this thesis. Particularly, the case of multivariate Gaussian factors is introduced, with mean vectors that are function of parameters to be estimated. The case of linear mean with respect to vectors of parameters is handled analytically, deriving mean and variance of the MLE, is represented geometrically by means of orthogonal projections, and is computed by different techniques to handle numerical issues. Then, the case of nonlinear differentiable functions is handled by means of algorithms. A few lemmas regarding linear combinations of FGO are presented. They provide equivalence between graphs, cases of singular graphs, and cases where nontrivial transformation leads to a new study. Specific type of omitted biases in observations are also handled thanks to these transformations.

This chapter relies on the definitions of random vector, continuous random vector, independence, conditional distributions, estimator and MLE for real-valued continuous random vectors. If necessary, readers can refer to Appendix A or to [32], among many other standard references for further details.

2.1 Background and Definitions

2.1.1 Applications of Factor Graph Optimization

Essentially, as in its first introduction [33], a factor graph is a representation of a function, and FGO refers to the set of algorithms and methods to optimize this function based on graph-specific approaches [34, 35] and/or sparse linear algebra techniques [36].

In the simplest case, the function to be optimized is differentiable and of Euclidean vari-

[1]See Appendix A for a discussion on the inclusion of other estimators (e.g., Bayesian) in the FGO framework.

This document may not be reproduced, modified, adapted, published, translated in any way, in whole or in part, nor disclosed to a third party without the prior written consent of ENAC. © 2025, ENAC

ables. For example, it can correspond to a function of the position of a system in the three dimensional world, or its speed (in a non relativistic way), or of a real number.

More generally, since its introduction within the robotics community [37, 38], some parameters to be estimated correspond to orientations of systems, that are not defined by Euclidean spaces. In that case, specific optimization methods can be used to take into account the structure of these sets. For example, optimization of functions on sets with a Lie group structure exists [39], as well as on commutative groups [40], or as is presented in the Precise Point Positioning (PPP) Section 1.3.2 where the ambiguity numbers are fixed in $\mathbb{Z}$. Also, multiple constraints on the variables can be taken into account in this optimization [41].

In this work, for simplicity, all variables considered are Euclidean, and all random vectors follow a Gaussian distribution. Both of them can be of any finite dimension.

Libraries of FGO exist, such as G^2o [42], CERES [43], GTSAM [44] and miniSAM [45]. Written in different programming languages and with different numerical optimization toolboxes, some of them are able to take into account the algebraic structure of the variables to be estimated.

The FGO is used in many engineering fields, such as robotics, autonomous vehicles, geodesy, computer vision and sensor fusion. In robotics, it is a core component of Simultaneous Localization And Mapping (SLAM) systems, where it allows for accurate and consistent estimation of the robot's trajectory and the surrounding environment [44]. In autonomous navigation, FGO is leveraged for multi-sensor fusion, combining inputs from Global Navigation Satellite System (GNSS), Inertial Measurement Unit (IMU), cameras, and LiDAR into a single consistent state estimate [46]. Similarly, in structure-from-motion, FGO allows for globally consistent 3D reconstructions by solving large-scale bundle adjustment problems [47]. In the field of sensor fusion, factor graph-based approaches provide a unified mathematical framework that accommodates heterogeneous measurements and constraints, making them suitable for complex systems like humanoid robots [48] or drones [49].

In the field of GNSS, FGO is increasingly employed to improve positioning accuracy, robustness, and convergence speed, especially in challenging environments such as urban canyons or under dense foliage. Traditional precise GNSS positioning relies on Weighted Least Squares (WLS) and/or Extended Kalman Filter (EKF), respectively processing observations independently and sequentially. In contrast, FGO enables a smoother, batch-based positioning by considering all available past and present observations, as well as future observations in the case of post-processing, in a unified graph structure. Each GNSS observation (e.g., code pseudorange, carrier-phase) is modeled as a factor that constrains the receiver's state, allowing for flexible integration with other sensors such as IMU. The winning solutions of the 2021 and 2022 editions of the Google Smartphone Decimeter Challenge (GSDC) [4, 5, 6], as well as the second place of the 2023 edition [7] rely on FGO.

One key advantage of FGO is its modularity. Each new sensor or information that is independent from other factors can be introduced into the system simply by defining a new factor, making it highly adaptable. Moreover, efficient solvers allow for real-time performance. As such, the FGO framework generalizes and unifies a variety of estimation problems under a single formalism.

Now that the general context and applications of factor graphs is presented, the formal definitions underlying FGO are introduced. They provide the mathematical framework necessary to rigorously formulate and solve estimation problems FGO. They serve as the foundation for the subsequent development of results throughout the rest of this thesis.

2.1.2 Definitions

This section begins with the deterministic formulation of FGO, where the objective consists in maximizing a function. This is followed by the stochastic case, in which uncertainties are incorporated through likelihood functions, providing a probabilistic framework. The discussion then focuses on the specific case of Gaussian random vectors.

2.1.2.1 Deterministic Factor Graph Optimization

Let $f : \Theta \subseteq \mathbb{R}^n \to \mathbb{R}$. Depending on f, it can be written as a product of k functions

$$f : \boldsymbol{\theta} \mapsto \prod_{i=1}^{k} f_i(S_i) \tag{2.1}$$

where S_i denotes the components of $\boldsymbol{\theta}$ that f_i depends on. The functions $(f_i)_{1 \leq i \leq k}$ are called *factors* of f. This name comes from the fact that f is a product of factors, i.e., f is factorized.

Providing a factorized function to Algorithm 2.1 leads to a graph that is referred to as *factor graph*. It has a specific structure: it is a bipartite graph, where the first type of nodes are variables, and the second type of nodes are factors, and the dependency between factors and variables is represented by edges.

Algorithm 2.1 Construction of a Factor Graph Representation

Require: Factorized function $f : \boldsymbol{\theta} \mapsto \prod_{i=1}^{k} f_i(S_i)$

```
for j = 1, ..., n do
    Create a variable node θ_j
end for
for each factor f_i, where i = 1, ..., k do
    Create a factor node f_i
    for each variable θ_j ∈ S_i do
        Add an undirected edge between f_i and θ_j
    end for
end for
```

This document may not be reproduced, modified, adapted, published, translated in any way, in whole or in part, nor disclosed to a third party without the prior written consent of ENAC. © 2025, ENAC

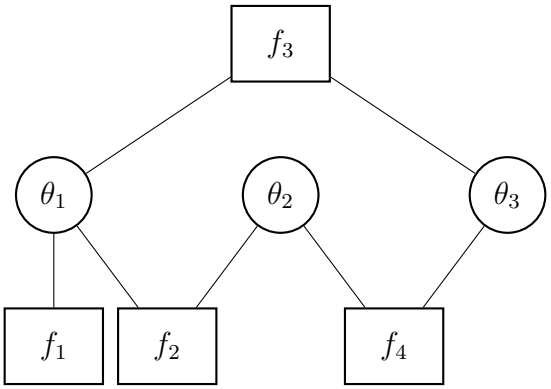

Figure 2.1: Representation of Equation (2.2) with a factor graph.

As an example, considering a function

$$f(\theta_1, \theta_2, \theta_3) = f_1(\theta_1) \times f_2(\theta_1, \theta_2) \times f_3(\theta_1, \theta_3) \times f_4(\theta_2, \theta_3), \tag{2.2}$$

its factorization is visible in Figure 2.1.

A classical challenge within the optimization community is to find values that maximize a function, i.e.,

$$\arg\max f. \tag{2.3}$$

Depending on f, the solution set of Equation (2.3) may contain multiple elements, a unique element, or none at all. This problem can be applied to a function that is factorized. In that case, in order to actually compute the solutions, specific graph-based approaches can be used thanks to the factor graph representation of f, hence the name FGO.

To conclude this section, a factor graph is simply a visual representation of a factorization of a function, and if this function is part of an optimization problem, then specific graph-based approaches can be used thanks to this representation.

2.1.2.2 Independence of Random Vectors

Now that the term FGO is defined, it can be used to see the MLE as an FGO. To do so, the notion of factorization of random vectors is necessary.

The following theorem and corollary are from probability theory. They provide a way to factorize random vectors.

Theorem 2.1.1. *Let $\boldsymbol{x} = (x_1, \ldots, x_k)^\mathsf{T}$ be a real-valued random vector of dimension k. The random variables $x_1, \ldots, x_k$ are independent with respective density functions $f_1, \ldots, f_k$ if and only if the density function f of $\boldsymbol{x}$ satisfies $f(t_1, \ldots, t_k) = \prod_{i=1}^{k} f_i(t_i)$.*

Corollary 2.1.1. *Let $\boldsymbol{x} = \left(\boldsymbol{x}_1^\mathsf{T}, \ldots, \boldsymbol{x}_k^\mathsf{T}\right)^\mathsf{T}$ be a real-valued random vector such that the random vectors $(\boldsymbol{x}_i)_{i \in \{1,\ldots,k\}}$ are of dimension m_i. The random vectors $\boldsymbol{x}_1, \ldots, \boldsymbol{x}_k$ are*

independent with respective density functions $f_1, \ldots, f_k$ *if and only if the density function* f *of* $\boldsymbol{x}$ *satisfies* $f : \mathbb{R}^{m_1} \times \ldots \times \mathbb{R}^{m_k} \to \mathbb{R}^+$, $(\boldsymbol{t}_1, \ldots, \boldsymbol{t}_k) \mapsto \prod_{i=1}^{k} f_i(\boldsymbol{t}_i)$.

2.1.2.3 Stochastic Factor Graph Optimization

An FGO is now constructed based on continuous real valued independent random vectors, using corresponding likelihood functions as defined in Appendix A.

Let $\boldsymbol{\theta} \in \Theta \subseteq \mathbb{R}^n$ be an unknown deterministic vector and let $\boldsymbol{x}$ be a continuous real-valued random vector. The objective is to estimate $\boldsymbol{\theta}$ from $\boldsymbol{x}$ by means of the MLE, i.e., by construction of the random vector

$$\widehat{\boldsymbol{\theta}}_{\text{MLE}} = \arg\max \mathcal{L}(\boldsymbol{x}), \tag{2.4}$$

where $\mathcal{L}(\boldsymbol{x}) : \Theta \subseteq \mathbb{R}^n \to \mathbb{R}^+$ is the likelihood function of $\boldsymbol{\theta}$ given $\boldsymbol{x}$, as defined in Appendix A.

Assuming that $\boldsymbol{x}$ is made of k independent real-valued random vectors, i.e., $\boldsymbol{x} = \left(\boldsymbol{x}_1^{\mathsf{T}}, \ldots, \boldsymbol{x}_k^{\mathsf{T}}\right)^{\mathsf{T}}$, with densities denoted $f_{1,\boldsymbol{\theta}}, \ldots, f_{k,\boldsymbol{\theta}}$, then from Corollary 2.1.1, the density of $\boldsymbol{x}$, denoted $f_{\boldsymbol{\theta}}$, satisfies $f_{\boldsymbol{\theta}}(\boldsymbol{t}_1, \ldots, \boldsymbol{t}_k) = \prod_{i=1}^{k} f_{i,\boldsymbol{\theta}}(\boldsymbol{t}_i)$.

Since $f_{\boldsymbol{\theta}}$ is factorized, it comes that by definition, the likelihood function $\mathcal{L}(\boldsymbol{x})$ is the product of the likelihood functions, i.e.,

$$\mathcal{L}(\boldsymbol{x}) = \prod_{i=1}^{k} \mathcal{L}(\boldsymbol{x}_i), \tag{2.5}$$

where $\mathcal{L}(\boldsymbol{x}_i)$ denotes the likelihood function of $\boldsymbol{\theta}$ given $\boldsymbol{x}_i$. At that point, the likelihood function $\mathcal{L}(\boldsymbol{x})$ is factorized.

Similarly to Equation (2.1), if S_i denotes specific components that the likelihood function $\mathcal{L}(\boldsymbol{x}_i)$ depends on, then the likelihood function $\mathcal{L}(\boldsymbol{x})$ satisfies

$$\mathcal{L}(\boldsymbol{x}) : \boldsymbol{\theta} \mapsto \prod_{i=1}^{k} \mathcal{L}(\boldsymbol{x}_i)(S_i). \tag{2.6}$$

Similarly to Equation (2.1), Equation (2.6) can be represented by a factor graph thanks to Algorithm 2.1, where each factor corresponds to a likelihood function $\mathcal{L}(\boldsymbol{x}_i)$, and is connected to the variables S_i that it depends on.

As an example, with a structure similar to Equation (2.2), considering a likelihood function

$$\mathcal{L}(\boldsymbol{x})(\theta_1, \theta_2, \theta_3) = \mathcal{L}(\boldsymbol{x}_1)(\theta_1) \times \mathcal{L}(\boldsymbol{x}_2)(\theta_1, \theta_2) \times \mathcal{L}(\boldsymbol{x}_3)(\theta_1, \theta_3) \times \mathcal{L}(\boldsymbol{x}_4)(\theta_2, \theta_3), \tag{2.7}$$

its factorization is visible in Figure 2.2.

Finally, as in Equation (2.4), since the objective is to construct the estimator $\widehat{\boldsymbol{\theta}}_{\text{MLE}}$ by

This document may not be reproduced, modified, adapted, published, translated in any way, in whole or in part, nor disclosed to a third party without the prior written consent of ENAC. © 2025, ENAC

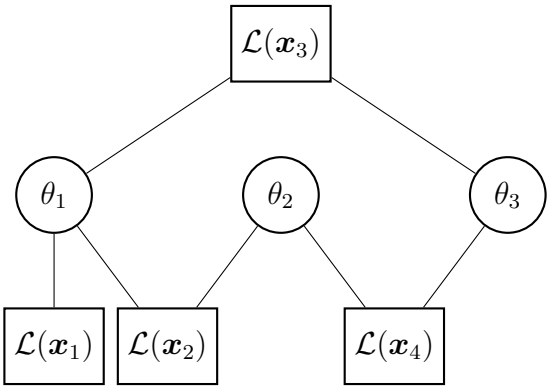

Figure 2.2: Representation of Equation (2.7) with a factor graph.

maximization of the function $\mathcal{L}(\boldsymbol{x})$, by means of Equation (2.6), i.e.,

$$\widehat{\boldsymbol{\theta}}_{\mathrm{MLE}} = \arg\max \left(\mathcal{L}(\boldsymbol{x}) : \boldsymbol{\theta} \mapsto \prod_{i=1}^{k} \mathcal{L}(\boldsymbol{x}_i)(S_i) \right), \tag{2.8}$$

specific graph-based approaches can be used to solve this optimization problem.

Indeed, if a sample $\boldsymbol{x}_i(\omega)$ is available for all random vector $\boldsymbol{x}_i$, then the functions $\mathcal{L}(\boldsymbol{x}_i(\omega))$ are deterministic functions and the problem is similar to Equation (2.3).

Now that the FGO is presented very generally, it is applied to the case of Gaussian random vectors.

2.1.2.4 Factor Graph Optimization with Gaussian Random Vector

Again, let $\boldsymbol{\theta} \in \Theta \subseteq \mathbb{R}^n$. If $\forall i \in \{1, \ldots, k\}$, $\boldsymbol{x}_i$ is a random vector such that $\boldsymbol{x}_i \sim \mathcal{N}(h_i(\boldsymbol{\theta}), \boldsymbol{R}_i)$ where $h_i : \Theta \subseteq \mathbb{R}^n \to \mathbb{R}^{m_i}$ and $\boldsymbol{R}_i \in \mathcal{M}_{m_i}(\mathbb{R})$ is symmetric positive-definite, then the likelihood given $\boldsymbol{x}_i$ is

$$\mathcal{L}(\boldsymbol{x}_i) : \boldsymbol{\theta} \mapsto \frac{1}{\sqrt{(2\pi)^{m_i} |\boldsymbol{R}_i|}} \exp\left(-\frac{1}{2} \left\| \boldsymbol{x}_i - h_i(\boldsymbol{\theta}) \right\|^2_{\boldsymbol{R}_i} \right). \tag{2.9}$$

where

$$\left\| \boldsymbol{x}_i - h_i\left(\boldsymbol{\theta}\right) \right\|^2_{\boldsymbol{R}_i} \triangleq \left(\boldsymbol{x}_i - h_i\left(\boldsymbol{\theta}\right) \right)^{\mathsf{T}} \boldsymbol{R}_i^{-1} \left(\boldsymbol{x}_i - h_i\left(\boldsymbol{\theta}\right) \right). \tag{2.10}$$

Defining

- the random vector $\boldsymbol{x} \triangleq \left(\boldsymbol{x}_1^{\mathsf{T}}, \ldots, \boldsymbol{x}_k^{\mathsf{T}} \right)^{\mathsf{T}}$ made of k independent Gaussian random vectors
- $m \triangleq \sum_{i=1}^{k} m_i$,
- the function $h : \Theta \subseteq \mathbb{R}^n \to \mathbb{R}^m, \boldsymbol{\theta} \mapsto \left(h_1(\boldsymbol{\theta})^{\mathsf{T}}, \ldots, h_k(\boldsymbol{\theta})^{\mathsf{T}} \right)^{\mathsf{T}}$,
- the covariance matrix $\boldsymbol{R} \triangleq \mathrm{diag}\left(\boldsymbol{R}_1, \ldots, \boldsymbol{R}_k \right) \in \mathcal{M}_m(\mathbb{R})$,

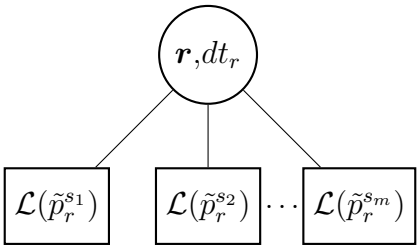

Figure 2.3: Representation of the SPP with a factor graph.

it comes that $\boldsymbol{x} \sim \mathcal{N}(h(\boldsymbol{\theta}), \boldsymbol{R})$ and the likelihood given $\boldsymbol{x}$ is the product of the likelihoods given $\boldsymbol{x}_i$, i.e.,

$$\mathcal{L}(\boldsymbol{x}) : \boldsymbol{\theta} \mapsto \prod_{i=1}^{k} \frac{1}{\sqrt{(2\pi)^{m_i} |\boldsymbol{R}_i|}} \exp\left(-\frac{1}{2} \|\boldsymbol{x}_i - h_i(\boldsymbol{\theta})\|_{\boldsymbol{R}_i}^2\right). \tag{2.11}$$

Since $\boldsymbol{R}^{-1} = \operatorname{diag}\left(\boldsymbol{R}_1^{-1}, \ldots, \boldsymbol{R}_k^{-1}\right)$ and $|\boldsymbol{R}| = \prod_{i=1}^{k} |\boldsymbol{R}_i|$, Equation (2.11) becomes

$$\mathcal{L}(\boldsymbol{x}) : \boldsymbol{\theta} \mapsto \frac{1}{\sqrt{(2\pi)^{m} |\boldsymbol{R}|}} \exp\left(-\frac{1}{2} \|\boldsymbol{x} - h(\boldsymbol{\theta})\|_{\boldsymbol{R}}^2\right). \tag{2.12}$$

As the log function is monotonic, the MLE is equivalently obtained by minimizing $-\log \mathcal{L}(\boldsymbol{x})$, leading to

$$\begin{aligned}
\widehat{\boldsymbol{\theta}}_{\text{MLE}} &= \arg\max \mathcal{L}(\boldsymbol{x}) \\
&= \arg\min \; -\log\left(\mathcal{L}(\boldsymbol{x})\right) \\
&= \arg\min \left(\boldsymbol{\theta} \mapsto \frac{m}{2} \log(2\pi) + \frac{1}{2} \log(|\boldsymbol{R}|) + \frac{1}{2} \|\boldsymbol{x} - h(\boldsymbol{\theta})\|_{\boldsymbol{R}}^2\right) \\
&= \arg\min \left(\boldsymbol{\theta} \mapsto \|\boldsymbol{x} - h(\boldsymbol{\theta})\|_{\boldsymbol{R}}^2\right).
\end{aligned} \tag{2.13}$$

At that point, the *residual* random vector is defined as

$$\boldsymbol{z} \triangleq \boldsymbol{x} - h(\widehat{\boldsymbol{\theta}}_{\text{MLE}}). \tag{2.14}$$

As an illustration, in the Single Point Positioning (SPP) introduced in Section 1.3.1, the positioning can be represented by an FGO, as it is done by means of construction of a Gaussian random vector.

The representation of SPP Equation (1.30) by an FGO is visible in Figure 2.3.

Now that a MLE under multivariate Gaussian distribution is defined in Equation (2.13), it has to be computed. The computation depends on the function h. The linear case is treated first, followed by the nonlinear case.

This document may not be reproduced, modified, adapted, published, translated in any way, in whole or in part, nor disclosed to a third party without the prior written consent of ENAC. © 2025, ENAC

2.2 Linear Case

The case of FGO with Gaussian random vectors is now introduced. The focus is placed on the linear case, which serves as a fundamental building block for more general models. The corresponding estimator is first presented, followed by a geometric interpretation that provides insight into its structure. Finally, numerical methods for efficiently computing the solution are discussed.

2.2.1 Estimator and Moments

In Equation (2.13), if h is a linear application, then it can be represented by a matrix $\boldsymbol{H} \in \mathcal{M}_{m,n}(\mathbb{R})$ and $h(\boldsymbol{\theta})$ is replaced by $\boldsymbol{H}\boldsymbol{\theta}$. In that case, if and only of $\operatorname{rank}(\boldsymbol{H}) = n$, which implies that $m \geq n$, it can be shown that

$$\widehat{\boldsymbol{\theta}}_{\mathrm{MLE}} = \arg\min \left(\boldsymbol{\theta} \mapsto \|\boldsymbol{x} - \boldsymbol{H}\boldsymbol{\theta}\|_{\boldsymbol{R}}^2 \right) = \left(\boldsymbol{H}^{\mathsf{T}} \boldsymbol{R}^{-1} \boldsymbol{H} \right)^{-1} \boldsymbol{H}^{\mathsf{T}} \boldsymbol{R}^{-1} \boldsymbol{x}. \tag{2.15}$$

A proof of this result is provided in Appendix B.

This estimator follows a multivariate Gaussian distribution. Its first order moment is

$$\mathbb{E}\left[\widehat{\boldsymbol{\theta}}_{\mathrm{MLE}}\right] = \left(\boldsymbol{H}^{\mathsf{T}} \boldsymbol{R}^{-1} \boldsymbol{H} \right)^{-1} \boldsymbol{H}^{\mathsf{T}} \boldsymbol{R}^{-1} \mathbb{E}[\boldsymbol{x}] = \boldsymbol{\theta}. \tag{2.16}$$

To compute the second order moment, a few key properties are needed,

- the inverse of a symmetric matrix, if it exists, is also symmetric,
- since $\boldsymbol{R}$ is the covariance matrix of $\boldsymbol{x}$, both $\boldsymbol{R}$ and its inverse $\boldsymbol{R}^{-1}$ are symmetric,
- by construction, $\boldsymbol{H}^{\mathsf{T}} \boldsymbol{R}^{-1} \boldsymbol{H}$ is symmetric, as is its inverse $\left(\boldsymbol{H}^{\mathsf{T}} \boldsymbol{R}^{-1} \boldsymbol{H} \right)^{-1}$.

Since $\mathbb{V}[\boldsymbol{x}] = \boldsymbol{R}$, the second order moment of $\widehat{\boldsymbol{\theta}}_{\mathrm{MLE}}$ is

$$\begin{aligned} \mathbb{V}\left[\widehat{\boldsymbol{\theta}}_{\mathrm{MLE}}\right] &= \left(\boldsymbol{H}^{\mathsf{T}} \boldsymbol{R}^{-1} \boldsymbol{H} \right)^{-1} \boldsymbol{H}^{\mathsf{T}} \boldsymbol{R}^{-1} \mathbb{V}[\boldsymbol{x}] \boldsymbol{R}^{-1} \boldsymbol{H} \left(\boldsymbol{H}^{\mathsf{T}} \boldsymbol{R}^{-1} \boldsymbol{H} \right)^{-1} \\ &= \left(\boldsymbol{H}^{\mathsf{T}} \boldsymbol{R}^{-1} \boldsymbol{H} \right)^{-1}. \end{aligned} \tag{2.17}$$

2.2.2 Orthogonal Projections

In Equation (2.15), the Cholesky decomposition of the covariance matrix $\boldsymbol{R} = \boldsymbol{L}\boldsymbol{L}^{\mathsf{T}}$, as defined in Appendix B, can be used to remove $\boldsymbol{R}$, i.e.,

$$\|\boldsymbol{x} - \boldsymbol{H}\boldsymbol{\theta}\|_{\boldsymbol{R}}^2 = \left\| \boldsymbol{L}^{-1} (\boldsymbol{x} - \boldsymbol{H}\boldsymbol{\theta}) \right\|_{\boldsymbol{I}}^2 = \left\| \boldsymbol{L}^{-1}\boldsymbol{x} - \boldsymbol{L}^{-1}\boldsymbol{H}\boldsymbol{\theta} \right\|_{\boldsymbol{I}}^2. \tag{2.18}$$

This process is referred to as whitening. Therefore, in Equation (2.15), $\boldsymbol{x}$ is replaced by the random vector $\boldsymbol{L}^{-1}\boldsymbol{x}$, $\boldsymbol{H}$ by the matrix $\boldsymbol{L}^{-1}\boldsymbol{H}$ which is still of rank n thanks to Proposition B.2.4 and $\boldsymbol{R}$ by an identity matrix. Thanks to this whitening procedure, without loss of generality, $\boldsymbol{R}$ is assumed to be equal to the identity matrix.

In that case,

$$\widehat{\boldsymbol{\theta}}_{\mathrm{MLE}} = \left(\boldsymbol{H}^{\mathsf{T}}\boldsymbol{H}\right)^{-1}\boldsymbol{H}^{\mathsf{T}}\boldsymbol{x}, \tag{2.19}$$

$$\mathbb{E}\left[\widehat{\boldsymbol{\theta}}_{\mathrm{MLE}}\right] = \boldsymbol{\theta}, \tag{2.20}$$

$$\mathbb{V}\left[\widehat{\boldsymbol{\theta}}_{\mathrm{MLE}}\right] = \left(\boldsymbol{H}^{\mathsf{T}}\boldsymbol{H}\right)^{-1}, \tag{2.21}$$

$$\boldsymbol{z} = \boldsymbol{x} - \boldsymbol{H}\widehat{\boldsymbol{\theta}}_{\mathrm{MLE}} = \left(\boldsymbol{I}_m - \boldsymbol{H}\left(\boldsymbol{H}^{\mathsf{T}}\boldsymbol{H}\right)^{-1}\boldsymbol{H}^{\mathsf{T}}\right)\boldsymbol{x}. \tag{2.22}$$

Denoting $\mathrm{Im}(\boldsymbol{H})$ the image set of the application $\boldsymbol{x} \mapsto \boldsymbol{H}\boldsymbol{x}$, since $\mathrm{rank}(\boldsymbol{H}) = n$, this subset of $\mathbb{R}^m$ is a vector space of dimension n.

Two vectors $\boldsymbol{v}$ and $\boldsymbol{w}$ are orthogonal if $\boldsymbol{v}^{\mathsf{T}}\boldsymbol{w} = 0$. By definition of the orthogonal complement

$$\mathbb{R}^m = \mathrm{Im}(\boldsymbol{H}) \oplus \mathrm{Im}(\boldsymbol{H})^{\perp}, \tag{2.23}$$

it comes

$$\mathrm{Im}\left(\boldsymbol{H}\right)^{\perp} = \left\{\boldsymbol{x} \in \mathbb{R}^m \;\middle|\; \boldsymbol{x}^{\mathsf{T}}\boldsymbol{H} = \boldsymbol{0}\right\} = \left\{\boldsymbol{x} \in \mathbb{R}^m \;\middle|\; \boldsymbol{H}^{\mathsf{T}}\boldsymbol{x} = \boldsymbol{0}\right\}, \tag{2.24}$$

and $\mathrm{Im}(\boldsymbol{H})^{\perp}$ is of dimension $m - n$.

Defining the matrix

$$\boldsymbol{P}_H \triangleq \boldsymbol{H}\left(\boldsymbol{H}^{\mathsf{T}}\boldsymbol{H}\right)^{-1}\boldsymbol{H}^{\mathsf{T}} \tag{2.25}$$

it can be shown that

$$\boldsymbol{P}_H^2 = \boldsymbol{P}_H \tag{2.26}$$

and that $\boldsymbol{P}_H$ is symmetric, i.e.,

$$\boldsymbol{P}_H^{\mathsf{T}} = \boldsymbol{P}_H \tag{2.27}$$

making $\boldsymbol{P}_H$ an orthogonal projector. This property is also true about the matrix $\boldsymbol{I}_m - \boldsymbol{P}_H$.

To understand where these projectors project onto, any vector of $\mathbb{R}^m$ can be decomposed thanks to Equation (2.23), i.e., any vector $\boldsymbol{v} \in \mathbb{R}^m$ can be written as $\boldsymbol{v}_H + \boldsymbol{v}_{H^{\perp}}$ where $\boldsymbol{v}_H = \boldsymbol{H}\boldsymbol{w}$ for a unique $\boldsymbol{w} \in \mathbb{R}^n$ and with $\boldsymbol{H}^{\mathsf{T}}\boldsymbol{v}_{H^{\perp}} = \boldsymbol{0}$. This decomposition leads to

$$\boldsymbol{P}_H\boldsymbol{v}_H = \boldsymbol{v}_H \tag{2.28}$$

which implies

$$\left(\boldsymbol{I}_m - \boldsymbol{P}_H\right)\boldsymbol{v}_H = \boldsymbol{0} \tag{2.29}$$

and

$$\boldsymbol{P}_H\boldsymbol{v}_{H^{\perp}} = \boldsymbol{0}. \tag{2.30}$$

which implies

$$\left(\boldsymbol{I}_m - \boldsymbol{P}_H\right)\boldsymbol{v}_{H^{\perp}} = \boldsymbol{v}_{H^{\perp}} \tag{2.31}$$

Equations (2.28) and (2.30) show that $\boldsymbol{P}_H$ is an orthogonal projector onto $\mathrm{Im}(\boldsymbol{H})$ and Equations (2.29) and (2.31) show that $\boldsymbol{I}_m - \boldsymbol{P}_H$ is an orthogonal projector onto $\mathrm{Im}(\boldsymbol{H})^{\perp}$.

Finally, the image by $\boldsymbol{H}$ of the estimator is obtained by an orthogonal projection of the

This document may not be reproduced, modified, adapted, published, translated in any way, in whole or in part, nor disclosed to a third party without the prior written consent of ENAC. © 2025, ENAC

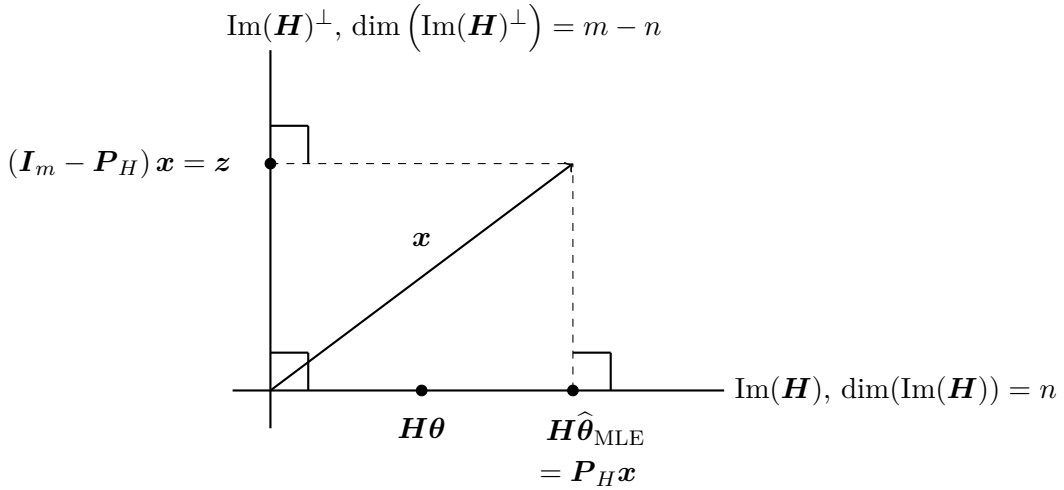

Figure 2.4: Representation of $\mathbb{R}^m$. $\widehat{\boldsymbol{\theta}}_{\mathrm{MLE}}$ is obtained by an orthogonal projection of $\boldsymbol{x}$ onto $\mathrm{Im}(\boldsymbol{H})$, the residual vector $\boldsymbol{z}$ is obtained by an orthogonal projection of $\boldsymbol{x}$ onto $\mathrm{Im}(\boldsymbol{H})^{\perp}$.

random vector $\boldsymbol{x}$, i.e.,

$$\boldsymbol{H}\widehat{\boldsymbol{\theta}}_{\mathrm{MLE}} = \boldsymbol{P}_H\boldsymbol{x} \tag{2.32}$$

and since $\mathrm{rank}(\boldsymbol{H}) = n$, then a unique vector $\widehat{\boldsymbol{\theta}}_{\mathrm{MLE}}$ satisfies Equation (2.32).

The residual vector is also obtained by an orthogonal projection of the random vector $\boldsymbol{x}$, i.e., Equation (2.22) becomes

$$\boldsymbol{z} = (\boldsymbol{I}_m - \boldsymbol{P}_H)\,\boldsymbol{x}. \tag{2.33}$$

These results are visible in Figure 2.4.

2.2.3 Computation of the Solution

Computing Equation (2.19) comes to solving the linear system

$$\boldsymbol{H}^{\mathsf{T}}\boldsymbol{H}\widehat{\boldsymbol{\theta}}_{\mathrm{MLE}} = \boldsymbol{H}^{\mathsf{T}}\boldsymbol{x}. \tag{2.34}$$

The matrix $\left(\boldsymbol{H}^{\mathsf{T}}\boldsymbol{H}\right)^{-1}$ is mathematically well defined. In practice, solving Equation (2.34) can be done by different methods. To compare them, a useful tool is given by the condition number.

Definition 2.2.1 (Condition number)**.** *Let $\boldsymbol{M} \in \mathcal{M}_{m,n}(\mathbb{R})$ with $m \geq n$ and with singular values $\{\sigma_1 \geq \ldots \geq \sigma_n \geq 0\}$. The condition number of $\boldsymbol{M}$ is defined as*

$$\kappa\left(\boldsymbol{M}\right) \triangleq \frac{\sigma_1}{\sigma_n}. \tag{2.35}$$

From this definition, it comes $1 \leq \kappa(\boldsymbol{M}) \leq +\infty$. It can be shown that $\mathrm{rank}(\boldsymbol{H}) = n \Leftrightarrow \sigma_n > 0 \Leftrightarrow \kappa(\boldsymbol{H}) < +\infty$. Therefore, if and only if $\mathrm{rank}(\boldsymbol{H}) = n$, the number $\kappa(\boldsymbol{H})$ is finite, but can be very large.

2.2.3.1 Direct Method

A direct approach to solve Equation (2.34) is to define a matrix $\boldsymbol{A} \triangleq \boldsymbol{H}^\mathsf{T}\boldsymbol{H}$ and invert it, define a vector $\boldsymbol{b} = \boldsymbol{H}^\mathsf{T}\boldsymbol{x}$ and compute $\boldsymbol{A}^{-1}\boldsymbol{b} = \widehat{\boldsymbol{\theta}}_{\text{MLE}}$. In that case, inverting $\boldsymbol{A}$ is mathematically well defined, but the result obtained numerically depends on the method that is used.

2.2.3.2 Cholesky

Another approach is to compute the Cholesky decomposition of $\boldsymbol{A} = \boldsymbol{L}\boldsymbol{L}^\mathsf{T}$ as defined in Appendix B. In that case, Equation (2.34) becomes

$$\boldsymbol{L}\boldsymbol{L}^\mathsf{T}\widehat{\boldsymbol{\theta}}_{\text{MLE}} = \boldsymbol{H}^\mathsf{T}\boldsymbol{x}. \tag{2.36}$$

This way, since $\boldsymbol{L}$ is lower triangular, a first triangular substitution with $\boldsymbol{L}$ followed by a second triangular substitution with $\boldsymbol{L}^\mathsf{T}$ leads to the solution, instead of computing $\boldsymbol{A}^{-1}$.

The computation of the solution by means of the Cholesky decomposition taking into account the sparsity of $\boldsymbol{H}$ is treated in [39, 50].

For both the direct inversion of $\boldsymbol{A}$ and its Cholesky decomposition, it can be shown that $\kappa(\boldsymbol{A}) = (\kappa(\boldsymbol{H}))^2$, so if $\boldsymbol{H}$ is badly conditioned, then $\boldsymbol{A}$ is very badly conditioned.

The following methods directly compute a solution from Equation (2.34) without computing the matrix $\boldsymbol{A}$. As a consequence, their condition number is lower, but these methods require more operations [51].

2.2.3.3 QR

The QR approach is based on the QR decomposition of $\boldsymbol{H}$

$$\boldsymbol{H} = \boldsymbol{Q}\begin{pmatrix}\boldsymbol{R}\\ \boldsymbol{0}_{m-n,n}\end{pmatrix} \tag{2.37}$$

with $\boldsymbol{Q} \in \mathcal{M}_m(\mathbb{R})$ is orthogonal and $\boldsymbol{R} \in \mathcal{M}_n(\mathbb{R})$ is upper triangular and invertible.

Denoting $\boldsymbol{Q}_1$ the first n columns and $\boldsymbol{Q}_2$ the last $m-n$ columns of $\boldsymbol{Q}$, i.e., $\boldsymbol{Q} = (\boldsymbol{Q}_1\ \boldsymbol{Q}_2)$, it comes

$$\begin{aligned}
\|\boldsymbol{x} - \boldsymbol{H}\boldsymbol{\theta}\|_{\boldsymbol{I}}^2 &= \left\|\boldsymbol{x} - \boldsymbol{Q}\begin{pmatrix}\boldsymbol{R}\\ \boldsymbol{0}_{m-n,n}\end{pmatrix}\boldsymbol{\theta}\right\|_{\boldsymbol{I}}^2 \\
&= \left\|\boldsymbol{Q}^\mathsf{T}\boldsymbol{x} - \begin{pmatrix}\boldsymbol{R}\\ \boldsymbol{0}_{m-n,n}\end{pmatrix}\boldsymbol{\theta}\right\|_{\boldsymbol{I}}^2 \text{ since } \boldsymbol{Q} \text{ does not change the norm,} \\
&= \left\|\boldsymbol{Q}_1^\mathsf{T}\boldsymbol{x} - \boldsymbol{R}\boldsymbol{\theta}\right\|_{\boldsymbol{I}}^2 + \left\|\boldsymbol{Q}_2^\mathsf{T}\boldsymbol{x}\right\|_{\boldsymbol{I}}^2 \text{ by the Pythagorean theorem.}
\end{aligned}$$

Therefore,

$$\widehat{\boldsymbol{\theta}}_{\text{MLE}} = \arg\min\left(\boldsymbol{\theta} \mapsto \left\|\boldsymbol{Q}_1^\mathsf{T}\boldsymbol{x} - \boldsymbol{R}\boldsymbol{\theta}\right\|_{\boldsymbol{I}}^2\right), \tag{2.38}$$

This document may not be reproduced, modified, adapted, published, translated in any way, in whole or in part, nor disclosed to a third party without the prior written consent of ENAC. © 2025, ENAC

and the residual $\boldsymbol{z}$ satisfies $\boldsymbol{z}^\mathsf{T}\boldsymbol{z} = \left\|\boldsymbol{Q}_2^\mathsf{T}\boldsymbol{x}\right\|_{\boldsymbol{I}}^2$. This problem is solved by one triangular substitution.

Different methods can be used to actually compute the QR decomposition of $\boldsymbol{H}$, and to take into account its sparsity [51, 39, 50].

2.2.3.4 SVD

The Singular Value Decomposition (SVD) approach is based on the SVD decomposition of $\boldsymbol{H}$

$$\boldsymbol{H} = \boldsymbol{U}\begin{pmatrix}\boldsymbol{S}\\ \boldsymbol{0}_{m-n,n}\end{pmatrix}\boldsymbol{V}^\mathsf{T} \tag{2.39}$$

with $\boldsymbol{U} \in \mathcal{M}_m(\mathbb{R})$ and $\boldsymbol{V} \in \mathcal{M}_n(\mathbb{R})$ are orthogonal and $\boldsymbol{S} \in \mathcal{M}_n(\mathbb{R})$ is diagonal, with diagonal elements $\{\sigma_1 \geq \ldots \geq \sigma_n\}$.

Denoting $\boldsymbol{U}_1$ the first n columns and $\boldsymbol{U}_2$ the last $m-n$ columns of $\boldsymbol{U}$, i.e., $\boldsymbol{U} = (\boldsymbol{U}_1\ \boldsymbol{U}_2)$, it comes

$$\begin{aligned}
\|\boldsymbol{x} - \boldsymbol{H}\boldsymbol{\theta}\|_{\boldsymbol{I}}^2 &= \left\|\boldsymbol{x} - \boldsymbol{U}\begin{pmatrix}\boldsymbol{S}\\ \boldsymbol{0}_{m-n,n}\end{pmatrix}\boldsymbol{V}^\mathsf{T}\boldsymbol{\theta}\right\|_{\boldsymbol{I}}^2 \\
&= \left\|\boldsymbol{U}^\mathsf{T}\boldsymbol{x} - \begin{pmatrix}\boldsymbol{S}\\ \boldsymbol{0}_{m-n,n}\end{pmatrix}\boldsymbol{V}^\mathsf{T}\boldsymbol{\theta}\right\|_{\boldsymbol{I}}^2 \text{ since } \boldsymbol{U} \text{ does not change the norm,} \\
&= \left\|\boldsymbol{U}_1^\mathsf{T}\boldsymbol{x} - \boldsymbol{S}\boldsymbol{V}^\mathsf{T}\boldsymbol{\theta}\right\|_{\boldsymbol{I}}^2 + \left\|\boldsymbol{U}_2^\mathsf{T}\boldsymbol{x}\right\|_{\boldsymbol{I}}^2 \text{ by the Pythagorean theorem.}
\end{aligned}$$

Therefore,

$$\widehat{\boldsymbol{\theta}}_{\text{MLE}} = \arg\min\left(\boldsymbol{\theta} \mapsto \left\|\boldsymbol{U}_1^\mathsf{T}\boldsymbol{x} - \boldsymbol{S}\boldsymbol{V}^\mathsf{T}\boldsymbol{\theta}\right\|_{\boldsymbol{I}}^2\right), \tag{2.40}$$

and the residual $\boldsymbol{z}$ satisfies $\boldsymbol{z}^\mathsf{T}\boldsymbol{z} = \left\|\boldsymbol{U}_2^\mathsf{T}\boldsymbol{x}\right\|_{\boldsymbol{I}}^2$. This problem is solved by inverting the diagonal matrix $\boldsymbol{S}$, which is doable since $\text{rank}\,(\boldsymbol{H}) = n \Leftrightarrow \sigma_n > 0$, scaling the vector $\boldsymbol{U}_1^\mathsf{T}\boldsymbol{x}$ by these inverted singular values, and then multiplying it by $\boldsymbol{V}$, obtained by transposition of $\boldsymbol{V}^\mathsf{T}$.

All these methods differ by the number of operations that they require, and on their stability. On one hand, this thesis does not require real-time computation. Therefore, this is not taken into account here. On the other hand, recalling that $\mathbb{V}\left[\widehat{\boldsymbol{\theta}}_{\text{MLE}}\right] = \left(\boldsymbol{H}^\mathsf{T}\boldsymbol{H}\right)^{-1}$, since $\kappa\left(\mathbb{V}\left[\widehat{\boldsymbol{\theta}}_{\text{MLE}}\right]\right) = \kappa\left(\left(\boldsymbol{H}^\mathsf{T}\boldsymbol{H}\right)^{-1}\right) = \kappa\left(\boldsymbol{H}^\mathsf{T}\boldsymbol{H}\right) = \kappa\left(\boldsymbol{H}\right)^2$, if $\kappa(\boldsymbol{H})$ is large, then at least one eigenvalue of $\mathbb{V}\left[\widehat{\boldsymbol{\theta}}_{\text{MLE}}\right]$ is very large compared to the smallest one, so no matter which method is used, the variance of the MLE is not well conditioned.

With the linear Gaussian case now addressed, the nonlinear case is treated in the next section.

2.3 Nonlinear Case

Considering h to be a nonlinear function allows for a broader class of models, where the relationships between variables are no longer assumed to be linear. The formulation, interpretation, and solution methods are adapted accordingly to handle the increased complexity introduced by nonlinearity. The analysis begins with the formulation of the equations underlying nonlinear FGO, highlighting specific hypotheses on h that are required and challenges due to this nonlinearity. Once these equations are established, the focus shifts to several solvers commonly used in practice to compute solutions.

2.3.1 Equations

In the general case, where h is not necessarily a linear and injective function, the computation of the MLE Equation (2.13) is not straightforward. Firstly, there might exist multiple solutions. Secondly, actually computing them is not directly doable. Instead, a computable approach is presented here, requiring additional assumptions on h.
Assuming that h is a differentiable function on an open set $S \subseteq \mathbb{R}^n$ such that $\Theta \subseteq S$, then $\forall \boldsymbol{x}_0 \in S$, it satisfies

$$\forall \boldsymbol{x} \in \mathbb{R}^n,\ h(\boldsymbol{x}) = h(\boldsymbol{x}_0) + \boldsymbol{H}_{\boldsymbol{x}_0}(\boldsymbol{x} - \boldsymbol{x}_0) + o\left(\|\boldsymbol{x} - \boldsymbol{x}_0\|\right) \tag{2.41}$$

where $\boldsymbol{H}_{\boldsymbol{x}_0} \in \mathcal{M}_{m,n}(\mathbb{R})$ represents the Jacobian matrix of h computed at $\boldsymbol{x}_0$.
Neglecting the higher order terms in Equation (2.41), the function h is approximated

$$h(\boldsymbol{x}) \approx h(\boldsymbol{x}_0) + \boldsymbol{H}_{\boldsymbol{x}_0}(\boldsymbol{x} - \boldsymbol{x}_0). \tag{2.42}$$

Now that an affine approximation of h is available, it can be treated similarly to the linear case. This is done by setting a vector $\boldsymbol{\theta}_0 \in \Theta$ and by means of the approximation of h: injecting Equation (2.42) into Equation (2.13) leads to

$$\widehat{\boldsymbol{\theta}} = \arg\min \left(\boldsymbol{\theta} \mapsto \|(\boldsymbol{x} - h(\boldsymbol{\theta}_0) + \boldsymbol{H}_{\boldsymbol{\theta}_0}\boldsymbol{\theta}_0) - \boldsymbol{H}_{\boldsymbol{\theta}_0}\boldsymbol{\theta}\|^2_{\boldsymbol{R}} \right). \tag{2.43}$$

The notation $\widehat{\boldsymbol{\theta}}$ indicates that it is not yet the $\widehat{\boldsymbol{\theta}}_{\text{MLE}}$. Equation (2.43) has a similar structure than what is presented in the linear case Equation (2.15): if and only if $\operatorname{rank}(\boldsymbol{H}_{\boldsymbol{\theta}_0}) = n$, which implies that $m \geq n$, the solution is given by

$$\begin{aligned} \widehat{\boldsymbol{\theta}} &= \left(\boldsymbol{H}_{\boldsymbol{\theta}_0}^{\mathsf{T}}\boldsymbol{R}^{-1}\boldsymbol{H}_{\boldsymbol{\theta}_0}\right)^{-1} \boldsymbol{H}_{\boldsymbol{\theta}_0}^{\mathsf{T}}\boldsymbol{R}^{-1}\left(\boldsymbol{x} - h(\boldsymbol{\theta}_0) + \boldsymbol{H}_{\boldsymbol{\theta}_0}\boldsymbol{\theta}_0\right) \\ &= \boldsymbol{\theta}_0 + \left(\boldsymbol{H}_{\boldsymbol{\theta}_0}^{\mathsf{T}}\boldsymbol{R}^{-1}\boldsymbol{H}_{\boldsymbol{\theta}_0}\right)^{-1} \boldsymbol{H}_{\boldsymbol{\theta}_0}^{\mathsf{T}}\boldsymbol{R}^{-1}\left(\boldsymbol{x} - h(\boldsymbol{\theta}_0)\right). \end{aligned} \tag{2.44}$$

After that, the function h can be approximated again, around the vector given by Equation (2.44). Therefore, from Equations (2.43) and (2.44), an iterative approach can be used to solve Equation (2.13), leading to the definition of the Gauss-Newton algorithm.

This document may not be reproduced, modified, adapted, published, translated in any way, in whole or in part, nor disclosed to a third party without the prior written consent of ENAC. © 2025, ENAC

Algorithm 2.2 Gauss-Newton

Require: Initial estimate $\boldsymbol{\theta}_0 \in \mathbb{R}^n$, differentiable function h, vector $\boldsymbol{x}(\omega) \in \mathbb{R}^m$, tolerance threshold $T > 0$

repeat

Compute Jacobian matrix $\boldsymbol{H}_{\boldsymbol{\theta}_0}$ and evaluation $h(\boldsymbol{\theta}_0)$, assert $\operatorname{rank}(\boldsymbol{H}_{\boldsymbol{\theta}_0}) = n$

$\widehat{\boldsymbol{\theta}} \leftarrow \left(\boldsymbol{H}_{\boldsymbol{\theta}_0}^{\mathsf{T}} \boldsymbol{R}^{-1} \boldsymbol{H}_{\boldsymbol{\theta}_0}\right)^{-1} \boldsymbol{H}_{\boldsymbol{\theta}_0}^{\mathsf{T}} \boldsymbol{R}^{-1} \left(\boldsymbol{x}(\omega) - h(\boldsymbol{\theta}_0) + \boldsymbol{H}_{\boldsymbol{\theta}_0} \boldsymbol{\theta}_0\right)$

$\Delta\widehat{\boldsymbol{\theta}} \leftarrow \widehat{\boldsymbol{\theta}} - \boldsymbol{\theta}_0$

$\boldsymbol{\theta}_0 \leftarrow \widehat{\boldsymbol{\theta}}$

until $\left\|\Delta\widehat{\boldsymbol{\theta}}\right\| < T$

return $\boldsymbol{\theta}_0$

The Gauss-Newton algorithm introduced for solving Equation (2.13) has its advantages and inconvenient,

- although multiple vectors might satisfy Equation (2.13), only a single one is returned by the algorithm,
- the returned vector is not necessarily a global maximizer of Equation (2.12), i.e., it can be what is called a local maximum,
- the returned vector depends on the initial estimate $\boldsymbol{\theta}_0$,
- depending on the initial estimate $\boldsymbol{\theta}_0$, the algorithm can diverge,
- the algorithm has a different behavior (in terms of sequence of linearization points and of number of iterations) for each input value $\boldsymbol{x}(\omega)$, making the computation of the distribution of the obtained estimator or of its moments not straightforward.

For these reasons, the vector returned by the Gauss-Newton algorithm might not satisfy Equation (2.13). However, in this thesis, the returned vector by this algorithm is called the MLE anyway, although a difference exists.

2.3.2 Solvers

In the case of independent Gaussian random vectors, the MLE built by means of FGO is a nonlinear WLS problem, as in Equation (2.13). An important amount of literature on solving such problems exists. The main results are presented here.

A straightforward approach is to approximate the function to minimize by a linear approximation, and follow the opposite direction of the gradient. This method is referred as steepest descent. Since the function to minimize is approximated by an affine function, this method is referred as first order method. It does not take into account the squared norm involved in the function to minimize, so this type of methods, on its own, is not adapted.

On the other hand, second order methods exist. For example, the Gauss-Newton algorithm works by approaching the function to minimize by positive-definite quadratic

forms. Refinement of this method exist, such as Dogleg and Levenberg-Marquardt [52, Chapter 15]. Dogleg [53] works by computing the Gauss-Newton and steepest descent updates, and combining them depending on the implementation. Levenberg-Marquardt is also an hybrid between steepest descent and Gauss-Newton, but in case of non-injective linear approximations of h, the Levenberg-Marquardt can converge anyway.

These different algorithms are explained with more details and are compared in [54]. [51] provides conditions to guarantee a convergence to at least a local extrema.

For nonlinear WLS problems that are not too nonlinear and that are well conditioned, the use of one or other method should not make a difference, which is assumed here. Otherwise, in all cases, the obtained estimators would be random vectors with a badly conditioned variance, so it is something to avoid. Therefore, all results presented in this thesis are obtained by means of the Gauss-Newton algorithm.

2.4 Transformations of FGO

This section explores a variety of transformations that can be applied to an FGO problem. These transformations aim to change the structure, in order to cancel unmodeled biases and adapt the formulation to specific GNSS positioning frameworks. Understanding these operations is essential for both theoretical analysis and practical implementation.

2.4.1 Linear Combinations of Observations

The case of an FGO made of linear Gaussian factors is finally equivalent to solving Equation (2.15). Instead of directly solving this problem, the objective of this section is to assess how linear combination of the random vector translates to the estimator.

To do so, the linear combination operator is represented by a matrix $\boldsymbol{D} \in \mathcal{M}_{p,m}(\mathbb{R})$. Since $\boldsymbol{x} \sim \mathcal{N}(\boldsymbol{H\theta}, \boldsymbol{R})$, with $\boldsymbol{H} \in \mathcal{M}_{m,n}(\mathbb{R})$ injective, it comes $\boldsymbol{Dx} \sim \mathcal{N}\left(\boldsymbol{DH\theta}, \boldsymbol{DRD}^\mathsf{T}\right)$.

In that case, replacing $\boldsymbol{x} \sim \mathcal{N}(\boldsymbol{H\theta}, \boldsymbol{R})$ by $\boldsymbol{Dx} \sim \mathcal{N}\left(\boldsymbol{DH\theta}, \boldsymbol{DRD}^\mathsf{T}\right)$ in Equation (2.15) gives

$$\widehat{\boldsymbol{\theta}}_{\mathrm{MLE,D}} = \arg\min \left(\boldsymbol{\theta} \mapsto \|\boldsymbol{Dx} - \boldsymbol{DH\theta}\|^2_{\boldsymbol{DRD}^\mathsf{T}}\right). \tag{2.45}$$

Equation (2.45) admits a unique solution if and only if $\operatorname{rank}(\boldsymbol{DH}) = n$. Depending on p, different cases are studied.

First, if $p > m$, then $\boldsymbol{DRD}^\mathsf{T}$ is positive semi-definite but not positive-definite, so $\left(\boldsymbol{DRD}^\mathsf{T}\right)^{-1}$ does not exist and the norm defined in Equation (2.10) is not defined. Therefore, this type of linear combination is to be avoided.

This document may not be reproduced, modified, adapted, published, translated in any way, in whole or in part, nor disclosed to a third party without the prior written consent of ENAC. © 2025, ENAC

Second, if $p = m$, assuming that $\boldsymbol{D}^{-1}$ exists,

$$\begin{aligned}\widehat{\boldsymbol{\theta}}_{\mathrm{MLE,D}} &= \left((\boldsymbol{DH})^{\mathsf{T}}\left(\boldsymbol{DRD}^{\mathsf{T}}\right)^{-1}\boldsymbol{DH}\right)^{-1}(\boldsymbol{DH})^{\mathsf{T}}\left(\boldsymbol{DRD}^{\mathsf{T}}\right)^{-1}\boldsymbol{Dx} \\ &= \left(\boldsymbol{H}^{\mathsf{T}}\boldsymbol{D}^{\mathsf{T}}\left(\boldsymbol{D}^{\mathsf{T}}\right)^{-1}\boldsymbol{R}^{-1}\boldsymbol{D}^{-1}\boldsymbol{DH}\right)^{-1}\boldsymbol{H}^{\mathsf{T}}\boldsymbol{D}^{\mathsf{T}}\left(\boldsymbol{D}^{\mathsf{T}}\right)^{-1}\boldsymbol{R}^{-1}\boldsymbol{D}^{-1}\boldsymbol{Dx} \\ &= \left(\boldsymbol{H}^{\mathsf{T}}\boldsymbol{R}^{-1}\boldsymbol{H}\right)^{-1}\boldsymbol{H}^{\mathsf{T}}\boldsymbol{R}^{-1}\boldsymbol{x} \\ &= \widehat{\boldsymbol{\theta}}_{\mathrm{MLE}}. \end{aligned} \tag{2.46}$$

Therefore, if $\boldsymbol{D}^{-1}$ exists, then $\boldsymbol{D}$ gives the same estimator.

If $\boldsymbol{D}^{-1}$ does not exist, $\widehat{\boldsymbol{\theta}}_{\mathrm{MLE,D}}$ is well defined if and only if $\operatorname{rank}(\boldsymbol{DH}) = n$. In that case, the estimator generally satisfies

$$\widehat{\boldsymbol{\theta}}_{\mathrm{MLE,D}} \neq \widehat{\boldsymbol{\theta}}_{\mathrm{MLE}} \tag{2.47}$$

meaning that the result depends on $\boldsymbol{D}$. Consequently, a case-by-case analysis is required.

Finally, if $p < m$, $\widehat{\boldsymbol{\theta}}_{\mathrm{MLE,D}}$ is well defined if and only if $\operatorname{rank}(\boldsymbol{DH}) = n$, which implies $p \geq n$. In that case, the estimator generally satisfies

$$\widehat{\boldsymbol{\theta}}_{\mathrm{MLE,D}} \neq \widehat{\boldsymbol{\theta}}_{\mathrm{MLE}} \tag{2.48}$$

meaning that the result depends on $\boldsymbol{D}$. Consequently, a case-by-case analysis is required.

2.4.2 Restriction of the Observation Model

In the case of an FGO as in Equation (2.12), the objective is to estimate a vector from a real-valued random vector and the function $h : \Theta \subseteq \mathbb{R}^n \to \mathbb{R}^m$.

Without loss of generality (possibly after reordering the components), assume that the first k components of the argument of h are fixed to some values $\boldsymbol{\theta}_{\mathrm{fix}}$. This defines the restriction of h

$$\begin{aligned} h|_{\boldsymbol{\theta}_{\mathrm{fix}}} : \mathbb{R}^{n-k} &\to \mathbb{R}^m \\ \boldsymbol{\theta} &\mapsto h(\boldsymbol{\theta}_{\mathrm{fix}}, \boldsymbol{\theta}). \end{aligned} \tag{2.49}$$

This formulation enables estimation of the unfixed components of the parameter vector while treating $\boldsymbol{\theta}_{\mathrm{fix}}$ as known.

2.4.3 Transformation of the Parameter Vector

Similarly, in the case of an FGO as in Equation (2.12), the objective is to estimate a vector from a real-valued random vector and an observation model.

Assume that the vector to estimate is $\boldsymbol{\theta}' \in \Theta' \subseteq \mathbb{R}^{n'}$, that the following functions are defined

- $g : \Theta' \subseteq \mathbb{R}^{n'} \to \mathbb{R}^n$,

- $h : \mathbb{R}^n \to \mathbb{R}^m$.

and that the observation model (the function h in Equation (2.12)) is given by the composition $h \circ g$, i.e., $\boldsymbol{x} \sim \mathcal{N}\left((h \circ g)\left(\boldsymbol{\theta}'\right), \boldsymbol{R}\right)$ and Equation (2.12) is written

$$\begin{aligned} \mathcal{L}(\boldsymbol{x}) : \Theta' \subseteq \mathbb{R}^{n'} &\to \mathbb{R} \\ \boldsymbol{\theta}' &\mapsto \frac{1}{\sqrt{(2\pi)^m |\boldsymbol{R}|}} \exp\left(-\frac{1}{2} \left\|\boldsymbol{x} - (h \circ g)\left(\boldsymbol{\theta}'\right)\right\|_{\boldsymbol{R}}^2\right). \end{aligned} \tag{2.50}$$

If the composite function $h \circ g$ allows for the estimation of $\boldsymbol{\theta}'$, then this section does not add anything new to what is proposed in previous sections.

On the other hand, in cases where $h \circ g$ does not permit to estimate $\boldsymbol{\theta}'$ (e.g., if $h \circ g$ is linear and its rank is strictly lower than n'), but h alone satisfies the conditions for estimation, then the MLE of the vector $\boldsymbol{\theta} \triangleq g(\boldsymbol{\theta}')$ is well defined.

This scenario is particularly useful in practice, as it enables reformulating the estimation problem in terms of a different parameter vector $\boldsymbol{\theta}$ even when the MLE of the original vector $\boldsymbol{\theta}'$ is not well defined.

2.4.4 Difference of Two Graphs and Differential Positioning

In GNSS differential positioning as presented in the Real-Time Kinematic (RTK) Section 1.3.3.1, a rover and a reference station are used to estimate the reference to rover vector by a difference of observations from common satellites, and the rover coordinates in a global frame are recovered from the reference global coordinates. This section formalizes this procedure with the difference of two FGO.

Let $\boldsymbol{\theta}_1 \in \Theta_1 \subseteq \mathbb{R}^{n_1}$ and $\boldsymbol{\theta}_2 \in \Theta_2 \subseteq \mathbb{R}^{n_2}$ be two unknown vectors.

In practice, in the case of differential positioning within an RTK framework, $\boldsymbol{\theta}_1$ and $\boldsymbol{\theta}_2$ correspond respectively to a reference station state vector and to the rover state vector.

Let $\boldsymbol{x}_1 \sim \mathcal{N}\left(h_1(\boldsymbol{\theta}_1), \boldsymbol{R}_1\right)$ and $\boldsymbol{x}_2 \sim \mathcal{N}\left(h_2(\boldsymbol{\theta}_2), \boldsymbol{R}_2\right)$ be two independent random vectors of dimension m, and with $h_1 : \Theta_1 \to \mathbb{R}^m$ and $h_2 : \Theta_2 \to \mathbb{R}^m$.

In practice, $\boldsymbol{x}_1$ and $\boldsymbol{x}_2$ correspond to common GNSS observations of the reference and rover, respectively.

The difference of these random vectors is defined

$$\boldsymbol{x} \triangleq \boldsymbol{x}_2 - \boldsymbol{x}_1 \sim \mathcal{N}\left(h_2(\boldsymbol{\theta}_2) - h_1(\boldsymbol{\theta}_1), \boldsymbol{R}_1 + \boldsymbol{R}_2\right) \tag{2.51}$$

and corresponds to the difference of two factor graphs. At that point, a likelihood function similar to Equation (2.12) can be built and maximized, depending on h_1 and h_2.

The differential positioning is obtained following Section 2.4.3. Let $g : \Theta_1 \times \Theta_2 \subseteq \mathbb{R}^{n_1+n_2} \to \Theta \subseteq \mathbb{R}^n$. Defining $\boldsymbol{\theta} \triangleq g\left(\boldsymbol{\theta}_1, \boldsymbol{\theta}_2\right)$, and $h : \Theta \subseteq \mathbb{R}^n \to \mathbb{R}^m$ a function such that $\forall \left(\boldsymbol{\theta}_1, \boldsymbol{\theta}_2\right) \in \Theta_1 \times \Theta_2$

$$h\left(g\left(\boldsymbol{\theta}_1, \boldsymbol{\theta}_2\right)\right) = h_2\left(\boldsymbol{\theta}_2\right) - h_1\left(\boldsymbol{\theta}_1\right), \tag{2.52}$$

This document may not be reproduced, modified, adapted, published, translated in any way, in whole or in part, nor disclosed to a third party without the prior written consent of ENAC. © 2025, ENAC

by injecting Equation (2.52) into Equation (2.51), it comes

$$\boldsymbol{x} \sim \mathcal{N}\left(h(\boldsymbol{\theta}), \boldsymbol{R}_1 + \boldsymbol{R}_2\right). \tag{2.53}$$

At that point, similarly to Section 2.4.3, a likelihood function similar to Equation (2.12) can be built and maximized if h satisfies the conditions developed in this chapter (i.e., if h is linear and $\text{rank}(h) = n$, or if h is differentiable, with a Jacobian matrix of rank n).

In the specific case of differential positioning, the estimated quantity is the vector from the reference station to the rover, which is defined as the difference between their respective positions, corresponding to a bilinear application of both coordinates.

Therefore, g is considered to be a bilinear application, that can be represented by a matrix $\boldsymbol{G} \in \mathcal{M}_{n,n_1+n_2}(\mathbb{R})$.

If h is either a linear mapping, denoted $\boldsymbol{H}$, or a differentiable nonlinear function whose Jacobian $\boldsymbol{H} \in \mathcal{M}_{m,n}(\mathbb{R})$, with $\text{rank}(\boldsymbol{H}) = n$ everywhere, then it can be shown that $\text{rank}(\boldsymbol{HG}) = \text{rank}(\boldsymbol{G})$. Therefore, for both $\boldsymbol{\theta}_1$ and $\boldsymbol{\theta}_2$ to be estimated by the MLE, it is necessary (and sufficient if h is a linear application) that $\text{rank}(\boldsymbol{G}) = n_1 + n_2$. On one hand, if it is the case, then this section does not add anything new to what is proposed in previous sections.

On the other hand, if $\text{rank}(\boldsymbol{G}) < n_1 + n_2$, then $\boldsymbol{\theta}$ is estimated by the MLE, but it does not permit to estimate both $\boldsymbol{\theta}_1$ and $\boldsymbol{\theta}_2$. This is typically the case of differential positioning: by differencing the common observations of the rover and the reference, their coordinates cannot be estimated jointly. Instead, only the reference to rover vector is estimated (i.e., $\boldsymbol{\theta} = \boldsymbol{\theta}_2 - \boldsymbol{\theta}_1$) since this vector is a non-injective bilinear application of the rover and reference coordinates.

2.4.5 Common Bias and Random Affine Bias

Another advantage of computing the difference of two FGO is that all common terms cancel. This is of particular interest in GNSS, as very often, unmodeled biases in observations exist and are highly correlated with respect to space and/or time. In particular, for two GNSS receivers at small distances or a single receiver at two close instants, these biases cancel thanks to this procedure.

2.4.5.1 Deterministic and Equal Biases

Similarly to Equation (2.51), if $\boldsymbol{\mu} \in \mathbb{R}^m$ is a bias contained in two independent Gaussian random vectors, i.e., $\boldsymbol{x}_1 \sim \mathcal{N}\left(h_1\left(\boldsymbol{\theta}_1\right) + \boldsymbol{\mu}, \boldsymbol{R}_1\right)$ and $\boldsymbol{x}_2 \sim \mathcal{N}\left(h_2\left(\boldsymbol{\theta}_2\right) + \boldsymbol{\mu}, \boldsymbol{R}_1\right)$, then by a difference, it comes

$$\boldsymbol{x}_2 - \boldsymbol{x}_1 \sim \mathcal{N}\left(h_2(\boldsymbol{\theta}_2) - h_1(\boldsymbol{\theta}_1), \boldsymbol{R}_1 + \boldsymbol{R}_2\right). \tag{2.54}$$

In practice, omitted biases in GNSS observations are never exactly equal in observations of two GNSS receivers, or in observations of a single receiver at two instants.

2.4.5.2 Random Affine Biases

In the case of a random bias $\boldsymbol{\mu}$ that is an affine function of the parameters vector to estimate, i.e., if the random bias is modeled as

$$\boldsymbol{\mu}(\omega) : \boldsymbol{\theta} \mapsto \boldsymbol{A}(\omega)\boldsymbol{\theta} + \boldsymbol{b}(\omega) \tag{2.55}$$

where $\boldsymbol{A}(\omega) \in \mathcal{M}_{m,n}(\mathbb{R})$ and $\boldsymbol{b}(\omega) \in \mathbb{R}^m$, and if $\boldsymbol{x}_1 \sim \mathcal{N}\left(h_1\left(\boldsymbol{\theta}_1\right) + \boldsymbol{\mu}(\omega)(\boldsymbol{\theta}_1), \boldsymbol{R}_1\right)$ and $\boldsymbol{x}_2 \sim \mathcal{N}\left(h_2\left(\boldsymbol{\theta}_2\right) + \boldsymbol{\mu}(\omega)(\boldsymbol{\theta}_2), \boldsymbol{R}_1\right)$, the difference of observations becomes

$$\boldsymbol{x}_2 - \boldsymbol{x}_1 \sim \mathcal{N}\left(h_2(\boldsymbol{\theta}_2) - h_1(\boldsymbol{\theta}_1) + \boldsymbol{A}(\omega)(\boldsymbol{\theta}_2 - \boldsymbol{\theta}_1), \boldsymbol{R}_1 + \boldsymbol{R}_2\right). \tag{2.56}$$

After that difference, slowly varying affine biases (i.e., biases such that $|||\boldsymbol{A}(\omega)||| \approx 0$, where $|||\cdot|||$ indicates a matrix norm) are canceled in the case of difference. This is also true if $\boldsymbol{\theta}_2 - \boldsymbol{\theta}_1 \approx \mathbf{0}$ or if $\boldsymbol{\theta}_2 - \boldsymbol{\theta}_1$ is within the null space of $\boldsymbol{A}(\omega)$.

In practice, many atmospheric biases within GNSS observations, as presented in Section 1.2.5 have such behavior.

To conclude the chapter, the Kalman Filter (KF) is examined and expressed within the FGO formalism. This representation highlights how FGO serves as a unifying formalism for a wide range of estimation algorithms.

2.5 Kalman Filter Update as an FGO

In this section, a link between FGO and the KF [55] is made. First are presented the classical equations of the KF, as well as a type of random process that it is designed for. Next, the update step is represented by an FGO.

2.5.1 Equations of the Kalman Filter

2.5.1.1 Random Process to Estimate

Let

$$\boldsymbol{\theta}_0 \sim \mathcal{N}\left(\boldsymbol{\mu}_0, \boldsymbol{\Sigma}_0\right) \tag{2.57}$$

and $\forall k \in \mathbb{N}$,

$$\boldsymbol{\theta}_{k+1} = \boldsymbol{F}_k\boldsymbol{\theta}_k + \boldsymbol{w}_k, \boldsymbol{w}_k \sim \mathcal{N}\left(\mathbf{0}, \boldsymbol{Q}_k\right), \tag{2.58}$$

$$\boldsymbol{y}_{k+1} = \boldsymbol{H}_{k+1}\boldsymbol{\theta}_{k+1} + \boldsymbol{v}_{k+1}, \boldsymbol{v}_{k+1} \sim \mathcal{N}\left(\mathbf{0}, \boldsymbol{R}_{k+1}\right), \tag{2.59}$$

with the random vectors $\boldsymbol{\theta}_0, \boldsymbol{w}_0, \ldots, \boldsymbol{w}_k, \boldsymbol{v}_1, \ldots, \boldsymbol{v}_{k+1}$ independent. Equations (2.57) to (2.59) define a random process that a KF is typically designed for.

To derive the KF equations, the notion of conditional random vector is used. For two

This document may not be reproduced, modified, adapted, published, translated in any way, in whole or in part, nor disclosed to a third party without the prior written consent of ENAC. © 2025, ENAC

random vectors $\boldsymbol{x}_1$ and $\boldsymbol{x}_2$, the notation $(\boldsymbol{x}_1 \,|\, \boldsymbol{x}_2 = \boldsymbol{x}_2(\omega))$ denotes the random vector $\boldsymbol{x}_1$ conditioned on the event that $\boldsymbol{x}_2$ takes the value $\boldsymbol{x}_2(\omega)$. The following theorem is used.

Theorem 2.5.1. *Let* $\boldsymbol{x} = \left(\boldsymbol{x}_1^\mathsf{T}, \boldsymbol{x}_2^\mathsf{T}\right)^\mathsf{T}$ *be a Gaussian random vector, with* $\mathbb{E}[\boldsymbol{x}] = \left(\boldsymbol{\mu}_1^\mathsf{T}, \boldsymbol{\mu}_2^\mathsf{T}\right)^\mathsf{T}$ *and* $\mathbb{V}[\boldsymbol{x}] = \begin{pmatrix} \boldsymbol{\Sigma}_1 & \boldsymbol{\Sigma}_{1,2} \\ \boldsymbol{\Sigma}_{2,1} & \boldsymbol{\Sigma}_2 \end{pmatrix}$. *It comes that* $(\boldsymbol{x}_1 \,|\, \boldsymbol{x}_2 = \boldsymbol{x}_2(\omega))$ *is a Gaussian random vector, with* $\mathbb{E}[(\boldsymbol{x}_1 \,|\, \boldsymbol{x}_2 = \boldsymbol{x}_2(\omega))] = \boldsymbol{\mu}_1 + \boldsymbol{\Sigma}_{1,2}\boldsymbol{\Sigma}_2^{-1}(\boldsymbol{x}_2(\omega) - \boldsymbol{\mu}_2)$ *and* $\mathbb{V}[(\boldsymbol{x}_1 \,|\, \boldsymbol{x}_2 = \boldsymbol{x}_2(\omega))] = \boldsymbol{\Sigma}_1 - \boldsymbol{\Sigma}_{1,2}\boldsymbol{\Sigma}_2^{-1}\boldsymbol{\Sigma}_{2,1}$.

2.5.1.2 Prior and Posterior Estimators

For a given value of k, the following random vectors are introduced

- the *a priori* estimator of $\boldsymbol{\theta}_{k+1}$ is denoted and defined as the random vector $\widehat{\boldsymbol{\theta}}_{k+1|k} \triangleq (\boldsymbol{\theta}_{k+1} \,|\, \boldsymbol{y}_1, \ldots, \boldsymbol{y}_k = \boldsymbol{y}_1(\omega), \ldots, \boldsymbol{y}_k(\omega))$, also denoted $\widehat{\boldsymbol{\theta}}_{k+1|k} \triangleq (\boldsymbol{\theta}_{k+1} \,|\, \boldsymbol{y}_{1:k} = \boldsymbol{y}_{1:k}(\omega))$, which is Gaussian from Theorem 2.5.1, with moments denoted $\boldsymbol{\mu}_{k+1|k} \triangleq \mathbb{E}\left[\widehat{\boldsymbol{\theta}}_{k+1|k}\right]$ and $\boldsymbol{\Sigma}_{k+1|k} \triangleq \mathbb{V}\left[\widehat{\boldsymbol{\theta}}_{k+1|k}\right]$,
- the *a posteriori* estimator of $\boldsymbol{\theta}_{k+1}$ is denoted and defined as the random vector $\widehat{\boldsymbol{\theta}}_{k+1|k+1} \triangleq (\boldsymbol{\theta}_{k+1} \,|\, \boldsymbol{y}_1, \ldots, \boldsymbol{y}_{k+1} = \boldsymbol{y}_1(\omega), \ldots, \boldsymbol{y}_{k+1}(\omega))$, also denoted $\widehat{\boldsymbol{\theta}}_{k+1|k+1} \triangleq (\boldsymbol{\theta}_{k+1} \,|\, \boldsymbol{y}_{1:k+1} = \boldsymbol{y}_{1:k+1}(\omega))$, which is Gaussian from Theorem 2.5.1, with moments denoted $\boldsymbol{\mu}_{k+1|k+1} \triangleq \mathbb{E}\left[\widehat{\boldsymbol{\theta}}_{k+1|k+1}\right]$ and $\boldsymbol{\Sigma}_{k+1|k+1} \triangleq \mathbb{V}\left[\widehat{\boldsymbol{\theta}}_{k+1|k+1}\right]$,

2.5.1.3 Prediction

At the prediction step is computed $\widehat{\boldsymbol{\theta}}_{k+1|k}$ from $\widehat{\boldsymbol{\theta}}_{k|k} \sim \mathcal{N}\left(\boldsymbol{\mu}_{k|k}, \boldsymbol{\Sigma}_{k|k}\right)$

$$\widehat{\boldsymbol{\theta}}_{k+1|k} = (\boldsymbol{F}_k\boldsymbol{\theta}_k + \boldsymbol{w}_k \,|\, \boldsymbol{y}_{1:k} = \boldsymbol{y}_{1:k}(\omega)). \tag{2.60}$$

From the independency of $\boldsymbol{w}_k$ with $\boldsymbol{y}_1, \ldots, \boldsymbol{y}_k$, it comes

$$\boldsymbol{\mu}_{k+1|k} = \boldsymbol{F}_k\mathbb{E}[(\boldsymbol{\theta}_k \,|\, \boldsymbol{y}_{1:k} = \boldsymbol{y}_{1:k}(\omega))] + \mathbb{E}[\boldsymbol{w}_k] = \boldsymbol{F}_k\boldsymbol{\mu}_{k|k}. \tag{2.61}$$

From the independency of $\boldsymbol{w}_k$ with $\boldsymbol{\theta}_k$, it comes

$$\boldsymbol{\Sigma}_{k+1|k} = \boldsymbol{F}_k\mathbb{V}[(\boldsymbol{\theta}_k \,|\, \boldsymbol{y}_{1:k} = \boldsymbol{y}_{1:k}(\omega))]\,\boldsymbol{F}_k^\mathsf{T} + \mathbb{V}[\boldsymbol{w}_k] = \boldsymbol{F}_k\boldsymbol{\Sigma}_{k|k}\boldsymbol{F}_k^\mathsf{T} + \boldsymbol{Q}_k. \tag{2.62}$$

2.5.1.4 Update

At the update step is computed $\widehat{\boldsymbol{\theta}}_{k+1|k+1}$ from $\widehat{\boldsymbol{\theta}}_{k+1|k}$ and $\boldsymbol{y}_{k+1}$. Building the random vector $(\boldsymbol{y}_{k+1} \,|\, \boldsymbol{y}_{1:k} = \boldsymbol{y}_{1:k}(\omega))$, which is Gaussian from Theorem 2.5.1, its first and second

moments are

$$\begin{aligned}\mathbb{E}\left[(\boldsymbol{y}_{k+1}\,|\,\boldsymbol{y}_{1:k}=\boldsymbol{y}_{1:k}(\omega))\right] &= \mathbb{E}\left[(\boldsymbol{H}_{k+1}\boldsymbol{\theta}_{k+1}+\boldsymbol{v}_{k+1}\,|\,\boldsymbol{y}_{1:k}=\boldsymbol{y}_{1:k}(\omega))\right]\\ &= \boldsymbol{H}_{k+1}\mathbb{E}\left[(\boldsymbol{\theta}_{k+1}\,|\,\boldsymbol{y}_{1:k}=\boldsymbol{y}_{1:k}(\omega))\right]+\mathbb{E}\left[\boldsymbol{v}_{k+1}\right]\\ &= \boldsymbol{H}_{k+1}\boldsymbol{\mu}_{k+1|k}\end{aligned} \tag{2.63}$$

and

$$\begin{aligned}\boldsymbol{S}_{k+1} &\triangleq \mathbb{V}\left[(\boldsymbol{y}_{k+1}\,|\,\boldsymbol{y}_{1:k}=\boldsymbol{y}_{1:k}(\omega))\right]\\ &= \mathbb{V}\left[(\boldsymbol{H}_{k+1}\boldsymbol{\theta}_{k+1}+\boldsymbol{v}_{k+1}\,|\,\boldsymbol{y}_{1:k}=\boldsymbol{y}_{1:k}(\omega))\right]\\ &= \boldsymbol{H}_{k+1}\mathbb{V}\left[(\boldsymbol{\theta}_{k+1}\,|\,\boldsymbol{y}_{1:k}=\boldsymbol{y}_{1:k}(\omega))\right]\boldsymbol{H}_{k+1}^{\mathsf{T}}+\mathbb{V}\left[\boldsymbol{v}_{k+1}\right]\\ &= \boldsymbol{H}_{k+1}\boldsymbol{\Sigma}_{k+1|k}\boldsymbol{H}_{k+1}^{\mathsf{T}}+\boldsymbol{R}_{k+1}.\end{aligned} \tag{2.64}$$

Considering the two Gaussian random vectors $\widehat{\boldsymbol{\theta}}_{k+1|k}$ and $(\boldsymbol{y}_{k+1}\,|\,\boldsymbol{y}_{1:k}=\boldsymbol{y}_{1:k}(\omega))$, by independency of $\boldsymbol{v}_{k+1}$ and $\widehat{\boldsymbol{\theta}}_{k+1|k}$, their covariance is equal to

$$\begin{aligned}\mathrm{Cov}\left(\widehat{\boldsymbol{\theta}}_{k+1|k},(\boldsymbol{y}_{k+1}\,|\,\boldsymbol{y}_{1:k}=\boldsymbol{y}_{1:k}(\omega))\right) &= \mathrm{Cov}\left(\widehat{\boldsymbol{\theta}}_{k+1|k},(\boldsymbol{H}_{k+1}\boldsymbol{\theta}_{k+1}+\boldsymbol{v}_{k+1}\,|\,\boldsymbol{y}_{1:k}=\boldsymbol{y}_{1:k}(\omega))\right)\\ &= \mathrm{Cov}\left(\widehat{\boldsymbol{\theta}}_{k+1|k},(\boldsymbol{\theta}_{k+1}\,|\,\boldsymbol{y}_{1:k}=\boldsymbol{y}_{1:k}(\omega))\right)\boldsymbol{H}_{k+1}^{\mathsf{T}}\\ &\quad+\mathrm{Cov}\left(\widehat{\boldsymbol{\theta}}_{k+1|k},\boldsymbol{v}_{k+1}\right)\\ &= \boldsymbol{\Sigma}_{k+1|k}\boldsymbol{H}_{k+1}^{\mathsf{T}}.\end{aligned} \tag{2.65}$$

Therefore, if the following Gaussian random vector is built

$$\begin{pmatrix}\widehat{\boldsymbol{\theta}}_{k+1|k}\\(\boldsymbol{y}_{k+1}\,|\,\boldsymbol{y}_{1:k}=\boldsymbol{y}_{1:k}(\omega))\end{pmatrix}\sim\mathcal{N}\left(\begin{pmatrix}\boldsymbol{\mu}_{k+1|k}\\\boldsymbol{H}_{k+1}\boldsymbol{\mu}_{k+1|k}\end{pmatrix},\begin{pmatrix}\boldsymbol{\Sigma}_{k+1|k}&\boldsymbol{\Sigma}_{k+1|k}\boldsymbol{H}_{k+1}^{\mathsf{T}}\\\boldsymbol{H}_{k+1}\boldsymbol{\Sigma}_{k+1|k}&\boldsymbol{S}_{k+1}\end{pmatrix}\right) \tag{2.66}$$

then, given a sample $\boldsymbol{y}_{k+1}(\omega)$, applying Theorem 2.5.1 to Equation (2.66) gives the random vector $\widehat{\boldsymbol{\theta}}_{k+1|k+1}$. Defining the Kalman gain

$$\boldsymbol{K}_{k+1}\triangleq\widehat{\boldsymbol{\Sigma}}_{k+1|k}\boldsymbol{H}_{k+1}^{\mathsf{T}}\boldsymbol{S}_{k+1}^{-1}, \tag{2.67}$$

the moments of $\widehat{\boldsymbol{\theta}}_{k+1|k+1}$ are

$$\boldsymbol{\mu}_{k+1|k+1}=\boldsymbol{\mu}_{k+1|k}+\boldsymbol{K}_{k+1}\left(\boldsymbol{y}_{k+1}(\omega)-\boldsymbol{H}_{k+1}\boldsymbol{\mu}_{k+1|k}\right) \tag{2.68}$$

and

$$\boldsymbol{\Sigma}_{k+1|k+1}=\left(\boldsymbol{I}-\boldsymbol{K}_{k+1}\boldsymbol{H}_{k+1}\right)\boldsymbol{\Sigma}_{k+1|k}. \tag{2.69}$$

This document may not be reproduced, modified, adapted, published, translated in any way, in whole or in part, nor disclosed to a third party without the prior written consent of ENAC. © 2025, ENAC

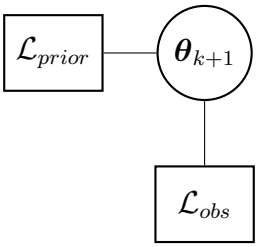

Figure 2.5: Representation of the KF update equations with a factor graph.

2.5.2 Representation of the Update with an FGO

The update step within a KF can be represented by an FGO: $\widehat{\boldsymbol{\theta}}_{k+1|k}$ is a random vector that defines a prior

$$\mathcal{L}_{prior} : \boldsymbol{\theta}_{k+1} \mapsto \frac{1}{\sqrt{(2\pi)^n \left|\boldsymbol{\Sigma}_{k+1|k}\right|}} \exp\left(-\frac{1}{2}\left\|\boldsymbol{\mu}_{k+1|k} - \boldsymbol{\theta}_{k+1}\right\|^2_{\boldsymbol{\Sigma}_{k+1|k}}\right), \tag{2.70}$$

and the sample $\boldsymbol{y}_{k+1}(\omega)$ of the observation $\boldsymbol{y}_{k+1}$ defines a likelihood

$$\mathcal{L}_{obs} : \boldsymbol{\theta}_{k+1} \mapsto \frac{1}{\sqrt{(2\pi)^m \left|\boldsymbol{R}_{k+1}\right|}} \exp\left(-\frac{1}{2}\left\|\boldsymbol{y}_{k+1}(\omega) - \boldsymbol{H}_{k+1}\boldsymbol{\theta}_{k+1}\right\|^2_{\boldsymbol{R}_{k+1}}\right). \tag{2.71}$$

Since the two random vectors $\widehat{\boldsymbol{\theta}}_{k+1|k}$ and $\boldsymbol{v}_{k+1}$ are independent, these two functions can be multiplied, leading to the factor graph visible in Figure 2.5.

Maximizing this product leads to a problem similar to Equation (2.15)

$$\boldsymbol{\mu}_{k+1|k+1} = \arg\min\left(\boldsymbol{\theta} \mapsto \left\|\boldsymbol{\mu}_{k+1|k} - \boldsymbol{\theta}\right\|^2_{\boldsymbol{\Sigma}_{k+1|k}} + \left\|\boldsymbol{y}_{k+1}(\omega) - \boldsymbol{H}_{k+1}\boldsymbol{\theta}\right\|^2_{\boldsymbol{R}_{k+1}}\right). \tag{2.72}$$

Appendix C shows that

$$\boldsymbol{\mu}_{k+1|k+1} = \boldsymbol{\mu}_{k+1|k} + \boldsymbol{K}_{k+1}\left(\boldsymbol{y}_{k+1}(\omega) - \boldsymbol{H}_{k+1}\boldsymbol{\mu}_{k+1|k}\right) \tag{2.73}$$

and the variance of the estimator associated to the estimate Equation (2.72) is

$$\boldsymbol{\Sigma}_{k+1|k+1} = \left(\boldsymbol{I} - \boldsymbol{K}_{k+1}\boldsymbol{H}_{k+1}\right)\boldsymbol{\Sigma}_{k+1|k} \tag{2.74}$$

which are the two KF update Equations (2.68) and (2.69).

As stated in Equations (2.57) to (2.59), the KF assumes strong assumptions on the random process that it is designed for. For example, in case of correlations between the a priori estimator and the observations, then the update equations do not apply. On the other hand, in comparison with the FGO, thanks to the a priori, there are no conditions on the rank of $\boldsymbol{H}_{k+1}$.

Finally, variants exists of the KF in case of nonlinear observations and transitions with respect to the state, such as the EKF. In that case, a linearization of these equations

is done, similarly to the FGO approach, but a single iteration is done, compared to the Gauss-Newton algorithm that iterates until a stopping criterion is met.

A deeper comparison between EKF and FGO is provided in [56].

2.6 Conclusion

This chapter presents FGO as a unified framework for modeling and solving estimation problems. The exposition begins with a deterministic formulation, then incorporates uncertainty through likelihood functions, leading to the stochastic case. Particular attention is given to Gaussian random vectors, where the optimization problem admits a structured formulation.

In the linear case, the estimator is expressed analytically, its statistical properties are derived, and a geometric interpretation through orthogonal projections is provided. Several numerical methods are examined to address conditioning and facilitate practical computation. The nonlinear case follows, with an emphasis on iterative solvers such as the Gauss-Newton algorithm, which adapt the linear strategy to nonlinear differentiable models.

Transformations of FGO are introduced to modify the graph structure, remove unmodeled biases, and tailor the formulation to specific estimation settings such as GNSS differential positioning. Finally, the KF update equations are reinterpreted within the FGO framework, showing how FGO encompasses classical filtering methods and extends naturally to broader scenarios.

With the foundations of GNSS and FGO now established, the focus turns to addressing GNSS positioning problems using FGO in the following chapters.

This document may not be reproduced, modified, adapted, published, translated in any way, in whole or in part, nor disclosed to a third party without the prior written consent of ENAC. © 2025, ENAC

Chapter 3

FGO-Based Cycle Slip Detection and Identification

The reliability and precision of Global Navigation Satellite System (GNSS)-based positioning depend on the integrity of observations, i.e., that they are only affected by errors with known distributions. Among the major threats of carrier-phase observations are Cycle Slip (CS), which manifest as a change in the integer ambiguity and can significantly degrade positioning accuracy if not detected and mitigated.

A review of CS detection and correction techniques is presented in [57], with a focus on residual-based methods. Several works [58, 59, 60] propose Time-Differenced Carrier Phase (TDCP)-based approaches similar to those considered in this chapter. However, these methods do not incorporate additional observations such as code pseudoranges, which are integrated here through the Factor Graph Optimization (FGO) framework.

This chapter presents a rigorous framework for detecting and identifying CS using FGO. In particular, the case of a single CS is studied extensively. By leveraging the residuals derived from factor graphs, a statistical test is constructed to detect faults modeled as integer biases. The detection process relies on the maximum likelihood estimation and Cochran's theorem, providing both theoretical guarantees and practical implementation. The Neyman-Pearson lemma is applied to set the decision threshold based on a desired false alarm probability.

Once detection is performed, a multiple hypothesis identification framework is proposed to isolate the satellite affected by the CS. This is achieved by constructing subgraphs that test each possible fault hypothesis individually. The method is validated using both real and synthetic datasets, with synthetic data offering a controlled environment and real data providing practical complexity. Empirical results confirm the method's ability to detect and identify single CS of smallest amplitude, equal to one cycle, with accuracy.

The developed framework is applied to a TDCP-based positioning scenario, using corrected GNSS observations from the TLSE and TLSG International GNSS Service (IGS) stations, allowing for residual-based analysis under realistic conditions.

This document may not be reproduced, modified, adapted, published, translated in any way, in whole or in part, nor disclosed to a third party without the prior written consent of ENAC. © 2025, ENAC

3.1 FGO-Based Fault Detection

This section presents a fault detection method based on the construction of a statistical test derived from a FGO framework, similarly to what is done in [61]. The FGO considered consists of Gaussian factors whose first order moments are functions of the parameters to be estimated. The method targets the detection of unmodeled constant biases that may be present in at most a single component of a single factor. The constructed statistic is used to determine the presence of a fault within a factor. As the objective is to detect CS, which correspond to a change of an integer ambiguity number, the types of faults addressed by this method are in a first step very general, and in a second step restricted to integer biases.

3.1.1 Statement of the Problem

Let $\boldsymbol{\theta} \in \Theta \subseteq \mathbb{R}^n$ be unknown and let $\boldsymbol{x}$ be a continuous real-valued random vector of dimension m. The objective is to estimate $\boldsymbol{\theta}$ from $\boldsymbol{x}$ by means of the Maximum Likelihood Estimator (MLE), i.e., by construction of the random vector

$$\widehat{\boldsymbol{\theta}}_{\text{MLE}} = \arg\max \mathcal{L}(\boldsymbol{x}), \tag{3.1}$$

where $\mathcal{L}(\boldsymbol{x}) : \Theta \subseteq \mathbb{R}^n \to \mathbb{R}^+$ is the likelihood function of $\boldsymbol{\theta}$ given $\boldsymbol{x}$, as defined in Appendix A.

Assume that $\boldsymbol{x}$ is a Gaussian random vector, with a first order moment being a function of $\boldsymbol{\theta}$, with an additional vector $\boldsymbol{\mu} \in \mathbb{R}^m$, i.e.,

$$\boldsymbol{x} \sim \mathcal{N}\left(h(\boldsymbol{\theta}) + \boldsymbol{\mu}, \boldsymbol{R}\right) \tag{3.2}$$

where $h : \mathbb{R}^n \to \mathbb{R}^m$. In Chapter 2 is developed an estimator of $\boldsymbol{\theta}$ by assuming that $\boldsymbol{\mu} = \boldsymbol{0}$. This section provides techniques to assess whether $\boldsymbol{\mu} = \boldsymbol{0}$ is true or false. First, these techniques are developed in the case where h is a linear function. In a second step, the nonlinear case is handled by a linearization procedure.

3.1.2 Linear Case, Random Vector, Likelihood and Residual

Most results presented in this section come from Section 2.2.2. In Equation (3.2), if h is a linear function, then the random vector $\boldsymbol{x}$ can be written

$$\boldsymbol{x} \sim \mathcal{N}\left(\boldsymbol{H}\boldsymbol{\theta} + \boldsymbol{\mu}, \boldsymbol{R}\right) \tag{3.3}$$

where $\boldsymbol{H} \in \mathcal{M}_{m,n}(\mathbb{R})$. Thanks to the whitening procedure presented in Section 2.2.2, without loss of generality, it is assumed that $\mathbb{V}[\boldsymbol{x}] = \boldsymbol{I}$, i.e.,

$$\boldsymbol{x} \sim \mathcal{N}\left(\boldsymbol{H}\boldsymbol{\theta} + \boldsymbol{\mu}, \boldsymbol{I}\right). \tag{3.4}$$

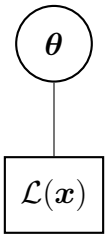

Figure 3.1: Representation of Equation (3.5) with a factor graph.

The likelihood function of $\boldsymbol{\theta}$ given $\boldsymbol{x}$, denoted $\mathcal{L}(\boldsymbol{x})$ is

$$\mathcal{L}(\boldsymbol{x}) : \boldsymbol{\theta} \mapsto \frac{1}{\sqrt{(2\pi)^m}} \exp\left(-\frac{1}{2} \|\boldsymbol{x} - \boldsymbol{H}\boldsymbol{\theta} - \boldsymbol{\mu}\|_{\boldsymbol{I}}^2\right). \tag{3.5}$$

Its factor graph representation is visible in Figure 3.1.

Similarly to Equation (2.13), the MLE is equivalently obtained by minimizing $-\log \mathcal{L}(\boldsymbol{x})$, leading to

$$\widehat{\boldsymbol{\theta}}_{\text{MLE}} = \arg\max \mathcal{L}(\boldsymbol{x}) = \arg\min \left(\boldsymbol{\theta} \mapsto \|\boldsymbol{x} - \boldsymbol{\mu} - \boldsymbol{H}\boldsymbol{\theta}\|_{\boldsymbol{I}}^2\right). \tag{3.6}$$

In that case, similarly to Equation (2.15), it can be shown that if and only if $\text{rank}\,(\boldsymbol{H}) = n$, which implies $m \geq n$, the MLE is

$$\widehat{\boldsymbol{\theta}}_{\text{MLE}} = \left(\boldsymbol{H}^\mathsf{T}\boldsymbol{H}\right)^{-1} \boldsymbol{H}^\mathsf{T} (\boldsymbol{x} - \boldsymbol{\mu}) \tag{3.7}$$

and the residual vector is the Gaussian random vector

$$\boldsymbol{z}_{\text{MLE}} = \boldsymbol{x} - \left(\boldsymbol{H}\widehat{\boldsymbol{\theta}}_{\text{MLE}} + \boldsymbol{\mu}\right). \tag{3.8}$$

As explained in Section 2.2.2, the matrix $\boldsymbol{P}_H = \boldsymbol{H}\left(\boldsymbol{H}^\mathsf{T}\boldsymbol{H}\right)^{-1}\boldsymbol{H}^\mathsf{T}$ defined in Equation (2.25) is the orthogonal projector onto $\text{Im}\,(\boldsymbol{H})$, a subspace of $\mathbb{R}^m$ of dimension n. Its complement, the matrix $\boldsymbol{I} - \boldsymbol{P}_H$, is the orthogonal projector onto $\text{Im}\,(\boldsymbol{H})^\perp$, which has dimension $m - n$.

Therefore, the residual random vector Equation (3.8) becomes

$$\begin{aligned}
\boldsymbol{z}_{\text{MLE}} &= \boldsymbol{x} - \left(\boldsymbol{H}\widehat{\boldsymbol{\theta}}_{\text{MLE}} + \boldsymbol{\mu}\right) \\
&= \boldsymbol{x} - \left(\boldsymbol{H}\left(\boldsymbol{H}^\mathsf{T}\boldsymbol{H}\right)^{-1}\boldsymbol{H}^\mathsf{T}(\boldsymbol{x} - \boldsymbol{\mu}) + \boldsymbol{\mu}\right) \\
&= \boldsymbol{x} - \left(\boldsymbol{P}_H(\boldsymbol{x} - \boldsymbol{\mu}) + \boldsymbol{\mu}\right) \\
&= (\boldsymbol{I} - \boldsymbol{P}_H)(\boldsymbol{x} - \boldsymbol{\mu}).
\end{aligned}$$

Since $\boldsymbol{I} - \boldsymbol{P}_H$ is symmetric and idempotent, i.e., $(\boldsymbol{I} - \boldsymbol{P}_H)^2 = \boldsymbol{I} - \boldsymbol{P}_H$, it comes

$$\mathbb{E}\left[\boldsymbol{z}_{\text{MLE}}\right] = (\boldsymbol{I} - \boldsymbol{P}_H)(\boldsymbol{H}\boldsymbol{\theta} + \boldsymbol{\mu} - \boldsymbol{\mu}) = \boldsymbol{0} \tag{3.9}$$

This document may not be reproduced, modified, adapted, published, translated in any way, in whole or in part, nor disclosed to a third party without the prior written consent of ENAC. © 2025, ENAC

and

$$\mathbb{V}\left[\boldsymbol{z}_{\text{MLE}}\right] = \left(\boldsymbol{I} - \boldsymbol{P}_H\right) \boldsymbol{I} \left(\boldsymbol{I} - \boldsymbol{P}_H\right)^{\mathsf{T}} = \left(\boldsymbol{I} - \boldsymbol{P}_H\right). \tag{3.10}$$

Therefore, the random vector $\boldsymbol{z}_{\text{MLE}}$ has the distribution of a white centered Gaussian random vector, multiplied by the orthogonal projector $\boldsymbol{I} - \boldsymbol{P}_H$.

3.1.3 Cochran's Theorem

By definition, the squared norm of a white centered Gaussian random vector $\boldsymbol{x}$ of dimension m follows a chi-squared distribution with m degrees of freedom, denoted $\|\boldsymbol{x}\|_{\boldsymbol{I}}^2 \sim \chi_m^2$. The density of such random variable is given by [62]

$$f_{\boldsymbol{0}} : x \mapsto \begin{cases} \dfrac{x^{\frac{m}{2}-1}\, e^{-\frac{x}{2}}}{2^{\frac{m}{2}}\, \Gamma\left(\frac{m}{2}\right)} & \text{if } x \geq 0, \\ 0 & \text{otherwise.} \end{cases} \tag{3.11}$$

Theorem 3.1.1 (Cochran). *Let $\boldsymbol{x} \sim \mathcal{N}\left(\boldsymbol{0}, \boldsymbol{I}\right)$ be of dimension m. Let E_1 and E_2 be two orthogonal subspaces of $\mathbb{R}^m$ of dimension m_1 and m_2 respectively, such that $E_1 \oplus E_2 = \mathbb{R}^m$. If $\boldsymbol{P}_1$ is the orthogonal projector onto E_1 and $\boldsymbol{P}_2$ is the orthogonal projector onto E_2, then*

- *$\boldsymbol{P}_1\boldsymbol{x} \sim \mathcal{N}\left(\boldsymbol{0}, \boldsymbol{P}_1\right)$ and $\boldsymbol{P}_2\boldsymbol{x} \sim \mathcal{N}\left(\boldsymbol{0}, \boldsymbol{P}_2\right)$ are independent,*
- *$\|\boldsymbol{P}_1\boldsymbol{x}\|_{\boldsymbol{I}}^2 \sim \chi_{m_1}^2$ and $\|\boldsymbol{P}_2\boldsymbol{x}\|_{\boldsymbol{I}}^2 \sim \chi_{m_2}^2$ are independent.*

Although not fundamental, the proof of Cochran's theorem is necessary to prove Corollary 3.1.1.

Proof. For the first item, if $\boldsymbol{y} = \begin{pmatrix} \boldsymbol{y}_1 \\ \boldsymbol{y}_2 \end{pmatrix} = \boldsymbol{A}\boldsymbol{x}$ with $\boldsymbol{A} = \begin{pmatrix} \boldsymbol{P}_1 \\ \boldsymbol{P}_2 \end{pmatrix}$, then $\boldsymbol{y} \sim \mathcal{N}\left(\boldsymbol{0}, \boldsymbol{A}\boldsymbol{A}^{\mathsf{T}}\right)$, with $\boldsymbol{A}\boldsymbol{A}^{\mathsf{T}} = \begin{pmatrix} \boldsymbol{P}_1 & \boldsymbol{0} \\ \boldsymbol{0} & \boldsymbol{P}_2 \end{pmatrix}$, so $\boldsymbol{y}_1 \sim \mathcal{N}\left(\boldsymbol{0}, \boldsymbol{P}_1\right)$ and $\boldsymbol{y}_2 \sim \mathcal{N}\left(\boldsymbol{0}, \boldsymbol{P}_2\right)$ are independent.
For the second item, if $\{\boldsymbol{u}_1, \ldots, \boldsymbol{u}_m\}$ is an orthonormal basis of $\mathbb{R}^m$ such that $\forall i \in \{1, \ldots, m_1\}$, $\boldsymbol{u}_i \in E_1$ and $\forall i \in \{m_1 + 1, \ldots, m\}$, $\boldsymbol{u}_i \in E_2$, then the matrix $\boldsymbol{U} = \begin{pmatrix} \boldsymbol{u}_1 & \ldots & \boldsymbol{u}_m \end{pmatrix} = \begin{pmatrix} \boldsymbol{U}_1 & \boldsymbol{U}_2 \end{pmatrix}$ is orthogonal. It comes $\|\boldsymbol{P}_1\boldsymbol{x}\|_{\boldsymbol{I}}^2 = \left\|\boldsymbol{U}^{\mathsf{T}}\boldsymbol{P}_1\boldsymbol{U}\boldsymbol{U}^{\mathsf{T}}\boldsymbol{x}\right\|_{\boldsymbol{I}}^2$ and $\|\boldsymbol{P}_2\boldsymbol{x}\|_{\boldsymbol{I}}^2 = \left\|\boldsymbol{U}^{\mathsf{T}}\boldsymbol{P}_2\boldsymbol{U}\boldsymbol{U}^{\mathsf{T}}\boldsymbol{x}\right\|_{\boldsymbol{I}}^2$. The matrices $\boldsymbol{U}^{\mathsf{T}}\boldsymbol{P}_1\boldsymbol{U}$ and $\boldsymbol{U}^{\mathsf{T}}\boldsymbol{P}_2\boldsymbol{U}$ are the expression of the projectors in the introduced basis. Therefore, $\boldsymbol{U}^{\mathsf{T}}\boldsymbol{P}_1\boldsymbol{U} = \begin{pmatrix} \boldsymbol{I}_{m_1} & \boldsymbol{0} \\ \boldsymbol{0} & \boldsymbol{0}_{m_2} \end{pmatrix}$ and $\boldsymbol{U}^{\mathsf{T}}\boldsymbol{P}_2\boldsymbol{U} = \begin{pmatrix} \boldsymbol{0}_{m_1} & \boldsymbol{0} \\ \boldsymbol{0} & \boldsymbol{I}_{m_2} \end{pmatrix}$. It comes $\|\boldsymbol{P}_1\boldsymbol{x}\|_{\boldsymbol{I}}^2 = \boldsymbol{x}^{\mathsf{T}}\boldsymbol{U}_1\boldsymbol{U}_1^{\mathsf{T}}\boldsymbol{x} = \sum_{i=1}^{m_1} \left(\boldsymbol{u}_i^{\mathsf{T}}\boldsymbol{x}\right)^2$ and $\|\boldsymbol{P}_2\boldsymbol{x}\|_{\boldsymbol{I}}^2 = \boldsymbol{x}^{\mathsf{T}}\boldsymbol{U}_2\boldsymbol{U}_2^{\mathsf{T}}\boldsymbol{x} = \sum_{i=m_1+1}^{m} \left(\boldsymbol{u}_i^{\mathsf{T}}\boldsymbol{x}\right)^2$. Since $\boldsymbol{U}\boldsymbol{x} \sim \mathcal{N}\left(\boldsymbol{0}, \boldsymbol{I}\right)$, then the Gaussian random variables $\left(\boldsymbol{u}_i^{\mathsf{T}}\boldsymbol{x}\right)_{i \in \{1,\ldots,m\}}$ are independent, centered and with unit variance. By definition of the chi-squared distribution, $\sum_{i=1}^{m_1} \left(\boldsymbol{u}_i^{\mathsf{T}}\boldsymbol{x}\right)^2 \sim \chi_{m_1}^2$ and $\sum_{i=m_1+1}^{m} \left(\boldsymbol{u}_i^{\mathsf{T}}\boldsymbol{x}\right)^2 \sim \chi_{m-m_1}^2$ are independent. □

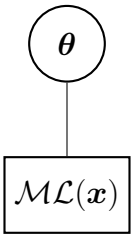

Figure 3.2: Representation of Equation (3.13) with a factor graph.

In Theorem 3.1.1, the dimensions are such that $m = m_1 + m_2$. Additionally, any vector $\boldsymbol{x} \in \mathbb{R}^m$ can be decomposed as $\boldsymbol{x} = \boldsymbol{P}_1\boldsymbol{x} + \boldsymbol{P}_2\boldsymbol{x}$ with $\boldsymbol{P}_1\boldsymbol{x} \perp \boldsymbol{P}_2\boldsymbol{x}$. It comes from the Pythagorean theorem that $\|\boldsymbol{x}\|_{\boldsymbol{I}}^2 = \|\boldsymbol{P}_1\boldsymbol{x}\|_{\boldsymbol{I}}^2 + \|\boldsymbol{P}_2\boldsymbol{x}\|_{\boldsymbol{I}}^2$. Therefore, Cochran's theorem can be viewed as a probabilistic analogue of the Pythagorean theorem: the squared norm of a Gaussian random vector decomposes into the sum of the squared norms of its orthogonal projections, and these components are not only orthogonal but also statistically independent and follow chi-squared distributions with degrees of freedom matching the dimension of the subspaces.

Since the random vector $\boldsymbol{z}_{\text{MLE}}$ has the distribution of a white centered Gaussian random vector, multiplied by the orthogonal projector $\boldsymbol{I} - \boldsymbol{P}_H$, applying Cochran's theorem gives

$$\|\boldsymbol{z}_{\text{MLE}}\|_{\boldsymbol{I}}^2 \sim \chi_{m-n}^2. \tag{3.12}$$

3.1.4 Misspecified Likelihood

In the estimation community, work on estimators built with misspecified models exist [63, 64, 65]. Such approaches rely on likelihood functions that do not correspond the true data-generating process. This motivates the formal definition of a *misspecified likelihood function*.

Definition 3.1.1 (Misspecified likelihood)**.** *Let $\boldsymbol{\theta} \in \Theta \subseteq \mathbb{R}^m$ and let $\boldsymbol{x}$ be a continuous real-valued random vector of dimension m. The likelihood function of $\boldsymbol{\theta}$ given $\boldsymbol{x}$, denoted $\mathcal{L}(\boldsymbol{x})$, satisfies $\mathcal{L}(\boldsymbol{x}) : \Theta \subseteq \mathbb{R}^n \to \mathbb{R}^+$. A* misspecified likelihood function*, denoted $\mathcal{ML}(\boldsymbol{x})$ is a function that maps Θ to $\mathbb{R}^+$ and that differs from the likelihood function $\mathcal{L}(\boldsymbol{x})$.*

Now, suppose that a new function is defined, similar to the likelihood (3.5), but that does not take into account $\boldsymbol{\mu}$. In that case, the misspecified likelihood function is

$$\mathcal{ML}(\boldsymbol{x}) : \boldsymbol{\theta} \mapsto \frac{1}{\sqrt{(2\pi)^m}} \exp\left(-\frac{1}{2}\|\boldsymbol{x} - \boldsymbol{H}\boldsymbol{\theta}\|_{\boldsymbol{I}}^2\right). \tag{3.13}$$

Its factor graph representation is visible in Figure 3.2.

A new estimator is defined. Based on the maximization of $\mathcal{ML}(\boldsymbol{x})$, the Misspecified Maximum Likelihood Estimator (MMLE) is defined

$$\widehat{\boldsymbol{\theta}}_{\text{MMLE}} \triangleq \arg\max \mathcal{ML}(\boldsymbol{x}). \tag{3.14}$$

This document may not be reproduced, modified, adapted, published, translated in any way, in whole or in part, nor disclosed to a third party without the prior written consent of ENAC. © 2025, ENAC

Similarly to Equations (2.13) and (2.15), it comes

$$\widehat{\boldsymbol{\theta}}_{\mathrm{MMLE}} = \arg\min\ -\log\left(\mathcal{ML}(\boldsymbol{x})\right) = \left(\boldsymbol{H}^{\mathsf{T}}\boldsymbol{H}\right)^{-1}\boldsymbol{H}^{\mathsf{T}}\boldsymbol{x}. \tag{3.15}$$

The misspecified residual vector is the Gaussian random vector

$$\begin{aligned}\boldsymbol{z}_{\mathrm{MMLE}} &= \boldsymbol{x} - \boldsymbol{H}\widehat{\boldsymbol{\theta}}_{\mathrm{MMLE}} \\ &= \boldsymbol{x} - \boldsymbol{H}\left(\boldsymbol{H}^{\mathsf{T}}\boldsymbol{H}\right)^{-1}\boldsymbol{H}^{\mathsf{T}}\boldsymbol{x} \\ &= \left(\boldsymbol{I} - \boldsymbol{P}_H\right)\boldsymbol{x}.\end{aligned}$$

Since $\boldsymbol{I} - \boldsymbol{P}_H$ is symmetric and idempotent, i.e., $\left(\boldsymbol{I} - \boldsymbol{P}_H\right)^2 = \boldsymbol{I} - \boldsymbol{P}_H$, it comes

$$\mathbb{E}\left[\boldsymbol{z}_{\mathrm{MMLE}}\right] = \left(\boldsymbol{I} - \boldsymbol{P}_H\right)\left(\boldsymbol{H}\boldsymbol{\theta} + \boldsymbol{\mu}\right) = \left(\boldsymbol{I} - \boldsymbol{P}_H\right)\boldsymbol{\mu}. \tag{3.16}$$

and

$$\mathbb{V}\left[\boldsymbol{z}_{\mathrm{MMLE}}\right] = \left(\boldsymbol{I} - \boldsymbol{P}_H\right)\boldsymbol{I}\left(\boldsymbol{I} - \boldsymbol{P}_H\right)^{\mathsf{T}} = \left(\boldsymbol{I} - \boldsymbol{P}_H\right). \tag{3.17}$$

Therefore, the random vector $\boldsymbol{z}_{\mathrm{MMLE}}$ has the distribution of a white Gaussian random vector with mean vector $\boldsymbol{\mu}$, multiplied by the orthogonal projector $\boldsymbol{I} - \boldsymbol{P}_H$.

3.1.5 Corollary of Cochran's Theorem

By definition, the squared norm of a white Gaussian random vector $\boldsymbol{x}$ of dimension m with mean vector $\boldsymbol{\mu}$ follows a noncentral chi-squared distribution with m degrees of freedom and noncentrality parameter $\lambda = \|\boldsymbol{\mu}\|_{\boldsymbol{I}}^2$, denoted $\|\boldsymbol{x}\|_{\boldsymbol{I}}^2 \sim \chi_{m,\lambda}^2$.
The density of such random variable is defined and denoted [62]

$$f_{\boldsymbol{\mu}} : x \mapsto \begin{cases} \dfrac{x^{\frac{m}{2}-1}e^{-\frac{x+\lambda}{2}}}{2^{\frac{m}{2}}} \displaystyle\sum_{k=0}^{+\infty} \frac{\left(\frac{\lambda x}{4}\right)^k}{k!\,\Gamma\left(\frac{m}{2}+k\right)} & \text{if } x \geq 0, \\ 0 & \text{otherwise.} \end{cases} \tag{3.18}$$

Corollary 3.1.1. *Let $\boldsymbol{x} \sim \mathcal{N}\left(\boldsymbol{\mu}, \boldsymbol{I}\right)$ be of dimension m. Let E_1 and E_2 be two orthogonal subspaces of $\mathbb{R}^m$ of dimension m_1 and m_2 respectively, such that $E_1 \oplus E_2 = \mathbb{R}^m$. If $\boldsymbol{P}_1$ is the orthogonal projector onto E_1 and $\boldsymbol{P}_2$ is the orthogonal projector onto E_2, then*

- *$\boldsymbol{P}_1\boldsymbol{x} \sim \mathcal{N}\left(\boldsymbol{P}_1\boldsymbol{\mu}, \boldsymbol{P}_1\right)$ and $\boldsymbol{P}_2\boldsymbol{x} \sim \mathcal{N}\left(\boldsymbol{P}_2\boldsymbol{\mu}, \boldsymbol{P}_2\right)$ are independent,*
- *$\|\boldsymbol{P}_1\boldsymbol{x}\|_{\boldsymbol{I}}^2 \sim \chi_{m_1,\lambda_1}^2$ with $\lambda_1 = \|\boldsymbol{P}_1\boldsymbol{\mu}\|_{\boldsymbol{I}}^2$ and $\|\boldsymbol{P}_2\boldsymbol{x}\|_{\boldsymbol{I}}^2 \sim \chi_{m_2,\lambda_2}^2$ with $\lambda_2 = \|\boldsymbol{P}_2\boldsymbol{\mu}\|^2$, are independent.*

Proof. The proof is very similar to the Cochran's theorem proof.

For the first item, if $\boldsymbol{y} = \begin{pmatrix} \boldsymbol{y}_1 \\ \boldsymbol{y}_2 \end{pmatrix} = \boldsymbol{A}\boldsymbol{x}$ with $\boldsymbol{A} = \begin{pmatrix} \boldsymbol{P}_1 \\ \boldsymbol{P}_2 \end{pmatrix}$, then $\boldsymbol{y} \sim \mathcal{N}\left(\boldsymbol{A}\boldsymbol{\mu}, \boldsymbol{A}\boldsymbol{A}^\mathsf{T}\right)$, with $\boldsymbol{A}\boldsymbol{A}^\mathsf{T} = \begin{pmatrix} \boldsymbol{P}_1 & \boldsymbol{0} \\ \boldsymbol{0} & \boldsymbol{P}_2 \end{pmatrix}$, so $\boldsymbol{y}_1 \sim \mathcal{N}\left(\boldsymbol{P}_1\boldsymbol{\mu}, \boldsymbol{P}_1\right)$ and $\boldsymbol{y}_2 \sim \mathcal{N}\left(\boldsymbol{P}_2\boldsymbol{\mu}, \boldsymbol{P}_2\right)$ are independent.
For the second item, the basis $\{\boldsymbol{u}_1, \ldots, \boldsymbol{u}_m\}$ and the matrix $\boldsymbol{U}$ defined in Cochran's theorem proof are used. Similarly, $\|\boldsymbol{P}_1\boldsymbol{x}\|_{\boldsymbol{I}}^2 = \sum_{i=1}^{m_1} \left(\boldsymbol{u}_i^\mathsf{T}\boldsymbol{x}\right)^2$ and $\|\boldsymbol{P}_2\boldsymbol{x}\|_{\boldsymbol{I}}^2 = \sum_{i=m_1+1}^{m} \left(\boldsymbol{u}_i^\mathsf{T}\boldsymbol{x}\right)^2$. Now, $\boldsymbol{U}\boldsymbol{x} \sim \mathcal{N}\left(\boldsymbol{U}\boldsymbol{\mu}, \boldsymbol{I}\right)$ so the Gaussian random variables $\left(\boldsymbol{u}_i^\mathsf{T}\boldsymbol{x}\right)_{i\in\{1,\ldots,m\}}$ are all independent, with mean $\boldsymbol{u}_i^\mathsf{T}\boldsymbol{\mu}$ and unit variance. By definition of the noncentral chi-squared distribution, $\sum_{i=1}^{m_1} \left(\boldsymbol{u}_i^\mathsf{T}\boldsymbol{x}\right)^2 \sim \chi^2_{m_1,\lambda_1}$ with $\lambda_1 = \sum_{i=1}^{m_1} \left(\boldsymbol{u}_i^\mathsf{T}\boldsymbol{\mu}\right)^2 = \boldsymbol{\mu}^\mathsf{T}\boldsymbol{U}_1\boldsymbol{U}_1^\mathsf{T}\boldsymbol{\mu} = \boldsymbol{\mu}^\mathsf{T}\boldsymbol{P}_1\boldsymbol{\mu} = \|\boldsymbol{P}_1\boldsymbol{\mu}\|_{\boldsymbol{I}}^2$ and $\sum_{i=m_1+1}^{m} \left(\boldsymbol{u}_i^\mathsf{T}\boldsymbol{x}\right)^2 \sim \chi^2_{m-m_1,\lambda_2}$ with $\lambda_2 = \sum_{i=m_1+1}^{m} \left(\boldsymbol{u}_i^\mathsf{T}\boldsymbol{\mu}\right)^2 = \boldsymbol{\mu}^\mathsf{T}\boldsymbol{U}_2\boldsymbol{U}_2^\mathsf{T}\boldsymbol{\mu} = \boldsymbol{\mu}^\mathsf{T}\boldsymbol{P}_2\boldsymbol{\mu} = \|\boldsymbol{P}_2\boldsymbol{\mu}\|_{\boldsymbol{I}}^2$ are independent. □

Since the random vector $\boldsymbol{z}_{\text{MMLE}}$ has the distribution of a white Gaussian random vector with mean vector $\boldsymbol{\mu}$, multiplied by the orthogonal projector $\boldsymbol{I} - \boldsymbol{P}_H$, applying Corollary 3.1.1 gives

$$\|\boldsymbol{z}_{\text{MMLE}}\|_{\boldsymbol{I}}^2 \sim \chi^2_{m-n,\lambda} \tag{3.19}$$

where $\lambda = \|\left(\boldsymbol{I} - \boldsymbol{P}_H\right)\boldsymbol{\mu}\|_{\boldsymbol{I}}^2$.
Now that the squared norm of the residual vector is characterized, it can be used to run a binary hypothesis test, in order to decide whether a fault is present in the observations or not.

3.1.6 Binary Hypothesis Testing

The hypothesis testing aims to determine whether a fault, such as a CS, is present based on a sample of a random variable. This is formulated as a binary hypothesis testing problem, where the decision relies on a scalar test statistic $z \in \mathbb{R}$.
The test distinguishes between two statistical models

- Null hypothesis: $\mathcal{H}_0$, which assumes no fault.
- Alternative hypothesis: $\mathcal{H}_1$, which assumes the presence of a fault.

The following outcomes define the quality of the decision,

- Correct detection (True Positive): The test correctly accepts $\mathcal{H}_1$ under $\mathcal{H}_1$,
- Correct rejection (True Negative): The test correctly accepts $\mathcal{H}_0$ under $\mathcal{H}_0$,
- False alarm (Type I Error): The test incorrectly signals a fault when $\mathcal{H}_0$ holds,
- Missed detection (Type II Error): The test fails to detect a fault when $\mathcal{H}_1$ holds.

This document may not be reproduced, modified, adapted, published, translated in any way, in whole or in part, nor disclosed to a third party without the prior written consent of ENAC. © 2025, ENAC

Table 3.1: Confusion matrix for a binary decision process.

Truth \ Decision	$\mathcal{H}_0$	$\mathcal{H}_1$
$\mathcal{H}_0$ (No Fault)	True Negative (TN)	False Positive (FP)
$\mathcal{H}_1$ (Fault Present)	False Negative (FN)	True Positive (TP)

These outcomes are organized in a confusion matrix, visible in Table 3.1.

In this work, the test relies on the Neyman-Pearson lemma, which provides the most powerful statistical test for distinguishing between two hypotheses under a fixed false alarm probability.

3.1.7 Neyman-Pearson Lemma

The Neyman-Pearson lemma [66] is a fundamental result in statistical hypothesis testing. It provides a systematic method for deciding between a null hypothesis $\mathcal{H}_0$ and an alternative hypothesis $\mathcal{H}_1$, in a way that maximizes the probability of detection, i.e., correctly rejecting $\mathcal{H}_0$, while maintaining a fixed probability of false alarm, i.e., incorrectly rejecting $\mathcal{H}_0$. This result forms the theoretical foundation for many classical hypothesis testing procedures.

Lemma 3.1.1. *Neyman-Pearson*

Let x be a real continuous random variable with density $f_{\boldsymbol{\mu}}$, where $\boldsymbol{\mu}$ is a vector of parameters that the density depends on. Given two vectors $\boldsymbol{\mu}_0$ and $\boldsymbol{\mu}_1$, the objective is to test the null hypothesis $\mathcal{H}_0 : \boldsymbol{\mu} = \boldsymbol{\mu}_0$, against the alternative hypothesis $\mathcal{H}_1 : \boldsymbol{\mu} = \boldsymbol{\mu}_1$.

Given a false alarm probability $\alpha \in [0, 1]$ and a sample $x(\omega)$ of x, $\mathcal{H}_1$ is decided if

$$L(x(\omega)) \triangleq \frac{f_{\boldsymbol{\mu}_1}(x(\omega))}{f_{\boldsymbol{\mu}_0}(x(\omega))} > \gamma \tag{3.20}$$

where γ is such that

$$\int_{\mathcal{D}} f_{\boldsymbol{\mu}_0}(t)\mathrm{d}t = \alpha \tag{3.21}$$

with $\mathcal{D} = \left\{ t \in \mathbb{R} \;\middle|\; \frac{f_{\boldsymbol{\mu}_1}(t)}{f_{\boldsymbol{\mu}_0}(t)} > \gamma \right\}$. Otherwise, $\mathcal{H}_0$ is decided.

The probability of detection is by definition

$$P_D = \int_{\mathcal{D}} f_{\boldsymbol{\mu}_1}(t)\mathrm{d}t. \tag{3.22}$$

Although Equation (3.20) is formally the ratio of two evaluations of densities, it is sometimes referred as likelihood ratio, as the evaluation of a density indicates how likely is the distribution associated to this density.

3.1.8 Application of the Neyman-Pearson Lemma

Let $z(\omega) \in \mathbb{R}^+$ be a sample of the random variable $\|\boldsymbol{z}_{\text{MMLE}}\|_{\boldsymbol{I}}^2$. From this sample, the objective is to assess if either

- $\mathcal{H}_0 : \boldsymbol{\mu} = \mathbf{0}$,
- $\mathcal{H}_1 : \boldsymbol{\mu} \neq \mathbf{0}$.

The Neyman-Pearson lemma applies to the comparison of two simple hypotheses. In the present context, the null hypothesis $\mathcal{H}_0$ is simple, while the alternative hypothesis $\mathcal{H}_1$ is composite. Instead, the Neyman-Pearson lemma can be used to provide a lower bound of probability of detection. To do so, the detection probability as a function of $\boldsymbol{\mu}$ is defined. Suppose that it exists a set $\mathcal{A} \subseteq \mathbb{R}^m \setminus \{\mathbf{0}\}$ such that

$$P_D : \mathcal{A} \to [0,1], \boldsymbol{\mu} \mapsto \int_{\mathcal{D}} f_{\boldsymbol{\mu}}(t)\mathrm{d}t. \tag{3.23}$$

where $f_{\boldsymbol{\mu}}$ is the noncentral chi-squared density as defined in Equation (3.18) with

$$\mathcal{D} = \left\{ t \in \mathbb{R} \;\middle|\; \frac{f_{\boldsymbol{\mu}}(t)}{f_{\mathbf{0}}(t)} > \gamma \right\} \tag{3.24}$$

and $f_{\mathbf{0}}$ is the chi-squared density as defined in Equation (3.11). Additionally, suppose that it exists a minimizer of P_D, i.e., suppose that it exists a vector $\boldsymbol{\mu}_{\text{wc}} \in \mathcal{A}$ such that $\forall \boldsymbol{\mu} \in \mathcal{A}$, $P_D(\boldsymbol{\mu}) \geq P_D(\boldsymbol{\mu}_{\text{wc}})$.
As a consequence, by restricting the alternative hypothesis to the value $\boldsymbol{\mu}_{\text{wc}}$, the Neyman-Pearson lemma provides a lower bound of probability of detection, referred to as a worst case.
The hypothesis test then becomes

$$\mathcal{H}_0 : \boldsymbol{\mu} = \mathbf{0} \quad \text{versus} \quad \mathcal{H}_1 : \boldsymbol{\mu} = \boldsymbol{\mu}_{\text{wc}}. \tag{3.25}$$

Applying the Neyman-Pearson lemma to these two hypotheses leads to the ratio of the evaluations of the densities, given in Equations (3.11) and (3.18), for $m - n$ degrees of freedom. Since $z(\omega) \in \mathbb{R}^+$, this ratio is well defined and given by

$$L(z(\omega)) = \frac{f_{\boldsymbol{\mu}_{\text{wc}}}(z(\omega))}{f_{\mathbf{0}}(z(\omega))} = e^{-\frac{\lambda_{\text{wc}}}{2}} \Gamma\left(\frac{m-n}{2}\right) \sum_{k=0}^{+\infty} \frac{\lambda_{\text{wc}}^k}{4^k\, k!\, \Gamma\left(\frac{m-n}{2} + k\right)} (z(\omega))^k \tag{3.26}$$

where $\lambda_{\text{wc}} = \|(\boldsymbol{I} - \boldsymbol{P}_H)\,\boldsymbol{\mu}_{\text{wc}}\|_{\boldsymbol{I}}^2$.

Proposition 3.1.1. *On $\mathbb{R}^+$, the function*

$$L : x \mapsto e^{-\frac{\lambda_{\text{wc}}}{2}} \Gamma\left(\frac{m-n}{2}\right) \sum_{k=0}^{+\infty} \frac{\lambda_{\text{wc}}^k}{4^k\, k!\, \Gamma\left(\frac{m-n}{2} + k\right)} x^k \tag{3.27}$$

This document may not be reproduced, modified, adapted, published, translated in any way, in whole or in part, nor disclosed to a third party without the prior written consent of ENAC. © 2025, ENAC

is strictly increasing if and only if $\lambda_{\text{wc}} > 0$.

Proof. The function L is the product of a constant factor with a power series,

$$L : x \mapsto e^{-\frac{\lambda_{\text{wc}}}{2}} \Gamma\left(\frac{m-n}{2}\right) \sum_{k=0}^{+\infty} u_k x^k, \tag{3.28}$$

where

$$u_k \triangleq \frac{\lambda_{\text{wc}}^k}{4^k \; k! \; \Gamma\left(\frac{m-n}{2} + k\right)}. \tag{3.29}$$

To analyze convergence, applying the d'Alembert ratio test gives

$$\lim_{k \to +\infty} \left| \frac{u_{k+1}}{u_k} \right| = \lim_{k \to +\infty} \frac{\lambda_{\text{wc}}}{4(k+1)\left(\frac{m-n}{2} + k\right)} = 0. \tag{3.30}$$

The result indicates that the power series $\sum_{k=0}^{+\infty} u_k x^k$ converges on $\mathbb{R}$. Term by term differentiation yields the derivative on $\mathbb{R}$

$$L' : x \mapsto e^{-\frac{\lambda_{\text{wc}}}{2}} \Gamma\left(\frac{m-n}{2}\right) \sum_{k=1}^{+\infty} \frac{\lambda_{\text{wc}}^k}{4^k \; (k-1)! \; \Gamma\left(\frac{m-n}{2} + k\right)} x^{k-1}. \tag{3.31}$$

Given that $m \geq n$ and $\lambda_{\text{wc}} > 0$, each term in the series is strictly positive for $x \geq 0$, implying that $L'(x) > 0$ for all $x \geq 0$, as it is a series of positive terms. Therefore, the function L is strictly increasing on $\mathbb{R}^+$. Finally, if $\lambda_{\text{wc}} = 0$, the function equals to one. □

According to Proposition 3.1.1, similarly to the binary hypothesis test proposed in [61, 58, 59], for the considered densities, the test defined in Equation (3.20) reduces to the simpler form

$$z(\omega) > \gamma \tag{3.32}$$

where γ is the decision threshold satisfying Equation (3.21). Since the Neyman-Pearson test reduces to Equation (3.32), the threshold γ in Equation (3.21) is such that

$$\int_{\{t \in \mathbb{R} \mid t > \gamma\}} f_{\mathbf{0}}(t) \mathrm{d}t = \int_{\gamma}^{+\infty} f_{\mathbf{0}}(t) \mathrm{d}t = \alpha \tag{3.33}$$

where $f_{\mathbf{0}}$ is the density defined in Equation (3.11), and the worst probability of detection $P_D\left(\boldsymbol{\mu}_{\text{wc}}\right)$ is

$$P_D\left(\boldsymbol{\mu}_{\text{wc}}\right) = \int_{\gamma}^{+\infty} f_{\boldsymbol{\mu}_{\text{wc}}}(t) \mathrm{d}t \tag{3.34}$$

where $f_{\boldsymbol{\mu}_{\text{wc}}}$ is the density defined in Equation (3.18).

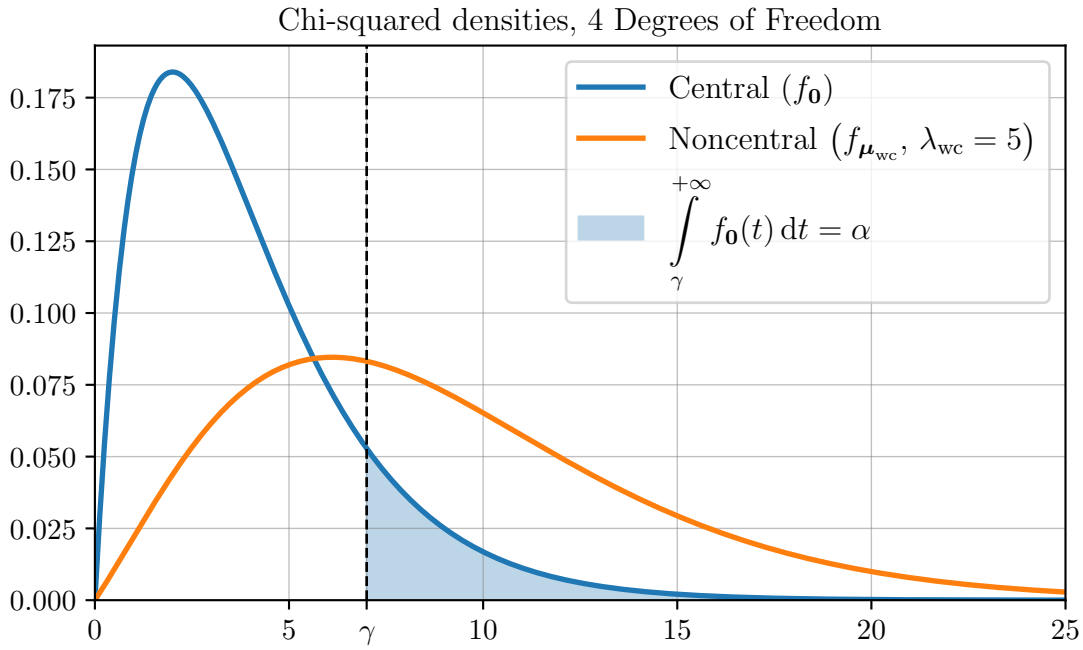

Figure 3.3: Illustration of the Neyman-Pearson lemma for a chi-squared density with $m - n = 4$ degrees of freedom and a noncentral chi-squared density with $m - n = 4$ degrees of freedom and noncentrality parameter $\lambda_{\text{wc}} = 5$.

The Neyman-Pearson lemma applied to a chi-squared and a noncentral chi-squared densities is visible in Figure 3.3.

3.1.9 Noncentrality Parameter Set of Values for Discrete Single Fault

The Neyman-Pearson-based hypothesis test presented relies on knowledge of the distribution of $\|\boldsymbol{z}_{\text{MMLE}}\|_{\boldsymbol{I}}^2 \sim \chi^2_{m-n,\lambda}$. In practice, λ is unknown since $\boldsymbol{\mu}$ is unknown.
The noncentrality parameter is now viewed as a function

$$\lambda : \mathcal{A} \subseteq \mathbb{R}^m \setminus \{\mathbf{0}\} \to \mathbb{R}^+,\ \boldsymbol{\mu} \mapsto \|(\boldsymbol{I} - \boldsymbol{P}_H)\,\boldsymbol{\mu}\|_{\boldsymbol{I}}^2 \tag{3.35}$$

and the probability of detection Equation (3.23) becomes

$$P_D : \mathcal{A} \to [0,1]\,,\ \boldsymbol{\mu} \mapsto \int_{\gamma}^{+\infty} f_{\boldsymbol{\mu}}(t)\mathrm{d}t \tag{3.36}$$

where $f_{\boldsymbol{\mu}}$ is the density of the noncentral chi-squared distribution Equation (3.18). The threshold γ is determined solely by the density $f_{\mathbf{0}}$ and the false alarm probability α. Therefore, it does not depend on $\boldsymbol{\mu}$.
It can be shown that P_D increases with the noncentrality parameter. Formally,

$$\forall\,(\boldsymbol{\mu}_1, \boldsymbol{\mu}_2) \in \mathcal{A}^2,\ \lambda\,(\boldsymbol{\mu}_1) \geq \lambda\,(\boldsymbol{\mu}_2) \Rightarrow P_D\,(\boldsymbol{\mu}_1) \geq P_D\,(\boldsymbol{\mu}_2)\,. \tag{3.37}$$

This document may not be reproduced, modified, adapted, published, translated in any way, in whole or in part, nor disclosed to a third party without the prior written consent of ENAC. © 2025, ENAC

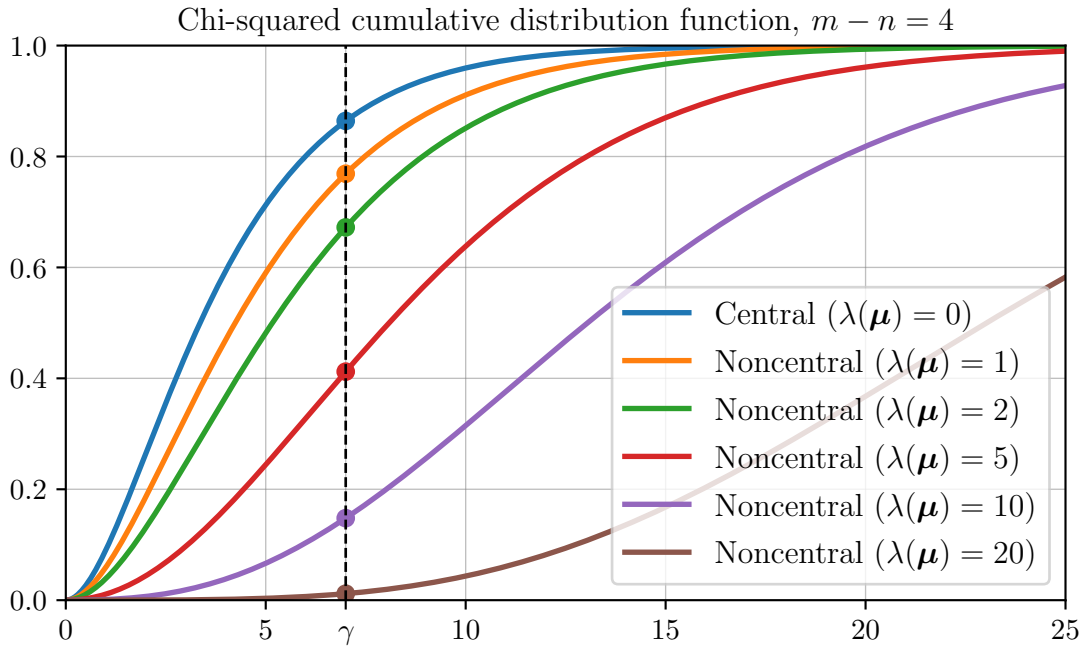

Figure 3.4: Illustration of cumulative distribution functions for noncentral chi-squared distributions, with $m - n = 4$ degrees of freedom and multiple noncentrality parameters.

This is equivalent to showing that the cumulative distribution function of a noncentral chi-squared distribution evaluated at γ decreases when the noncentrality parameter increases. Although not being a formal proof, this conjecture is visible in Figures 3.4, 3.5 and 3.6.

To provide a lower bound of detection probability, as stated in the previous section, it is assumed that $\exists \boldsymbol{\mu}_{\text{wc}} \in \mathcal{A}$ such that $\forall \boldsymbol{\mu} \in \mathcal{A},\ P_D(\boldsymbol{\mu}) \geq P_D(\boldsymbol{\mu}_{\text{wc}})$.

Suppose that $\exists \boldsymbol{\mu}_{\text{wc}} \in \mathcal{A}$ such that $\forall \boldsymbol{\mu} \in \mathcal{A},\ \lambda(\boldsymbol{\mu}) \geq \lambda(\boldsymbol{\mu}_{\text{wc}})$. In that case, Equation (3.37) implies that $\forall \boldsymbol{\mu} \in \mathcal{A},\ P_D(\boldsymbol{\mu}) \geq P_D(\boldsymbol{\mu}_{\text{wc}})$. Therefore, to provide a lower bound of probability detection, a minimizer of λ in Equation (3.35) has to be found.

Suppose the following structure for the bias vector $\boldsymbol{\mu} \in \mathcal{A}$: all components of $\boldsymbol{\mu}$ are zero, except for exactly one, belonging to $\mathbb{Z}^*$. Formally, assume that

$$\mathcal{A} = \bigsqcup_{i=1}^{m} \{\mu \boldsymbol{e}_i \mid \mu \in \mathbb{Z}^*\}, \tag{3.38}$$

where $\boldsymbol{e}_i$ is the i-th vector of the canonical basis of $\mathbb{R}^m$.

Under this model, it can be shown that the smallest value that λ can take is given by

$$\lambda_{\text{wc}} = \lambda(\boldsymbol{\mu}_{\text{wc}}) = \min \lambda = \min \operatorname{diag}(\boldsymbol{I} - \boldsymbol{P}_H), \tag{3.39}$$

and $\boldsymbol{\mu}_{\text{wc}} = \pm 1 \boldsymbol{e}_i$, where i corresponds to the index of the minimum on the diagonal of $\boldsymbol{I} - \boldsymbol{P}_H$.

This value characterizes the worst-case detection scenario. For any other $\boldsymbol{\mu} \in \mathcal{A}$, the

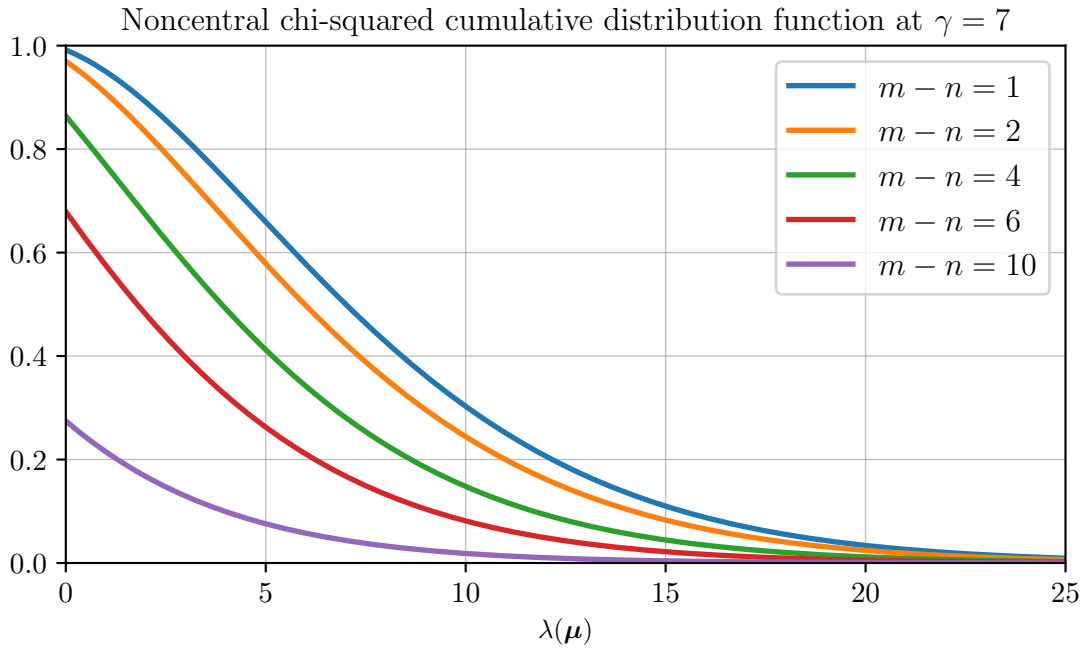

Figure 3.5: Illustration of the evaluation of the cumulative distribution function for non-central chi-squared distributions, for multiple degrees of freedom, as a function of the noncentrality parameter.

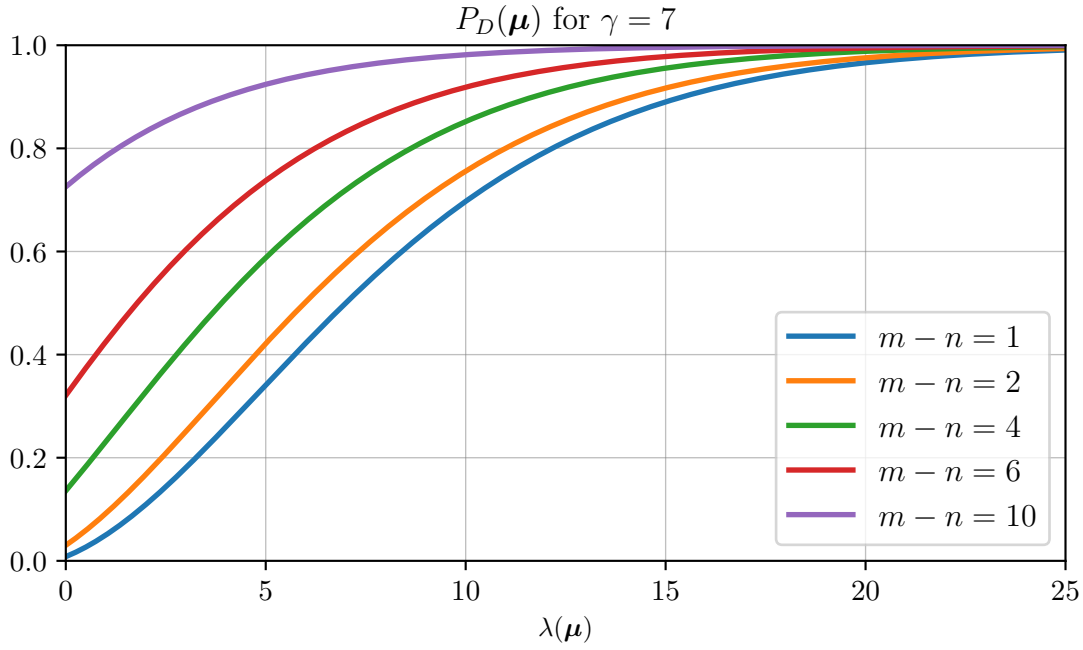

Figure 3.6: Illustration of the probability of detection, for multiple degrees of freedom, as a function of the noncentrality parameter.

This document may not be reproduced, modified, adapted, published, translated in any way, in whole or in part, nor disclosed to a third party without the prior written consent of ENAC. © 2025, ENAC

corresponding noncentrality parameter satisfies $\lambda(\boldsymbol{\mu}) \geq \lambda(\boldsymbol{\mu}_{\text{wc}})$, and consequently, the detection probability satisfies $P_D(\boldsymbol{\mu}) \geq P_D(\boldsymbol{\mu}_{\text{wc}})$.

Therefore, although the test is derived for a specific value $\boldsymbol{\mu}_{\text{wc}}$ within the alternative hypothesis $\mathcal{H}_1$, the resulting decision rule remains valid across the entire set $\mathcal{A}$. Moreover, the test exhibits improved detection performance for all $\boldsymbol{\mu} \in \mathcal{A}$.

In contrast, the probability of detection for vectors $\boldsymbol{\mu} \notin \mathcal{A}$ can be lower than $P_D(\boldsymbol{\mu}_{\text{wc}})$. For instance, if $\mathcal{A}$ is defined as the set of vectors with a single non-zero component, but the actual fault involves multiple non-zero components, there may exist vectors with lower probabilities of detection than the worst-case vector in $\mathcal{A}$.

3.1.10 Extension to Nonlinear Models

In the previous sections is presented a procedure for fault detection. This procedure assumes that the observation random vector $\boldsymbol{x}$ is Gaussian, with a first order moment that is an affine function of $\boldsymbol{\theta}$, as in Equation (3.4).

More generally, suppose that $\boldsymbol{x}$ is a Gaussian random variable whose mean is expressed as a differentiable function h, i.e.,

$$\boldsymbol{x} \sim \mathcal{N}(h(\boldsymbol{\theta}) + \boldsymbol{\mu}, \boldsymbol{I}). \tag{3.40}$$

In that case, similarly to the case where h is a linear function, the likelihood and a misspecified likelihood function are defined, where the misspecified likelihood does not take into account $\boldsymbol{\mu}$, i.e.,

$$\mathcal{L}(\boldsymbol{x}) : \boldsymbol{\theta} \mapsto \frac{1}{\sqrt{(2\pi)^m}} \exp\left(-\frac{1}{2}\|\boldsymbol{x} - h(\boldsymbol{\theta}) - \boldsymbol{\mu}\|_{\boldsymbol{I}}^2\right). \tag{3.41}$$

and

$$\mathcal{ML}(\boldsymbol{x}) : \boldsymbol{\theta} \mapsto \frac{1}{\sqrt{(2\pi)^m}} \exp\left(-\frac{1}{2}\|\boldsymbol{x} - h(\boldsymbol{\theta})\|_{\boldsymbol{I}}^2\right). \tag{3.42}$$

In that case, the MLE and the MMLE are given by

$$\widehat{\boldsymbol{\theta}}_{\text{MLE}} = \arg\min\left(\boldsymbol{\theta} \mapsto \|\boldsymbol{x} - h(\boldsymbol{\theta}) - \boldsymbol{\mu}\|_{\boldsymbol{I}}^2\right) \tag{3.43}$$

and

$$\widehat{\boldsymbol{\theta}}_{\text{MMLE}} = \arg\min\left(\boldsymbol{\theta} \mapsto \|\boldsymbol{x} - h(\boldsymbol{\theta})\|_{\boldsymbol{I}}^2\right). \tag{3.44}$$

These random vectors are Gaussian if and only if h is a linear or affine function. But in general, computing their distribution or statistical properties is not straightforward. Instead, an approximation of these random vectors is defined.

Assuming that h is a differentiable function on an open set $S \subseteq \mathbb{R}^n$ such that $\Theta \subseteq S$, then

$\forall \boldsymbol{x}_0 \in S$, it satisfies

$$\forall \boldsymbol{x} \in \mathbb{R}^n,\ h(\boldsymbol{x}) = h(\boldsymbol{x}_0) + \boldsymbol{H}_{\boldsymbol{x}_0}(\boldsymbol{x} - \boldsymbol{x}_0) + o\left(\|\boldsymbol{x} - \boldsymbol{x}_0\|\right) \tag{3.45}$$

where $\boldsymbol{H}_{\boldsymbol{x}_0} \in \mathcal{M}_{m,n}(\mathbb{R})$ represents the Jacobian matrix of h computed at $\boldsymbol{x}_0$.
Neglecting the higher order terms in Equation (3.45), the function h is approximated

$$h(\boldsymbol{x}) \approx h(\boldsymbol{x}_0) + \boldsymbol{H}_{\boldsymbol{x}_0}(\boldsymbol{x} - \boldsymbol{x}_0). \tag{3.46}$$

Now that an affine approximation of h is available, it can be treated similarly to the linear case: given a sample $\boldsymbol{x}(\omega)$ of the random vector $\boldsymbol{x}$, under certain conditions on the function h, the Gauss-Newton algorithm is guaranteed to converge to a local minima $\boldsymbol{\theta}_0 \in \Theta$ [51]. The proposed approach assumes that the function h is not too nonlinear and that $\boldsymbol{\theta}_0 \approx \boldsymbol{\theta}$. Then, by means of the approximation of h around $\boldsymbol{\theta}_0$, injecting Equation (3.46) into Equation (3.40) leads to

$$\boldsymbol{x} \sim \mathcal{N}\left(h\left(\boldsymbol{\theta}_0\right) + \boldsymbol{H}_{\boldsymbol{\theta}_0}\left(\boldsymbol{\theta} - \boldsymbol{\theta}_0\right) + \boldsymbol{\mu}, \boldsymbol{I}\right) \tag{3.47}$$

so the MLE Equation (3.43) and MMLE Equation (3.44) become

$$\widehat{\boldsymbol{\theta}}_{\text{MLE}} \approx \arg\min\ \left(\boldsymbol{\theta} \mapsto \|(\boldsymbol{x} - h(\boldsymbol{\theta}_0) + \boldsymbol{H}_{\boldsymbol{\theta}_0}\boldsymbol{\theta}_0 - \boldsymbol{\mu}) - \boldsymbol{H}_{\boldsymbol{\theta}_0}\boldsymbol{\theta}\|_{\boldsymbol{I}}^2\right). \tag{3.48}$$

and

$$\widehat{\boldsymbol{\theta}}_{\text{MMLE}} \approx \arg\min\ \left(\boldsymbol{\theta} \mapsto \|(\boldsymbol{x} - h(\boldsymbol{\theta}_0) + \boldsymbol{H}_{\boldsymbol{\theta}_0}\boldsymbol{\theta}_0) - \boldsymbol{H}_{\boldsymbol{\theta}_0}\boldsymbol{\theta}\|_{\boldsymbol{I}}^2\right). \tag{3.49}$$

and have a unique solution if and only if $\operatorname{rank}\left(\boldsymbol{H}_{\boldsymbol{\theta}_0}\right) = n$, given by

$$\widehat{\boldsymbol{\theta}}_{\text{MLE}} \approx \left(\boldsymbol{H}_{\boldsymbol{\theta}_0}^{\mathsf{T}}\boldsymbol{H}_{\boldsymbol{\theta}_0}\right)^{-1}\boldsymbol{H}_{\boldsymbol{\theta}_0}^{\mathsf{T}}\left(\boldsymbol{x} - h(\boldsymbol{\theta}_0) + \boldsymbol{H}_{\boldsymbol{\theta}_0}\boldsymbol{\theta}_0 - \boldsymbol{\mu}\right). \tag{3.50}$$

and

$$\widehat{\boldsymbol{\theta}}_{\text{MMLE}} \approx \left(\boldsymbol{H}_{\boldsymbol{\theta}_0}^{\mathsf{T}}\boldsymbol{H}_{\boldsymbol{\theta}_0}\right)^{-1}\boldsymbol{H}_{\boldsymbol{\theta}_0}^{\mathsf{T}}\left(\boldsymbol{x} - h(\boldsymbol{\theta}_0) + \boldsymbol{H}_{\boldsymbol{\theta}_0}\boldsymbol{\theta}_0\right). \tag{3.51}$$

In this case, both $\widehat{\boldsymbol{\theta}}_{\text{MLE}}$ and $\widehat{\boldsymbol{\theta}}_{\text{MMLE}}$ are approximated by Gaussian random vectors. The residual vectors are given by

$$\begin{aligned}
\boldsymbol{z}_{\text{MLE}} &= \boldsymbol{x} - \left(h\left(\boldsymbol{\theta}_0\right) + \boldsymbol{H}_{\boldsymbol{\theta}_0}\left(\widehat{\boldsymbol{\theta}}_{\text{MLE}} - \boldsymbol{\theta}_0\right) + \boldsymbol{\mu}\right) \\
&= \left(\boldsymbol{I} - \boldsymbol{H}_{\boldsymbol{\theta}_0}\left(\boldsymbol{H}_{\boldsymbol{\theta}_0}^{\mathsf{T}}\boldsymbol{H}_{\boldsymbol{\theta}_0}\right)^{-1}\boldsymbol{H}_{\boldsymbol{\theta}_0}^{\mathsf{T}}\right)\left(\boldsymbol{x} - h\left(\boldsymbol{\theta}_0\right) + \boldsymbol{\mu}\right) \\
&= \left(\boldsymbol{I} - \boldsymbol{P}_{\boldsymbol{H}_{\boldsymbol{\theta}_0}}\right)\left(\boldsymbol{x} - h\left(\boldsymbol{\theta}_0\right) + \boldsymbol{\mu}\right)
\end{aligned} \tag{3.52}$$

This document may not be reproduced, modified, adapted, published, translated in any way, in whole or in part, nor disclosed to a third party without the prior written consent of ENAC. © 2025, ENAC

and

$$\begin{aligned} \boldsymbol{z}_{\mathrm{MMLE}} &= \boldsymbol{x} - \left(h\left(\boldsymbol{\theta}_0\right) + \boldsymbol{H}_{\boldsymbol{\theta}_0}\left(\widehat{\boldsymbol{\theta}}_{\mathrm{MMLE}} - \boldsymbol{\theta}_0\right)\right) \\ &= \left(\boldsymbol{I} - \boldsymbol{H}_{\boldsymbol{\theta}_0}\left(\boldsymbol{H}_{\boldsymbol{\theta}_0}^{\mathsf{T}}\boldsymbol{H}_{\boldsymbol{\theta}_0}\right)^{-1}\boldsymbol{H}_{\boldsymbol{\theta}_0}^{\mathsf{T}}\right)\left(\boldsymbol{x} - h\left(\boldsymbol{\theta}_0\right)\right) \\ &= \left(\boldsymbol{I} - \boldsymbol{P}_{\boldsymbol{H}_{\boldsymbol{\theta}_0}}\right)\left(\boldsymbol{x} - h\left(\boldsymbol{\theta}_0\right)\right). \end{aligned} \tag{3.53}$$

The linearization of h around $\boldsymbol{\theta}_0$ enables the adoption of fault detection techniques developed under the assumption of a linear measurement model: both residuals vectors $\boldsymbol{z}_{\mathrm{MLE}}$ and $\boldsymbol{z}_{\mathrm{MMLE}}$ are orthogonal projections of white Gaussian random vectors, their squared norm follow central and noncentral chi-squared distributions. Therefore, through this linearization strategy, the framework for residual-based fault detection developed under linearity assumptions remains applicable even in the presence of nonlinearities in the model, thereby extending the utility of these techniques to a broader class of estimation problems.

If a fault is detected by the constructed detector, it can be identified, as discussed in the following section.

3.2 FGO-Based Fault Identification

In Section 3.1 is provided a procedure to detect faults based on FGO. If a fault is detected, i.e., if $\mathcal{H}_1$ is decided, then the fault can be identified. This problem, commonly referred to as fault identification, is well-known in the GNSS community and is treated in works such as [67].

3.2.1 Statement of the Problem

Recalling Equation (3.40)

$$\boldsymbol{x} \sim \mathcal{N}\left(h(\boldsymbol{\theta}) + \boldsymbol{\mu}, \boldsymbol{I}\right) \tag{3.54}$$

where $\boldsymbol{x}$ is of dimension m and $\boldsymbol{\mu} \in \mathcal{A}$. What can be done is to estimate both $\boldsymbol{\theta}$ and $\boldsymbol{\mu}$ by defining the likelihood function

$$\begin{aligned} &\mathcal{L}(\boldsymbol{x}) : (\Theta \times \mathcal{A}) \subseteq \mathbb{R}^{n+m} \to \mathbb{R}^{+} \\ &\qquad (\boldsymbol{\theta}, \boldsymbol{\mu}) \mapsto \frac{1}{\sqrt{(2\pi)^m}} \exp\left(-\frac{1}{2}\|\boldsymbol{x} - h(\boldsymbol{\theta}) - \boldsymbol{\mu}\|_{\boldsymbol{I}}^2\right). \end{aligned} \tag{3.55}$$

Recalling the necessary condition $m \geq n$ to be able to estimate $\boldsymbol{\theta}$, here both $\boldsymbol{\theta}$ and $\boldsymbol{\mu}$ are parameters of the likelihood function. In that case, for the MLE to be well defined, it is necessary that $m \geq n + m$, which is obviously false for $n > 0$. Therefore, without more assumptions on the set of values that $\boldsymbol{\mu}$ can take, the vectors $\boldsymbol{\theta}$ and $\boldsymbol{\mu}$ cannot be estimated.

Table 3.2: Confusion matrix for a multiple hypothesis test. In all cases, $i \to j$ indicates that $\mathcal{H}_i$ holds and $\mathcal{H}_j$ is decided. Each off-diagonal entry corresponds to a specific misclassification between hypotheses.

Truth \ Decision	$\mathcal{H}_1$	$\cdots$	$\mathcal{H}_m$
$\mathcal{H}_1$	$1 \to 1$	$\cdots$	$1 \to m$
$\vdots$	$\vdots$	$\ddots$	$\vdots$
$\mathcal{H}_m$	$m \to 1$	$\cdots$	$m \to m$

3.2.2 Multiple Hypothesis Testing

The multiple hypothesis test extends the binary framework to distinguish between more than two hypotheses. In this context, the goal is to decide on a hypothesis $\mathcal{H}_j$ among a set of m competing hypotheses $\{\mathcal{H}_1, \mathcal{H}_2, \ldots, \mathcal{H}_m\}$, where each hypothesis corresponds to a specific model.

The quality of the decision is characterized by a generalized confusion matrix, where each row represents the true hypothesis and each column represents the decided hypothesis.

Table 3.2 illustrates the structure of this matrix for the multiple hypothesis case.

The diagonal entries represent correct decisions, while the off-diagonal entries indicate different types of wrong decisions.

3.2.3 Maximum Likelihood Rule for Model Selection Among Observations

In this setting are given a set of random variables, where each random variable follows a different probability distribution, and are given one realization of each random variable. Among these random variables, one of them follows a known reference distribution, while the others follow alternative distributions. The goal is to identify which realization is most likely to have been drawn from the reference distribution.

This leads to a model selection problem: among a set of realizations, decide which one was generated by the reference distribution.

Definition 3.2.1 (Maximum Likelihood-Based Selection)**.** *Let $\{z_1, \ldots, z_m\}$ be random variables. Assume that one of them has density f, while the others follow alternative distributions. Under hypothesis $\mathcal{H}_j$, z_j follows a distribution with density f. Given realizations $\{z_1(\omega), \ldots, z_m(\omega)\}$ of the random variables, $\mathcal{H}_j$ is decided if*

$$f(z_j(\omega)) = \max\{f(z_1(\omega)), \ldots, f(z_m(\omega))\}. \tag{3.56}$$

Unlike traditional hypothesis testing, this framework does not compare the likelihoods of different models for a single sample, but rather compares different samples under a

This document may not be reproduced, modified, adapted, published, translated in any way, in whole or in part, nor disclosed to a third party without the prior written consent of ENAC. © 2025, ENAC

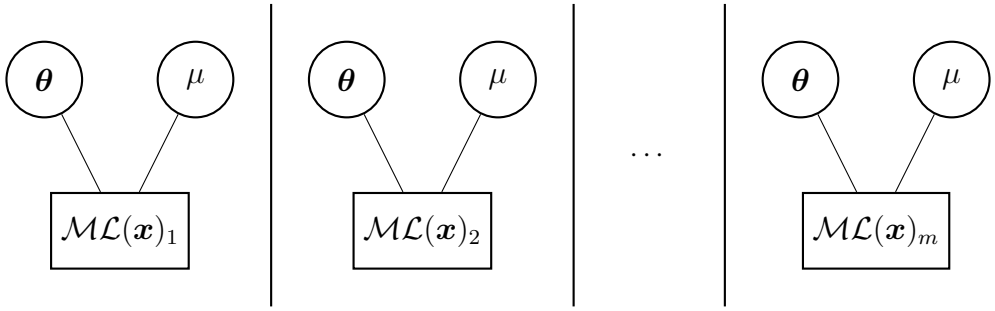

Figure 3.7: Representation of Equation (3.58) with a factor graph, for somes values of $j \in \{1, \dots, m\}$.

common model. It is particularly well-suited to fault identification tasks where a single non-faulty measurement is expected among a set of potentially biased ones.

3.2.4 Sub-graphs for Single Fault

In the detection procedure, Equation (3.38) states that $\boldsymbol{\mu} = \mu \boldsymbol{e}_i$, for some $\mu \in \mathbb{Z}^*$ and $i \in \{1, \dots, m\}$, with $\boldsymbol{e}_i$ the i-th vector of the canonical basis of $\mathbb{R}^m$. It comes

$$\boldsymbol{x} \sim \mathcal{N}\left(h(\boldsymbol{\theta}) + \mu \boldsymbol{e}_i, \boldsymbol{I}\right). \tag{3.57}$$

In practice, both μ and i are unknown, i.e., the component of $\boldsymbol{\mu}$ that is not 0 is unknown. Therefore, in order to identify the component of $\boldsymbol{\mu}$ that is not zero, $\forall j \in \{1, \dots, m\}$, a misspecified likelihood function can be defined from Equation (3.55)

$$\begin{aligned} \mathcal{ML}(\boldsymbol{x})_j : (\Theta \times \mathbb{Z}^*) \subseteq \mathbb{R}^{n+1} &\to \mathbb{R}^+ \\ (\boldsymbol{\theta}, \mu) &\mapsto \frac{1}{\sqrt{(2\pi)^m}} \exp\left(-\frac{1}{2} \|\boldsymbol{x} - h(\boldsymbol{\theta}) - \mu \boldsymbol{e}_j\|_{\boldsymbol{I}}^2\right). \end{aligned} \tag{3.58}$$

This misspecified likelihood function is well specified if and only if $i = j$. This set of functions is represented with a set of FGO in Figure 3.7. In order to compute a maximum of this (misspecified) likelihood function, it is necessary that $m \geq n+1$, and the estimators are given by

$$\left(\widehat{\boldsymbol{\theta}}_{\mathrm{MMLE}_j}, \widehat{\mu}_{\mathrm{MMLE}_j}\right) = \arg\max \mathcal{ML}\left(\boldsymbol{x}\right)_j. \tag{3.59}$$

3.2.5 Law of Faulty FGO and Fault-Free FGO

In Equations (3.57) and (3.58), suppose that $h : \mathbb{R}^n \to \mathbb{R}^m$ is a linear application. In that case, the distribution of $\boldsymbol{x}$ Equation (3.57) can be written

$$\boldsymbol{x} \sim \mathcal{N}\left(\begin{pmatrix} \boldsymbol{H} & \boldsymbol{e}_i \end{pmatrix} \begin{pmatrix} \boldsymbol{\theta} \\ \mu \end{pmatrix}, \boldsymbol{I}\right) \tag{3.60}$$

and the misspecified likelihood Equation (3.58) can be written

$$\begin{aligned}\mathcal{ML}(\boldsymbol{x})_j : (\Theta \times \mathbb{Z}^*) \subseteq \mathbb{R}^{n+1} &\to \mathbb{R}^+ \\ \begin{pmatrix}\boldsymbol{\theta} \\ \mu\end{pmatrix} &\mapsto \frac{1}{\sqrt{(2\pi)^m}} \exp\left(-\frac{1}{2}\left\|\boldsymbol{x} - \begin{pmatrix}\boldsymbol{H} & \boldsymbol{e}_j\end{pmatrix}\begin{pmatrix}\boldsymbol{\theta} \\ \mu\end{pmatrix}\right\|_{\boldsymbol{I}}^2\right). \end{aligned} \tag{3.61}$$

Defining the matrix $\boldsymbol{H}_j \triangleq \begin{pmatrix}\boldsymbol{H} & \boldsymbol{e}_j\end{pmatrix}$, the MMLE is, if and only if $\operatorname{rank}(\boldsymbol{H}_j) = n+1$, the unique vector that maximizes this function, given by

$$\begin{pmatrix}\widehat{\boldsymbol{\theta}}_{\mathrm{MMLE}_j} \\ \widehat{\mu}_{\mathrm{MMLE}_j}\end{pmatrix} = \left(\boldsymbol{H}_j^\intercal \boldsymbol{H}_j\right)^{-1} \boldsymbol{H}_j^\intercal \boldsymbol{x}. \tag{3.62}$$

Although $\mathcal{ML}(\boldsymbol{x})_j$ is defined on $\Theta \times \mathbb{Z}^*$, the obtained maximizer lies in $\mathbb{R}^{n+1}$. The residual vector is the Gaussian random vector

$$\begin{aligned}\boldsymbol{z}_{\mathrm{MMLE},j} &= \boldsymbol{x} - \boldsymbol{H}_j \begin{pmatrix}\widehat{\boldsymbol{\theta}}_{\mathrm{MMLE}_j} \\ \widehat{\mu}_{\mathrm{MMLE}_j}\end{pmatrix} \\ &= \boldsymbol{x} - \boldsymbol{H}_j \left(\boldsymbol{H}_j^\intercal \boldsymbol{H}_j\right)^{-1} \boldsymbol{H}_j^\intercal \boldsymbol{x} \\ &= \left(\boldsymbol{I} - \boldsymbol{P}_{H_j}\right)\boldsymbol{x} \end{aligned} \tag{3.63}$$

where $\boldsymbol{P}_{H_j} \triangleq \boldsymbol{H}_j \left(\boldsymbol{H}_j^\intercal \boldsymbol{H}_j\right)^{-1} \boldsymbol{H}_j^\intercal$ is the orthogonal projector onto $\operatorname{Im}(\boldsymbol{H}_j) \subseteq \mathbb{R}^m$, and $\boldsymbol{I} - \boldsymbol{P}_{H_j}$ is the orthogonal projector onto $\operatorname{Im}(\boldsymbol{H}_j)^\perp \subseteq \mathbb{R}^m$.
Denoting $\boldsymbol{H}_i \triangleq \begin{pmatrix}\boldsymbol{H} & \boldsymbol{e}_i\end{pmatrix}$, since $\dim\left(\operatorname{Im}(\boldsymbol{H}_j)^\perp\right) = m - n - 1$, Corollary 3.1.1 states that

$$\|\boldsymbol{z}_{\mathrm{MMLE},j}\|_{\boldsymbol{I}}^2 \sim \chi^2_{m-n-1,\lambda_j} \tag{3.64}$$

where $\lambda_j = \left\|\left(\boldsymbol{I} - \boldsymbol{P}_{\boldsymbol{H}_j}\right)\mathbb{E}[\boldsymbol{x}]\right\|_{\boldsymbol{I}}^2 = \left\|\left(\boldsymbol{I} - \boldsymbol{P}_{\boldsymbol{H}_j}\right)\boldsymbol{H}_i \begin{pmatrix}\boldsymbol{\theta} \\ \mu\end{pmatrix}\right\|_{\boldsymbol{I}}^2$.
From the properties of $\boldsymbol{P}_{H_j}$, it can be shown that $\left(\boldsymbol{I} - \boldsymbol{P}_{H_j}\right)\boldsymbol{H}_j = \boldsymbol{0}$ and that in general, $\left(\boldsymbol{I} - \boldsymbol{P}_{H_j}\right)\boldsymbol{H}_i \neq \boldsymbol{0}$. Therefore, if $i = j$, then $\lambda_i = 0$ and the squared norm of the residual vector follows a central chi-squared distribution with $m-n-1$ degrees of freedom. Applying the maximum likelihood rule for model selection with the density $f_{\boldsymbol{0}}$ of a central chi-squared distribution with $m - n - 1$ degrees of freedom, as in Equation (3.11), and from the set $\left\{\|\boldsymbol{z}_{\mathrm{MMLE}_1}\|_{\boldsymbol{I}}^2, \ldots, \|\boldsymbol{z}_{\mathrm{MMLE}_m}\|_{\boldsymbol{I}}^2\right\}$, the most likely component of $\boldsymbol{\mu}$ that is not null is given by

$$\widehat{i} = \arg\max\left(j \mapsto f_{\boldsymbol{0}}\left(\|\boldsymbol{z}_{\mathrm{MMLE},j}\|_{\boldsymbol{I}}^2\right)\right). \tag{3.65}$$

This way, $\widehat{i}$ corresponds to the fault identification, while the truth corresponds to i. This way, faults are identified. Filling the confusion matrix for multiple hypothesis testing provides a way to quantify how efficient is the fault identification method presented here.

This document may not be reproduced, modified, adapted, published, translated in any way, in whole or in part, nor disclosed to a third party without the prior written consent of ENAC. © 2025, ENAC

3.3 Application: TDCP & FGO-Based Single CS Detection

The fault detection and identification methods presented in this work can be applied to the detection and identification of CS in GNSS carrier-phase observations. To this end, positioning is performed using both code pseudorange and TDCP measurements. The TDCP observations are obtained by differentiating the carrier-phase measurements between consecutive epochs, which naturally suppresses constant biases such as the integer ambiguity. Once the positioning solution is estimated, a residual vector is computed, representing the mismatch between the predicted and actual measurements under the nominal model. This residual serves as the input to the statistical tests introduced previously. By evaluating the residuals against their expected statistical behavior, the framework determines whether a CS has likely occurred, thereby enabling both detection and identification of the faulty observation.

3.3.1 Observations and Corrections

Both code pseudorange and carrier-phase GNSS observations are used in the positioning, fault detection and identification process. The code pseudorange measurements provide information with lower precision but are not sensitive to CS. In contrast, the carrier-phase measurements offer ambiguous high-precision observations, which are essential for applications requiring fine accuracy. By combining these two types of observations, the system benefits from the robustness of the code and the precision of the carrier-phase, allowing for reliable detection and identification of faults such as CS.

At a given instant, given a GNSS receiver of unknown coordinates $\boldsymbol{r} \in \mathbb{R}^3$ and a satellite of known coordinates $\boldsymbol{s}_i \in \mathbb{R}^3$, as in Equation (1.8), the code pseudoranges are modeled as

$$P_r^{s_i} = \rho_r^{s_i} + c \cdot (dt_r - dt^{s_i} + \delta t^{\mathrm{rel},s_i}) + I_r^{s_i} + T_r^{s_i} + \mathrm{sag}_r^{s_i} + d_r - d^{s_i} + \xi_r^{s_i} + \varepsilon_P^{s_i}, \tag{3.66}$$

and as in Equation (1.9), the carrier-phase observations are modeled as

$$\Phi_r^{s_i} = \rho_r^{s_i} + c \cdot (dt_r - dt^{s_i} + \delta t^{\mathrm{rel},s_i}) - I_r^{s_i} + T_r^{s_i} + \mathrm{sag}_r^{s_i} + \lambda \cdot (N_r^{s_i} + \omega_r^{s_i}) + \delta_r - \delta^{s_i} + \zeta_r^{s_i} + \varepsilon_\Phi^{s_i}, \tag{3.67}$$

where the terms are defined as follows (all quantities are expressed in meters unless stated otherwise)

- $P_r^{s_i}$ is the measured code pseudorange,
- $\Phi_r^{s_i}$ is the measured carrier-phase,
- $\rho_r^{s_i} = \|\boldsymbol{r} - \boldsymbol{s}_i\|$ is the range between the receiver and the emitting satellite,
- dt_r and dt^{s_i} refer to respectively receiver and satellite clock bias (with respect to the constellation time coordinates system), in seconds,

- $\delta t^{\text{rel},s_i}$ refers to relativistic effects, in seconds,
- $I_r^{s_i}$ refers to the ionospheric delay,
- $T_r^{s_i}$ refers to the tropospheric delay,
- $\text{sag}_r^{s_i}$ refers to the Sagnac effect delay,
- λ refers to the carrier's wavelength,
- $N_r^{s_i}$ refers to the integer number of cycles between the receiver and the satellite and is unitless,
- $\omega_r^{s_i}$ refers to the phase wind-up, which takes into account orientations of the receiver and satellite antennas, in steradians,
- d_r and d^{s_i} refer respectively to the receiver and satellite hardware delays for code observations,
- δ_r and δ^{s_i} refer respectively to the receiver and satellite hardware delay for carrier-phase observations,
- $\xi_r^{s_i}$ refers to hardware delay variations for code observations,
- $\zeta_r^{s_i}$ refers to hardware delays variation for carrier-phase observations,
- $\varepsilon_P^{s_i}$ refers to multipath and receiver error for code observations,
- $\varepsilon_\Phi^{s_i}$ refers to multipath and receiver error for carrier-phase observations.

After corrections, the code pseudorange is modeled as

$$\tilde{P}_r^{s_i} = \rho_r^{s_i} + c \cdot dt_r + \tilde{\varepsilon}_P^{s_i}, \tag{3.68}$$

and the carrier-phase is modeled as

$$\tilde{\Phi}_r^{s_i} = \rho_r^{s_i} + c \cdot dt_r + \lambda \cdot N_r^{s_i} + \tilde{\varepsilon}_\Phi^{s_i}, \tag{3.69}$$

where

- $\tilde{P}_r^{s_i}$ is the corrected pseudorange measurement to satellite i,
- $\tilde{\Phi}_r^{s_i}$ is the corrected carrier-phase measurement to satellite i,
- $\tilde{\varepsilon}_P^{s_i}$ is a random variable that corresponds to the sum of $\varepsilon_P^{s_i}$ and of all code pseudorange correction errors,
- $\tilde{\varepsilon}_\Phi^{s_i}$ is a random variable that corresponds to the sum of $\varepsilon_\Phi^{s_i}$ and of all carrier-phase correction errors.

This document may not be reproduced, modified, adapted, published, translated in any way, in whole or in part, nor disclosed to a third party without the prior written consent of ENAC. © 2025, ENAC



Figure 3.8: The TLSE GNSS receiver's antenna used in this study, part of the IGS network.

3.3.2 First GNSS Receiver & Dataset Characterization

3.3.2.1 Selected GNSS Receiver

This study relies on data collected from the TLSE GNSS receiver, a fixed station located in Toulouse, France, and part of the IGS network. The TLSE station provides publicly available, high-quality multi-constellation GNSS observations. For the analysis, the complete dataset from January 1, 2024 is used.

An illustration of the TLSE receiver is shown in Figure 3.8.

Thanks to its stability, continuous operation, and high-quality data, the TLSE station provides an ideal benchmark for validating the fault detection and identification methods developed in this work.

3.3.2.2 Considered Observations

The considered dataset includes all L1 Global Positioning System (GPS) code pseudorange and carrier-phase observations, collected over the course of the day. Formally, the following random vector is considered

$$\boldsymbol{x} = \left(\tilde{\boldsymbol{P}}_r^{s_1\mathsf{T}}, \ldots, \tilde{\boldsymbol{P}}_r^{s_{32}\mathsf{T}}, \tilde{\boldsymbol{\Phi}}_r^{s_1\mathsf{T}}, \ldots, \tilde{\boldsymbol{\Phi}}_r^{s_{32}\mathsf{T}} \right)^{\mathsf{T}} \tag{3.70}$$

where $\forall i$, $\tilde{\boldsymbol{P}}_r^{s_i}$ and $\tilde{\boldsymbol{\Phi}}_r^{s_i}$ are the random vectors made of respectively all corrected code pseudorange and corrected carrier-phase random variables between the receiver and the satellite Pseudo Random Noise (PRN) i. Their sizes correspond to the number of instants at which each satellite s_i is visible from the receiver, which varies depending on the satel-

lite's trajectory during the day. As a result, these vectors differ in length across satellites PRN, and represent time-series of corrected measurements recorded at these instants.

3.3.2.3 Assumptions for Characterization

The objective of this section is to empirically characterize the GNSS measurements produced by the TLSE station on that given day.

A single realization of the random vector Equation (3.70) is available, which makes the statistical characterization challenging. Still, by aggregating a large number of observations across time, the aim is to provide statistical properties of the measurement errors $\tilde{\varepsilon}_P^{s_i}$ and $\tilde{\varepsilon}_\Phi^{s_i}$.

To do so, a number of simplifying assumptions are introduced, many of which are known to be inaccurate or even strictly false. These assumptions are not justified nor discussed in detail, as the purpose is not to provide a rigorous theoretical framework, but rather to explore the data in a practical and empirical manner. It should be noted that the resulting characterization is specific to the selected day and location, and may not generalize to other days or different stations.

The following assumptions are considered,

- $\forall(t,t')$, $\forall(i,j)$, the random variables $\tilde{\varepsilon}_P^{s_i}(t)$ and $\tilde{\varepsilon}_\Phi^{s_j}(t')$ are independent, i.e., the code pseudorange and carrier-phase observations are independent, which enables their separate analysis and characterization,
- $\forall(t,t')$, $\forall(i,j)$, $i \neq j$, the random variables $\tilde{\varepsilon}_P^{s_i}(t)$ and $\tilde{\varepsilon}_P^{s_j}(t')$ are independent, i.e., the code pseudorange observations are independent across satellites, allowing to analyze and characterize the code pseudorange observations individually for each satellite, without accounting for inter-satellite correlations,
- $\forall(t,t')$, $\forall(i,j)$, $i \neq j$, the random variables $\tilde{\varepsilon}_\Phi^{s_i}(t)$ and $\tilde{\varepsilon}_\Phi^{s_j}(t')$ are independent, i.e., the carrier-phase observations are independent across satellites, allowing to analyze and characterize the carrier-phase observations individually for each satellite, without accounting for inter-satellite correlations,
- $\forall i$, $\forall(t,t')$, the random variables $\tilde{\varepsilon}_P^{s_i}(t)$ and $\tilde{\varepsilon}_P^{s_i}(t')$ are independent, i.e., for a given satellite, the code pseudorange observations are independent across time,
- $\forall i$, $\forall(t,t')$, the random variables $\tilde{\varepsilon}_\Phi^{s_i}(t)$ and $\tilde{\varepsilon}_\Phi^{s_i}(t')$ are independent, i.e., for a given satellite, the carrier-phase observations are independent across time.

3.3.2.4 Corrected Observations and Geometric Range

First, from raw observations, as in Equations (3.66) and (3.67), are computed corrected observations, as in Equations (3.68) and (3.69).

This document may not be reproduced, modified, adapted, published, translated in any way, in whole or in part, nor disclosed to a third party without the prior written consent of ENAC. © 2025, ENAC

To characterize the random variables $\tilde{\varepsilon}_P^{s_i}$ and $\tilde{\varepsilon}_\Phi^{s_i}$, one approach is to isolate them in Equations (3.68) and (3.69).

In order to subtract the geometric range between the receiver and the satellite from the corrected observations, precise satellite ephemerides are retrieved from IGS final products, and highly accurate receiver coordinates are computed using RTKLIB [68], an open-source GNSS software, by means of a Precise Point Positioning (PPP)-static algorithm, using forward-backward filtering and solid Earth tide corrections. By processing all available observations throughout that day, RTKLIB provides a millimeter-level estimate of the receiver's position. This accurate reference is used as a ground truth to evaluate and characterize the measurement errors affecting both the code pseudorange and the carrier-phase observations.

At that point, the receiver clock bias is still unknown, as well as the integer ambiguities associated with the carrier-phase measurements. As a result are available the left hand side of the following equations, at all instant t and for all visible satellite,

$$\tilde{P}_r^{s_i}(t) - \rho_r^{s_i}(t) = c \cdot dt_r(t) + \tilde{\varepsilon}_P^{s_i}(t), \tag{3.71}$$

and

$$\tilde{\Phi}_r^{s_i}(t) - \rho_r^{s_i}(t) = c \cdot dt_r(t) + \lambda \cdot N_r^{s_i}(t) + \tilde{\varepsilon}_\Phi^{s_i}(t), \tag{3.72}$$

leaving unknown the receiver clock bias $dt_r(t)$, the integer ambiguities $N_r^{s_i}(t)$, and the random variables $\tilde{\varepsilon}_P^{s_i}(t)$ and $\tilde{\varepsilon}_\Phi^{s_i}(t)$.

3.3.2.5 Code Pseudorange Characterization

To isolate $\tilde{\varepsilon}_P^{s_i}(t)$, the receiver clock bias $dt_r(t)$ must be known.

A new assumption is introduced, which may be imprecise or even incorrect from a rigorous theoretical standpoint, but is adopted here in line with the empirical and exploratory nature of the analysis,

- $\forall t$, considering the set of all code pseudoranges from all visible satellites at this given instant, the mean value of $\left(\tilde{P}_r^{s_i}(t) - \rho_r^{s_i}(t)\right)$ is assumed to be the receiver clock bias at that instant multiplied by the speed of light, i.e., equal to $c \cdot dt_r(t)$.

At that point, excepted $\tilde{\varepsilon}_P^{s_i}(t)$, all terms in equation (3.68) are known, i.e., all terms in the left hand side of the following equation are known,

$$\tilde{P}_r^{s_i}(t) - \rho_r^{s_i}(t) - c \cdot dt_r(t) = \tilde{\varepsilon}_P^{s_i}(t). \tag{3.73}$$

Therefore, a sample of $\tilde{\varepsilon}_P^{s_i}(t)$ for all satellite and for all instant is available.

Histograms of these samples are visible in Figure 3.9.

Each histogram represents realizations of code errors observed for a given satellite throughout the day. As previously stated, the random variables $\{\tilde{\varepsilon}_P^{s_i}(t_1), \tilde{\varepsilon}_P^{s_i}(t_2), \ldots\}$ are assumed

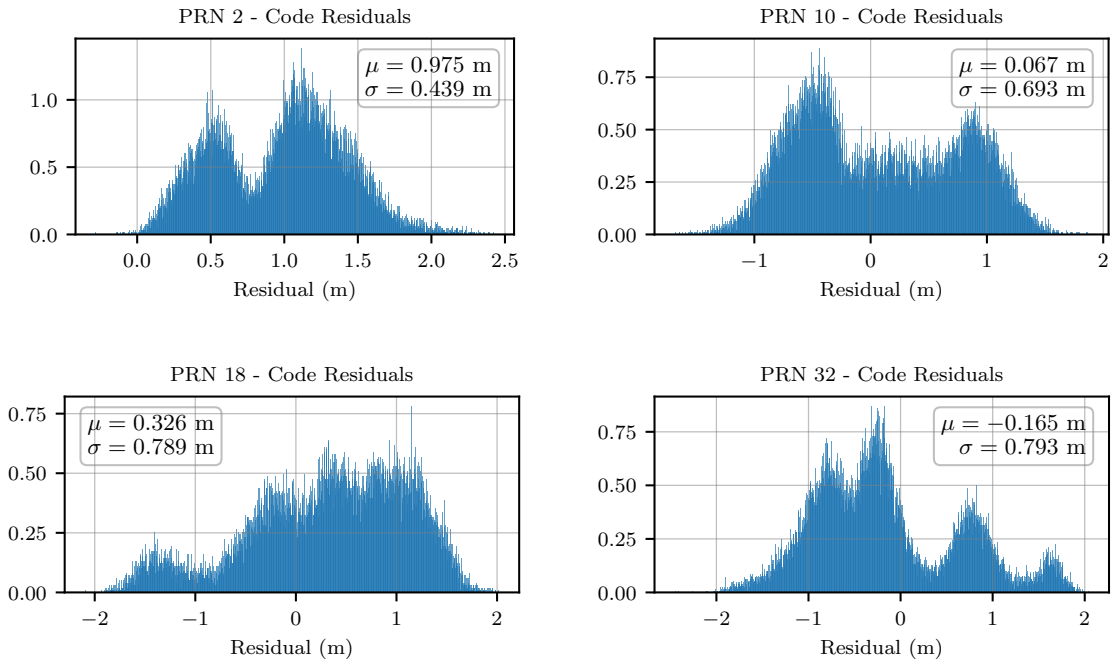

Figure 3.9: Distribution of code pseudorange residuals for selected satellites at station TLSE.

independent. A new assumption, which may be imprecise or even incorrect from a rigorous theoretical standpoint, is added to the characterization of the data,

- $\forall(t, t')$, the random variables $\tilde{\varepsilon}_P^{s_i}(t)$ and $\tilde{\varepsilon}_P^{s_i}(t')$ are identically distributed.

Thanks to this additional assumption, the histograms can be used to empirically estimate the distribution of these random variables.

In that case, the histograms indicate that the random variables $\{\tilde{\varepsilon}_P^{s_i}(t_1), \tilde{\varepsilon}_P^{s_i}(t_2), \ldots\}$ are not Gaussian.

3.3.2.6 Carrier-Phase Characterization

To characterize the random variables $\tilde{\varepsilon}_\Phi^{s_i}(t)$, the ambiguity terms $N_r^{s_i}(t)$ must be known. These ambiguities are unknown and cannot be directly corrected from the raw observations. Nonetheless, RTKLIB can process RINEX files and compute geometric combinations of observations to detect CS, which are changes of values of these ambiguity numbers. In the absence of CS, the ambiguity term remains constant over time. Consequently, by identifying continuous segments of phase observations that are free of CS, it is possible to isolate and examine the statistical behavior of the residual noise. Histograms of these segments are then plotted, revealing the distribution of the carrier-phase residuals. Although the absolute value of the residuals is shifted due to the unknown ambiguity bias, their spread and shape provide meaningful insight into the underlying noise characteristics.

Histograms of these samples are visible in Figure 3.10.

This document may not be reproduced, modified, adapted, published, translated in any way, in whole or in part, nor disclosed to a third party without the prior written consent of ENAC. © 2025, ENAC

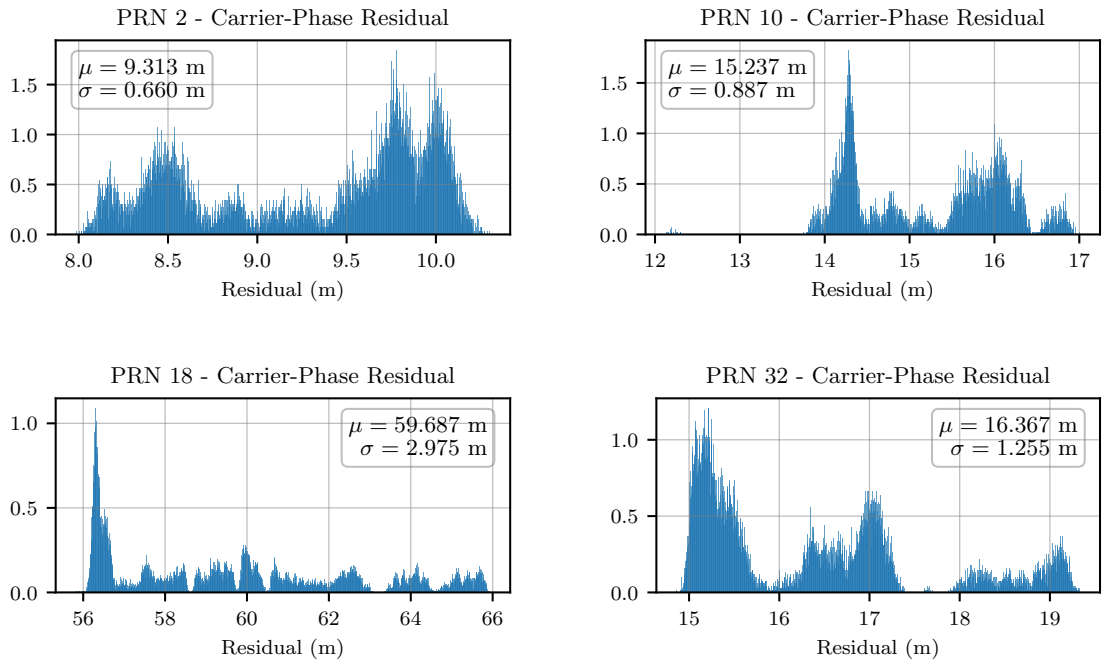

Figure 3.10: Distribution of carrier-phase residuals for selected satellites over CS-free periods at station TLSE.

Similarly, a new assumption, which may be imprecise or even incorrect from a rigorous theoretical standpoint, is added to the characterization of the data,

- $\forall (t, t')$, $\forall i$, with no CS between t and t', the random variables $\tilde{\varepsilon}_{\Phi}^{s_i}(t)$ and $\tilde{\varepsilon}_{\Phi}^{s_i}(t')$ are identically distributed.

Thanks to this additional assumption, the histograms can be used to empirically estimate the distribution of these random variables.

Similarly, the histograms indicate that the random variables $\{\tilde{\varepsilon}_{\Phi}^{s_i}(t_1), \tilde{\varepsilon}_{\Phi}^{s_i}(t_2), \ldots\}$ are not Gaussian.

Under the proposed assumptions, the code pseudorange and carrier-phase characterizations indicate that the random variables $\tilde{\varepsilon}_{P}^{s_i}$ and $\tilde{\varepsilon}_{\Phi}^{s_i}$ are not Gaussian.

As explained in Section 1.3.3.1, by means of a second receiver with known coordinates and of differential positioning techniques, better absolute positioning can be achieved. For this reason, a second receiver, closely located to TLSE, is introduced.

Because these two receivers experience similar atmospheric errors due to their proximity, the differential technique allows for the reduction of these common-mode errors.

3.3.3 Second GNSS Receiver & Dataset Characterization

In this section, a second receiver is introduced, allowing for the computation and characterization of observation differences.



Figure 3.11: The TLSG GNSS receiver's antenna used in this study, part of the IGS network.

3.3.3.1 Selected GNSS Receiver

Like TLSE, the TLSG GNSS receiver is a fixed station in Toulouse, France, and part of the IGS network. It is located 1265 m from TLSE. It provides publicly available, high-quality multi-constellation GNSS observations. For the analysis, the complete dataset from January 1, 2024 is used.

An illustration of the TLSG receiver is shown in Figure 3.11.

Thanks to its stability, continuous operation, and high-quality data, the TLSG station also provides an ideal benchmark for validating the fault detection and identification methods developed in this work.

3.3.3.2 Considered Observations

Similarly to the single receiver case, the only observations that are considered in this study are the code pseudorange and carrier-phase observations from the L1 band of GPS satellites, that are visible by both receivers. This ensures that differential corrections between the two receivers are based on consistent, matching measurements, which is essential for accurate differential processing and reliable noise characterization.

3.3.3.3 Differentiation of Observations

Here, $\boldsymbol{r}_1 \in \mathbb{R}^3$ indicates the coordinates of TLSE, while $\boldsymbol{r}_2 \in \mathbb{R}^3$ indicates the coordinates of TLSG.

The code pseudorange and carrier-phase observations of both receivers are corrected by RTKLIB. For TLSE, the code pseudorange observations are modeled as

$$\tilde{P}_{r_1}^{s_i} = \rho_{r_1}^{s_i} + c \cdot dt_{r_1} + \tilde{\varepsilon}_{P_1}^{s_i}, \tag{3.74}$$

This document may not be reproduced, modified, adapted, published, translated in any way, in whole or in part, nor disclosed to a third party without the prior written consent of ENAC. © 2025, ENAC

and the carrier-phase observations are modeled as

$$\tilde{\Phi}_{r_1}^{s_i} = \rho_{r_1}^{s_i} + c \cdot dt_{r_1} + \lambda \cdot N_{r_1}^{s_i} + \tilde{\varepsilon}_{\Phi_1}^{s_i}, \tag{3.75}$$

while for TLSG, the code pseudorange observations are modeled as

$$\tilde{P}_{r_2}^{s_i} = \rho_{r_2}^{s_i} + c \cdot dt_{r_2} + \tilde{\varepsilon}_{P_2}^{s_i}, \tag{3.76}$$

and the carrier-phase observations are modeled as

$$\tilde{\Phi}_{r_2}^{s_i} = \rho_{r_2}^{s_i} + c \cdot dt_{r_2} + \lambda \cdot N_{r_2}^{s_i} + \tilde{\varepsilon}_{\Phi_2}^{s_i}, \tag{3.77}$$

where

- $\tilde{P}_{r_1}^{s_i}$ and $\tilde{P}_{r_2}^{s_i}$ are the corrected pseudorange measurements to satellite i for TLSE and TLSG, respectively,
- $\tilde{\Phi}_{r_1}^{s_i}$ and $\tilde{\Phi}_{r_2}^{s_i}$ are the corrected carrier-phase measurements to satellite i for TLSE and TLSG, respectively,
- $\tilde{\varepsilon}_{P_1}^{s_i}$ and $\tilde{\varepsilon}_{P_2}^{s_i}$ are random variables that corresponds to the sum of all code pseudorange errors, for TLSE and TLSG, respectively,
- $\tilde{\varepsilon}_{\Phi_1}^{s_i}$ and $\tilde{\varepsilon}_{\Phi_2}^{s_i}$ are random variables that corresponds to the sum of all carrier-phase errors, for TLSE and TLSG, respectively.

In GNSS, as presented in Section 1.3.3.1, a Single Difference (SD) refers to the difference between quantities from two receivers. Therefore, anytime the Δ symbol appears, it indicates the difference of two common quantities between two receivers, i.e., for some quantities a_1 and a_2,

$$\Delta a_{1,2} = a_2 - a_1. \tag{3.78}$$

From these corrected observations are computed their differences, i.e.,

$$\Delta\tilde{P}_{1,2}^{s_i} = \left(\tilde{P}_{r_2}^{s_i} - \tilde{P}_{r_1}^{s_i}\right) = \Delta\rho_{1,2}^{s_i} + c \cdot \Delta dt_{1,2} + \Delta\tilde{\varepsilon}_{P_{1,2}}^{s_i}, \tag{3.79}$$

and

$$\Delta\tilde{\Phi}_{1,2}^{s_i} = \left(\tilde{\Phi}_{r_2}^{s_i} - \tilde{\Phi}_{r_1}^{s_i}\right) = \Delta\rho_{1,2}^{s_i} + c \cdot \Delta dt_{1,2} + \lambda \cdot \Delta N_{1,2}^{s_i} + \Delta\tilde{\varepsilon}_{\Phi_{1,2}}^{s_i}. \tag{3.80}$$

The objective of the following sections is to characterize the random variables $\Delta\tilde{\varepsilon}_{P_{1,2}}^{s_i}$ and $\Delta\tilde{\varepsilon}_{\Phi_{1,2}}^{s_i}$.

3.3.3.4 Assumptions for Characterization

Similarly to the case of a single receiver, the objective of this section is to empirically characterize the difference of GNSS measurements produced by the TLSE and TLSG stations on that given day.

For both receivers, a single realization of the random vector Equation (3.70) is available, which makes the statistical characterization challenging. Still, by aggregating a large number of observations across time, the aim is to estimate some key statistical properties of the measurement errors $\Delta\tilde{\varepsilon}^{s_i}_{P_{1,2}}$ and $\Delta\tilde{\varepsilon}^{s_i}_{\Phi_{1,2}}$.

Similarly, a number of simplifying assumptions are introduced, many of which are known to be inaccurate or even strictly false. These assumptions are not justified nor discussed in detail, as the purpose is not to provide a rigorous theoretical framework, but rather to explore the data in a practical and empirical manner. It should be noted that the resulting characterization is specific to the selected day and locations, and may not generalize to other days or different stations.

The following assumptions are considered,

- $\forall(t,t')$, $\forall(i,j)$, the random variables $\Delta\tilde{\varepsilon}^{s_i}_{P_{1,2}}(t)$ and $\Delta\tilde{\varepsilon}^{s_j}_{\Phi_{1,2}}(t')$ are independent, i.e., the difference of code pseudorange and the difference of carrier-phase observations are independent, which enables their separate analysis and characterization,
- $\forall(t,t')$, $\forall(i,j)$, $i \neq j$, the random variables $\Delta\tilde{\varepsilon}^{s_i}_{P_{1,2}}(t)$ and $\Delta\tilde{\varepsilon}^{s_j}_{P_{1,2}}(t')$ are independent, i.e., the difference of code pseudorange observations are independent across satellites, allowing to analyze and characterize the difference of code pseudorange observations individually for each satellite, without accounting for inter-satellite correlations,
- $\forall(t,t')$, $\forall(i,j)$, $i \neq j$, the random variables $\Delta\tilde{\varepsilon}^{s_i}_{\Phi_{1,2}}(t)$ and $\Delta\tilde{\varepsilon}^{s_j}_{\Phi_{1,2}}(t')$ are independent, i.e., the difference of carrier-phase observations are independent across satellites, allowing to analyze and characterize the difference of carrier-phase observations individually for each satellite, without accounting for inter-satellite correlations,
- $\forall i$, $\forall(t,t')$, the random variables $\Delta\tilde{\varepsilon}^{s_i}_{P_{1,2}}(t)$ and $\Delta\tilde{\varepsilon}^{s_i}_{P_{1,2}}(t')$ are independent, i.e., for a given satellite, the difference of code pseudorange observations are independent across time,
- $\forall i$, $\forall(t,t')$, the random variables $\Delta\tilde{\varepsilon}^{s_i}_{\Phi_{1,2}}(t)$ and $\Delta\tilde{\varepsilon}^{s_i}_{\Phi_{1,2}}(t')$ are independent, i.e., for a given satellite, the difference of carrier-phase observations are independent across time.

3.3.3.5 Corrected Observations and Geometric Range

Similarly to the single receiver study, first, from raw observations, as in Equations (3.66) and (3.67), are computed corrected observations, as in Equations (3.74), (3.75), (3.76) and (3.77) by PRX[1] .

In a second step, the difference of these equations is computed, leading to Equations (3.79) and (3.80).

Similarly to TLSE, the precise coordinates of TLSG are computed using RTKLIB by applying the same PPP-static algorithm, which incorporates forward-backward filtering

[1]The `prx` tool, available at `github.com/jtec/prx`, is a parser for RINEX files that produces enriched outputs including precise satellite positions, corrected observations, and other relevant data.

This document may not be reproduced, modified, adapted, published, translated in any way, in whole or in part, nor disclosed to a third party without the prior written consent of ENAC. © 2025, ENAC

and solid Earth tide corrections. Precise satellite ephemerides are also retrieved from IGS final products to accurately calculate the geometric ranges between satellites and TLSG. By processing all available observations throughout the day, RTKLIB delivers a millimeter-level estimate of TLSG coordinates. This high-precision reference enables a consistent and reliable evaluation of the difference of measurement errors affecting both the difference of code pseudorange and the difference of carrier-phase observations.

At that point, the geometric ranges are known, but the difference of receiver clock bias is still unknown, as well as the difference of integer ambiguities associated with the carrier-phase measurements. As a result, the left hand side of the following equations are known at all instant t and for all visible satellite by both receivers,

$$\Delta\tilde{P}_{1,2}^{s_i}(t) - \Delta\rho_{1,2}^{s_i}(t) = c \cdot \Delta dt_{1,2}(t) + \Delta\tilde{\varepsilon}_{P_{1,2}}^{s_i}(t), \tag{3.81}$$

and

$$\Delta\tilde{\Phi}_{1,2}^{s_i}(t) - \Delta\rho_{1,2}^{s_i} = c \cdot \Delta dt_{1,2}(t) + \lambda \cdot \Delta N_{1,2}^{s_i}(t) + \Delta\tilde{\varepsilon}_{\Phi_{1,2}}^{s_i}(t), \tag{3.82}$$

leaving unknown the difference of receiver clock bias $\Delta dt_{1,2}(t)$, the difference of integer ambiguities $\Delta N_{1,2}^{s_i}(t)$, and the random variables $\Delta\tilde{\varepsilon}_{P_{1,2}}^{s_i}(t)$ and $\Delta\tilde{\varepsilon}_{\Phi_{1,2}}^{s_i}(t)$.

3.3.3.6 Code Pseudorange Characterization

To isolate $\Delta\tilde{\varepsilon}_{P_{1,2}}^{s_i}(t)$, the difference of receiver clock bias $\Delta dt_{1,2}(t)$ must be known.
A new assumption is introduced, which may be imprecise or even incorrect from a rigorous theoretical standpoint, but is adopted here in line with the empirical and exploratory nature of the analysis,

- $\forall t$, considering the set of all code pseudoranges from all visible satellites by both receivers at this given instant, the mean value of $\Delta\tilde{P}_{1,2}^{s_i}(t) - \Delta\rho_{1,2}^{s_i}(t)$ is assumed to be the difference of receiver clock bias at that instant multiplied by the speed of light, i.e., equal to $c \cdot \Delta dt_{1,2}(t)$.

At that point, excepted $\Delta\tilde{\varepsilon}_{P_{1,2}}^{s_i}(t)$, all terms in equation (3.79) are known, i.e., all terms of the left hand side of the following equation are known,

$$\Delta\tilde{P}_{1,2}^{s_i}(t) - \Delta\rho_{1,2}^{s_i}(t) - c \cdot \Delta dt_{1,2}(t) = \Delta\tilde{\varepsilon}_{P_{1,2}}^{s_i}(t). \tag{3.83}$$

Therefore, a sample of $\Delta\tilde{\varepsilon}_{P_{1,2}}^{s_i}(t)$ for all satellite and for all instant is available.
Histograms of these samples are visible in Figure 3.12.
Each histogram represents realizations of difference of code errors observed for a given satellite throughout the day. As previously stated, the random variables $\left\{\Delta\tilde{\varepsilon}_{P_{1,2}}^{s_i}(t_1), \Delta\tilde{\varepsilon}_{P_{1,2}}^{s_i}(t_2), \ldots\right\}$ are assumed independent.
For each satellite individually, in order to assess the behavior of the differences of code pseudorange observations with respect to satellite elevation, the observations are grouped

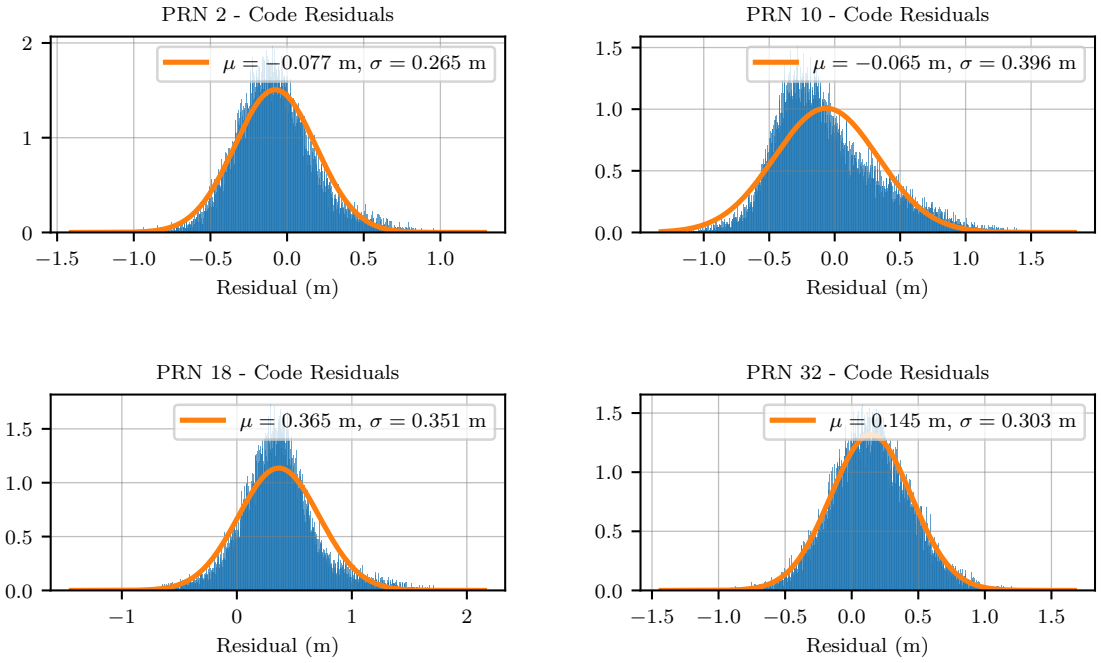

Figure 3.12: Distribution and Gaussian fits of SD of code pseudorange residuals between TLSE and TLSG for selected satellites.

into bins spanning 10° intervals from 10° to 90°. Within each elevation bin, statistical metrics are calculated using only the available observations that fall within the corresponding elevation range.

For each satellite, the obtained mean value as a function of elevation is visible in Figure 3.13, while the standard deviation is visible in Figure 3.14.

To model the relationship between the standard deviation of difference of code pseudorange observation and satellite elevation, a nonlinear fit of the form [69]

$$\frac{a}{\sin(\text{elevation})} + b \tag{3.84}$$

is computed. This function reflects the expected increase in code pseudorange measurement noise at lower elevations due to longer signal paths and greater atmospheric interference. The parameters a and b are estimated using an FGO, with factors that are the computed standard deviation, for all satellites and all elevation bins.

To conclude on the characterization of the difference of code pseudorange observations, following the assumptions on these observations, all of them are independent. Additionally, it is now assumed that they follow centered Gaussian distributions, with a standard deviation following the obtained fit in Figure 3.14, i.e.,

$$\forall t, \forall i,\ \Delta\tilde{\varepsilon}^{s_i}_{P_{1,2}}(t) \sim \mathcal{N}\left(0, \left(\frac{0.088}{\sin\left(\text{elevation}\right)} + 0.087\right)^2\right). \tag{3.85}$$

This document may not be reproduced, modified, adapted, published, translated in any way, in whole or in part, nor disclosed to a third party without the prior written consent of ENAC. © 2025, ENAC

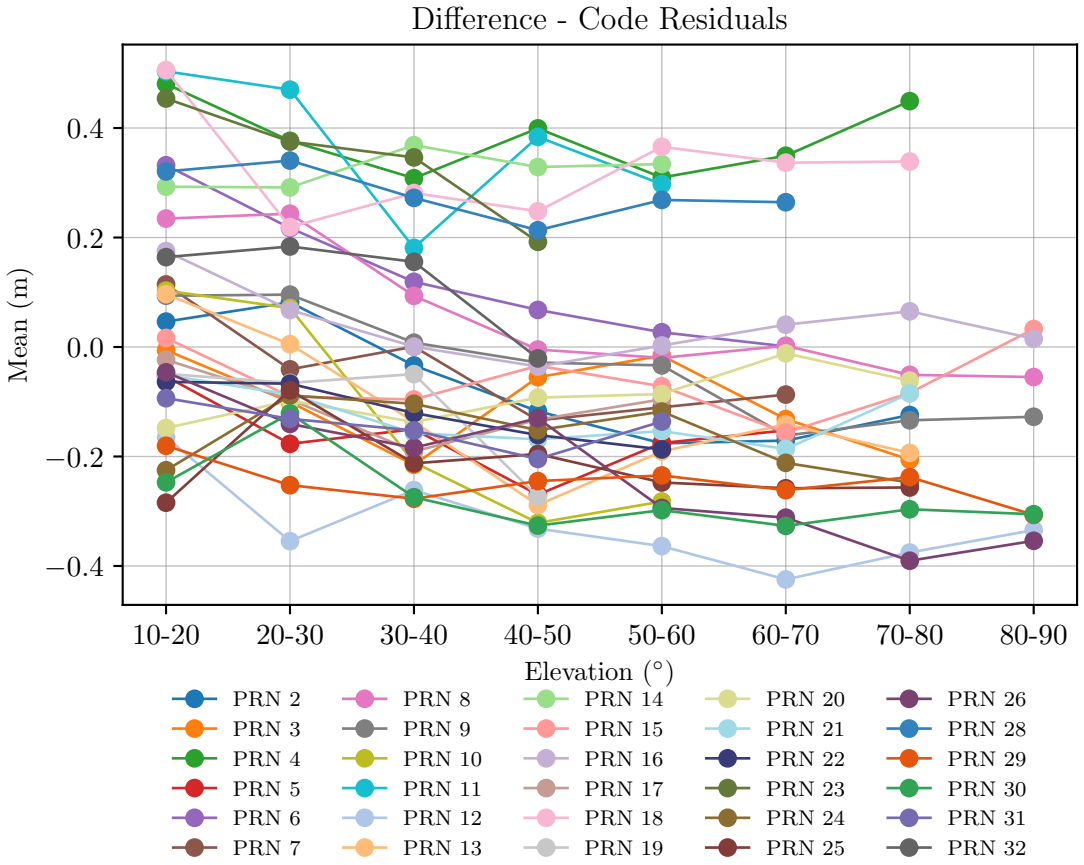

Figure 3.13: Mean of SD of code pseudorange residuals between TLSE and TLSG with respect to elevation.

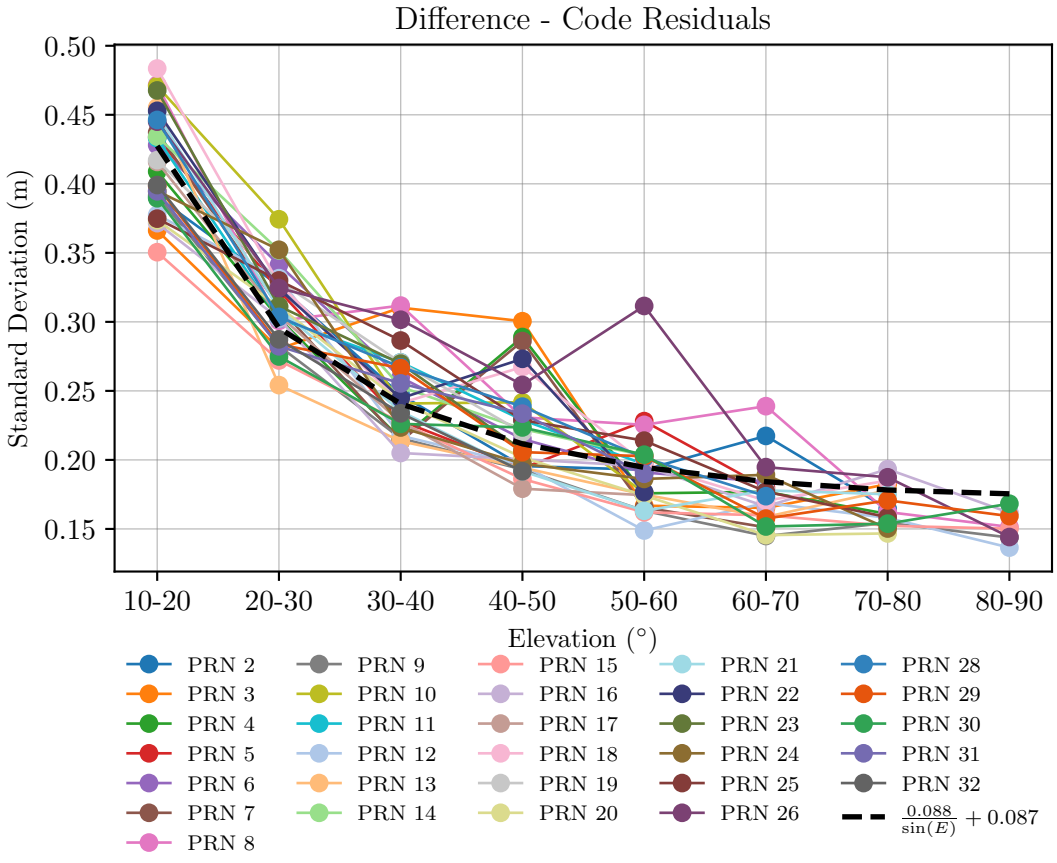

Figure 3.14: Standard deviation of SD of code pseudorange residuals between TLSE and TLSG with respect to elevation.

This document may not be reproduced, modified, adapted, published, translated in any way, in whole or in part, nor disclosed to a third party without the prior written consent of ENAC. © 2025, ENAC

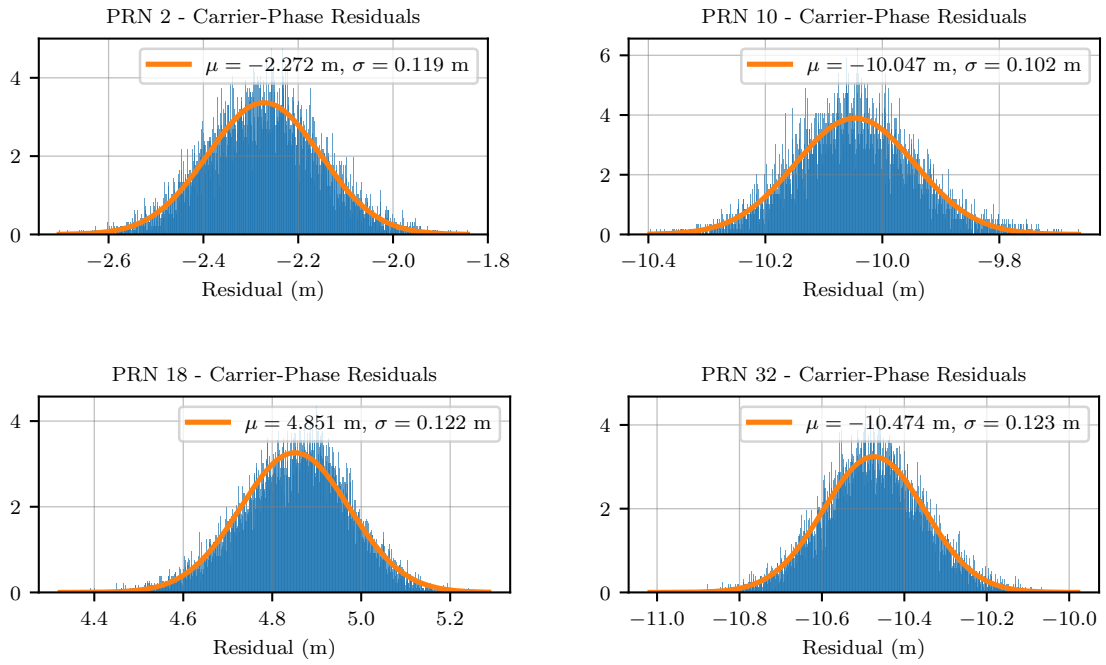

Figure 3.15: Distribution and Gaussian fits of SD of carrier-phase residuals between TLSE and TLSG for selected satellites.

3.3.3.7 Carrier-Phase Characterization

Similarly, to characterize $\Delta\tilde{\varepsilon}^{s_i}_{\Phi_{1,2}}(t)$, the difference of ambiguity terms $\Delta N^{s_i}_{1,2}(t)$ must be known. These ambiguities are unknown and cannot be directly corrected from the raw observations. Nonetheless, RTKLIB can process RINEX files and compute geometric combinations of observations to detect CS, which are changes of values of these ambiguity numbers. In the absence of CS, the ambiguity term remains constant over time. Consequently, by identifying continuous segments of phase observations that are free of CS, it is possible to isolate and examine the statistical behavior of the residual noise. Histograms of these segments are then plotted, revealing the distribution of the carrier-phase residuals. Although the absolute value of the residuals is shifted due to the unknown ambiguity bias, their spread and shape provide meaningful insight into the underlying noise characteristics.

Histograms of these samples are visible in Figure 3.15.

For each satellite individually, in order to assess the behavior of the differences of carrier-phase observations with respect to satellite elevation, the observations are grouped into bins spanning 10° intervals from 10° to 90°. Within each elevation bin, statistical metrics are calculated using only the available observations that fall within the corresponding elevation range.

For each satellite, the obtained mean value as a function of elevation is visible in Figure 3.16, while the standard deviation is visible in Figure 3.17.

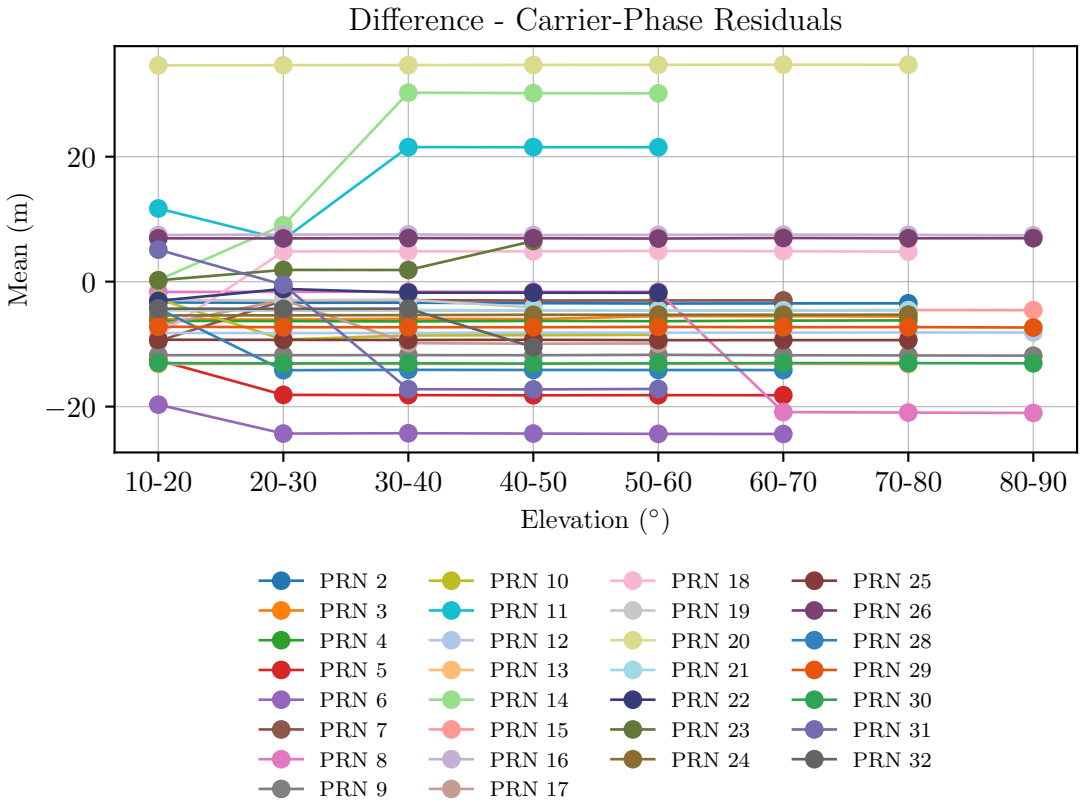

Figure 3.16: Mean of SD of carrier-phase residuals between TLSE and TLSG with respect to elevation.

This document may not be reproduced, modified, adapted, published, translated in any way, in whole or in part, nor disclosed to a third party without the prior written consent of ENAC. © 2025, ENAC

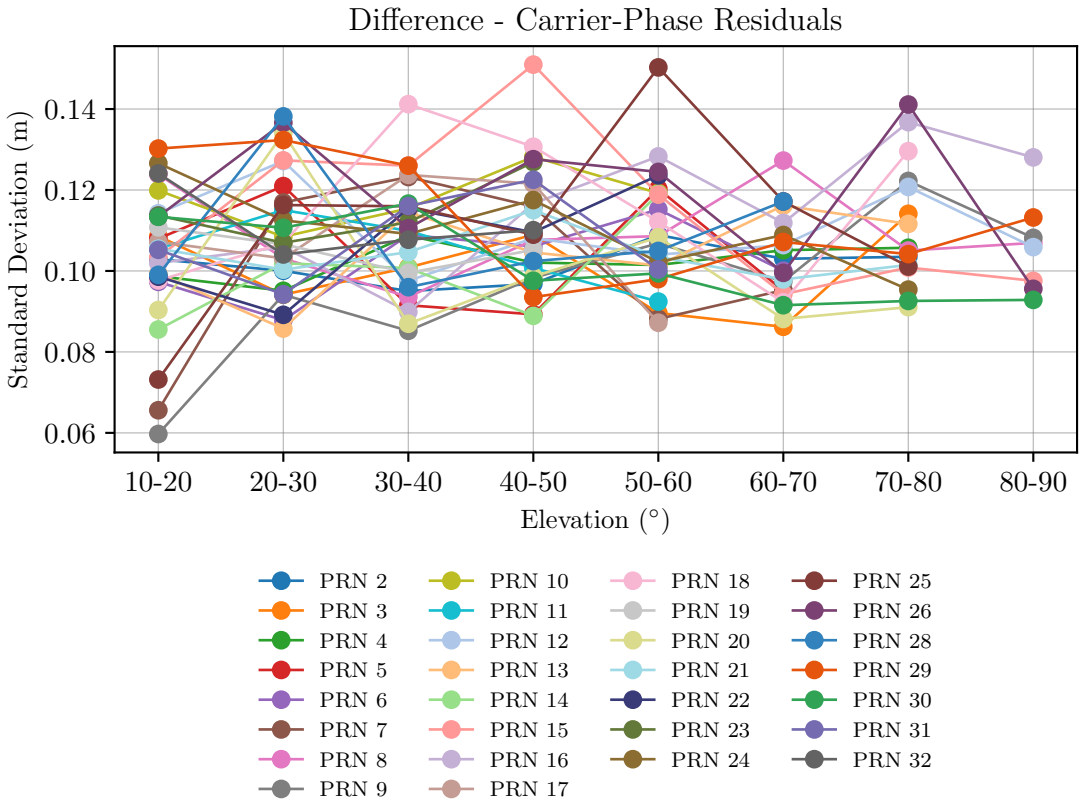

Figure 3.17: Standard deviation of SD of carrier-phase residuals between TLSE and TLSG with respect to elevation.

It can be seen that the mean varies. This is because different continuous observation periods are considered, each free of CS, but from one segment to another, the carrier-phase ambiguities can change.

Also, the standard deviation of the difference of carrier-phase observations is not as much related to the satellite elevation as it is the case for the difference of code pseudorange observations.

To conclude on the characterization of the difference of carrier-phase observations, following the assumptions on these observations, all of them are independent. Additionally, it is now assumed that they follow centered Gaussian distributions, with a standard deviation as in Figure 3.17, i.e.,

$$\forall t, \forall i,\ \Delta\tilde{\varepsilon}^{s_i}_{\Phi_{1,2}}(t) \sim \mathcal{N}\left(0, (0.12)^2\right). \tag{3.86}$$

To conclude this section, the characterization of code and carrier phase measurements is a complex and demanding task that, in itself, could constitute the focus of an entire thesis. While this effort is essential for improving positioning algorithms, if the data were perfectly modeled, then working with synthetic data would be equivalent to working with real data. Therefore, maintaining some level of imperfection in the modeling is actually beneficial (without it, synthetic data alone would be sufficient for all testing purposes).

Now that the statistical behavior of the code pseudorange differences and the carrier-phase differences between receivers has been characterized through the computation of their distribution across elevation bins, a CS detector is designed. This detector leverages the insights and theoretical framework established in the previous sections, using the known noise properties of both observables to identify discontinuities in the difference of integer ambiguities, indicative of a CS.

3.4 Cycle Slip Detection

Based on the previously characterized differences of code and carrier-phase observations between TLSE and TLSG on January 1, 2024, as well as the absolute position of TLSG on that day, the objective is now to estimate the coordinates of TLSE. This is done by means of an FGO that incorporates the differences in code measurements between the two stations. Additionally, from the differences in carrier-phase measurements, a linear combination that eliminates the phase ambiguities is applied, leading to the formation of TDCP observations, which are used to constrain the coordinates of TLSE with high precision.

These observations assume the absence of CS. Based on the estimated position, a residual is computed, and a detection and identification test for CS is implemented to ensure the consistency of the TDCP.

This document may not be reproduced, modified, adapted, published, translated in any way, in whole or in part, nor disclosed to a third party without the prior written consent of ENAC. © 2025, ENAC

3.4.1 Statement of the Problem

The first receiver, of coordinates $\boldsymbol{r}_1 \in \mathbb{R}^3$, corresponds to TLSE, while the second receiver, of coordinates $\boldsymbol{r}_2 \in \mathbb{R}^3$ corresponds to TLSG. The absolute position of TLSG is known and used as a reference, while TLSE is seen as the rover within a differential positioning framework.

At given instants t and t', given k visible satellites at these instants, the set of all differences of corrected code pseudoranges and corrected carrier-phase observations is considered. These observations are organized in the following manner: the observation vector is structured as a row vector composed of both difference of corrected code pseudorange and difference of corrected carrier-phase measurements. The first half contains the differences of corrected code pseudorange observations, while the second half contains the difference of corrected carrier-phase observations. In both halves, the measurements are ordered first by satellite (from satellite 1 to k) and for each satellite, chronologically by time (t and t'), i.e.,

$$\begin{pmatrix} \Delta\tilde{P}_{1,2}^{s_1}(t) \\ \Delta\tilde{P}_{1,2}^{s_1}(t') \\ \vdots \\ \Delta\tilde{P}_{1,2}^{s_k}(t) \\ \Delta\tilde{P}_{1,2}^{s_k}(t') \\ \Delta\tilde{\Phi}_{1,2}^{s_1}(t) \\ \Delta\tilde{\Phi}_{1,2}^{s_1}(t') \\ \vdots \\ \Delta\tilde{\Phi}_{1,2}^{s_k}(t) \\ \Delta\tilde{\Phi}_{1,2}^{s_k}(t') \end{pmatrix} = \begin{pmatrix} \Delta\rho_{1,2}^{s_1}(t) \\ \Delta\rho_{1,2}^{s_1}(t') \\ \vdots \\ \Delta\rho_{1,2}^{s_k}(t) \\ \Delta\rho_{1,2}^{s_k}(t') \\ \Delta\rho_{1,2}^{s_1}(t) \\ \Delta\rho_{1,2}^{s_1}(t') \\ \vdots \\ \Delta\rho_{1,2}^{s_k}(t) \\ \Delta\rho_{1,2}^{s_k}(t') \end{pmatrix} + c \cdot \begin{pmatrix} \Delta dt_{1,2}(t) \\ \Delta dt_{1,2}(t') \\ \vdots \\ \Delta dt_{1,2}(t) \\ \Delta dt_{1,2}(t') \\ \Delta dt_{1,2}(t) \\ \Delta dt_{1,2}(t') \\ \vdots \\ \Delta dt_{1,2}(t) \\ \Delta dt_{1,2}(t') \end{pmatrix} + \lambda \cdot \begin{pmatrix} 0 \\ 0 \\ \vdots \\ 0 \\ 0 \\ \Delta N_{1,2}^{s_1}(t) \\ \Delta N_{1,2}^{s_1}(t') \\ \vdots \\ \Delta N_{1,2}^{s_k}(t) \\ \Delta N_{1,2}^{s_k}(t') \end{pmatrix} + \underbrace{\begin{pmatrix} \Delta\tilde{\varepsilon}_{P_{1,2}}^{s_1}(t) \\ \Delta\tilde{\varepsilon}_{P_{1,2}}^{s_1}(t') \\ \vdots \\ \Delta\tilde{\varepsilon}_{P_{1,2}}^{s_k}(t) \\ \Delta\tilde{\varepsilon}_{P_{1,2}}^{s_k}(t') \\ \Delta\tilde{\varepsilon}_{\Phi_{1,2}}^{s_1}(t) \\ \Delta\tilde{\varepsilon}_{\Phi_{1,2}}^{s_1}(t') \\ \vdots \\ \Delta\tilde{\varepsilon}_{\Phi_{1,2}}^{s_k}(t) \\ \Delta\tilde{\varepsilon}_{\Phi_{1,2}}^{s_k}(t') \end{pmatrix}}_{\triangleq\, \Delta\tilde{\boldsymbol{\varepsilon}}} . \quad (3.87)$$

As explained in Section 3.3, the random vector containing all errors terms in the right hand side of Equation (3.87), denoted simply $\Delta\tilde{\boldsymbol{\varepsilon}}$, is characterized as a centered Gaussian random vector, with a diagonal covariance matrix $\boldsymbol{R}$, detailed in Section 3.3.

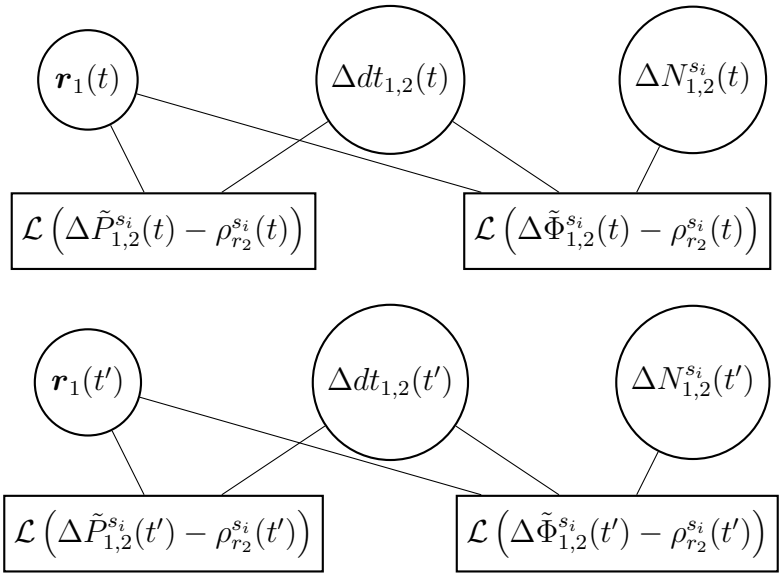

Figure 3.18: Representation of Equation (3.88) with a factor graph, considering a single satellite $\boldsymbol{s}_i$. To fully represent it, factors from other satellites have to be added, as well as additional ambiguity terms.

3.4.2 Factor Graph Representation

Since $\boldsymbol{r}_2$ is known, all the terms $\rho_{r_2}^{s_i}(t)$ and $\rho_{r_2}^{s_i}(t')$ are known, so can be moved to the left hand side of Equation (3.87)

$$\begin{pmatrix} \Delta\tilde{P}_{1,2}^{s_1}(t) \\ \Delta\tilde{P}_{1,2}^{s_1}(t') \\ \vdots \\ \Delta\tilde{P}_{1,2}^{s_k}(t) \\ \Delta\tilde{P}_{1,2}^{s_k}(t') \\ \Delta\tilde{\Phi}_{1,2}^{s_1}(t) \\ \Delta\tilde{\Phi}_{1,2}^{s_1}(t') \\ \vdots \\ \Delta\tilde{\Phi}_{1,2}^{s_k}(t) \\ \Delta\tilde{\Phi}_{1,2}^{s_k}(t') \end{pmatrix} - \begin{pmatrix} \rho_{r_2}^{s_1}(t) \\ \rho_{r_2}^{s_1}(t') \\ \vdots \\ \rho_{r_2}^{s_k}(t) \\ \rho_{r_2}^{s_k}(t') \\ \rho_{r_2}^{s_1}(t) \\ \rho_{r_2}^{s_1}(t') \\ \vdots \\ \rho_{r_2}^{s_k}(t) \\ \rho_{r_2}^{s_k}(t') \end{pmatrix} = - \begin{pmatrix} \rho_{r_1}^{s_1}(t) \\ \rho_{r_1}^{s_1}(t') \\ \vdots \\ \rho_{r_1}^{s_k}(t) \\ \rho_{r_1}^{s_k}(t') \\ \rho_{r_1}^{s_1}(t) \\ \rho_{r_1}^{s_1}(t') \\ \vdots \\ \rho_{r_1}^{s_k}(t) \\ \rho_{r_1}^{s_k}(t') \end{pmatrix} + c \cdot \begin{pmatrix} \Delta dt_{1,2}(t) \\ \Delta dt_{1,2}(t') \\ \vdots \\ \Delta dt_{1,2}(t) \\ \Delta dt_{1,2}(t') \\ \Delta dt_{1,2}(t) \\ \Delta dt_{1,2}(t') \\ \vdots \\ \Delta dt_{1,2}(t) \\ \Delta dt_{1,2}(t') \end{pmatrix} + \lambda \cdot \begin{pmatrix} 0 \\ 0 \\ \vdots \\ 0 \\ 0 \\ \Delta N_{1,2}^{s_1}(t) \\ \Delta N_{1,2}^{s_1}(t') \\ \vdots \\ \Delta N_{1,2}^{s_k}(t) \\ \Delta N_{1,2}^{s_k}(t') \end{pmatrix} + \Delta\tilde{\varepsilon}. \quad (3.88)$$

Equation (3.88) describes a set of Gaussian observations, whose values depend on $\boldsymbol{r}_1$ at instants t and t', on the difference of clock biases $\Delta dt_{1,2}$ at instants t and t', on the difference of ambiguities $\Delta N_{1,2}^{s_i}$ for all satellites at instants t and t', and on the distribution of $\Delta\tilde{\varepsilon}$.

An FGO representation of Equation (3.88) is visible in Figure 3.18.

As $\Delta\tilde{\varepsilon}$ is characterized as a centered Gaussian random vector with a diagonal covariance matrix, all of its components are independent. Therefore, from Chapter 2, each row of Equation (3.88) is associated to its own factor in the factor graph representation.

This document may not be reproduced, modified, adapted, published, translated in any way, in whole or in part, nor disclosed to a third party without the prior written consent of ENAC. © 2025, ENAC

What can be seen is that these two graphs are separated, so there is no temporal link between the two instants t and t' yet.

3.4.3 Construction of the TDCP

As explained in Section 2.4.1, a linear application can be applied to an FGO. In this case, it can be used to build the TDCP factors.
Considering the following matrix $\boldsymbol{D} \in \mathcal{M}_{3k,4k}(\mathbb{R})$

$$\boldsymbol{D} = \left(\begin{array}{c|ccccccccc} \boldsymbol{I}_{2k} & \multicolumn{8}{c}{\mathbf{0}} \\ \hline & -1 & 1 & 0 & 0 & & & & \\ & 0 & 0 & -1 & 1 & & & & \\ \mathbf{0} & & & & & \ddots & & & \\ & & & & & & -1 & 1 & 0 & 0 \\ & & & & & & 0 & 0 & -1 & 1 \end{array}\right). \tag{3.89}$$

Multiplying both sides of Equation (3.88) by $\boldsymbol{D}$ on the left leads to unmodified differences of code pseudorange observations and to the TDCP: the left hand side becomes

$$\boldsymbol{D}\left(\begin{pmatrix} \Delta\tilde{P}^{s_1}_{1,2}(t) \\ \Delta\tilde{P}^{s_1}_{1,2}(t') \\ \vdots \\ \Delta\tilde{P}^{s_k}_{1,2}(t) \\ \Delta\tilde{P}^{s_k}_{1,2}(t') \\ \Delta\tilde{\Phi}^{s_1}_{1,2}(t) \\ \Delta\tilde{\Phi}^{s_1}_{1,2}(t') \\ \vdots \\ \Delta\tilde{\Phi}^{s_k}_{1,2}(t) \\ \Delta\tilde{\Phi}^{s_k}_{1,2}(t') \end{pmatrix} - \begin{pmatrix} \rho^{s_1}_{r_2}(t) \\ \rho^{s_1}_{r_2}(t') \\ \vdots \\ \rho^{s_k}_{r_2}(t) \\ \rho^{s_k}_{r_2}(t') \\ \rho^{s_1}_{r_2}(t) \\ \rho^{s_1}_{r_2}(t') \\ \vdots \\ \rho^{s_k}_{r_2}(t) \\ \rho^{s_k}_{r_2}(t') \end{pmatrix}\right) = \begin{pmatrix} \Delta\tilde{P}^{s_1}_{1,2}(t) \\ \Delta\tilde{P}^{s_1}_{1,2}(t') \\ \vdots \\ \Delta\tilde{P}^{s_k}_{1,2}(t) \\ \Delta\tilde{P}^{s_k}_{1,2}(t') \\ \Delta\tilde{\Phi}^{s_1}_{1,2}(t') - \Delta\tilde{\Phi}^{s_1}_{1,2}(t) \\ \vdots \\ \Delta\tilde{\Phi}^{s_k}_{1,2}(t') - \Delta\tilde{\Phi}^{s_k}_{1,2}(t) \end{pmatrix} - \begin{pmatrix} \rho^{s_1}_{r_2}(t) \\ \rho^{s_1}_{r_2}(t') \\ \vdots \\ \rho^{s_k}_{r_2}(t) \\ \rho^{s_k}_{r_2}(t') \\ \rho^{s_1}_{r_2}(t') - \rho^{s_1}_{r_2}(t) \\ \vdots \\ \rho^{s_k}_{r_2}(t') - \rho^{s_k}_{r_2}(t) \end{pmatrix}, \tag{3.90}$$

the geometric term of the right hand side becomes

$$\boldsymbol{D}\begin{pmatrix} \rho^{s_1}_{r_1}(t) \\ \rho^{s_1}_{r_1}(t') \\ \vdots \\ \rho^{s_k}_{r_1}(t) \\ \rho^{s_k}_{r_1}(t') \\ \rho^{s_1}_{r_1}(t) \\ \rho^{s_1}_{r_1}(t') \\ \vdots \\ \rho^{s_k}_{r_1}(t) \\ \rho^{s_k}_{r_1}(t') \end{pmatrix} = \begin{pmatrix} \rho^{s_1}_{r_1}(t) \\ \rho^{s_1}_{r_1}(t') \\ \vdots \\ \rho^{s_k}_{r_1}(t) \\ \rho^{s_k}_{r_1}(t') \\ \rho^{s_1}_{r_1}(t') - \rho^{s_1}_{r_1}(t) \\ \vdots \\ \rho^{s_k}_{r_1}(t') - \rho^{s_k}_{r_1}(t) \end{pmatrix}, \tag{3.91}$$

the clock biases term of the right hand side becomes

$$\boldsymbol{D}\begin{pmatrix}\Delta dt_{1,2}(t)\\ \Delta dt_{1,2}(t')\\ \vdots\\ \Delta dt_{1,2}(t)\\ \Delta dt_{1,2}(t')\\ \Delta dt_{1,2}(t)\\ \Delta dt_{1,2}(t')\\ \vdots\\ \Delta dt_{1,2}(t)\\ \Delta dt_{1,2}(t')\end{pmatrix} = \begin{pmatrix}\Delta dt_{1,2}(t)\\ \Delta dt_{1,2}(t')\\ \vdots\\ \Delta dt_{1,2}(t)\\ \Delta dt_{1,2}(t')\\ \Delta dt_{1,2}(t') - \Delta dt_{1,2}(t)\\ \vdots\\ \Delta dt_{1,2}(t') - \Delta dt_{1,2}(t)\end{pmatrix} \tag{3.92}$$

and the ambiguity term of the right hand side becomes

$$\boldsymbol{D}\begin{pmatrix}0\\ 0\\ \vdots\\ 0\\ 0\\ \Delta N_{1,2}^{s_1}(t)\\ \Delta N_{1,2}^{s_1}(t')\\ \vdots\\ \Delta N_{1,2}^{s_k}(t)\\ \Delta N_{1,2}^{s_k}(t')\end{pmatrix} = \begin{pmatrix}0\\ 0\\ \vdots\\ 0\\ 0\\ \Delta N_{1,2}^{s_1}(t') - \Delta N_{1,2}^{s_1}(t)\\ \vdots\\ \Delta N_{1,2}^{s_k}(t') - \Delta N_{1,2}^{s_k}(t)\end{pmatrix}. \tag{3.93}$$

Assuming that the difference of integer ambiguities remains constant between the two instants t and t', i.e., $\forall i,\ \Delta N_{1,2}^{s_i}(t) = \Delta N_{1,2}^{s_i}(t')$, then the right hand side of Equation (3.93) is equal to the null vector.

As explained in Section 2.4.3, an application $\boldsymbol{G}$ that removes the ambiguities can be applied to the whole set of variables, leading to the state vector

$$\boldsymbol{\theta} = \begin{pmatrix}\boldsymbol{r}_1(t)\\ \Delta dt_{1,2}(t)\\ \boldsymbol{r}_1(t')\\ \Delta dt_{1,2}(t')\end{pmatrix} = \boldsymbol{G}\begin{pmatrix}\boldsymbol{r}_1(t)\\ \Delta dt_{1,2}(t)\\ \boldsymbol{r}_1(t')\\ \Delta dt_{1,2}(t')\\ \Delta N_{1,2}^{s_1}(t)\\ \Delta N_{1,2}^{s_1}(t')\\ \vdots\end{pmatrix}. \tag{3.94}$$

The matrix $\boldsymbol{G}$ has rank 8, the vector $\boldsymbol{\theta}$ does not include ambiguity terms. Therefore, these are no longer treated as variables in the FGO.

An FGO representation of $\boldsymbol{D}$ times Equation (3.88) without ambiguities is visible in Figure 3.19.

This document may not be reproduced, modified, adapted, published, translated in any way, in whole or in part, nor disclosed to a third party without the prior written consent of ENAC. © 2025, ENAC

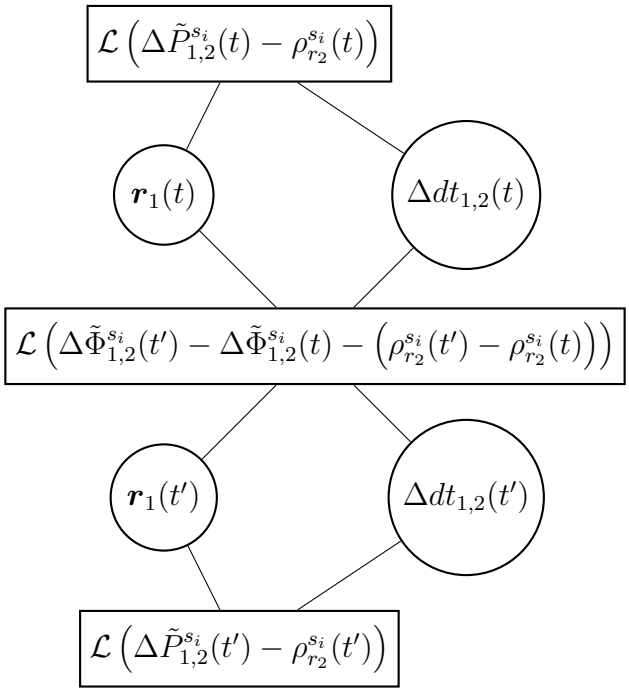

Figure 3.19: Representation of $\boldsymbol{D}$ times Equation (3.88) with a factor graph, considering a single satellite $\boldsymbol{s}_i$. To fully represent it, factors from other satellites have to be added.

Also, it can be checked that the random vector $\boldsymbol{D}\tilde{\boldsymbol{\varepsilon}}$ is Gaussian, with a diagonal covariance matrix. Therefore, from Chapter 2, each row of $\boldsymbol{D}$ times Equation (3.88) is associated to its own factor in the factor graph representation.

What can be seen is that now, the TDCP factors are functions of all variables at the two instants t and t', creating a link between them.

In the construction of this FGO, it is assumed that the right hand side of Equation (3.93) is null. In practice, since the ambiguity terms are integers, then the right hand side of Equation (3.93) is either null or is a vector made of integer values. In that case, this is due to a CS with a certain value that happened to one of the receivers between the instants t and t', and that did not happen to the other receiver. Therefore, the previously presented fault detection and identification methodology can be applied to the detection and identification of CS.

3.4.4 Positioning Error Analysis Using FGO

This section evaluates the positioning accuracy of FGO using both synthetic and real GNSS datasets collected continuously over the entire day of January 1, 2024, at a rate of 1 Hz, corresponding to 86 400 instants. For each pair of consecutive epochs, differences in code pseudorange and carrier-phase observations are computed from the real data. For the synthetic data, these differences are generated according to the error characterizations given by Equation (3.85) for the code pseudorange measurements and Equation (3.86) for the carrier-phase measurements. A corresponding FGO is constructed, as illustrated

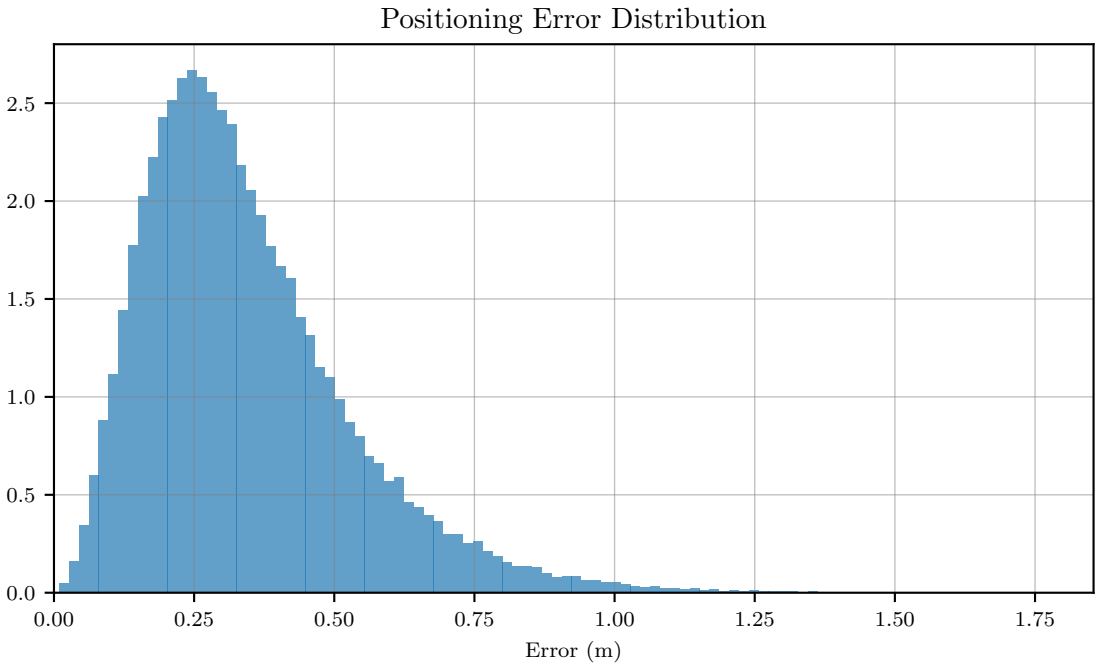

Figure 3.20: Histogram of the Euclidean norm of positioning errors obtained from **synthetic** data using FGO.

in Figure 3.19, and the resulting estimated positions are compared to the known TLSE coordinates to quantify the positioning error.

Both synthetic and real datasets are CS-free. For synthetic data, this is trivially ensured due to the controlled generation process. For real data, CS detection and correction is performed using RTKLIB forward-backward Kalman Filter (KF), using a full day of multi-constellation set of observations.

3.4.4.1 Evaluation on Synthetic Data

Figure 3.20 shows a histogram of the Euclidean norm of the positioning errors derived from synthetic data. Histograms of the horizontal and vertical components are shown in Figure 3.21, while Figure 3.22 shows a scatter plot of the horizontal errors across time or space.

3.4.4.2 Evaluation on Real Data

The same analysis is performed on real GNSS data. Figure 3.23 shows the Euclidean norm of the positioning errors. Horizontal and vertical error histograms are shown in Figure 3.24, and the corresponding scatter plot of horizontal positioning errors appears in Figure 3.25.

A comparison between synthetic and real datasets reveals that positioning errors are smaller and more tightly distributed in the synthetic case. This is expected, as syn-

This document may not be reproduced, modified, adapted, published, translated in any way, in whole or in part, nor disclosed to a third party without the prior written consent of ENAC. © 2025, ENAC

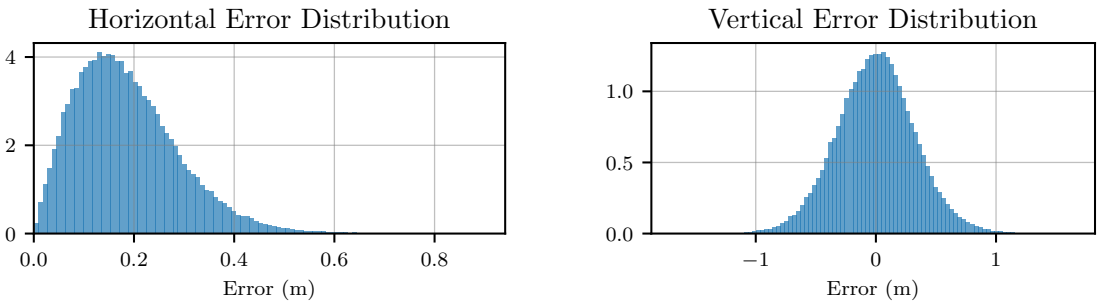

Figure 3.21: Histograms of the horizontal (left) and vertical (right) positioning errors from **synthetic** data.

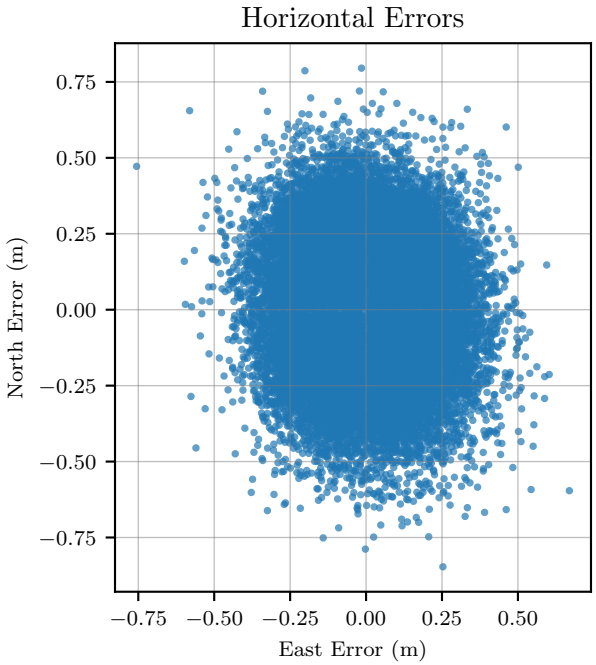

Figure 3.22: Scatter plot of horizontal positioning errors from **synthetic** data.

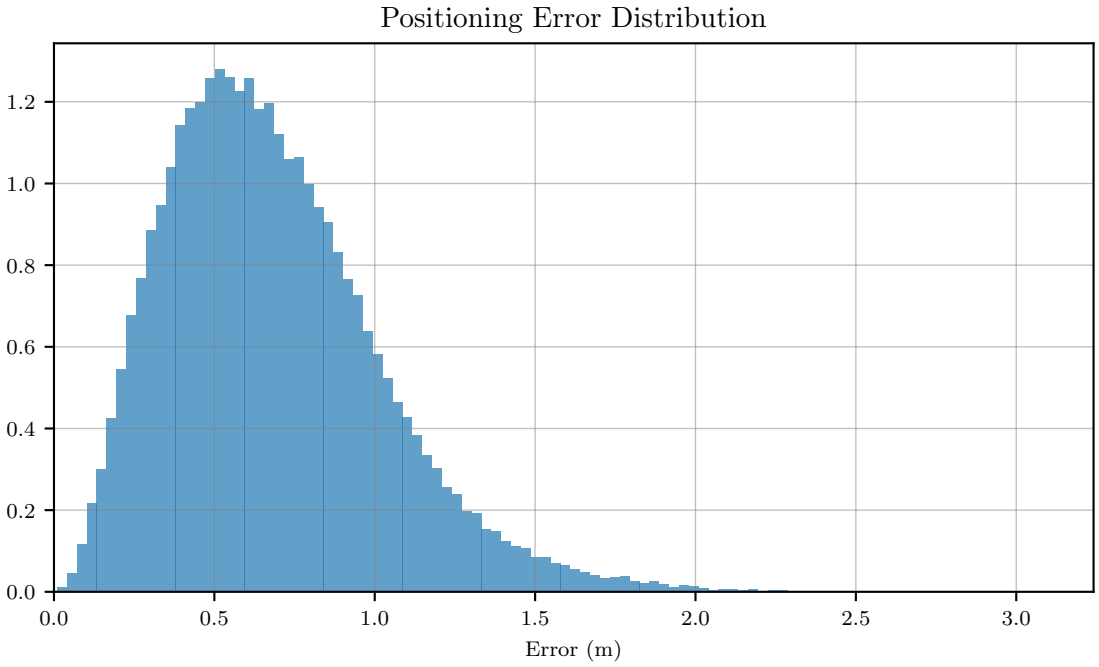

Figure 3.23: Histogram of the Euclidean norm of positioning errors obtained from **real** data using FGO.

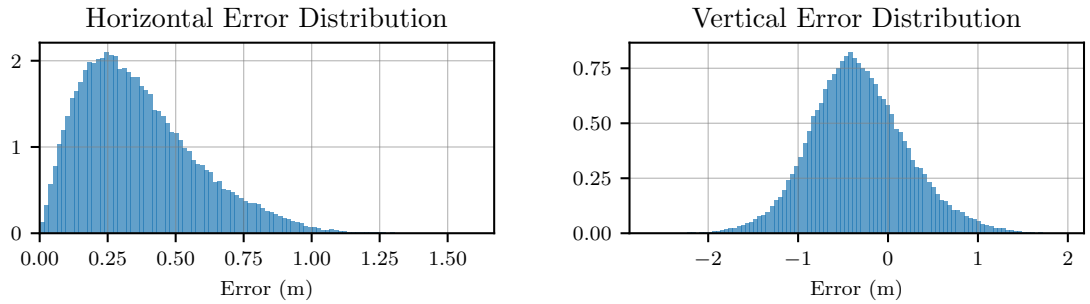

Figure 3.24: Histograms of the horizontal (left) and vertical (right) positioning errors from **real** data.

This document may not be reproduced, modified, adapted, published, translated in any way, in whole or in part, nor disclosed to a third party without the prior written consent of ENAC. © 2025, ENAC

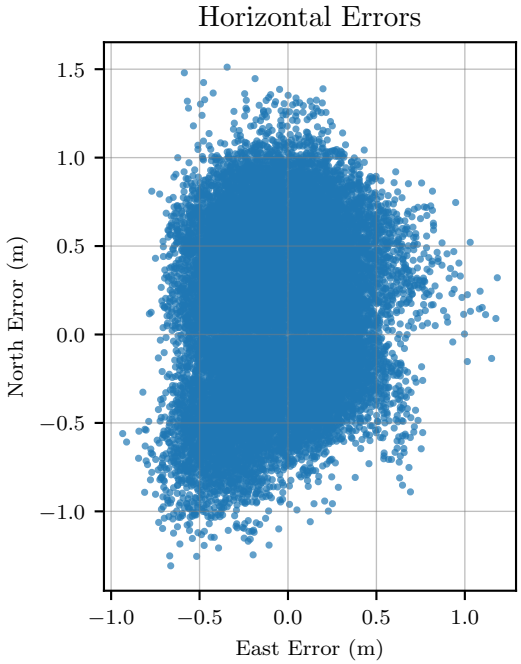

Figure 3.25: Scatter plot of horizontal positioning errors from **real** data.

thetic data is generated under ideal conditions with perfect modeling and no noise beyond what is explicitly introduced.

In contrast, the real dataset, despite being pre-processed to remove CS, still reflects the complexities and imperfections of real-world signal propagation, multipath effects, atmospheric delays, and receiver noise.

Nonetheless, the error distributions for real data remain reasonable and demonstrate the robustness of the FGO approach under both ideal and real conditions.

3.4.5 Cycle Slip Detection Using FGO Residuals

In addition to position estimation, the residuals of each factor graph can be leveraged for CS detection, as introduced earlier in this chapter. The core idea is that a significant increase in the residuals, particularly from carrier-phase measurements, may indicate a discontinuity in the integer ambiguities, i.e., a CS.

To assess the effectiveness of this detection method, artificial CS are introduced into both the generated and real datasets. Specifically, each factor graph (i.e., each pair of epochs) is assigned a 10% probability of containing a CS. To stay aligned with the assumptions used in the theoretical derivation of the detection test, only one CS is introduced per affected graph, and the ambiguity change is fixed to 1 cycle, corresponding to a change in the difference of carrier-phase observations equal to one carrier wavelength.

The detector operates under a predefined false alarm probability of $\alpha = 0.1$.

Table 3.3: Confusion matrix of the CS detection test using **synthetic** data. A 10% of single CS injection rate is applied, with an amplitude of 1, and the decision threshold set such that the false alarm probability equals to 0.1.

Truth \ Decision	$\mathcal{H}_0$ (No CS detected)	$\mathcal{H}_1$ (CS detected)
$\mathcal{H}_0$ (No CS)	0.811	0.089
$\mathcal{H}_1$ (CS present)	0.086	0.012

Table 3.4: Confusion matrix of the CS detection test using **real** data with artificially injected CS.

Truth \ Decision	$\mathcal{H}_0$ (No CS detected)	$\mathcal{H}_1$ (CS detected)
$\mathcal{H}_0$ (No CS)	0.733	0.168
$\mathcal{H}_1$ (CS present)	0.079	0.020

3.4.5.1 Evaluation on Synthetic Data

The confusion matrix Table 3.3 summarizes the performance of the CS detector on synthetic data, with a single CS happening in 10% of the graphs of value 1, with a false alarm probability set to $\alpha = 0.1$. The empirical value of the probability of false alarm is equal to $0.089/(0.811 + 0.089) \approx 0.1$, while the probability of missed detection is equal to $0.086/(0.012 + 0.086) \approx 0.88$. It is important to note that the analysis is based on single-constellation, single-frequency observations, with injected CS of amplitude equal to 1, introducing a bias of one wavelength. This wavelength is not significantly larger than the standard deviation of the noise, which is generated according to Equation (3.86).

3.4.5.2 Evaluation on Real Data

A similar confusion matrix in Table 3.4 is obtained using real GNSS data. As with positioning errors, CS are first mitigated using RTKLIB, which applies forward-backward Kalman smoothing with multi-constellation data to detect and correct CS. To evaluate the detector, artificial CS of 1 cycle are injected into the dataset. These injected CS serve as the ground truth for assessing detection performance.

These results allow an empirical evaluation of the false alarm rate of the residual-based detector under realistic and ideal conditions. The empirical value of the probability of false alarm is equal to $0.168/(0.733 + 0.168) \approx 0.19$, while the probability of missed detection is equal to $0.079/(0.079 + 0.020) \approx 0.80$. Again, it is important to note that the analysis is based on single-constellation, single-frequency observations, with injected CS of amplitude equal to one, introducing a bias of one wavelength.

This document may not be reproduced, modified, adapted, published, translated in any way, in whole or in part, nor disclosed to a third party without the prior written consent of ENAC. © 2025, ENAC

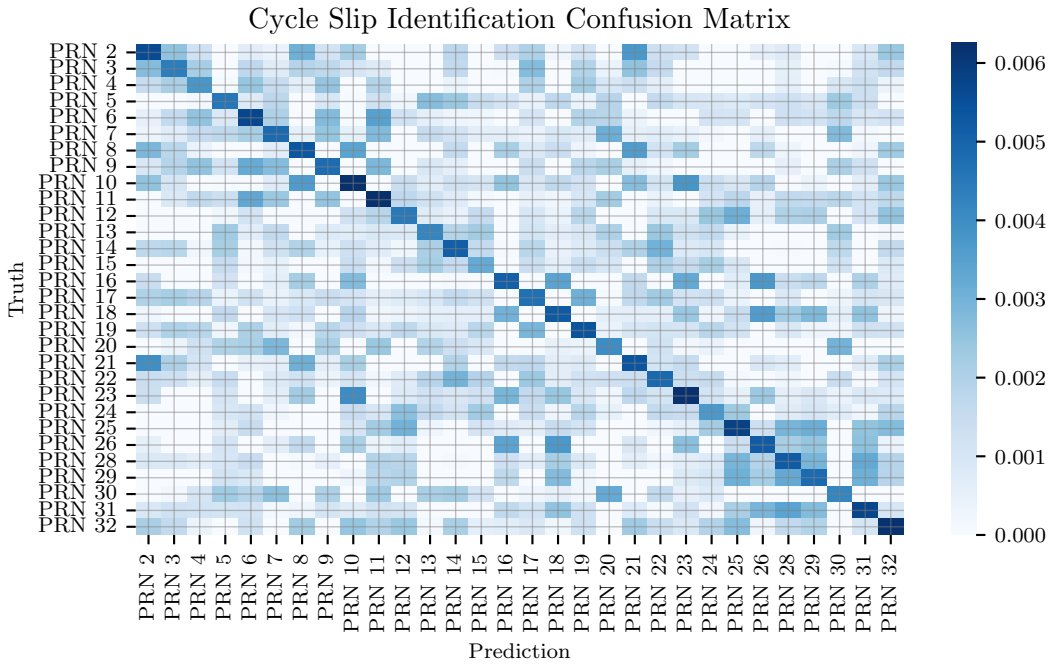

Figure 3.26: Confusion matrix for CS identification using **synthetic** data. Each row corresponds the true PRN affected by the CS, and each column to the PRN identified by the algorithm.

3.4.6 Cycle Slip Identification Using FGO Residuals

To evaluate the performance of the developed CS identification method, both synthetic and real GNSS datasets are used. In contrast to detection, where CS may or may not be present, here, every factor graph contains exactly one CS of magnitude 1 cycle, corresponding to a change in the difference of integer ambiguities of 1.

Prior to the experiment, the real dataset is ensured to be free of CS by following the same approach described in the detection section. Then, in both the synthetic and real datasets, a single artificial CS of value 1 is injected into each factor graph, affecting one visible satellite chosen randomly. The goal of the identification algorithm is to correctly determine which satellite experienced the CS, so that its carrier-phase observations can be excluded from the estimation process, ultimately leading to improved positioning accuracy.

3.4.6.1 Evaluation on Synthetic Data

For synthetic data, where modeling and noise characteristics are ideal, the identification performance is evaluated using a confusion matrix, as defined in Table 3.2, that treats each satellite as a distinct hypothesis.

The results of the identification are visible in Figure 3.26.

The confusion matrix obtained from synthetic data reflects the performance of the CS identification test across all PRNs. While the matrix reveals patterns of confusion between

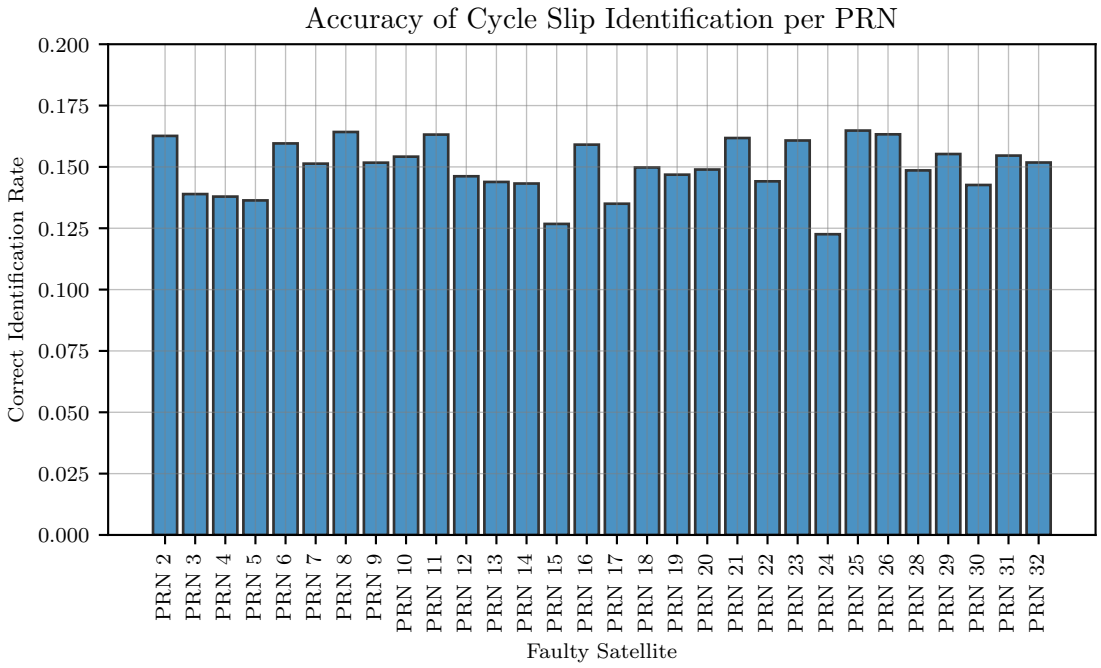

Figure 3.27: Correct identification rate per PRN using **synthetic** data. Each bar represents the proportion of correct identifications for a given PRN, computed as the number of correct identifications divided by the total number of identification decisions for that PRN.

certain satellites, interpreting these results is not straightforward. The satellite-receiver geometry, which influences identification performance, varies continuously throughout the day, making it difficult to attribute confusion to specific geometric configurations. Furthermore, when a cell in the matrix is zero, it can indicate two distinct situations: either the corresponding satellites are never confused, suggesting high quality identification, or the two satellites are never simultaneously visible, meaning no opportunity for confusion. As such, the structure of the confusion matrix must be analyzed with care, taking into account both the stochastic nature of the simulation and the dynamic observation conditions.

To further analyze the identification performance, the proportion of correct identifications is computed individually for each satellite. It provides a clearer, more interpretable view of how reliably the algorithm identifies CS for each PRN. The resulting values are shown in Figure 3.27, highlighting variations in detection performance across satellites.

The values are all roughly centered around 0.15, which may appear low. However, it is important to recall that this experiment is conducted under challenging conditions: single-constellation, single-frequency observations, and a CS amplitude of 1, corresponding to a bias of one wavelength, which is small relative to the standard deviation of the measurement noise, as characterized in Equation (3.86).

This document may not be reproduced, modified, adapted, published, translated in any way, in whole or in part, nor disclosed to a third party without the prior written consent of ENAC. © 2025, ENAC

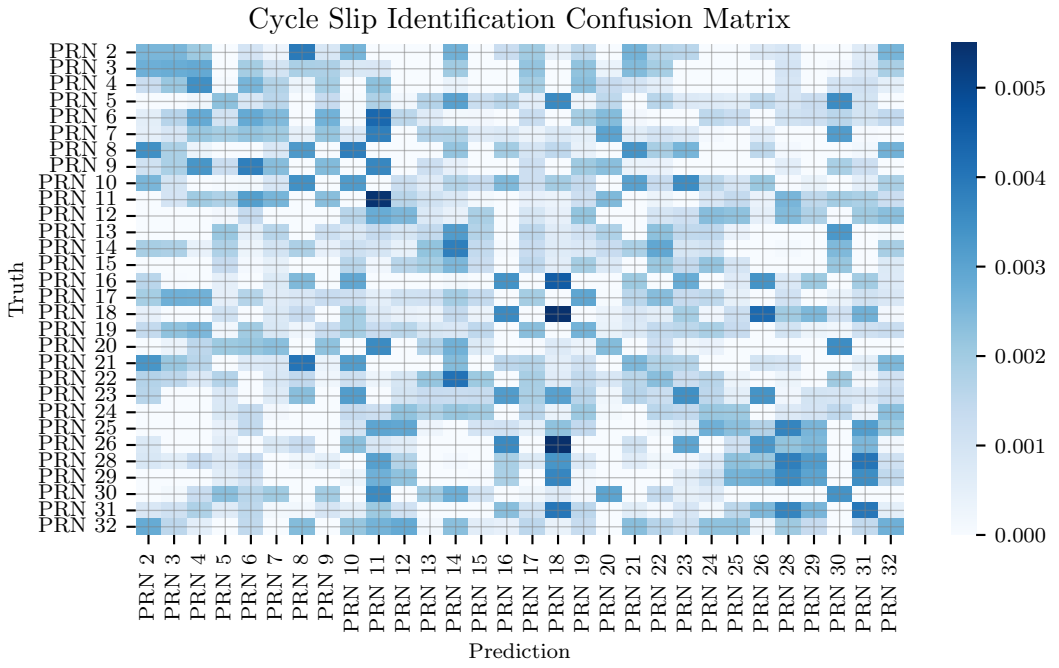

Figure 3.28: Confusion matrix for CS identification using **real** data. Each row corresponds to the true PRN affected by the CS, and each column to the PRN identified by the algorithm.

3.4.6.2 Evaluation on Real Data

A similar experiment is conducted on real GNSS data. Again, the dataset is preprocessed to ensure it is free of CS, and a single CS of value 1 is introduced in each graph. The same identification procedure is applied, and the results are summarized in the confusion matrix in Figure 3.28.

As with synthetic data, interpreting the confusion matrix derived from real data remains challenging due to the constantly changing satellite geometry throughout the day. A zero in the confusion matrix may indicate either a perfect distinction between satellites or simply the absence of simultaneous visibility, which prevents confusion altogether. Per-satellite identification performance is shown in Figure 3.29, revealing lower overall accuracy compared to the synthetic case, with more pronounced variations in identification performance across satellites.

In the confusion matrix shown in Figure 3.28, satellites G18 and G26 are frequently confused with each other. To better understand this, their geometry is analyzed.

Figure 3.30 displays the skyplot for these two satellites during the period when they are both simultaneously visible, from 15:00 to midnight. While their trajectories start at different azimuth angles, their elevations remain quite similar throughout their trajectory, as illustrated in Figure 3.31. This similarity in elevation likely contributes to the frequent confusion between these satellites.

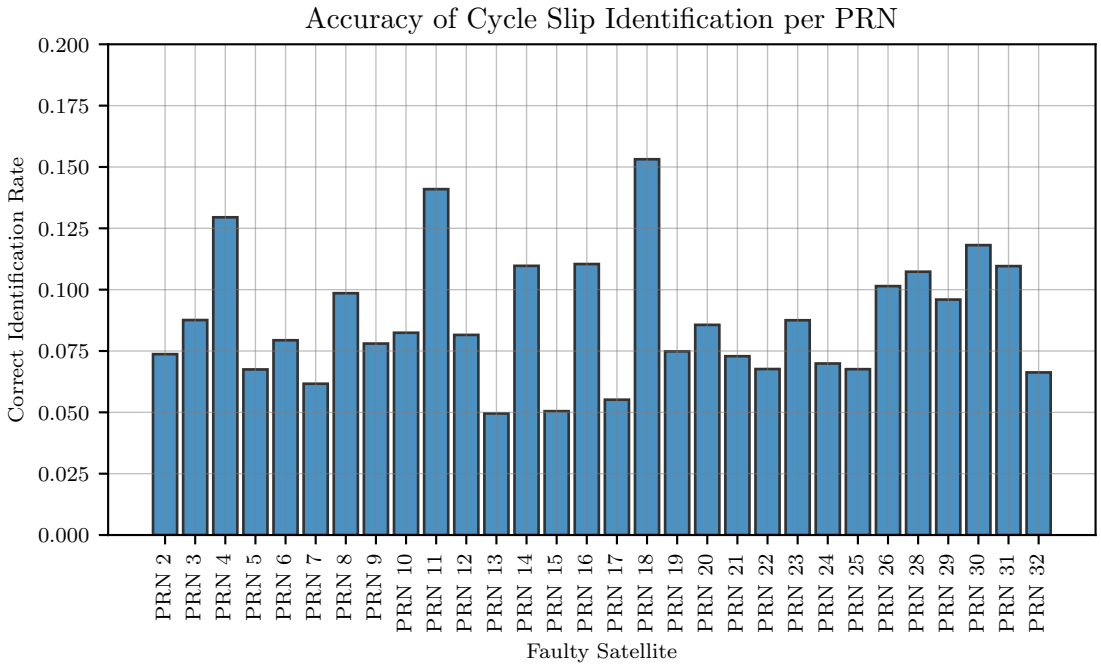

Figure 3.29: Correct identification rate per PRN using **real** data. Each bar represents the proportion of correct identifications for a given PRN, computed as the number of correct identifications divided by the total number of identification decisions for that PRN.

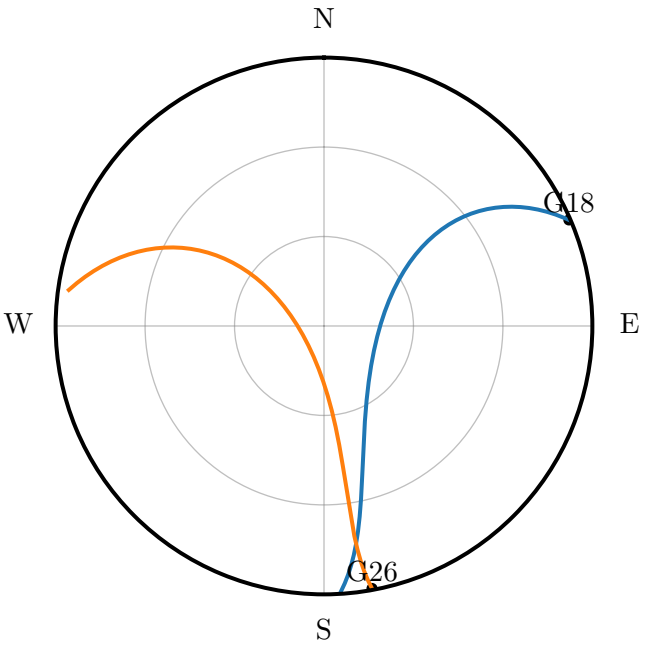

Figure 3.30: Skyplot showing the trajectories of satellites G18 and G26 observed between 15:00 and midnight at the receiver location.

This document may not be reproduced, modified, adapted, published, translated in any way, in whole or in part, nor disclosed to a third party without the prior written consent of ENAC. © 2025, ENAC

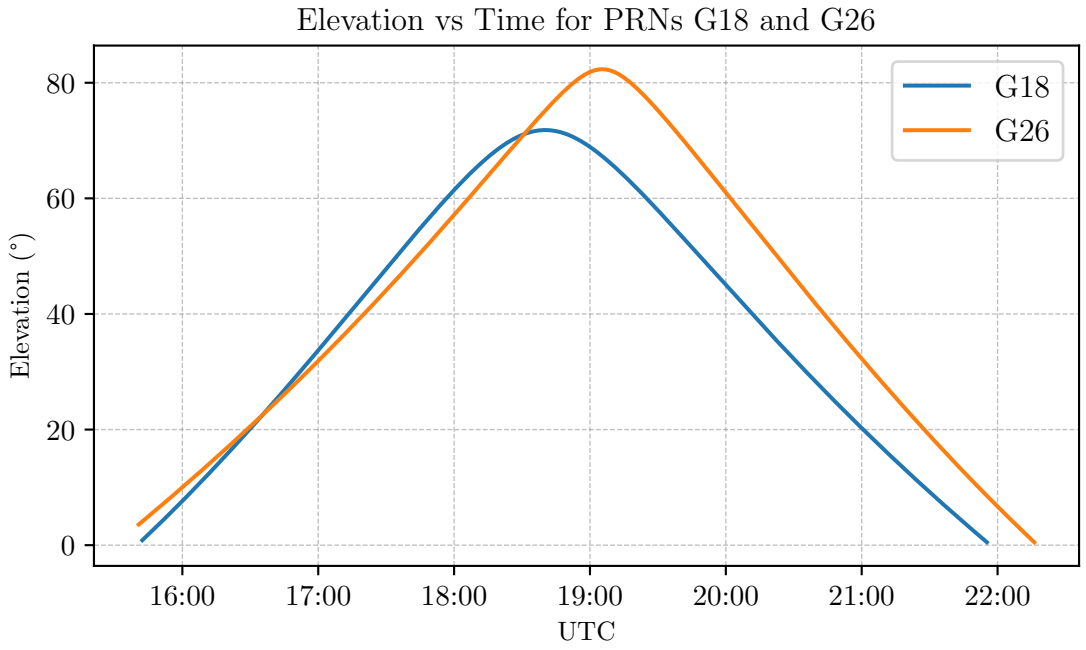

Figure 3.31: Elevation angle over time for satellites G18 and G26, during the period of their simultaneous visibility.

3.5 FGO-based Multiple Cycle Slip Detection and Identification

In practical GNSS positioning scenarios, the number of occurring CS is generally unknown. While the present work assumes the presence of at most one CS per factor graph, real-world conditions may involve multiple CS, either simultaneous or closely spaced in time. Addressing this complexity is essential for extending the applicability of the proposed detection and identification framework.

A naive extension to handle multiple CS is to repeat the detection-identification procedure iteratively. However, this approach lacks theoretical guarantees. Specifically, the combined effect of two or more CS may, in some configurations, lead to a residual increase smaller than that caused by a single CS. As a result, these multi-CS scenarios could reduce detection capabilities.

A more principled solution involves redefining the set $\mathcal{A}$ of admissible faults. Previously, $\mathcal{A}$ consisted of sparse vectors with a single non-zero integer element, corresponding to a single fault (i.e., one CS). To account for the possibility of multiple CS, $\mathcal{A}$ can be expanded to include vectors with multiple non-zero integer components, each representing a CS on a different satellite. This extended model enables cleaner detection and identification, with formal guarantees on the probability of detection.

However, this approach still implicitly relies on prior knowledge of the maximum number of faults. For instance, if $\mathcal{A}$ includes only up to two simultaneous CS, a scenario with three

or more CS does not provides guarantees on probability of detection. Therefore, a more robust strategy is needed: one that does not depend on the number of assumed faults.

Future research should explore detection frameworks that are agnostic to the number of CS. This could involve probabilistic or adaptive methods capable of dynamically inferring both the occurrence and multiplicity of faults.

3.6 Conclusion

This chapter introduces an approach for single CS detection and identification in GNSS carrier-phase observations using the FGO framework. The detection process leverages the statistical properties of the FGO residuals with a hypothesis testing framework using the Neyman-Pearson lemma. By modeling the fault as an integer ambiguity jump, the methodology is tailored to the nature of GNSS carrier-phase CS.

An identification procedure is also developed to determine the exact satellite affected by the fault. The identification method relies on a multiple hypothesis testing strategy, evaluating candidate fault models using residual-based likelihoods. The decision process selects the most likely hypothesis and enables targeted correction of the faulty observation, improving overall positioning robustness.

Empirical evaluations on both synthetic and real data demonstrate the effectiveness of the proposed methods. While synthetic data provides a clean, controlled validation scenario, real GNSS datasets from TLSE and TLSG stations offer a realistic test with complex measurement noise and environmental effects.

Nonetheless, one significant limitation remains: the assumption that only a single CS occurs per graph. In real-world conditions, the number of CS is unknown, and multiple CS can occur simultaneously. A naive iterative application of the single-fault procedure lacks guarantees and can fail in certain cases. A more robust alternative involves redefining the set of considered faults $\mathcal{A}$ to include vectors with multiple non-zero entries, though this again assumes a known maximum number of faults.

A future work can focus on developing a fault detection and identification framework that does not rely on prior knowledge of the number of CS by means of techniques capable of handling variable fault cardinality.

This chapter is supported by the following peer-reviewed conference paper

[8] H. Cherfi, J. Lesouple, J. Solà, and P. Thevenon, “Single Frequency GNSS Carrier Phase Cycle Slip Detection and Identification Using a Factor Graph Approach,” in *Proc. ION Pacific PNT 2024*, (Honolulu, HI, USA), pp. 344 – 355, Apr. 2024.

Now that an FGO-based method is proposed to detect and identify CS in carrier-phase observations, TDCP observations can be constructed with greater reliability. The next chapter focuses on TDCP, outlining its role and applications in the GNSS literature.

This document may not be reproduced, modified, adapted, published, translated in any way, in whole or in part, nor disclosed to a third party without the prior written consent of ENAC. © 2025, ENAC

Chapter 4

Uncertainty Quantifiation of TDCP Factor for Displacement Estimation in an FGO

Odometry is a fundamental technique used in robotics, autonomous vehicles, and geospatial applications for estimating the change in position of a moving system. It relies on sensors or data from systems like wheel encoders, Inertial Measurement Unit (IMU), vision sensors, lasers, or Global Navigation Satellite System (GNSS) to measure the motion of a vehicle or object. GNSS-based odometry has become an essential tool for achieving precise and reliable positioning and displacement estimation over long distances.

As stated in Chapter 1, one of the most precise GNSS observations is the carrier-phase. It is particularly valuable because it provides much higher accuracy compared to code pseudorange observations, making it ideal for precise positioning and odometry. However, this observation is ambiguous, the ambiguity being the integer number of wavelengths traveled by the signal. As done in Chapter 3, one way to get rid of this ambiguity, assuming no Cycle Slip (CS), is to use the subtraction of two consecutive carrier-phase observations and form the Time-Differenced Carrier Phase (TDCP) observation.

Although inherently a function of a receiver coordinates at two instants, the TDCP model can be formulated in a restricted form by assuming one of the positions to be known. In that case, the TDCP model, in its restricted form, i.e., when the receiver's position at one instant is assumed to be known, becomes a function of the other position, or equivalently, of the receiver's displacement. However, this assumed position is never perfectly accurate in practice, and any error in this reference position can propagate into the estimated displacement.

This chapter investigates the consequences of using an inaccurate reference position in the restricted TDCP model. Specifically, it aims to assess the impact of such inaccuracies on displacement estimation. This analysis is crucial for understanding potential error margins and for ensuring the robustness of GNSS-based odometry in real-world applications, even in the presence of position uncertainties.

This document may not be reproduced, modified, adapted, published, translated in any way, in whole or in part, nor disclosed to a third party without the prior written consent of ENAC. © 2025, ENAC

To isolate and quantify model-induced errors, synthetic data is used throughout the chapter, ensuring full control over the observations and elimination of measurement noise and CS.

Most of the results presented in this chapter have been published in a peer-reviewed journal article [70]. This publication contains a detailed exposition of the methodology and findings, and serves as a foundation for the analyses discussed in the following sections.

4.1 Review of TDCP Models

The following section presents a review of models commonly used in the literature for TDCP processing. These models vary in their assumptions regarding the receiver position and the formulation of the geometric component of the TDCP observable. Particular attention is given to how each model handles or approximates the receiver motion and the role of prior information, such as known receiver positions.

Using a GNSS receiver, a system could estimate its velocity vector at a given instant by means of Doppler observations. Once integrated, these speeds provide an estimation of the system's displacement. It is known that the Doppler observations, when integrated, are noisier than carrier-phase observations, though not sensitive to cycle slip [71]. For this reason, it is interesting to estimate a receiver displacement between two instants by means of TDCP.

In [72], the authors assume perfectly known receiver position at the first instant and use this information to run a Kalman Filter (KF) with TDCP and subtracted TDCP observations between satellites, along with a cycle slip detector. The source of first position is not specified in the experiments. Also, the receiver to satellite unit vectors at the two instants are known. To assess potential cycle slips, the cycle slip detector first generates a set of valid solutions (from a previous estimate, integrated IMU measurements and IMU specifications), and checks if the TDCP solution is within that set.

In [72, 73], the authors build subtracted TDCP, i.e., the subtraction of TDCP between two different satellites, in order to remove the receiver clock bias difference. The subtraction is done with the satellite with highest elevation, as the receiver most likely receives a direct signal from this one. Still, to estimate the receiver displacement with these subtracted TDCP, the authors assume known receiver to satellite vectors and receiver position at first instant of subtracted TDCP.

Some authors go further in the approximations of the TDCP model. In [74, 75], the receiver to satellite unit vectors are assumed constant at the two TDCP instants, leading to a unique receiver to satellite vector. It should be noted that this approximation requires the knowledge of the receiver position. Then, the receiver and satellite displacement vectors are projected onto this vector thanks to a scalar product. This makes the TDCP a linear model of the receiver displacement.

The same approximation is made in [71, 76], where the author explains that the TDCP

model is linearized around the estimated position at previous instant. Also, the authors build the single difference of carrier phase observations between satellites and between instants.

In [77], a similar TDCP model is built, with a time between the two instants ranging from 1 s up to 60 s. Regarding the geometric part, the model includes two terms, the first one being a change of range between the satellite and the receiver, which requires the receiver position, and a second term where the estimated receiver displacement vector is projected onto the unit line-of-sight vector at the second instant, which also requires the receiver position to be known. Also, a single line-of-sight vector is considered, even if the time of interval is of 60 s. This TDCP model is used to build a TDCP factor inside a Factor Graph Optimization (FGO) problem. At the first instant, a first position is set from a prior factor, and for other instants, the first position is set from previous nodes. It should be noted that cycle slip factors are used to handle cycle slips.

In [78], the geometric part of the TDCP model is split into three terms, the first one due to the satellite motion along the line-of-sight, a second term that contains the receiver position at the first instant, and the last term is a linear term of the receiver displacement and of the line-of-sight vector at the second instant. All these terms require the knowledge of the receiver coordinates at the two instants.

In [79], the authors leave the TDCP model as a function of the two receiver positions. The TDCP are used in a factor of a factor graph optimization problem, where relative displacement factors from preintegrated inertial measurements are used. In the experimental part of their work, their proposed method outperforms two filtering methods that also use TDCP observations. This is likely due to a prior factor that sets the receiver position at the first instant, although no details are given regarding this assumption.

Overall, within the GNSS community, many approximations of the TDCP model are proposed, which all assume that the receiver's coordinates are known at a given instant in order to estimate a displacement.

The following sections focus on quantifying the impact of an incorrect initial position on the estimation of displacement. This analysis contributes to the Uncertainty Quantification (UQ) of TDCP-based positioning by evaluating how sensitive the estimated displacement is to errors in the assumed initial receiver coordinates.

4.2 Temporal Difference of Carrier-Phase Observations

This section provides a detailed formulation of the TDCP observation model. It begins by introducing the carrier-phase observation and its correction. Then, the construction of the TDCP is presented as the difference between two carrier-phase measurements acquired at successive instants. Building on this foundation, the model is subsequently restricted to express the TDCP as a function of the receiver coordinates at a single instant.

At a given instant, given a Global Positioning System (GPS) receiver of unknown coor-

This document may not be reproduced, modified, adapted, published, translated in any way, in whole or in part, nor disclosed to a third party without the prior written consent of ENAC. © 2025, ENAC

dinates $\boldsymbol{r} \in \mathbb{R}^3$ and a satellite of known coordinates $\boldsymbol{s}_i \in \mathbb{R}^3$, as in Equation (3.69), the corrected carrier-phase observations are modeled as

$$\tilde{\Phi}_r^{s_i} = \rho_r^{s_i} + c \cdot dt_r + \lambda \cdot N_r^{s_i} + \tilde{\varepsilon}_\Phi^{s_i}, \tag{4.1}$$

where the terms are defined as follows (all quantities are expressed in meters unless stated otherwise)

- $\tilde{\Phi}_r^{s_i}$ is the corrected carrier-phase measurement to satellite i,
- $\rho_r^{s_i} = \|\boldsymbol{r} - \boldsymbol{s}_i\|$ is the range between the receiver and the emitting satellite,
- dt_r refers to the receiver clock bias (with respect to the constellation time coordinates system), in seconds,
- λ refers to the carrier's wavelength,
- $N_r^{s_i}$ refers to the integer number of cycles between the receiver and the satellite and is unitless,
- $\tilde{\varepsilon}_\Phi^{s_i}$ is a random variable that corresponds to the sum of the carrier-phase error and of correction errors.

In this chapter, the symbol Δ indicates the temporal difference of a quantity, i.e., for some quantity a at two instants t and t',

$$\Delta a \triangleq a(t') - a(t). \tag{4.2}$$

while δ indicates the difference of an assumption and a truth, i.e., for an assumption $\widehat{a}$ of a,

$$\delta a \triangleq \widehat{a} - a. \tag{4.3}$$

Considering the corrected carrier-phase observations between the receiver and a satellite as in Equation (4.1) at two instants t and t', their difference is given by

$$\Delta\tilde{\Phi}_r^{s_i} = \Delta\rho_r^{s_i} + c \cdot \Delta dt_r + \lambda \cdot \Delta N_r^{s_i} + \Delta\tilde{\varepsilon}_\Phi^{s_i}. \tag{4.4}$$

In Equation (4.4), the term $\Delta N_r^{s_i}$ corresponds to the difference of carrier-phase integer ambiguities between the two instants. Under nominal conditions (i.e., when the carrier-phase tracking is continuous and uninterrupted), this difference is equal to zero. However, if a CS occurs between the two instants t and t', this difference becomes nonzero and introduces an unknown bias in the observation.

A method for detecting CS is presented in Chapter 3. Alternatively, any other CS detection method available in the literature may be employed.

In the remainder of this work, the difference $\Delta N_r^{s_i}$ is assumed to be zero, reflecting the absence of CS between the two instants. Under this assumption, the observation model

can be simplified accordingly. In particular, Section 2.4.2 describes how this assumption enables a restriction of the observation model.

Assuming that the random variable $\Delta\tilde{\varepsilon}_{\Phi}^{s_i}$ is such that

$$\Delta\tilde{\varepsilon}_{\Phi}^{s_i} \sim \mathcal{N}(0, \sigma^2_{\text{TDCP}}) \tag{4.5}$$

it comes

$$\Delta\tilde{\Phi}_r^{s_i} \sim \mathcal{N}\left(h_i\left(\boldsymbol{\theta}\right), \sigma^2_{\text{TDCP}}\right) \tag{4.6}$$

where

$$\boldsymbol{\theta} = \left(\boldsymbol{r}(t)^{\mathsf{T}}\ dt_r(t)\ \boldsymbol{r}(t')^{\mathsf{T}}\ dt_r(t')\right)^{\mathsf{T}} \in \mathbb{R}^8 \tag{4.7}$$

is the unknown vector to estimate and

$$h_i : (\boldsymbol{r}(t),\ dt_r(t),\ \boldsymbol{r}(t'),\ dt_r(t')) \mapsto \|\boldsymbol{r}(t') - \boldsymbol{s}_i(t')\| - \|\boldsymbol{r}(t) - \boldsymbol{s}_i(t)\| + c \cdot (dt_r(t') - dt_r(t))\,. \tag{4.8}$$

Therefore, $\Delta\Phi_r^{s_i}$ is a Gaussian random variable, with a mean value that depends on the unknowns $\boldsymbol{r}(t)$, $\boldsymbol{r}(t')$, $dt_r(t)$ and $dt_r(t')$. The likelihood function given $\Delta\tilde{\Phi}_r^{s_i}$ is defined as

$$\begin{aligned}\mathcal{L}(\Delta\tilde{\Phi}_r^{s_i}) : \Theta \subseteq \mathbb{R}^8 &\to \mathbb{R}^+ \\ \boldsymbol{\theta} &\mapsto \frac{1}{\sqrt{2\pi\sigma^2_{\text{TDCP}}}} \exp\left(-\frac{1}{2\sigma^2_{\text{TDCP}}}\left(\Delta\tilde{\Phi}_r^{s_i} - h_i(\boldsymbol{\theta})\right)^2\right),\end{aligned} \tag{4.9}$$

where h_i is as in Equation (4.8). The FGO representation of Equation (4.9) is visible in Figure 4.1. By combining observations from multiple satellites, an FGO can be built to estimate the receiver coordinates and clock bias at the two instants t and t'.

Written this way, Equation (4.9) is a function of the receiver coordinates $\boldsymbol{r}(t)$ and $\boldsymbol{r}(t')$ and the receiver clock biases $dt_r(t)$ and $dt_r(t')$. While the use of multiple TDCP observations from other satellites (at least 8) with a similar model would still permit to estimate all these quantities, depending on the change of geometry between the two instants t and t', the obtained result would be highly sensitive to noise. This is due to the fact that between two instants, the receiver to satellite unit vectors would not change much, hence a Jacobian matrix, as defined in Equation (2.41), with nearly linearly dependent columns. As a consequence, the matrix becomes ill-conditioned, as discussed in Section 2.2.3, making the linearized system highly sensitive to measurement noise. This point discourages a user to estimate all these quantities directly using TDCP observations only, unless considering a very large time interval between the two considered instants.

4.3 Restriction of the TDCP Model

The model introduced in Equation (4.8) involves eight unknowns: the three-dimensional receiver positions at instants t and t', and the receiver clock biases at these instants. As discussed previously, estimating all these variables simultaneously from TDCP observa-

This document may not be reproduced, modified, adapted, published, translated in any way, in whole or in part, nor disclosed to a third party without the prior written consent of ENAC. © 2025, ENAC

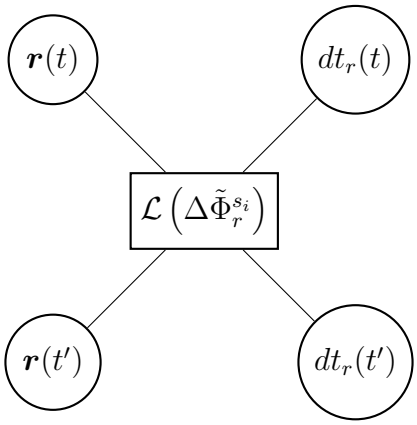

Figure 4.1: Factor graph representation of the TDCP observation model given in Equation (4.9) for a single satellite of coordinates $\boldsymbol{s}_i$. The factor node encodes the likelihood of the difference of corrected carrier-phase observations between two instants t and t' as a function of the receiver's positions and clock biases at these instants. To fully represent the model, similar factors must be added for each additional satellite.

tions only may lead to an ill-conditioned problem, due to limited change of geometry between t and t'.

4.3.1 Correct TDCP Model

In the GNSS community, the TDCP model is most commonly expressed as a function of the receiver displacement between the two instants and the receiver clock bias difference. To achieve this, a new formulation of the model is adopted in which the receiver position at the first instant t is assumed to be known. This assumption corresponds to a restriction of the original model, as described in Section 2.4.2. It allows to write the model as a function of two variables, as described in Section 2.4.3, which are the receiver displacement vector $\Delta\boldsymbol{r} = \boldsymbol{r}(t') - \boldsymbol{r}(t)$ and the clock bias difference $\Delta dt_r = dt_r(t') - dt_r(t)$. This assumption is justified in practical scenarios where a prior position fix is available from other sensors or previous estimates.

Instead of estimating the positions and clock biases at both instants, the model is now parametrized in terms of the receiver displacement $\Delta\boldsymbol{r}$ and the clock bias difference Δdt_r, i.e., Equation (4.7) becomes

$$\boldsymbol{\theta} = \left(\Delta\boldsymbol{r}^\mathsf{T}\ \Delta dt_r\right)^\mathsf{T} \in \mathbb{R}^4, \tag{4.10}$$

Equation (4.8) becomes a function of a reduced parameter vector

$$h_{\boldsymbol{r}(t),i} : (\Delta\boldsymbol{r},\ \Delta dt_r) \mapsto \left\|\boldsymbol{r}(t) + \Delta\boldsymbol{r} - \boldsymbol{s}_i(t')\right\| - \left\|\boldsymbol{r}(t) - \boldsymbol{s}_i(t)\right\| + c \cdot \Delta dt_r \tag{4.11}$$

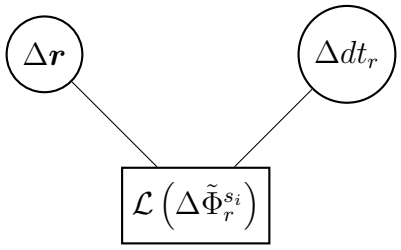

Figure 4.2: Factor graph representation of the TDCP observation model given in Equation (4.12), with fixed receiver coordinates $\boldsymbol{r}(t)$. The parameter $\boldsymbol{r}(t)$ is **known** and not estimated. This reduces the number of unknowns and improves the conditioning of the estimation problem.

and Equation (4.9) becomes

$$\mathcal{L}(\Delta\tilde{\Phi}_r^{s_i}) : \Theta \subseteq \mathbb{R}^4 \to \mathbb{R}^+$$
$$\boldsymbol{\theta} \mapsto \frac{1}{\sqrt{2\pi\sigma^2_{\text{TDCP}}}} \exp\left(-\frac{1}{2\sigma^2_{\text{TDCP}}}\left(\Delta\tilde{\Phi}_r^{s_i} - h_{\boldsymbol{r}(t),i}(\boldsymbol{\theta})\right)^2\right) \tag{4.12}$$

where $h_{\boldsymbol{r}(t),i}$ is as in Equation (4.11). The FGO representation of Equation (4.12) is visible in Figure 4.2. This restriction improves the conditioning of the estimation problem. By combining observations from multiple satellites, an FGO can be built to estimate the receiver displacement $\Delta\boldsymbol{r}$ and clock bias difference Δdt_r.

This restricted model is widely adopted in the literature and forms the basis of several methods for TDCP-based displacement estimation.

4.3.2 Assumed TDCP Model

The model $h_{\boldsymbol{r}(t),i}$ in Equation (4.11) assumes perfect knowledge of the true receiver coordinates $\boldsymbol{r}(t) \in \mathbb{R}^3$. In practice, these coordinates can be inaccurate. Given an assumed value $\widehat{\boldsymbol{r}}(t)$ of the initial position $\boldsymbol{r}(t)$, the error between the true coordinates and the assumed ones is defined as

$$\delta\boldsymbol{r}(t) \triangleq \widehat{\boldsymbol{r}}(t) - \boldsymbol{r}(t). \tag{4.13}$$

From these notations, the correct TDCP model is the one in Equation (4.11) while the assumed one is

$$h_{\widehat{\boldsymbol{r}}(t),i} : (\Delta\boldsymbol{r},\ \Delta dt_r) \mapsto \left\|\widehat{\boldsymbol{r}}(t) + \Delta\boldsymbol{r} - \boldsymbol{s}_i(t')\right\| - \left\|\widehat{\boldsymbol{r}}(t) - \boldsymbol{s}_i(t)\right\| + c \cdot \Delta dt_r \tag{4.14}$$

leading to a misspecified likelihood

$$\mathcal{ML}\left(\Delta\tilde{\Phi}_r^{s_i}\right)_{\widehat{\boldsymbol{r}}(t)} : \Theta \subseteq \mathbb{R}^4 \to \mathbb{R}^+$$
$$\boldsymbol{\theta} \mapsto \frac{1}{\sqrt{2\pi\sigma^2_{\text{TDCP}}}} \exp\left(-\frac{1}{2\sigma^2_{\text{TDCP}}}\left(\Delta\tilde{\Phi}_r^{s_i} - h_{\widehat{\boldsymbol{r}}(t),i}(\boldsymbol{\theta})\right)^2\right) \tag{4.15}$$

This document may not be reproduced, modified, adapted, published, translated in any way, in whole or in part, nor disclosed to a third party without the prior written consent of ENAC. © 2025, ENAC

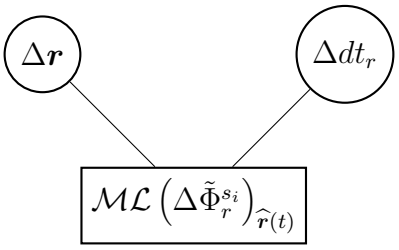

Figure 4.3: Factor graph representation of the TDCP model given in Equation (4.15) with fixed receiver coordinates at instant t. The parameter $\boldsymbol{r}(t)$ is **assumed** to be equal to $\widehat{\boldsymbol{r}}(t)$ and is not estimated.

where $h_{\widehat{\boldsymbol{r}}(t),i}$ is as in Equation (4.14). The FGO representation of Equation (4.15) is visible in Figure 4.3. Similarly, by combining observations from multiple satellites, an FGO can be built to estimate the receiver displacement $\Delta\boldsymbol{r}$ and clock bias difference Δdt_r.

It can be noticed that

$$\delta\boldsymbol{r}(t) = \mathbf{0} \Leftrightarrow \widehat{\boldsymbol{r}}(t) = \boldsymbol{r}(t) \Leftrightarrow h_{\widehat{\boldsymbol{r}}(t)} = h_{\boldsymbol{r}(t)}. \tag{4.16}$$

To assess the impact of model accuracy on displacement estimation, the following section introduces the difference between the well-specified and misspecified TDCP models.

4.3.3 Difference Between Correct and Assumed TDCP Models

In order to quantify the difference between the two models as a function of $\delta\boldsymbol{r}(t)$, the difference between the assumed model Equation (4.14) and the correct model Equation (4.11) is expressed as a function of the error $\delta\boldsymbol{r}(t)$, evaluated at the true receiver displacement $\Delta\boldsymbol{r}$ and the true receiver clock bias difference Δdt_r, i.e.,

$$\begin{aligned} &\delta h_i : \mathbb{R}^3 \to \mathbb{R} \\ &\quad \delta\boldsymbol{r}(t) \mapsto h_{\boldsymbol{r}(t)+\delta\boldsymbol{r}(t),i}(\Delta\boldsymbol{r}, \Delta dt_r) - h_{\boldsymbol{r}(t),i}(\Delta\boldsymbol{r}, \Delta dt_r). \end{aligned} \tag{4.17}$$

It can be noted that this application cancels all the clock bias terms, and only the difference in the geometric ranges remains

$$\begin{aligned} \delta h_i(\delta\boldsymbol{r}(t)) = &\left\|\boldsymbol{r}(t) + \delta\boldsymbol{r}(t) + \Delta\boldsymbol{r} - \boldsymbol{s}_i(t')\right\| - \left\|\boldsymbol{r}(t) + \delta\boldsymbol{r}(t) - \boldsymbol{s}_i(t)\right\| \\ &- \left\|\boldsymbol{r}(t) + \Delta\boldsymbol{r} - \boldsymbol{s}_i(t')\right\| + \left\|\boldsymbol{r}(t) - \boldsymbol{s}_i(t)\right\| \end{aligned} \tag{4.18}$$

which is not null in general. Therefore, the error $\delta\boldsymbol{r}(t)$ may have an impact on the estimated receiver displacement and clock bias difference.

In general, the use of a misspecified model to estimate parameters has an impact on the estimation. The objective of the following sections is to experimentally assess the TDCP model error and receiver displacement estimation error due to an error $\delta\boldsymbol{r}(t) \neq \mathbf{0}$.

4.4 Uncertainty Quantification of the Position in the TDCP Model

This study uses synthetic data generated under ideal conditions, as if it were recorded by the TLSE GNSS receiver, a fixed station located in Toulouse, France, and part of the International GNSS Service (IGS) network, starting from January 1, 2024, at 12:00 Coordinated Universal Time (UTC).

To enable a clear UQ, noise-free and CS-free TDCP observations are generated based on the true receiver coordinates $\boldsymbol{r}(t)$ and $\boldsymbol{r}(t')$. This setup removes the influence of measurement noise and time-varying receiver dynamics, allowing the analysis to focus solely on model uncertainty. Specifically, the restricted TDCP model is evaluated using an incorrect initial position, introducing a deterministic modeling error. The resulting impact on displacement estimation is analyzed, providing insight into the model's sensitivity and the propagation of reference position inaccuracies.

4.4.1 TDCP Model Error

The first experiment characterizes the TDCP model error as in Equation (4.17), for a single satellite (G17). For each value of $\delta\boldsymbol{r}(t)$, a value of $\delta h_i\left(\delta\boldsymbol{r}(t)\right)$ is obtained, indicating the discrepancy between the two TDCP models.

4.4.1.1 Model Error for Small and Constant Norm of First Position Error

In Figure 4.4, the set of values taken by $\delta\boldsymbol{r}(t)$ is the unit sphere and the time interval between the two instants is set to $t' - t = 1\,\mathrm{s}$, which is a common value in standard receivers. This spherical representation is chosen to analyze how the direction of $\delta\boldsymbol{r}(t)$ influences the discrepancy between the two TDCP models. To provide a more readable result, Figure 4.5 presents the same results but using local elevation and azimuth angles as defined in the East, North, Up (ENU) frame. In this representation, each point on the sphere is mapped by its corresponding elevation (angle above the horizon) and azimuth (angle from north), allowing a clearer visualization of the angular dependence. Both figures indicate that the discrepancy between the two models is maximum and minimum on two antipodal points, is null on the equator defined by these two antipodal points, and is continuous, as there is no rapid change of value.

In Appendix D, it is shown that the largest absolute errors are in the direction given by the vector $\boldsymbol{s}_i(t') - \boldsymbol{s}_i(t) - \Delta\boldsymbol{r}$, which approximately corresponds to the satellite displacement direction, and the error is null for orthogonal vectors to this direction.

Overall, the error is low compared to the norm of the first position error, with a maximum error that is approximately 10^4 lower than $\|\delta\boldsymbol{r}(t)\|$.

This document may not be reproduced, modified, adapted, published, translated in any way, in whole or in part, nor disclosed to a third party without the prior written consent of ENAC. © 2025, ENAC

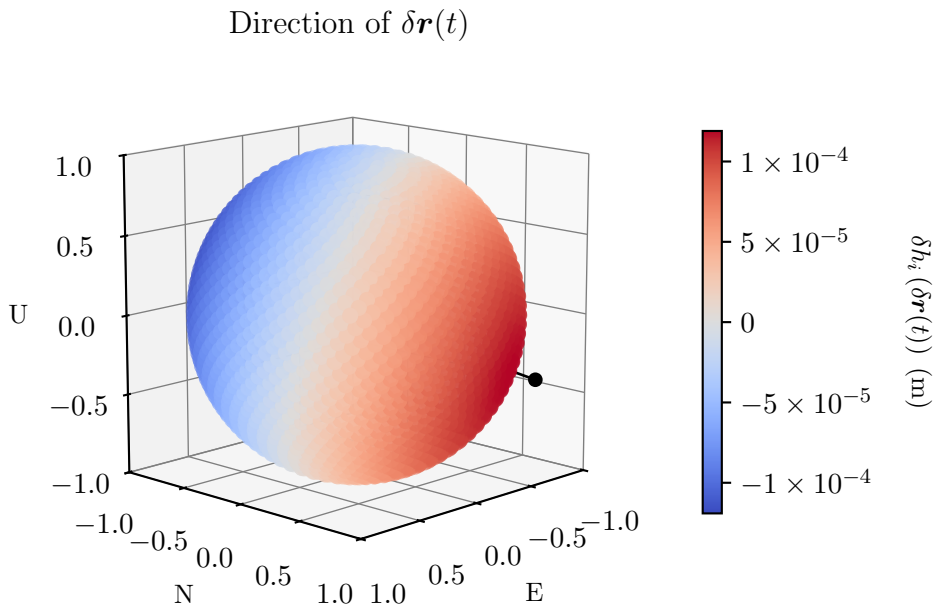

Figure 4.4: $\|\delta \boldsymbol{r}(t)\| = 1\,\mathrm{m}$, $t' - t = 1\,\mathrm{s}$. E, N and U indicate the components of $\delta \boldsymbol{r}(t)$ in the ENU frame. The black dot indicates the direction of $\boldsymbol{s}_i(t') - \boldsymbol{s}_i(t) - \Delta \boldsymbol{r}$.

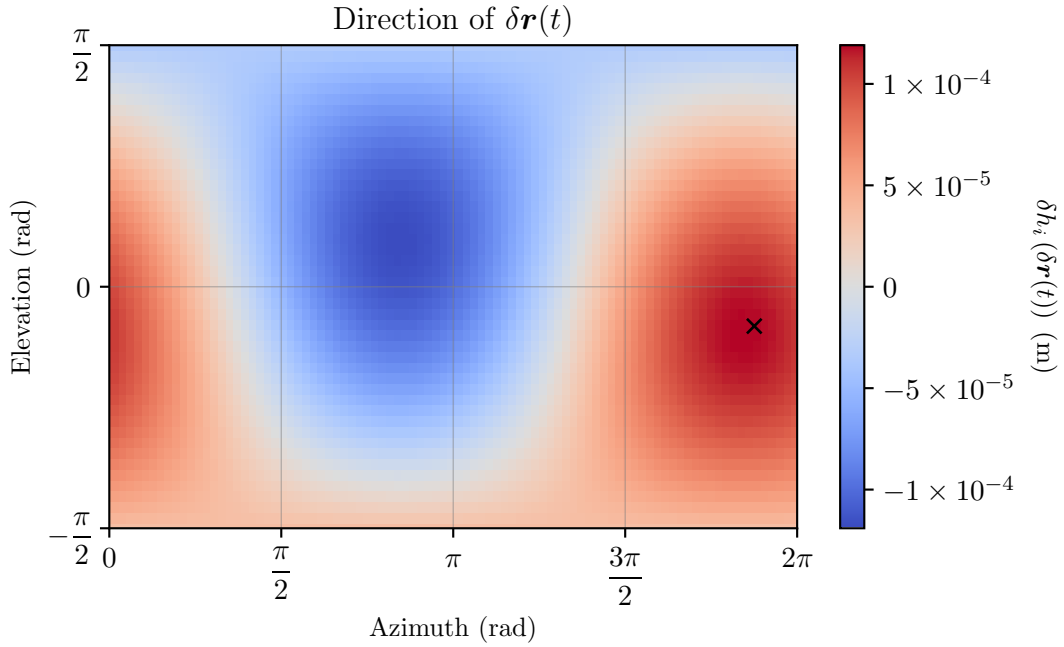

Figure 4.5: $\|\delta \boldsymbol{r}(t)\| = 1\,\mathrm{m}$, $t' - t = 1\,\mathrm{s}$. The black cross indicates the direction of $\boldsymbol{s}_i(t') - \boldsymbol{s}_i(t) - \Delta \boldsymbol{r}$.

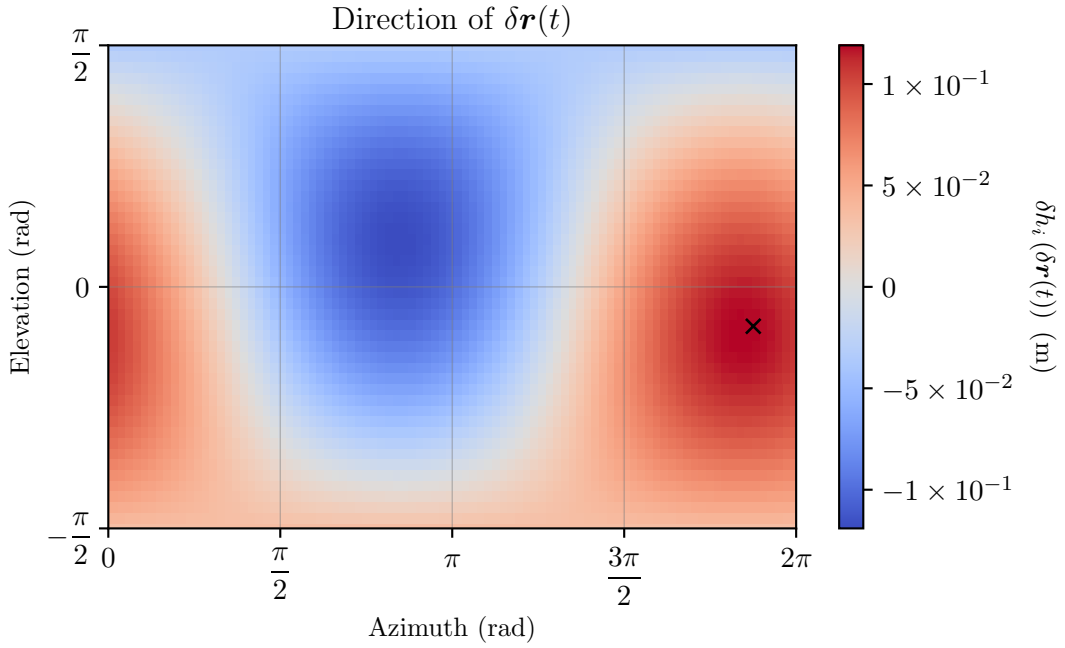

Figure 4.6: $\|\delta \boldsymbol{r}(t)\| = 1\,\text{km}$, $t' - t = 1\,\text{s}$. The black cross indicates the direction of $\boldsymbol{s}_i(t') - \boldsymbol{s}_i(t) - \Delta \boldsymbol{r}$.

4.4.1.2 Model Error for Large and Constant Norm of First Position Error

The same experiment as in Section 4.4.1.1 is conducted, but with a much higher error (i.e., a larger sphere) set to $\|\delta \boldsymbol{r}(t)\| = 1\,\text{km}$. The results are visible in Figure 4.6. Again, it shows that the discrepancy between the two models is maximum and minimum on two antipodal points, is null on the equator defined by these two antipodal points, and is continuous, as there is no rapid change of value, that the maximum and minimum errors are in the direction given by the vector $\boldsymbol{s}_i(t') - \boldsymbol{s}_i(t) - \Delta \boldsymbol{r}$, which approximately corresponds to the satellite displacement, and that the error is low compared to the norm of the first position error, with a maximum error that is approximately 10^4 lower than $\|\delta \boldsymbol{r}(t)\|$.

4.4.1.3 Model Error for First Position Error in the Worst Direction

The study of the worst case direction is further extended, this time by observing the values taken by δh_i on the set $\left\{\delta \boldsymbol{r}(t) \in \mathbb{R}^3 \;\middle|\; \delta \boldsymbol{r}(t) = \lambda \left(\boldsymbol{s}_i(t') - \boldsymbol{s}_i(t) - \Delta \boldsymbol{r}\right),\ \lambda \in \mathbb{R}^+\right\}$, which represents the subspace spanned by the worst-case direction. The analysis is is conducted for multiple time intervals $t' - t$. The results are visible in Figure 4.7. For convenience, a log-log plot is used. For all the considered time intervals $t' - t$, the plots indicate a linear relation between the model mismatch δh_i and the norm of the first-fix error $\|\delta \boldsymbol{r}(t)\|$, since the slope of all the curves are equal to 1 and from Equation (4.18), $\delta h_i\left(\mathbf{0}\right) = 0$. For each value of the time interval, the linear coefficient between δh_i and $\|\delta \boldsymbol{r}(t)\|$ can be read at $\|\delta \boldsymbol{r}(t)\| = 1\,\text{m}$. For example, in the case of $t' - t = 1\,\text{s}$, this coefficient is equal to 1.2×10^{-4}.

This document may not be reproduced, modified, adapted, published, translated in any way, in whole or in part, nor disclosed to a third party without the prior written consent of ENAC. © 2025, ENAC

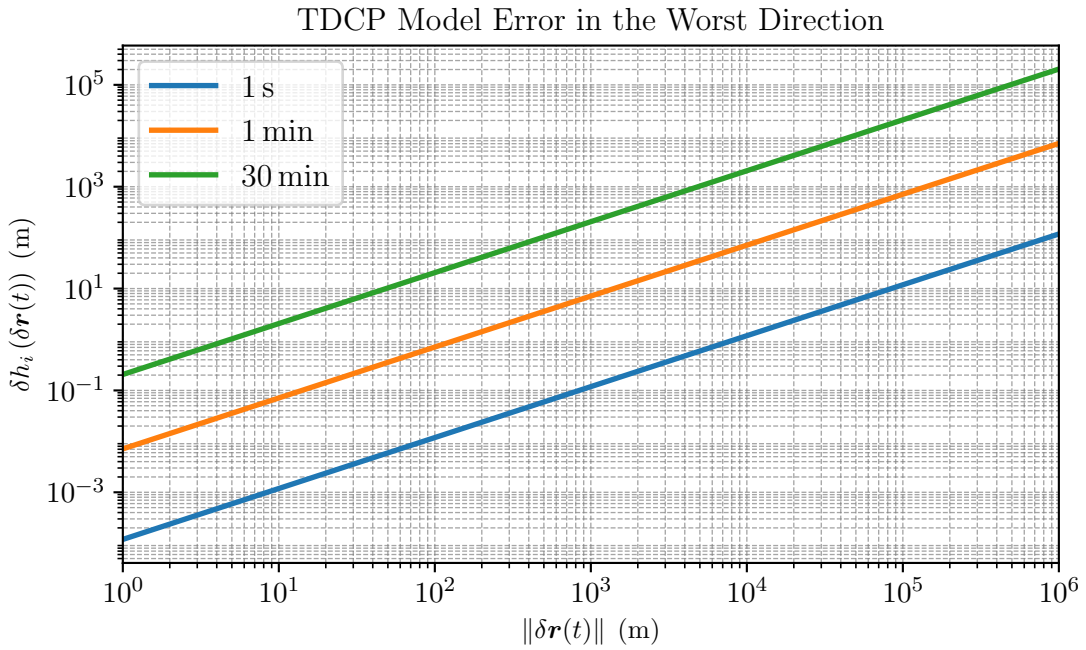

Figure 4.7: TDCP model error for three values of $t' - t$, with $\delta \boldsymbol{r}(t)$ in the direction given by the vector $\boldsymbol{s}_i(t') - \boldsymbol{s}_i(t) - \Delta \boldsymbol{r}$, which corresponds to the worst direction.

In Appendix D is provided a computation of these values. It is visible that the linear coefficient depends on the time interval, as the greater the time interval, the greater the coefficient. To conclude this section, for a given value of $\|\delta \boldsymbol{r}(t)\|$, the greater the time interval, the greater the model mismatch.

Having characterized the model error for a single satellite, the next section extends the analysis to multi-satellite configurations and investigates how the initial position uncertainty affects the estimated displacement vector.

4.4.1.4 Largest Model Error for Multiple Time Intervals And Position Error Norm

Finally, the largest value taken by δh_i is computed, for a set of values of $\|\delta \boldsymbol{r}(t)\|$ and of time intervals $t' - t$ between the two observation instants. This is done in order to explore how the movement of satellites over time would affect the model mismatch. By extending the time between successive observations, the GNSS satellites in the sky change their positions more significantly due to their dynamics. The purpose of this application is to capture a wider range of applications, which can influence the accuracy and reliability of the positioning solutions. These values are visible in Table 4.1. Omitting rounding errors, the values taken show a close to bilinear relation with $\|\delta \boldsymbol{r}(t)\|$ and $t' - t$. This result is hard to predict, as δh_i is not a linear function of $\delta \boldsymbol{r}(t)$, and is even harder to predict for $t' - t$, as the time interval does not explicitly appear in δh_i.

Now that the model mismatch is characterized for a single satellite, multiple satellites are

Table 4.1: Maximum value of δh_i as in Equation (4.17) with respect to $\|\delta \boldsymbol{r}(t)\|$ and $t' - t$ for GPS satellite G17.

$\|\delta \boldsymbol{r}(t)\|$ \ $t' - t$	1 s	1 min	30 min
1 m	1.2×10^{-4} m	7.1×10^{-3} m	2.1×10^{-1} m
10 m	1.2×10^{-3} m	7.1×10^{-2} m	2.1 m
1 km	1.2×10^{-1} m	7.1 m	2.1×10^{2} m
1000 km	1.2×10^{2} m	7.1×10^{3} m	2.0×10^{5} m

used to estimate the receiver's displacement and clock bias difference by building the FGO represented in Figure 4.3.

4.4.2 Receiver Displacement Estimation Error

In this experiment, the synthetic receiver true positions $\boldsymbol{r}(t)$ and $\boldsymbol{r}(t')$ are assigned coordinates corresponding to the location of TLSE, and the receiver's clock bias difference Δdt_r is set to 0 s. The set of all visible GPS satellites at two instants t and t' is used to generate noiseless synthetic TDCP observations following Equation (4.4), with $\sigma_{\text{TDCP}} = 0$ m and $\Delta N_r^{si} = 0$. These observations are used to estimate the receiver displacement $\Delta \boldsymbol{r}$ and clock bias difference Δdt_r between the two instants by solving the FGO represented in Figure 4.3. These estimates are denoted $\widehat{\Delta} \boldsymbol{r}$ and $\widehat{\Delta} dt_r$. The choice regarding noiseless measurements is made in order to obtain a displacement estimation error that is only due to the error $\delta \boldsymbol{r}(t)$.

A skyplot illustrating the satellite visibility over the time period used in the experiments is shown in Figure 4.8. In all cases, the initial time t is fixed at 12:00 UTC, and the final time t' varies within the interval covered by the skyplot (12:00 to 12:30).

4.4.2.1 Displacement Estimation Error for Constant Norm of First Position Error

To quantify the displacement estimation error, its Euclidean norm is computed, i.e., $\left\| \widehat{\Delta} \boldsymbol{r} - \Delta \boldsymbol{r} \right\|$ is used as a scalar measure of the displacement estimation error caused by the incorrect initial position $\widehat{\boldsymbol{r}}(t)$.

In Figure 4.9 and Figure 4.10, the set of values taken by $\delta \boldsymbol{r}(t)$ corresponds to two spheres, with different radius, i.e., for two values of $\|\delta \boldsymbol{r}(t)\|$ equal to 1 m and 1 km. The time interval is set to $t' - t = 1$ s. These two plots have the same shape, corresponding to two modes, whose peaks are close to antipodal and there is no direction where the estimation error in null. Although these figures look similar, they differ by the magnitude of the values. More generally, experiments lead to the conclusion that for any value of $\|\delta \boldsymbol{r}(t)\|$, the obtained plot has a shape similar to the ones in Figure 4.9 and Figure 4.10, and that the set of values taken by $\left\| \widehat{\Delta} \boldsymbol{r} - \Delta \boldsymbol{r} \right\|$ is approximately linear with respect to $\|\delta \boldsymbol{r}(t)\|$.

This document may not be reproduced, modified, adapted, published, translated in any way, in whole or in part, nor disclosed to a third party without the prior written consent of ENAC. © 2025, ENAC

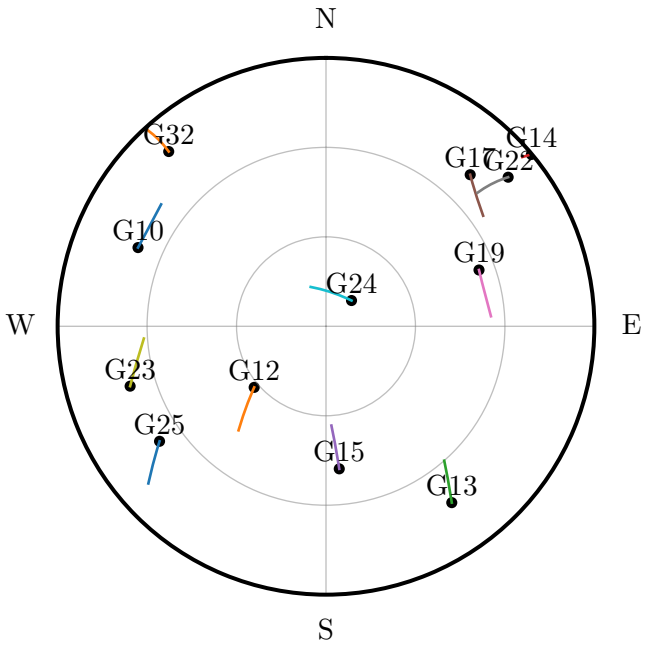

Figure 4.8: Skyplot of GPS satellites at TLSE, on January 1, 2024, 12:30 UTC, with their trace from 12:00 UTC.

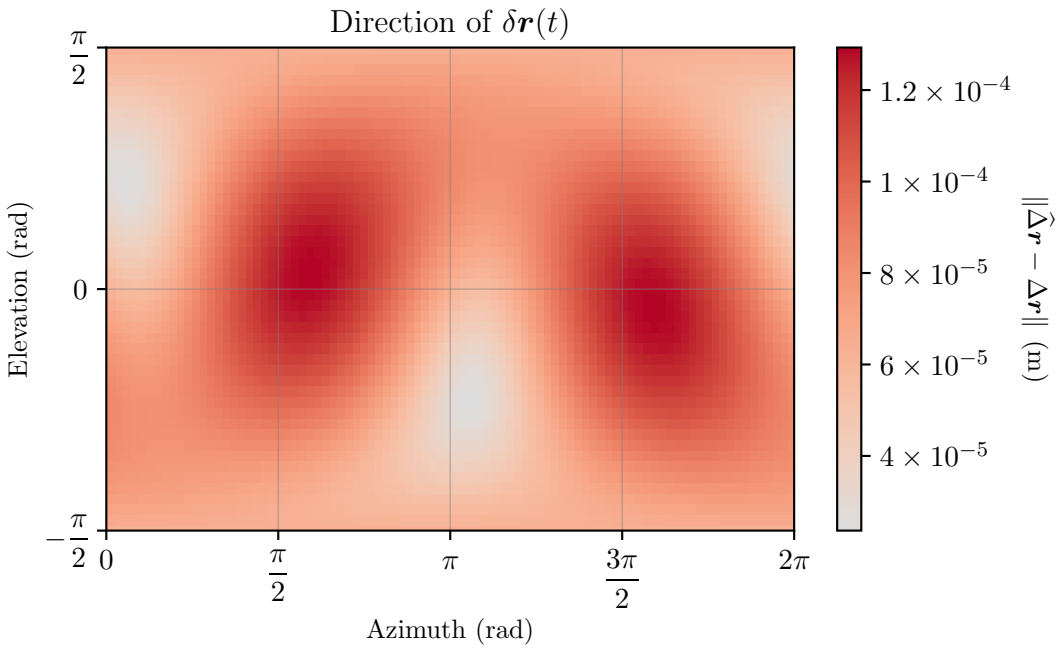

Figure 4.9: $\left\|\widehat{\Delta \boldsymbol{r}} - \Delta \boldsymbol{r}\right\|$, with $\|\delta \boldsymbol{r}(t)\| = 1\,\text{m}$, $t' - t = 1\,\text{s}$.

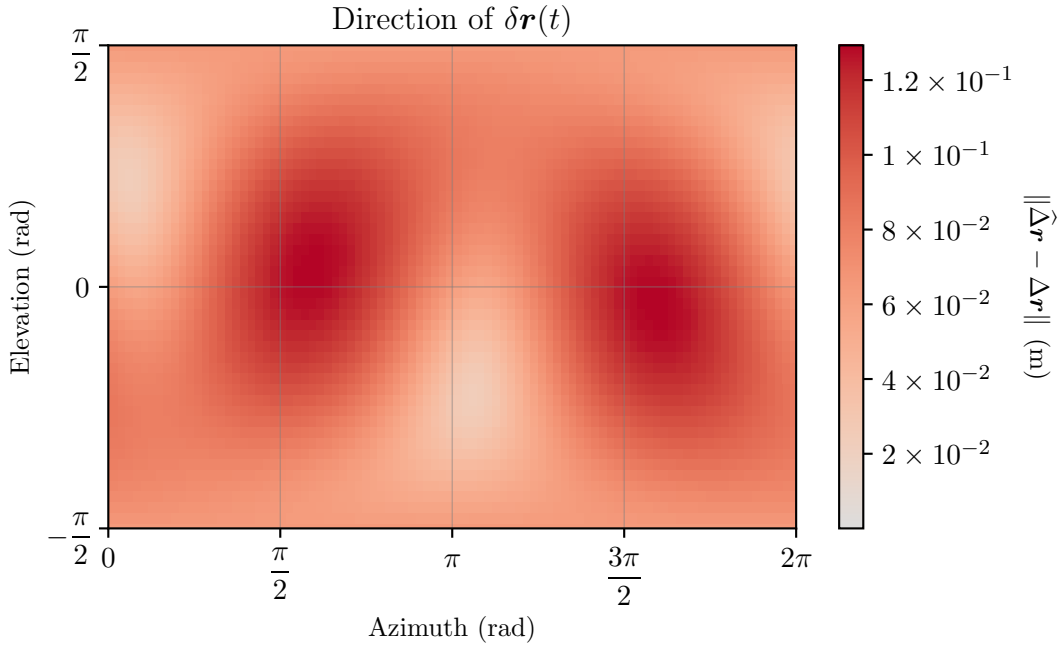

Figure 4.10: $\left\|\widehat{\Delta \boldsymbol{r}} - \Delta \boldsymbol{r}\right\|$, with $\|\delta \boldsymbol{r}(t)\| = 1\,\text{km}$, $t' - t = 1\,\text{s}$.

4.4.2.2 Horizontal and Vertical Displacement Estimation Error, Constant Norm

To gain further insight into the nature of the displacement estimation error, the displacement estimation error vector $\widehat{\Delta \boldsymbol{r}} - \Delta \boldsymbol{r}$ is decomposed into its horizontal and vertical components thanks to the local ENU frame. This decomposition allows a clearer analysis of how the direction of the displacement and the error in the initial position influence the vertical and horizontal parts of the estimated displacement independently.

Figures 4.11 and 4.12 present the norms of the horizontal and vertical components, respectively, for the same conditions as in Figure 4.9. The patterns observed in these plots exhibit distinct characteristics: the vertical component is somehow similar to the total error norm, as in Figure 4.9, and with larger values than the horizontal components. As with the total error norm, the variations are continuous, and the maximum values occur near the same directions that correspond to the peaks in the total error.

This decomposition confirms that the error introduced by an incorrect reference position affects the different components of the estimated displacement in distinct ways, with vertical components generally more sensitive.

4.4.2.3 Displacement Estimation Error, Constant Direction

In order to show the approximate linearity between the displacement estimation error and the first position error, the displacement estimation error is studied in a given direction, which is defined by an elevation angle of $\frac{\pi}{30}$ rad $= 6°$ and an azimuth angle of $\frac{3\pi}{5}$ rad $=$

This document may not be reproduced, modified, adapted, published, translated in any way, in whole or in part, nor disclosed to a third party without the prior written consent of ENAC. © 2025, ENAC

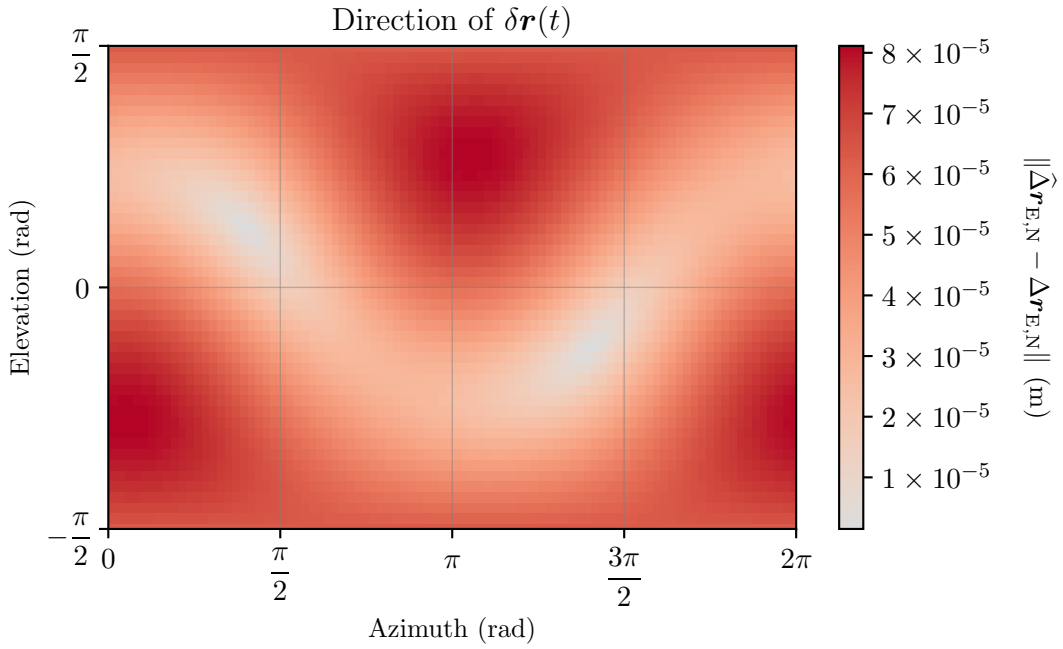

Figure 4.11: Norm of horizontal component of $\widehat{\Delta}\boldsymbol{r} - \Delta\boldsymbol{r}$, with $\|\delta\boldsymbol{r}(t)\| = 1\,\mathrm{m}$, $t' - t = 1\,\mathrm{s}$.

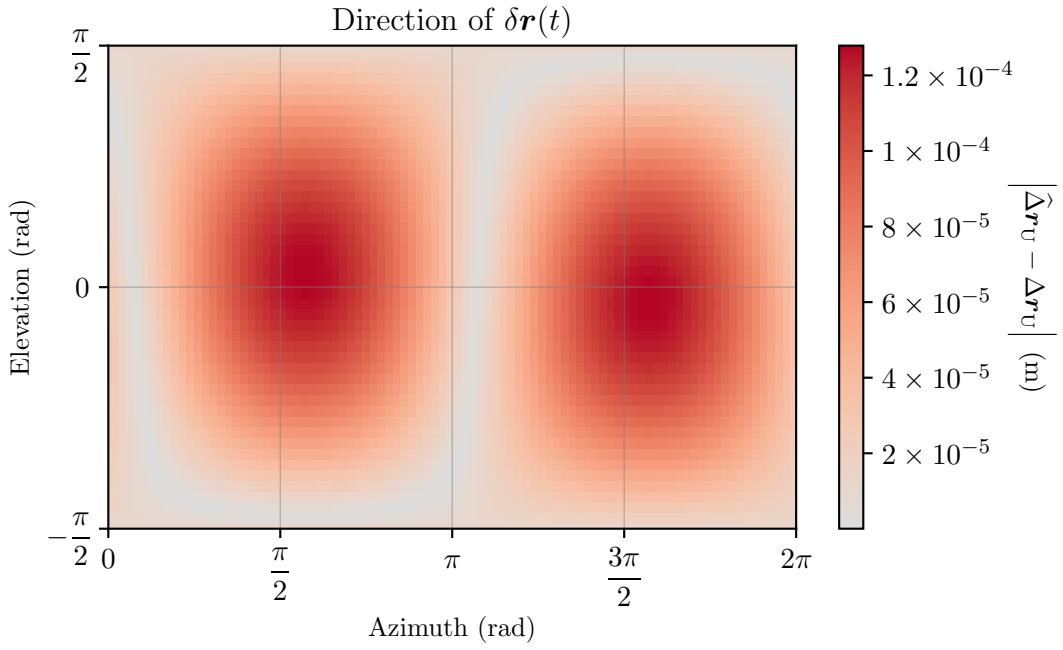

Figure 4.12: Norm of vertical component of $\widehat{\Delta}\boldsymbol{r} - \Delta\boldsymbol{r}$, with $\|\delta\boldsymbol{r}(t)\| = 1\,\mathrm{m}$, $t' - t = 1\,\mathrm{s}$.

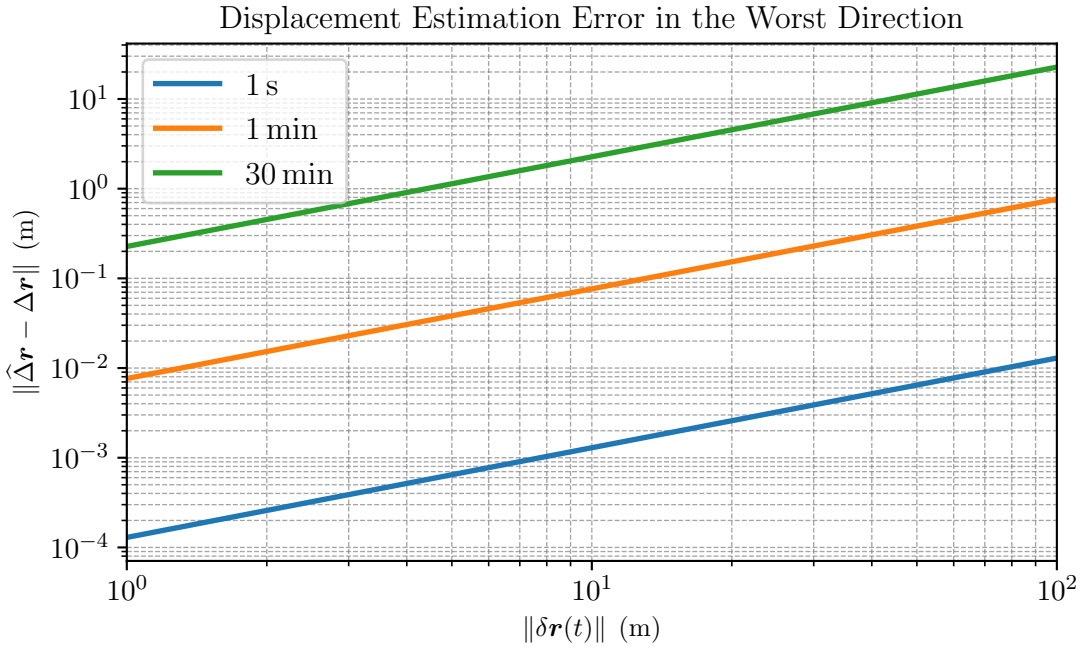

Figure 4.13: $\left\|\widehat{\Delta}\boldsymbol{r} - \Delta\boldsymbol{r}\right\|$ for three values of $t' - t$, as a function of $\|\delta\boldsymbol{r}(t)\|$, with $\delta\boldsymbol{r}(t)$ in the direction given by an elevation angle of $\frac{\pi}{30}$ rad $= 6°$ and an azimuth angle of $\frac{3\pi}{5}$ rad $= 108°$.

$108°$. The reason why this direction is chosen is that it corresponds approximately to the one where $\left\|\widehat{\Delta}\boldsymbol{r} - \Delta\boldsymbol{r}\right\|$ is maximum for a given value of $\|\delta\boldsymbol{r}(t)\| = 1\,\text{m}$ and $t' - t = 1\,\text{s}$, as in Figure 4.9.

First, in Figure 4.13, the estimation error is displayed as a function of $\|\delta\boldsymbol{r}(t)\|$, for multiple time intervals. It shows a linear relation between the estimation error and the norm of the first-fix error, for all the time intervals, as the slope of the curves are all equal to 1. The linear coefficient between $\left\|\widehat{\Delta}\boldsymbol{r} - \Delta\boldsymbol{r}\right\|$ and $\|\delta\boldsymbol{r}(t)\|$ can be read at $\|\delta\boldsymbol{r}(t)\| = 1\,\text{m}$. The greater the time interval, the greater the coefficient. Again, the linearity is hard to predict, as writing $\left\|\widehat{\Delta}\boldsymbol{r} - \Delta\boldsymbol{r}\right\|$ as a linear function of $\delta\boldsymbol{r}(t)$, when restricted to a specific direction, is not straightforward.

In Figure 4.14, the estimation error is displayed as a function of $t' - t$, for multiple values of $\|\delta\boldsymbol{r}(t)\|$. Again, it shows a linear relation between the estimation error $\left\|\widehat{\Delta}\boldsymbol{r} - \Delta\boldsymbol{r}\right\|$ and the time interval $t' - t$, for all the values of $\|\delta\boldsymbol{r}(t)\|$, as the slope of the curves are all equal to 1. The linear coefficient between $\left\|\widehat{\Delta}\boldsymbol{r} - \Delta\boldsymbol{r}\right\|$ and $t' - t$ can be read at $t' - t = 1\,\text{s}$. The greater $\|\delta\boldsymbol{r}(t)\|$, the greater the coefficient. This result is hard to predict, as $\left\|\widehat{\Delta}\boldsymbol{r} - \Delta\boldsymbol{r}\right\|$ is not an explicit function of $t' - t$.

This document may not be reproduced, modified, adapted, published, translated in any way, in whole or in part, nor disclosed to a third party without the prior written consent of ENAC. © 2025, ENAC

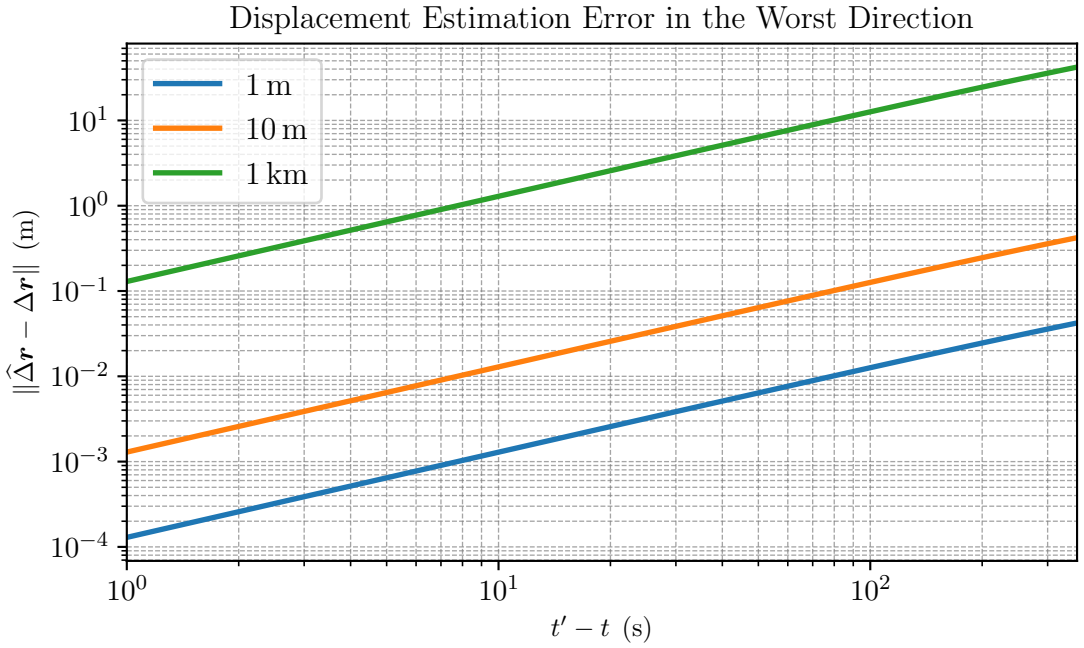

Figure 4.14: $\left\|\widehat{\Delta}\boldsymbol{r} - \Delta\boldsymbol{r}\right\|$ for three values of $\|\delta\boldsymbol{r}(t)\|$, as a function of $t' - t$, with $\delta\boldsymbol{r}(t)$ in the direction given by an elevation angle of $\frac{\pi}{30}$ rad $= 6°$ and an azimuth angle of $\frac{3\pi}{5}$ rad $= 108°$.

4.4.2.4 Largest Displacement Estimation Error

Finally, in Table 4.2 are visible maximum values of $\left\|\widehat{\Delta}\boldsymbol{r} - \Delta\boldsymbol{r}\right\|$, for multiple values of $t' - t$ and for multiple values of $\|\delta\boldsymbol{r}(t)\|$. Decomposing $\widehat{\Delta}\boldsymbol{r} - \Delta\boldsymbol{r}$ in its horizontal and vertical components, Table 4.3 and Table 4.4 provide maximum values of their norms in the horizontal plane and vertical line, respectively, for multiple values of $t' - t$ and for multiple values of $\|\delta\boldsymbol{r}(t)\|$. Omitting rounding errors and cases where both $\|\delta\boldsymbol{r}(t)\|$ and $t' - t$ are very large, both the minimum and maximum values are linear with respect to $\|\delta\boldsymbol{r}(t)\|$, but not linear with respect to $t' - t$. The non-linearity with respect to time is due to the disappearance of satellite G14 after a few minutes, as visible in Figure 4.15, meaning it is not considered in the solution for $t' - t = 30\,\text{min}$. Again, the linearity is hard to predict, as the maximum value of $\left\|\widehat{\Delta}\boldsymbol{r} - \Delta\boldsymbol{r}\right\|$ over a sphere of radius $\|\delta\boldsymbol{r}(t)\|$ is not trivially a linear function of that radius. From these tables, conclusions can be made regarding the validity of the first position approximation. For example, if one has to estimate a receiver displacement such that $\left\|\widehat{\Delta}\boldsymbol{r} - \Delta\boldsymbol{r}\right\| \leq 1.3\,\text{mm}$, for a time interval of 1 s, for an initial error of worst amplitude $\|\delta\boldsymbol{r}(t)\| = 10\,\text{m}$, then the approximation $\boldsymbol{r}(t) \approx \widehat{\boldsymbol{r}}(t)$ is not acceptable, without considering any other source of perturbation.

Overall, it is experimentally shown that the greater is $\|\delta\boldsymbol{r}(t)\|$, the greater is $\left\|\widehat{\Delta}\boldsymbol{r} - \Delta\boldsymbol{r}\right\|$, with a linear factor between these two quantities that depends on the time interval $t' - t$.

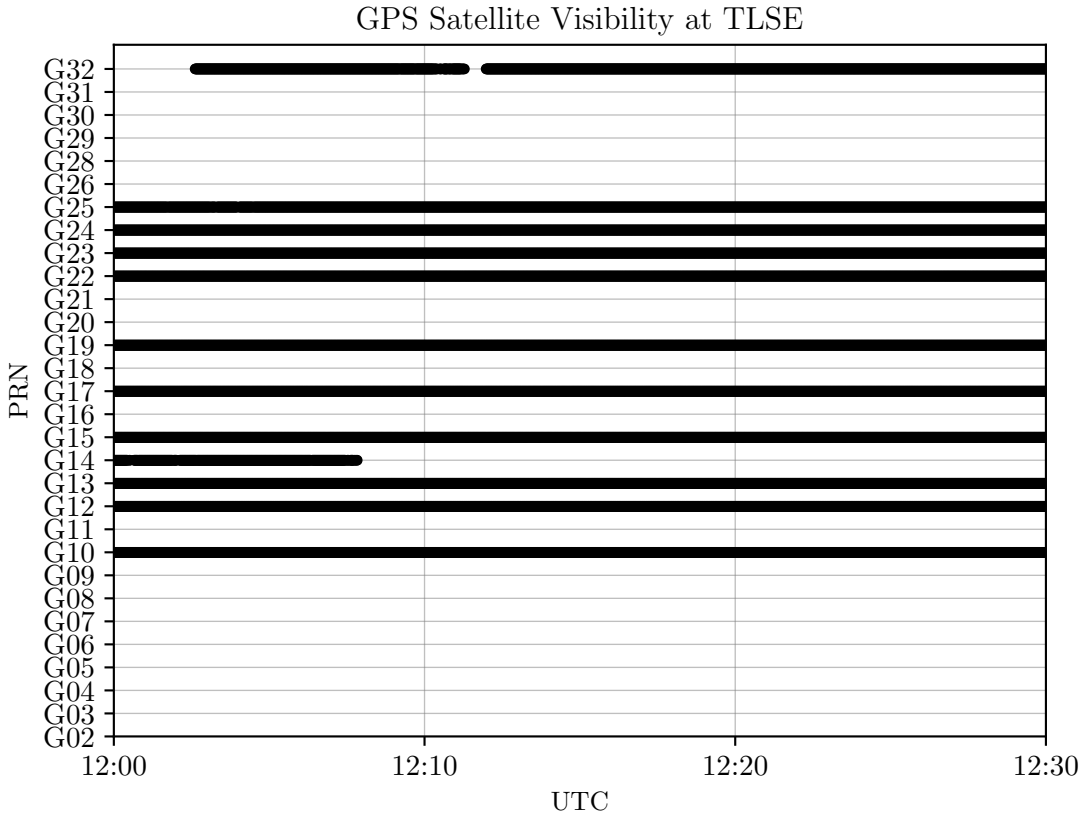

Figure 4.15: Satellite Visibility at TLSE on January 1, 2024.

Table 4.2: Maximum values of $\left\|\widehat{\Delta \boldsymbol{r}} - \Delta \boldsymbol{r}\right\|$ with respect to $\|\delta \boldsymbol{r}(t)\|$ and $t' - t$.

$\|\delta \boldsymbol{r}(t)\|$ \ $t' - t$	1 s	1 min	30 min
1 m	1.3×10^{-4} m	7.7×10^{-3} m	3.8×10^{-1} m
10 m	1.3×10^{-3} m	7.7×10^{-2} m	3.8 m
1 km	1.3×10^{-1} m	7.7 m	3.8×10^{2} m
1000 km	1.3×10^{2} m	7.8×10^{3} m	3.8×10^{5} m

Table 4.3: Maximum values of the norm of the horizontal component of $\widehat{\Delta \boldsymbol{r}} - \Delta \boldsymbol{r}$ with respect to $\|\delta \boldsymbol{r}(t)\|$ and $t' - t$.

$\|\delta \boldsymbol{r}(t)\|$ \ $t' - t$	1 s	1 min	30 min
1 m	8.1×10^{-5} m	4.9×10^{-3} m	1.3×10^{-1} m
10 m	8.1×10^{-4} m	4.9×10^{-2} m	1.3 m
1 km	8.1×10^{-2} m	4.9 m	1.3×10^{2} m
1000 km	8.2×10^{1} m	4.9×10^{3} m	1.4×10^{5} m

This document may not be reproduced, modified, adapted, published, translated in any way, in whole or in part, nor disclosed to a third party without the prior written consent of ENAC. © 2025, ENAC

Table 4.4: Maximum values of the norm of the vertical component of $\widehat{\Delta}\boldsymbol{r} - \Delta\boldsymbol{r}$ with respect to $\|\delta\boldsymbol{r}(t)\|$ and $t' - t$.

$\|\delta\boldsymbol{r}(t)\|$ \ $t' - t$	1 s	1 min	30 min
1 m	1.3×10^{-4} m	7.6×10^{-3} m	3.7×10^{-1} m
10 m	1.3×10^{-3} m	7.6×10^{-2} m	3.7 m
1 km	1.3×10^{-1} m	7.6 m	3.7×10^{2} m
1000 km	1.3×10^{2} m	7.7×10^{3} m	3.7×10^{5} m

These results provide practitioners with concrete thresholds on the initial position accuracy required to meet specific displacement estimation goals, depending on the TDCP interval.

4.5 Conclusion

This chapter addresses the impact of an inaccurate initial receiver position on displacement estimation using the TDCP model. By comparing a well-specified and a misspecified version of the TDCP model, it is shown that even small errors in the assumed initial position can introduce systematic model errors and affect the accuracy of estimated displacements. Through a series of synthetic experiments under controlled conditions, it is demonstrated that the model mismatch and displacement estimation error depend both on the magnitude and direction of the initial position error. In particular, the estimation error exhibits directional sensitivity and a nearly linear relationship with respect to the norm of the position error, especially in the worst-case direction.

Moreover, the decomposition of the displacement estimation error into horizontal and vertical components revealed that the vertical component is generally more affected, which is relevant for applications requiring precise altitude estimation. The dependence of estimation accuracy on the time interval between observations is also quantified, highlighting that larger intervals amplify the impact of position errors due to increased satellite motion.

These results contribute to a better understanding of the uncertainty propagation in TDCP-based odometry and emphasize the importance of accurate initial positioning. They provide quantitative guidance on the validity of the fixed-position assumption commonly used in practice and define operational limits for achieving reliable displacement estimates.

Perspectives for future work include extending the uncertainty quantification to stronger approximations of the TDCP model, such as linearized formulations, as well as evaluating their applicability in the context of Low Earth Orbit (LEO) satellite navigation, where the dynamics and geometry differ significantly from traditional GNSS configurations.

This chapter is supported by a peer-reviewed journal article

[70] H. Cherfi, J. Lesouple, J. Solà, and P. Thevenon, “Uncertainty Quantification of

First Fix in a Time-Differenced Carrier Phase Observation Model," *Sensors*, vol. 25, May 2025.

The next chapter addresses the application of FGO by combining multiple instants, as commonly done in the literature, in order to achieve positioning using multiple code and TDCP observations. This multi-epoch formulation enables more robust and accurate state estimation by leveraging the temporal correlation between successive measurements.

This document may not be reproduced, modified, adapted, published, translated in any way, in whole or in part, nor disclosed to a third party without the prior written consent of ENAC. © 2025, ENAC

Chapter 5

Impact of TDCP Correlations on Positioning

This chapter investigates Factor Graph Optimization (FGO) that span multiple instants and include both code pseudorange and Time-Differenced Carrier Phase (TDCP) observations. These graphs model Global Navigation Satellite System (GNSS) variables across time, introducing temporal dependencies that extend beyond the instantaneous measurement model typically used in Single Point Positioning (SPP) formulations.

Several FGO architectures are constructed and compared using both synthetic and real GNSS code pseudorange and carrier-phase observations, with a focus on how different modeling choices affect estimation quality. Architectures that include TDCP factors are analyzed in detail. When TDCP observations from the same satellite share common epochs, statistical correlations arise between them. Despite this, a widespread practice in the GNSS community treats such factors as independent. This chapter examines the impact of neglecting these correlations by quantifying their influence on solution accuracy.

In addition, the effect of graph length, defined as the number of instants included in the FGO, is analyzed. The results identify conditions under which longer graphs improve performance and highlight the point at which additional epochs no longer provide significant benefit. This evaluation informs the selection of an optimal graph length that balances accuracy and computational cost in FGO-based GNSS positioning.

5.1 FGO-Based GNSS Positioning with Code and Carrier-Phase

This section reviews key studies that apply FGO to GNSS positioning using code pseudorange and TDCP observations. While TDCP is commonly used for its high precision and robustness to multipath, especially in challenging environments, temporal correlations between successive TDCP measurements are often neglected.

Several studies incorporate TDCP measurements into estimation frameworks but treat them as pairwise, temporally independent constraints. For example, in [80] is proposed a

This document may not be reproduced, modified, adapted, published, translated in any way, in whole or in part, nor disclosed to a third party without the prior written consent of ENAC. © 2025, ENAC

GNSS/odometer integration scheme using TDCP with vehicular motion constraints and robust regression. In their formulation, TDCP is used as an average velocity constraint. However, each TDCP observation is processed independently, and no temporal correlation structure is considered beyond the immediate pair of epochs.

In [81, 5, 6, 77], the authors build several FGO architectures, most of them for different editions of the Google Smartphone Decimeter Challenge (GSDC). In each of these works, TDCP factors are incorporated into the FGO, without taking into account correlations between the TDCP observations, as they appear as separate factors, which implicitly assumes that they are statistically independent. Despite this simplification, the proposed architectures consistently yield strong positioning performance, demonstrating the practical effectiveness of TDCP integration even without considering correlations. These results suggest that, in many cases, the inclusion of TDCP measurements alone, regardless of whether their correlations are considered, can significantly enhance GNSS positioning accuracy. Nonetheless, the omission of correlations could be a limitation that may restrict further performance gains, especially in scenarios where extended temporal context is available and could be exploited.

In [78] is developed a velocity estimation algorithm using TDCP measurements with a Weighted Least Squares (WLS) approach. While the method achieves millimeter-per-second accuracy in the experimental section by differencing consecutive carrier-phase observations, the velocity estimates are assumed independent, which assumes independence between successive TDCP observations and does not model the underlying temporal dependencies.

More recently, in [82] is presented a positioning framework combining Precise Point Positioning (PPP) and Real-Time Kinematic (RTK) within an FGO formulation. Their first architecture includes pseudorange and carrier-phase observations, while the second architecture is made of factors resulting from the first architecture, as well as TDCP factors to enforce positioning consistency across epochs. Despite the progress shown in the experimental section, temporal correlations between TDCP observations remain unmodeled, each factor linking only two adjacent states, limiting the potential benefits.

In [83], the authors introduce a novel use of TDCP within an FGO, employing it as a loop closure factor rather than using the traditional consecutive formulation. In this architecture, TDCP observations are constructed between non-consecutive epochs, specifically between the current epoch and a fixed reference epoch, which results in all TDCP factors sharing a common carrier-phase observation. As a consequence, all TDCP observations from a same satellite are correlated. A main drawback of this architecture is that an undetected Cycle Slip (CS) at a given instant introduces biases in all TDCP observations made of a first carrier-phase observation before the CS and a second carrier-phase observation after the CS.

In [84], the authors acknowledge that consecutive TDCP observations are correlated. To avoid the consideration of these correlations, they adopt a strategy where TDCP are con-

structed between alternating pairs of time instants. This ensures that the included TDCP measurements are uncorrelated. However, this comes at the expense of discarding useful temporal information, effectively halving the number of usable TDCP observations. While this simplification avoids the challenge of correlation modeling, it is potentially suboptimal, as retaining all TDCP measurements while properly accounting for their dependencies could improve the overall estimation accuracy.

In [85], the authors acknowledge that consecutive TDCP observations are correlated, and these correlations are taken into account. To do so, an extra component is added to the state vector of the Extended Kalman Filter (EKF) developed. While this filtering-based approach takes the correlation into account, requiring important changes to the architecture of their estimation algorithm, this work does not apply to smoothing, as done with the FGO.

In [86] is introduced a Window Carrier Phase (WCP) factor that models temporal correlations across multiple epochs using a dense null-space projection. In their formulation, TDCP is mentioned as a special case of WCP. However, the implementation treats TDCP as a pairwise constraint and does not incorporate a temporally correlated TDCP model. This approach again reflects the prevailing assumption in the literature that TDCP observations can be processed independently.

In summary, to the best of the author's knowledge, across the literature, TDCP is recognized as a valuable factor for GNSS positioning within FGO frameworks. However, all existing works treat TDCP observations as independent, and none explicitly model the temporal correlations. Even in advanced formulations such as WCP in [86], where time correlations are central, the TDCP variant is still handled as a non-correlated special case.

This thesis addresses this critical gap by introducing an FGO formulation that incorporates temporal correlations between TDCP observations. The proposed approach is evaluated through experiments that compare positioning accuracy, with and without correlation modeling.

5.2 FGO Architectures

This section is organized in three different subsections, each describing an FGO architecture that incorporates code pseudorange and TDCP observations, with or without TDCP correlation modeling. All architectures are applied in a differential positioning context, assuming knowledge of a reference station's coordinates, as done in Chapter 3.

In this chapter, the symbol Δ indicates a difference of a common quantity of two different receivers, i.e., if a_{r_1} and a_{r_2} correspond to a quantity a from two different receivers, the Single Difference (SD) of a is

$$\Delta a_{1,2} = a_{r_2} - a_{r_1}. \tag{5.1}$$

The symbol ∇ indicates a temporal difference, i.e., given a quantity a at two different

This document may not be reproduced, modified, adapted, published, translated in any way, in whole or in part, nor disclosed to a third party without the prior written consent of ENAC. © 2025, ENAC

instants t_1 and t_2,

$$\nabla_{1,2}(a) \triangleq a(t_2) - a(t_1). \tag{5.2}$$

With these notations, the first FGO architecture is introduced.

5.2.1 Architecture 1: Code Pseudorange Only

The first FGO architecture is based exclusively on SD of code pseudorange measurements, computed between a rover and a reference station, at each instant. In this configuration, carrier-phase observations are not used yet, and no temporal links are introduced in the FGO. As a result, each epoch is processed independently, without exploiting any inter-epoch constraints. This approach serves as a baseline for comparison with more advanced architectures that incorporate temporal information through TDCP.

At a given instant t_k is considered a first Global Positioning System (GPS) receiver of unknown coordinates $\boldsymbol{r}_1(t_k) \in \mathbb{R}^3$ and a second GPS receiver of known coordinates $\boldsymbol{r}_2(t_k) \in \mathbb{R}^3$. At the same instant, a satellite of known coordinates $\boldsymbol{s}_i(t_k) \in \mathbb{R}^3$ is visible from both receivers, leading to SD of corrected carrier-phase observations

$$\Delta\tilde{P}_{1,2}^{s_i}(t_k) - \rho_{r_2}^{s_i}(t_k) = -\rho_{r_1}^{s_i}(t_k) + c \cdot \Delta dt_{1,2}(t_k) + \Delta\tilde{\varepsilon}_{P_{1,2}}^{s_i}(t_k)\,. \tag{5.3}$$

where the terms are defined as follows (all quantities are expressed in meters unless stated otherwise)

- $\Delta\tilde{P}_{1,2}^{s_i}(t_k)$ is the SD of corrected code pseudorange measurement to satellite s_i,
- $\rho_{r_1}^{s_i}(t_k) = \|\boldsymbol{r}_1(t_k) - \boldsymbol{s}_i(t_k)\|$ and $\rho_{r_2}^{s_i}(t_k) = \|\boldsymbol{r}_2(t_k) - \boldsymbol{s}_i(t_k)\|$ are the ranges between the receivers and the emitting satellite,
- $\Delta dt_{1,2}(t_k)$ refers to the SD of receiver clock bias (with respect to the constellation time coordinates system), in seconds,
- $\Delta\tilde{\varepsilon}_{P_{1,2}}^{s_i}(t_k)$ is a random variable that corresponds to the SD of code pseudorange errors and of all corrections errors.

Similarly to what is done in Chapter 3, given that $\boldsymbol{r}_2(t_k)$ is known, the term $\rho_{r_2}^{s_i}(t_k)$ is on the left-hand side of Equation (5.3), while the unknown quantities are $\rho_{r_1}^{s_i}(t_k)$ and $\Delta dt_{1,2}(t_k)$.

The set of random variables $\Delta\tilde{\varepsilon}_{P_{1,2}}^{s_i}(t_k)$ are characterized in Section 3.3 as zero-mean Gaussian random variables whose standard deviations depend on the satellite elevation angles. These random variables are also assumed to be independent across satellites and across time. Therefore, Equation (5.3) can be written

$$\Delta\tilde{P}_{1,2}^{s_i}(t_k) - \rho_{r_2}^{s_i}(t_k) \sim \mathcal{N}\left(-\rho_{r_1}^{s_i}(t_k) + c \cdot \Delta dt_{1,2}(t_k)\,, \left(\sigma_{\tilde{P}}^{s_i}(t_k)\right)^2\right). \tag{5.4}$$

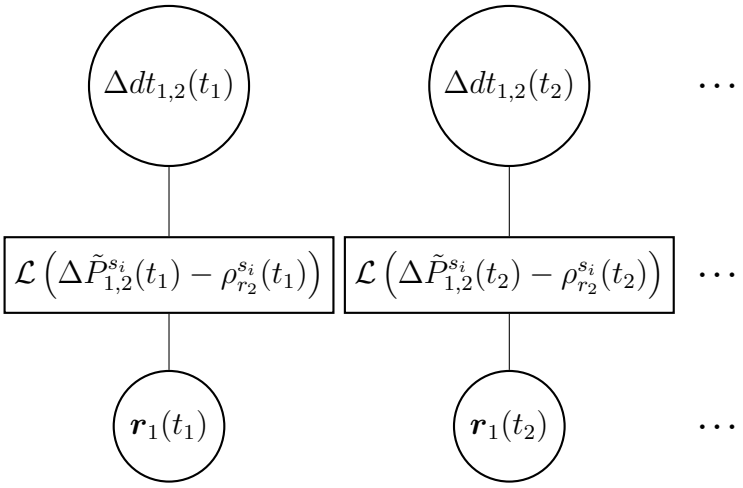

Figure 5.1: Representation of the first architecture for a single satellite s_i. To fully represent the FGO, similar factors must be added for each additional visible satellite.

In Equation (5.4), the mean depends on $\boldsymbol{r}_1(t_k)$ and $\Delta dt_{1,2}(t_k)$, which are jointly estimated. To do so, the likelihood function $\mathcal{L}\left(\Delta\tilde{P}^{s_i}_{1,2}(t_k) - \rho^{s_i}_{r_2}(t_k)\right)$ of $\boldsymbol{r}_1(t_k)$ and $\Delta dt_{1,2}(t_k)$ is defined, following the notations given in Equation (2.4). Therefore, the FGO consists of a state node representing the receiver position $\boldsymbol{r}_1(t_k)$ and a state node for the clock bias difference $\Delta dt_{1,2}(t_k)$, both connected to multiple SD of code pseudorange factors, one per satellite. The representation of this architecture is visible in Figure 5.1.

With the first FGO architecture now defined, the second is introduced, incorporating SD of carrier-phase observations.

5.2.2 Architecture 2: Code and Correlated TDCP

The second FGO architecture introduces TDCP observations alongside code pseudorange observations. Unlike the first architecture, this configuration incorporates temporal links between instants by differencing carrier-phase observations in time. As a result, each epoch is no longer treated in isolation, i.e., the FGO integrates information from both past and future observations to estimate the receiver's coordinates at a given instant. This temporal coupling should enhance positioning consistency and smoothness. This architecture serves as the benchmark for the third architecture.

When a temporal window of length w is considered, each time instant within the window is associated with a distinct receiver coordinates and clock bias difference. The unknown vector to estimate is thus of size $4 \times w$ and defined as

$$\boldsymbol{\theta} = \begin{pmatrix} \boldsymbol{r}_1(t_1) \\ \Delta dt_{1,2}(t_1) \\ \vdots \\ \boldsymbol{r}_1(t_w) \\ \Delta dt_{1,2}(t_w) \end{pmatrix} \in \mathbb{R}^{4\times w}. \tag{5.5}$$

This document may not be reproduced, modified, adapted, published, translated in any way, in whole or in part, nor disclosed to a third party without the prior written consent of ENAC. © 2025, ENAC

In this window, both receivers observe the same set of satellites. For each instant within this window, SD of code pseudorange and carrier-phase measurements are computed using the common observations. These differenced measurements provide the observations to be used to estimate $\boldsymbol{\theta}$ with an FGO.

In this architecture, SD of code pseudorange observations are used at each instant, similarly to the first architecture. The focus here, however, is on the construction of the TDCP observations between each pair of consecutive instants.

Similarly to the first architecture, at a given instant t_k is considered a first GPS receiver of unknown coordinates $\boldsymbol{r}_1(t_k) \in \mathbb{R}^3$ and a second GPS receiver of known coordinates $\boldsymbol{r}_2(t_k) \in \mathbb{R}^3$. At the same instant, a satellite of known coordinates $\boldsymbol{s}_i(t_k) \in \mathbb{R}^3$ is visible from both receivers, leading to SD of carrier-phase observations

$$\Delta\tilde{\Phi}^{s_i}_{1,2}(t_k) - \rho^{s_i}_{r_2}(t_k) = -\rho^{s_i}_{r_1}(t_k) + c \cdot \Delta dt_{1,2}(t_k) + \lambda \cdot \Delta N^{s_i}_{1,2}(t_k) + \Delta\tilde{\varepsilon}^{s_i}_{\Phi_{1,2}}(t_k) \tag{5.6}$$

where the new terms are defined as follows (all quantities are expressed in meters unless stated otherwise)

- $\Delta\tilde{\Phi}^{s_i}_{1,2}(t_k)$ is the SD of corrected carrier-phase measurement to satellite s_i,
- λ refers to the carrier's wavelength,
- $\Delta N^{s_i}_{1,2}(t_k)$ refers to the SD of integer number of cycles between the receivers and the satellite and is unitless,
- $\Delta\tilde{\varepsilon}^{s_i}_{\Phi_{1,2}}(t_k)$ is a random variable that corresponds to the SD of carrier-phase errors and all corrections errors.

All corrected SD of carrier-phase measurements for a given satellite s_i are grouped into a single vector of dimension w

$$\boldsymbol{\Delta\Phi}^{s_i}_{1,2} \triangleq \begin{pmatrix} \Delta\tilde{\Phi}^{s_i}_{1,2}(t_1) - \rho^{s_i}_{r_2}(t_1) \\ \vdots \\ \Delta\tilde{\Phi}^{s_i}_{1,2}(t_w) - \rho^{s_i}_{r_2}(t_w) \end{pmatrix}. \tag{5.7}$$

The set of random variables $\Delta\tilde{\varepsilon}^{s_i}_{\Phi_{1,2}}(t_k)$ are characterized in Section 3.3 as zero-mean Gaussian random variables whose standard deviations is the same for all satellites. These random variables are also assumed to be independent across satellites and across time. Therefore, the Gaussian random vector of dimension w made of SD of corrected carrier-phase observations from satellite s_i is given by

$$\boldsymbol{\Delta\Phi}^{s_i}_{1,2} \sim \mathcal{N}\left(\begin{pmatrix} -\rho^{s_i}_{r_1}(t_1) \\ \vdots \\ -\rho^{s_i}_{r_1}(t_w) \end{pmatrix} + c \begin{pmatrix} \Delta dt_{1,2}(t_1) \\ \vdots \\ \Delta dt_{1,2}(t_w) \end{pmatrix} + \lambda \begin{pmatrix} \Delta N^{s_i}_{1,2} \\ \vdots \\ \Delta N^{s_i}_{1,2} \end{pmatrix}, \sigma^2_{\tilde{\Phi}} \boldsymbol{I}_w \right) \tag{5.8}$$

where the value of $\sigma_{\tilde{\Phi}}$ is given in Equation (3.86).

In Equation (5.8), the mean depends on the first receiver coordinates at all instants, i.e., $\boldsymbol{r}_1(t_1), \ldots, \boldsymbol{r}_1(t_w)$, on the SD of receiver clock bias at all instants, i.e., $\Delta dt_{1,2}(t_1), \ldots, \Delta dt_{1,2}(t_w)$ and on the SD of integer ambiguities $\Delta N_{1,2}^{s_i}$. However, because ambiguities are constant over time in the absence of CS (i.e., when the carrier-phase tracking is continuous and uninterrupted for both receivers), a temporal difference can be applied to eliminate them, leading to TDCP observations. Note that a method for detecting CS is presented in Chapter 3. Alternatively, any other CS detection method available in the literature may be employed. To express temporal differencing in a form consistent with Section 2.4.1, a difference matrix $\boldsymbol{D}$ is introduced to model consecutive instants differencing. More formally, the difference matrix $\boldsymbol{D} \in \mathcal{M}_{w-1,w}(\mathbb{R})$ is given by

$$\boldsymbol{D} = \begin{pmatrix} -1 & 1 & & \\ & \ddots & \ddots & \\ & & -1 & 1 \end{pmatrix} \tag{5.9}$$

and enables the computation of temporal differences between successive instants of SD of carrier-phase observations. Multiplying Equation (5.8) by $\boldsymbol{D}$ on the left yields the vector of consecutive TDCP observations for satellite s_i, i.e.,

$$\boldsymbol{D}\boldsymbol{\Delta}\boldsymbol{\Phi}_{1,2}^{s_i} \sim \mathcal{N}\left(\begin{pmatrix} \nabla_{1,2}\left(-\rho_{r_1}^{s_i} + c \cdot \Delta dt_{1,2}\right) \\ \vdots \\ \nabla_{w-1,w}\left(-\rho_{r_1}^{s_i} + c \cdot \Delta dt_{1,2}\right) \end{pmatrix}, \sigma_{\tilde{\Phi}}^2 \boldsymbol{D}\boldsymbol{D}^\mathsf{T}\right). \tag{5.10}$$

According to the general definition of the FGO in Section 2.1.2.3, the joint density of the TDCP observations admits a factorized representation if and only if the components are independent. The covariance matrix of this random vector is the tridiagonal matrix

$$\mathbb{V}\left[\boldsymbol{D}\boldsymbol{\Delta}\boldsymbol{\Phi}_{1,2}^{s_i}\right] = \sigma_{\tilde{\Phi}}^2 \boldsymbol{D}\boldsymbol{D}^\mathsf{T} = \sigma_{\tilde{\Phi}}^2 \begin{pmatrix} 2 & -1 & & \\ -1 & 2 & \ddots & \\ & \ddots & \ddots & -1 \\ & & -1 & 2 \end{pmatrix}. \tag{5.11}$$

This matrix is real, symmetric and positive-definite since $\boldsymbol{D}$ satisfies the hypothesis given in Section 2.4.1. The key contribution of this chapter is the observation that the resulting matrix is not diagonal, indicating that the consecutive TDCP observations are correlated across epochs. Therefore, a single factor incorporating the full vector of TDCP observations from a given satellite is used instead, i.e., corresponding to the likelihood function $\mathcal{L}\left(\boldsymbol{D}\boldsymbol{\Delta}\boldsymbol{\Phi}_{1,2}^{s_i}\right)$ of $\boldsymbol{\theta}$ is defined, following the notations given in Equation (2.4).
The representation of this architecture is visible in Figure 5.2.

Focusing on the first and second components of the random vector given in Equation (5.10), i.e., on the first and second TDCP observations $\nabla_{1,2}\left(\Delta\tilde{\Phi}_{1,2}^{s_i} - \rho_{r_2}^{s_i}\right)$ and

This document may not be reproduced, modified, adapted, published, translated in any way, in whole or in part, nor disclosed to a third party without the prior written consent of ENAC. © 2025, ENAC

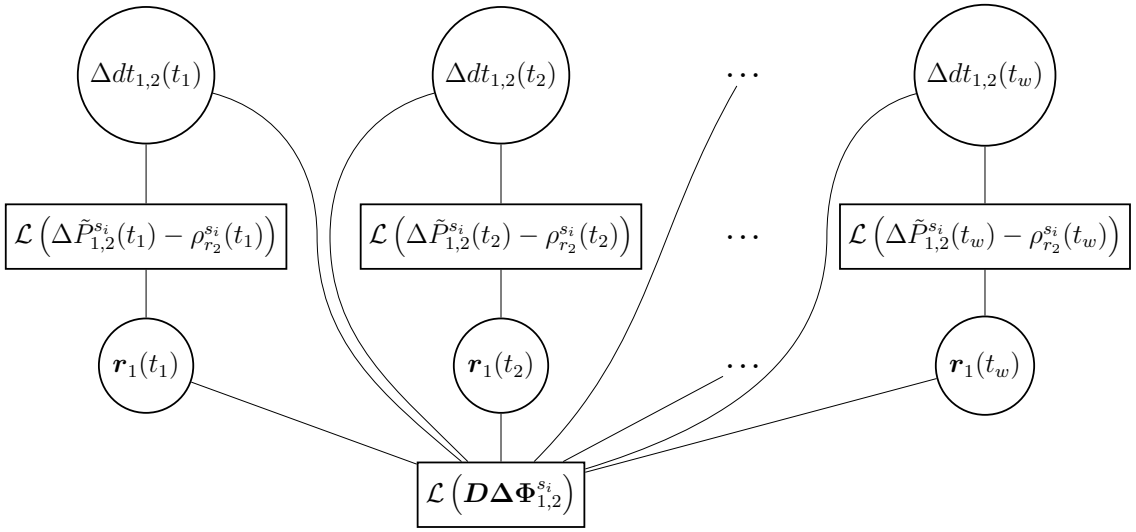

Figure 5.2: Representation of the second architecture for a single satellite s_i. To fully represent the model, similar factors must be added for each additional satellite.

$\nabla_{2,3}\left(\Delta\tilde{\Phi}^{s_i}_{1,2} - \rho^{s_i}_{r_2}\right)$, both expressions involve the SD of carrier-phase observation at instant t_2, which induces a non-zero covariance.

The linear correlation coefficient between these two TDCP observations is equal to

$$\frac{\mathrm{Cov}\left(\nabla_{1,2}\left(\Delta\tilde{\Phi}^{s_i}_{1,2} - \rho^{s_i}_{r_2}\right), \nabla_{2,3}\left(\Delta\tilde{\Phi}^{s_i}_{1,2} - \rho^{s_i}_{r_2}\right)\right)}{\sqrt{\mathbb{V}\left[\nabla_{1,2}\left(\Delta\tilde{\Phi}^{s_i}_{1,2} - \rho^{s_i}_{r_2}\right)\right]}\sqrt{\mathbb{V}\left[\nabla_{2,3}\left(\Delta\tilde{\Phi}^{s_i}_{1,2} - \rho^{s_i}_{r_2}\right)\right]}} = \frac{-\sigma^2_{\tilde{\Phi}}}{\sqrt{2\sigma^2_{\tilde{\Phi}}}\sqrt{2\sigma^2_{\tilde{\Phi}}}} = -\frac{1}{2}. \tag{5.12}$$

It is worth noting that TDCP observations are most commonly constructed by differencing consecutive carrier-phase observations. However, other formulations also exist in the GNSS literature, where non-consecutive epochs are differenced instead. If a linear bijection exists between two such vectors of TDCP measurements, then, as demonstrated in Equation (2.46), the underlying estimation problem remains fundamentally unchanged, given that the TDCP observation equations are approximately linear. These different formulations are equivalent and should produce identical state estimates in the absence of modeling errors and strong nonlinearity. This observation reinforces the generality and flexibility of the proposed approach.

With the second FGO architecture being defined, the third architecture is introduced.

5.2.3 Architecture 3: Code and Uncorrelated TDCP

The third architecture is similar to the second, with the exception that correlations between TDCP observations are omitted, i.e., a misspecified model is assumed, and the covariance matrix of the TDCP observations is assumed to satisfy

$$\mathbb{V}\left[\boldsymbol{D}\boldsymbol{\Delta}\boldsymbol{\Phi}^{s_i}_{1,2}\right] \overset{\text{assumed}}{=} 2\sigma^2_{\tilde{\Phi}}\boldsymbol{I}_{w-1}. \tag{5.13}$$

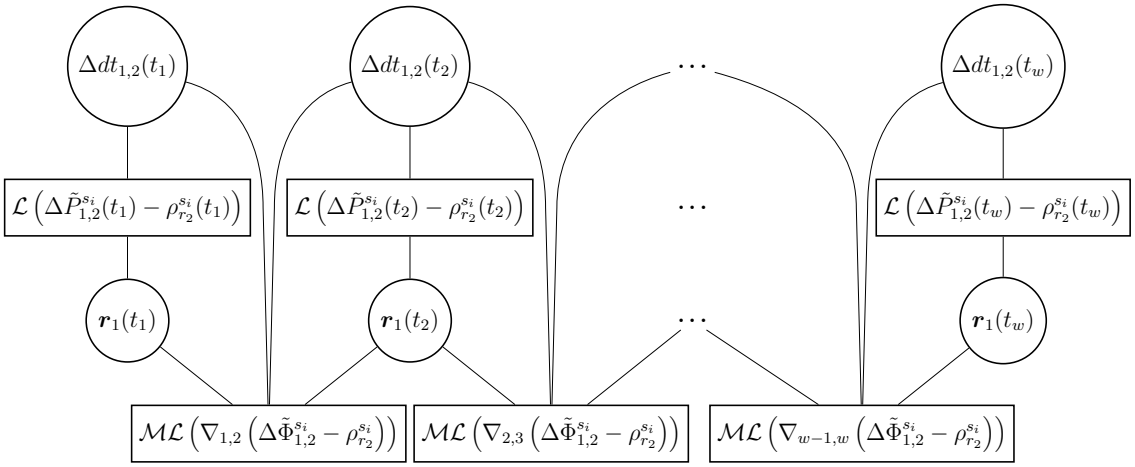

Figure 5.3: Representation of the third architecture for a single satellite s_i. To fully represent the model, similar factors must be added for each additional satellite.

This diagonal covariance structure neglects the temporal dependencies between consecutive TDCP observations and leads to a simplified but misspecified architecture. For this reason, the misspecified likelihood notation $\mathcal{ML}$ is used, and the likelihood function can be written as a product of likelihood functions, i.e., the TDCP observations are represented by $w-1$ distinct scalar factors, while in architecture 2, the TDCP are contained within a single factor of dimension $w-1$.

The FGO representation of this architecture is visible in Figure 5.3. The three FGO architectures are summarized in Table 5.1. The three FGO architectures being defined, the following section introduces experiments to evaluate the impact of these design choices.

Table 5.1: Overview of the considered FGO architectures.

Architecture	Code pseudorange	TDCP	TDCP Correlations
1	Yes	No	N.A.
2	Yes	Yes	Yes
3	Yes	Yes	No

5.3 Experiments

Following the definition and structural description of the three FGO architectures, this section presents an empirical evaluation of their performance using both real and synthetic GNSS data, in order to analyze their behavior under varying observational and modeling conditions.

This document may not be reproduced, modified, adapted, published, translated in any way, in whole or in part, nor disclosed to a third party without the prior written consent of ENAC. © 2025, ENAC

5.3.1 Context

This evaluation relies on both real and synthetic GNSS datasets, consisting of GPS L1 code pseudorange and carrier-phase observations. The real data are collected from two closely located International GNSS Service (IGS) network receivers, TLSE and TLSG, both located in Toulouse, France, shown in Figure 3.8 and Figure 3.11. The experiments use data from January 1, 2024 at a rate of 1 Hz. The coordinates of both receivers are computed using the RTKLIB [68] software through a static PPP solution, applied to multi-frequency GPS observations with forward-backward filtering and solid Earth tide corrections. This procedure yields millimeter-level positioning accuracy. TLSG serves as a reference station with known coordinates, while TLSE is the receiver whose position is estimated using FGO. The RTKLIB-derived position of TLSE is used as ground truth to compute positioning errors. The real GPS L1 carrier-phase observations are verified to be CS-free. This is done by means of CS detection and correction using RTKLIB with a forward-backward Kalman Filter (KF), using a full day of multi-constellation set of observations. These CS-free carrier-phase observations enables the construction of reliable TDCP observations. The real code pseudorange and carrier-phase observations are first corrected by means of PRX[1]. Then, for real observations, SD measurements are formed between TLSE and TLSG using these corrected code pseudorange and carrier-phase observations on the GPS L1 band. In the case of synthetic data, the SD measurement noise and error properties follow the statistical characterization described in Section 3.3. The resulting SD observations serve as inputs to the three FGO architectures evaluated in this section. For each value of the temporal window length w, the full day of observations is segmented into non-overlapping temporal windows of size w instants. Within each window, the observations are processed independently using the three FGO architectures. This yields a sequence of estimated receiver positions, one per instant. By comparing these estimates to the known ground-truth positions, a positioning error is computed for each instant. These error values across all windows are then aggregated to construct distributions of positioning errors, reflecting the performance of each architecture at the given window size. This non-overlapping windowing approach ensures statistical independence between segments and avoids multiple estimates of a same instant due to overlapping windows. This experimental setup provides a consistent and realistic framework for analyzing the behavior and accuracy of different FGO architectures. A more detailed description of the experimental setup is provided in Chapter 3.

5.3.2 Impact of Omitted Correlations

In the following experiments, the three FGO architectures are evaluated and compared across three distinct scenarios, characterized by the number of temporal instants w, taking the values 2, 10 and 60, corresponding to 2, 10 and 60 s of observations, respectively. For

[1]The `prx` tool, available at `github.com/jtec/prx`, is a parser for RINEX files that produces enriched outputs including precise satellite positions, corrected observations, and other relevant data.

Table 5.2: Distribution of the Euclidean norm of positioning errors obtained from **synthetic** observations. Each row corresponds to one of the three FGO architectures, and each column corresponds to a different temporal window size w.

Arch.	$w = 2$	$w = 10$	$w = 60$
1	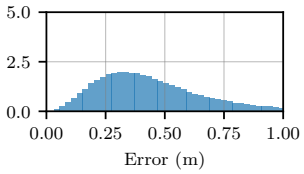	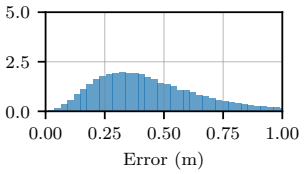	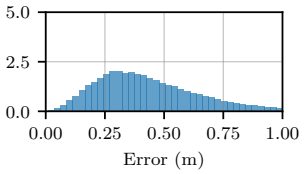
2	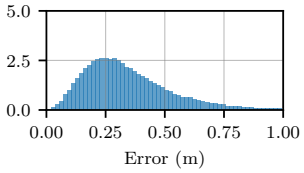	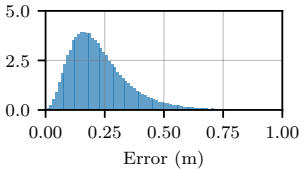	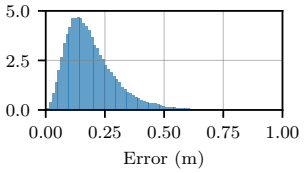
3	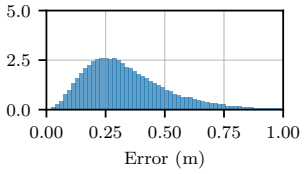	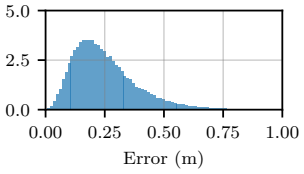	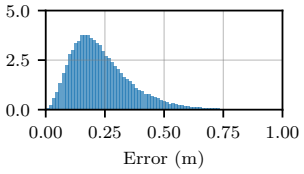

the case with only 2 instants, no correlations are omitted, as each satellite contributes a single TDCP observation, ensuring full correlation representation. The same applies to the first architecture, as it is made of SD of code pseudorange only. However, in the cases with 10 and 60 instants, correlations between TDCP are omitted in the third architecture. This omission is expected to introduce differences in the performance of this architecture, making these scenarios particularly relevant for analyzing the trade-offs between model complexity and estimation accuracy.

In Table 5.2 and Table 5.3 are visible the distribution of positioning errors, measured as the Euclidean norm of the position error, for synthetic and real data, respectively. These distributions are shown for all three FGO architectures across the three temporal window lengths.

To complement these visual distributions, Table 5.4 and Table 5.5 provide summary statistics of the positioning errors for synthetic and real data, respectively. For each FGO architecture and each temporal window size w, the mean, median, the 67th and 95th percentiles of the Euclidean positioning error are reported. These quantitative metrics allow for a more direct comparison of the performance across configurations.

For both the synthetic and real datasets, the distribution of positioning errors obtained using the first architecture remains unchanged across all three temporal window lengths ($w = 2$, 10, and 60). This consistency is expected and can be directly explained by

This document may not be reproduced, modified, adapted, published, translated in any way, in whole or in part, nor disclosed to a third party without the prior written consent of ENAC. © 2025, ENAC

Table 5.3: Distribution of the Euclidean norm of positioning errors obtained from **real** observations. Each row corresponds to one of the three FGO architectures, and each column corresponds to a different temporal window size w.

Arch.	$w = 2$	$w = 10$	$w = 60$
1	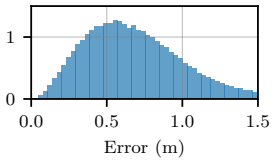	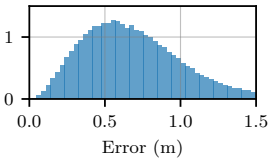	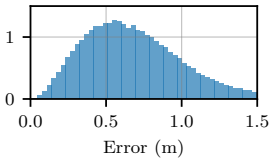
2	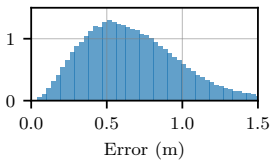	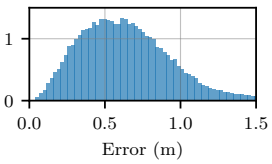	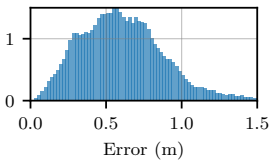
3	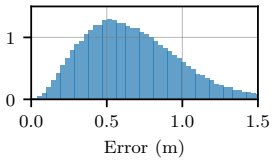	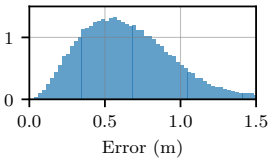	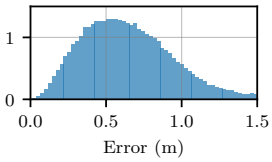

Table 5.4: Positioning error statistics as a function of the FGO architecture and the number of instants w, using **synthetic** observations.

Arch.	w	Mean (m)	Median (m)	67th perc. (m)	95th perc. (m)
1	2	0.450	0.405	0.510	0.911
	10	0.450	0.405	0.510	0.911
	60	0.450	0.405	0.510	0.911
2	2	0.345	0.310	0.391	0.700
	10	0.227	0.203	0.256	0.465
	60	0.192	0.170	0.216	0.398
3	2	0.345	0.310	0.391	0.700
	10	0.254	0.226	0.287	0.519
	60	0.239	0.213	0.270	0.489

Table 5.5: Positioning error statistics as a function of the FGO architecture and the number of instants w, using **real** observations.

Arch.	w	Mean (m)	Median (m)	67th perc. (m)	95th perc. (m)
1	2	0.694	0.647	0.802	1.324
	10	0.694	0.647	0.802	1.324
	60	0.694	0.647	0.802	1.324
2	2	0.681	0.637	0.789	1.293
	10	0.646	0.613	0.750	1.207
	60	0.613	0.588	0.716	1.124
3	2	0.681	0.637	0.789	1.293
	10	0.659	0.619	0.765	1.240
	60	0.654	0.616	0.760	1.226

the absence of TDCP factors in this architecture. Since only SD of code pseudorange observations are used, the structure of the FGO is invariant with respect to the value of w. As a result, regardless of the window size w, the same observations are used and the same estimation process is applied, leading to identical positioning errors.

In contrast, architectures 2 and 3 incorporate TDCP observations, and their error distributions show a dependency on the temporal window length. This is particularly visible in the synthetic dataset case. For these architectures, the error distributions become progressively sharper and more concentrated near zero as the value of w increases. This trend illustrates the benefit of using a longer temporal window: by incorporating information across multiple instants, the system becomes more constrained, and the positioning estimates are more accurate. In particular, the transition from $w = 2$ to $w = 60$ leads to significant improvements in the sharpness of the distributions, confirming that longer temporal windows have a positive effect.

It can also be observed that the benefit of incorporating TDCP is more pronounced in the synthetic data than in the real data. In the synthetic case, where the models are perfectly respected and no unmodeled noise is present, the use of TDCP with a large temporal window leads to a significant reduction in positioning error. However, for real data, the improvement brought by TDCP is less substantial. This is likely due to the fact that real-world observations deviate from the idealized models, i.e., errors may exist in the true receiver position, satellite ephemerides, and in the statistical properties of the observation noise, thereby limiting the gain achievable through TDCP integration.

The distinction between correlated and uncorrelated architectures becomes particularly important as w increases. For $w = 10$ and $w = 60$, the omitted correlations in architecture 3 leads to degraded performance in comparison with architecture 2. The error distributions are broader and less concentrated near zero compared to architecture 2, where the TDCP correlations are considered. This observation highlights the importance of considering the correlations of TDCP observations when working with long temporal windows.

This document may not be reproduced, modified, adapted, published, translated in any way, in whole or in part, nor disclosed to a third party without the prior written consent of ENAC. © 2025, ENAC

Overall, the best results, characterized by the sharpest distributions and the highest density of small errors, are obtained with architecture 2 at $w = 60$. This configuration combines long temporal window with correct modeling of TDCP correlations, leading to better positioning accuracy. The advantage is particularly visible in the synthetic dataset.

Complementary results showing the horizontal and vertical components of the positioning error from the same experiment are visible in Appendix E. They confirm the benefits of extended temporal windows and of considering correlations, improving both horizontal and vertical accuracy.

The following experiment highlights the relationship between the average positioning error and the size of the temporal window w in more details.

5.3.3 Impact of Time Window Length

This experiment analyzes how positioning accuracy evolves with increasing temporal window size w, ranging from 2 to 210 instants, corresponding to a maximum temporal span of 3 minutes and 30 seconds. For each value of w, the dataset collected on January 1, 2024 is processed using the three FGO architectures. The aim is to provide insights into how temporal window and model fidelity jointly influence positioning performance.

In Figure 5.4 is visible the evolution of the mean of the Euclidean norm of the positioning error, as a function of the temporal window length w, for all three FGO architectures in the case of synthetic observations. In Figure 5.5 are visible the mean positioning error and the 95th percentile in the case of real observations. These figures reveal how increasing the temporal window length w influences accuracy, under both synthetic and real observations.

The corresponding horizontal and vertical positioning errors for this experiment are provided in Appendix E.

Except for architecture 1, which uses only code pseudorange measurements and remains unaffected by the temporal window size, increasing the temporal window length w leads to a reduction in positioning error. This is evident in both the synthetic and real datasets, and holds whether or not TDCP correlations are considered. However, the extent of improvement decreases progressively with larger w, as indicated by the flattening of the error curves.

On the other hand, the benefits of considering TDCP correlations become increasingly apparent as the window size w increases. In the real dataset in particular, the decrease in error continues at a more favorable rate when TDCP correlations are included. This observation supports the use of longer temporal windows in real-world scenarios. In contrast, for architecture 3 that omits correlation modeling, the improvement in accuracy is more or less constant for approximately $w \geq 30$, indicating that without considering TDCP correlations, increasing the temporal window length provides limited benefit.

These findings emphasize the critical role of considering TDCP correlations in FGO-based GNSS positioning.

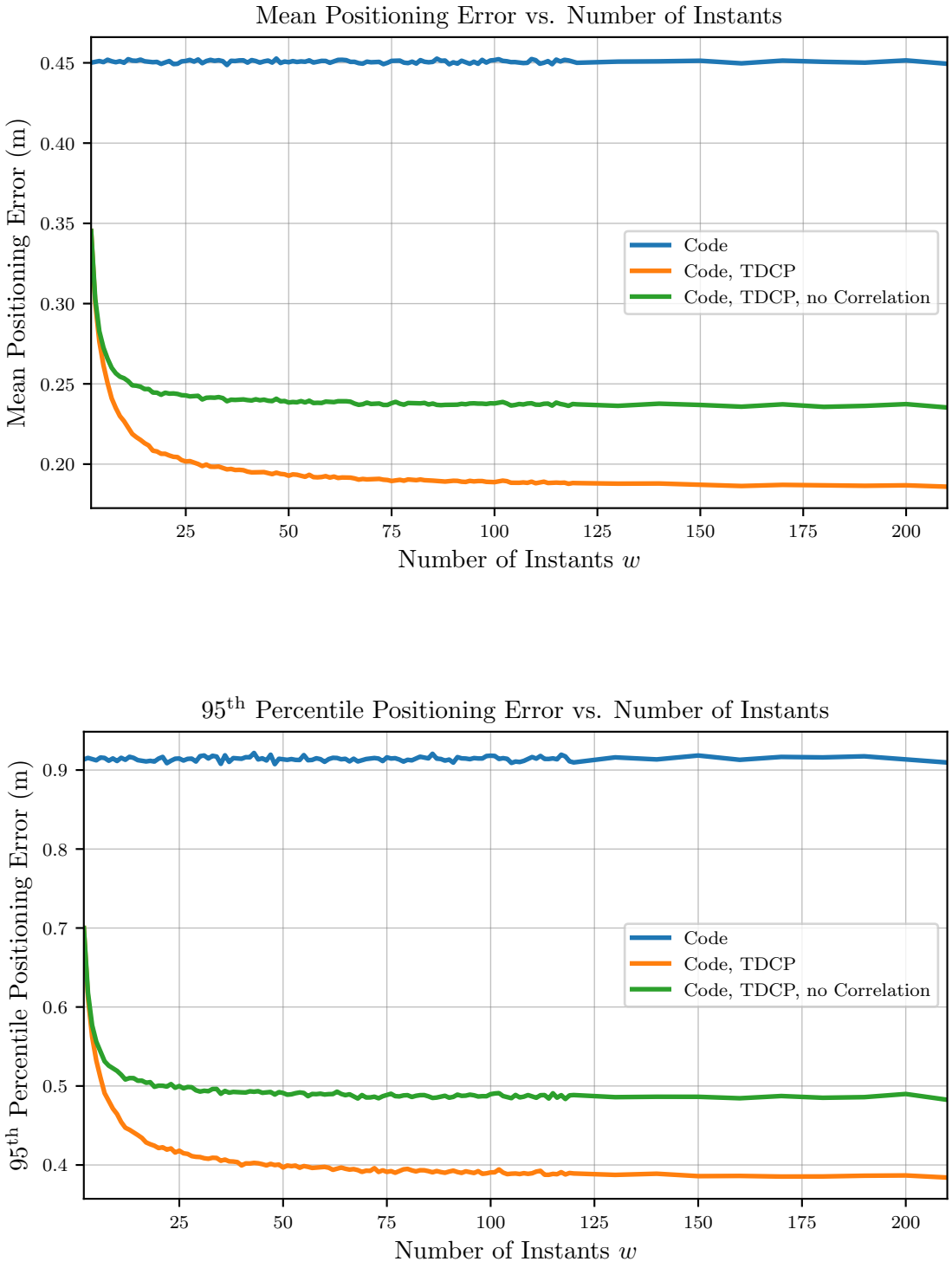

Figure 5.4: Positioning errors for **synthetic** observations as a function of temporal window size w, for all three FGO architectures. Top: mean positioning error. Bottom: 95th percentile positioning error. The curve is plotted with points sampled every 1 unit from $w = 2$ to $w = 120$ and every 10 units from $w = 120$ to $w = 220$, resulting in slower variations in the second part.

This document may not be reproduced, modified, adapted, published, translated in any way, in whole or in part, nor disclosed to a third party without the prior written consent of ENAC. © 2025, ENAC

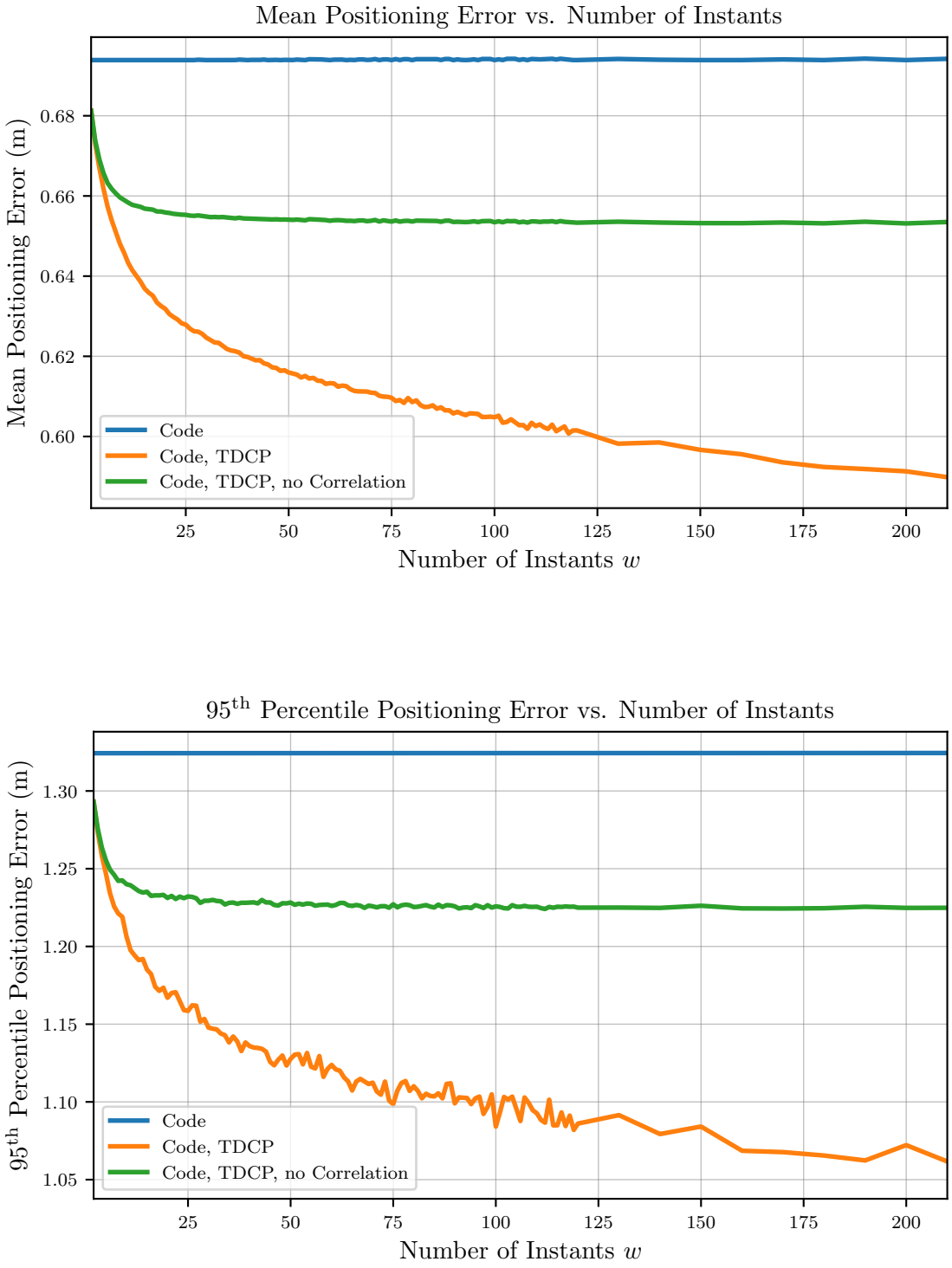

Figure 5.5: Positioning errors for **real** observations as a function of temporal window size w, for all three FGO architectures. Top: mean positioning error. Bottom: 95th percentile positioning error. The curve is plotted with points sampled every 1 unit from $w = 2$ to $w = 120$ and every 10 units from $w = 120$ to $w = 220$, resulting in slower variations in the second part.

The results obtained in the real observation case are not as important than in the synthetic case. The two receivers TLSE and TLSG are not made by the same company, so internal differences of manufacturing might be a potential source of bias when computing SD of observations. Also, the results obtained in the vertical direction visible in Table E.4 indicate a bias in the positioning, as the modes of all distributions do not coincide with zero. Therefore, a finer modeling of SD of code pseudorange could be beneficial to this study. In particular, Equation (3.85) could adopt a different strategy regarding the results obtained in Figure 3.13.

Finally, the numerical results show that for a temporal window length of 60 s, the mean global positioning error is reduced by approximately 5 cm when considering correlations. This accuracy improvement continues for larger values of w, demonstrating the practical advantage of using large windows in combination with consideration of TDCP correlations.

5.4 Conclusion

This final chapter investigates the role of temporal correlations in TDCP observations within the context of FGO-based GNSS positioning. While TDCP is recognized for its precision in relative positioning, the underlying temporal correlations between consecutive measurements are often overlooked in the GNSS literature and in practice. Through a series of experiments, across synthetic and real datasets, and under various temporal window lengths, this chapter demonstrates that neglecting these correlations can degrade positioning performance, particularly as the temporal context increases.

The results consistently show that architectures incorporating a proper correlation model achieve substantially lower positioning errors compared to those that treat TDCP observations as independent. This performance gap becomes increasingly pronounced with longer temporal windows, confirming that the benefit of smoothing over time can only be fully realized when the correlation structure is accurately modeled.

While this work focuses on improving TDCP modeling within the GNSS domain, it also opens several avenues for future research. First, the FGO framework naturally allows for the integration of heterogeneous sensor modalities. Additional factors derived from Inertial Measurement Unit (IMU), odometry, barometers, or visual-inertial systems could be introduced to further constrain the trajectory, especially in GNSS-degraded environments. Second, incorporating a dynamic motion model could enhance smoothing and robustness by regularizing the solution based on physical assumptions about the receiver's motion (e.g., constant position or velocity). These perspectives point to a rich landscape of future developments for achieving better positioning in complex real-world scenarios.

This document may not be reproduced, modified, adapted, published, translated in any way, in whole or in part, nor disclosed to a third party without the prior written consent of ENAC. © 2025, ENAC

Conclusion and Future Works

1 Conclusion

This thesis investigates the application of Factor Graph Optimization (FGO) to precise Global Navigation Satellite System (GNSS) positioning. While FGO is a general framework for optimization problems, its use in the GNSS community is often more interpreted as a way to incorporate temporal information over multiple instants within an estimation problem. The work presented here bridges this gap, offering both a theoretical and experimental exploration of FGO in the context of high-precision GNSS positioning, with a particular focus on the carrier-phase observation and Time-Differenced Carrier Phase (TDCP) modeling.

Carrier-phase observations are one way to target precise positioning because of their high accuracy. However, their use introduces challenges, especially the presence of Cycle Slip (CS), which act as unknown biases in the measurements. One of the core aims of this thesis is to investigate the integration of carrier-phase observations in FGO architectures, while properly handling the complexities introduced by TDCP modeling and the consequences of unmodeled correlations.

The contributions of this thesis span theoretical formalizations and practical algorithms, all validated through simulation and real-data experiments.

Understanding How FGO can be Used for Precise GNSS Positioning: The first objective is to explore the diversity of how FGO is used in the GNSS literature. While FGO is inherently a flexible optimization framework, its application in GNSS takes multiple forms, depending on which measurements are included and how variables are connected over time. Through this study, it is clear that TDCP plays a central role in many GNSS-FGO configurations due to its ability to provide positioning constraints with high precision. The thesis also investigates linear combinations of factors, establishing criteria to determine which combinations lead to the same estimator, which should be avoided, and which require case-by-case analysis due to the absence of general results. Additionally, the study of linear combinations and restrictions on variables offers a generalization of differential GNSS positioning within the FGO framework.

This document may not be reproduced, modified, adapted, published, translated in any way, in whole or in part, nor disclosed to a third party without the prior written consent of ENAC. © 2025, ENAC

Characterization of Code Pseudorange and Carrier-Phase Observations: Another important contribution of this thesis lies in the detailed characterization of code pseudorange and carrier-phase observations, as well as their single differences. Presented in Chapter 3, this analysis provides distributions to construct synthetic observations. The noise properties of both code pseudorange and carrier-phase observations are examined, and their behavior under Single Difference (SD), commonly used to remove common biases in observations, is modeled. To support this characterization, numerous assumptions are stated clearly and explicitly. This formalization ensures that the resulting models are transparent and reproducible. It is shown that the SD of code pseudoranges exhibit noise on the order of meters, with a clear dependency on satellite elevation, while the SD of carrier-phase observations display lower noise, with no observable dependency on elevation.

Handling the Cycle Slip Problem: In Chapter 3, since TDCP observations are sensitive to CS, a fault detection and identification strategy is proposed, specifically tailored to FGO. A binary hypothesis test is developed to detect the presence of CS using a residual-based statistic, and a multi-hypothesis approach is used for their identification. The detection strategy relies on the Neyman–Pearson lemma, ensuring that the test maximizes the probability of detection for a given false alarm probability. The distribution of the test statistic, defined as the squared norm of the residual vector, is derived using Cochran's theorem, which states that this quantity follows a chi-squared distribution under Gaussian assumptions. This knowledge enables threshold selection based on analytical expressions of the noncentral and central chi-squared probability density functions. As a result, the proposed method enables safe and reliable use of TDCP measurements within the FGO framework. To validate the approach, a two-instant FGO using SD of code pseudorange and TDCP is constructed, and a false alarm probability of 0.1. In the worst-case CS scenario, the empirical false alarm rate matches the target, and the probability of missed detection reaches 0.88, highlighting that while the method is statistically consistent, a single CS of amplitude 1 on the least favorable satellite remains particularly difficult to detect. Regarding identification performance, the probability of correctly identifying the faulty satellite ranges from 0.12 to 0.17 across all satellites, which is far from perfect, reflecting the inherent difficulty of identifying a single CS of amplitude 1. Moreover, the approach is general and can be extended to detect and identify other types of faults beyond CS.

This work is supported by a peer-reviewed conference paper

[8] H. Cherfi, J. Lesouple, J. Solà, and P. Thevenon, "Single Frequency GNSS Carrier Phase Cycle Slip Detection and Identification Using a Factor Graph Approach," in *Proc. ION Pacific PNT 2024*, (Honolulu, HI, USA), pp. 344 – 355, Apr. 2024.

Uncertainty Quantification of the First Position Fix in Displacement-Based TDCP Modeling: TDCP observations are constructed by differencing two carrier-phase measurements from the same satellite at two instants. Although TDCP is often used for displacement or velocity estimation, its formulation still depends on the GNSS receiver's coordinates at both instants. In particular, when TDCP is modeled as a function of displacement, it requires a restriction of the model. The quality of the first position fix is never perfect in practical implementations. Uncertainty Quantification (UQ) of the initial position on how it propagates through displacement estimates is provided in Chapter 4, particularly by providing maximum displacement estimation error due to this first fix. This UQ offers guidance for initialization strategies in TDCP-based odometry systems. For the considered geometry, i.e., the TLSE receiver on January 1st, 2024, at 12:00 UTC, a receiver position error of 10 m introduces a worst-case bias of approximately 1 mm in the estimated displacement when using TDCP measurements over a temporal interval of 1 s from visible satellites.

This work is supported by a peer-reviewed journal article

[70] H. Cherfi, J. Lesouple, J. Solà, and P. Thevenon, "Uncertainty Quantification of First Fix in a Time-Differenced Carrier Phase Observation Model," *Sensors*, vol. 25, May 2025.

Assessing the Impact of TDCP Correlations: A major contribution of this thesis is the investigation of temporal correlations between TDCP observations. In multi-instants FGO problems, TDCP measurements, due to their construction from carrier-phase observations, are correlated. In much of the GNSS literature, these correlations are ignored, as TDCP factors are modeled as independent. Chapter 5 introduces three FGO architectures, with and without proper modeling of TDCP correlations. Through experiments on both synthetic and real observations, it is shown that properly accounting for these correlations improves positioning accuracy. The benefits of correlation modeling are particularly pronounced when longer temporal windows are used. Larger temporal windows provide better positioning results, and they also amplify the impact of unmodeled correlations. The results demonstrate that combining long temporal windows with accurate correlation modeling yields the most precise positioning. Importantly, this improvement is achieved without introducing additional observations or variables, as it simply involves modifying the weighting of the optimization problem to account for these correlations. For synthetic data consistent with the observation models characterized in Chapter 3, considering TDCP correlations reduces the overall positioning error by approximately 5 cm when using temporal windows longer than 30 s. Moreover, increasing the window size beyond this value offers no significant additional benefit.

This document may not be reproduced, modified, adapted, published, translated in any way, in whole or in part, nor disclosed to a third party without the prior written consent of ENAC. © 2025, ENAC

2 Future Works

The contributions presented in this thesis open up several directions for future research.

Cycle Slip Handling: The proposed FGO-based CS detection and identification method can be extended to include more diverse observation types, such as Inertial Measurement Unit (IMU) observations or motion models, which may improve obtained results. Longer temporal windows could also be leveraged to increase detection reliability. Furthermore, the fault detection strategy could be refined for scenarios where a worst-case fault may not exist or cannot be anticipated, raising questions about detection under weaker assumptions. Finally, an alternative test statistic could be explored based on the full residual vector directly, rather than relying on a function of its norm.

First Fix Uncertainty in Displacement-Based TDCP: The UQ carried out in this thesis is based on a fixed geometry and a specific satellite configuration. Extending this study to multiple locations, GNSS constellations, or even to Low Earth Orbit (LEO) satellites, would provide more general conclusions. Additionally, simplified TDCP models widely used in the GNSS community, such as those assuming fixed receiver-to-satellite unit vectors, could be compared to the full TDCP model to assess how such approximations impact displacement estimation accuracy in practice.

TDCP Correlation Modeling: Further experiments could explore the benefits of correlation modeling under different conditions, such as very long temporal windows or low sampling rates. While correlation modeling may have an impact on computation time, it would be useful to quantify the exact trade-off between computational cost and positioning performance, particularly for real-time applications or embedded systems with limited resources.

Finally, all methods presented in this thesis could be evaluated using a standalone receiver instead of a differential framework. Additionally, consumer-grade GNSS receivers, such as those found in smartphones, where observation quality is lower and modeling accuracy becomes even more critical, could be considered, targeting the Google Smartphone Decimeter Challenge (GSDC).

In summary, this thesis contributes to the deeper understanding and practical enhancement of FGO-based precise GNSS positioning. It highlights both the benefits and challenges of working with ambiguous carrier-phase observations, especially the TDCP. By addressing fault detection and identification, UQ, and correlation modeling within a unified FGO framework, this work lays the foundation for flexible GNSS positioning systems that can be extended to future applications.

Discussion and Perspectives This thesis relies on key assumptions about the nature of the estimated state variables and the probabilistic models used in the factors.

In particular, all variables are assumed to belong to Euclidean spaces, enabling the application of classical optimization techniques. While the space of 3D rotations lacks an Euclidean structure and instead forms a Lie group, the thesis avoids fusion with IMU data for this reason, although future work could incorporate IMU pre-integration to add motion constraints. Each factor is modeled as the likelihood function of a Gaussian random vector, aligning with standard GNSS practices and allowing for a well-defined Maximum Likelihood Estimator (MLE) in Euclidean space. Ambiguity resolution techniques like Least Squares Ambiguity Decorrelation Adjustment (LAMBDA) [29] and bootstrapping [87] are not addressed due to their incompatibility with the Euclidean-space formulation and because the use of TDCP inherently cancels integer ambiguities. A potential research direction would be to develop optimization methods on spaces with weaker algebraic structure than Euclidean spaces, allowing these algorithms to be naturally integrated into the FGO framework. Additionally, GNSS positioning benefits from well-established observation models that capture the physics of signal propagation, unlike machine learning approaches that are typically used when such models are unavailable. While combining FGO and machine learning remains an open question, it could offer avenues to refine difficult-to-model effects. The computational cost of FGO is acknowledged, and although the thesis focuses on post-processing, thus removing real-time constraints, future work could explore solver optimization. A promising direction would be to test the methods on low-cost receivers, such as smartphones, to assess their scalability and limitations.

This document may not be reproduced, modified, adapted, published, translated in any way, in whole or in part, nor disclosed to a third party without the prior written consent of ENAC. © 2025, ENAC

Acronyms

A-GNSS Assisted GNSS

BPSK Binary Phase Shift Keying

CDMA Code Division Multiple Access

CS Cycle Slip

C/N0 Carrier-to-noise Density Ratio

DD Double Difference

DLL Delay Lock Loop

DGNSS Differential GNSS

DOP Dilution Of Precision

DSSS Direct Sequence Spread Spectrum

ECEF Earth-Centered Earth-Fixed

ECI Earth-Centered Inertial

EKF Extended Kalman Filter

ENU East, North, Up

FFT Fast Fourier Transform

FGO Factor Graph Optimization

GDOP Geometric Dilution Of Precision

GEO Geostationary Earth Orbit

GNSS Global Navigation Satellite System

GPS Global Positioning System

GSDC Google Smartphone Decimeter Challenge

HDOP Horizontal Dilution Of Precision

IGS International GNSS Service

ILS Integer Least Squares

IMU Inertial Measurement Unit

KF Kalman Filter

This document may not be reproduced, modified, adapted, published, translated in any way, in whole or in part, nor disclosed to a third party without the prior written consent of ENAC. © 2025, ENAC

LAMBDA Least Squares Ambiguity Decorrelation Adjustment

LEO Low Earth Orbit

LOS Line-Of-Sight

MEO Medium Earth orbit

MLE Maximum Likelihood Estimator

MMLE Misspecified Maximum Likelihood Estimator

NLOS Non-Line-Of-Sight

PDOP Position Dilution Of Precision

PLL Phase Lock Loop

PPP Precise Point Positioning

PRN Pseudo Random Noise

PVT Position, Velocity and Time

RF Radio Frequency

RTK Real-Time Kinematic

SD Single Difference

SDR Software Defined Radio

SLAM Simultaneous Localization And Mapping

SPP Single Point Positioning

SVD Singular Value Decomposition

TDCP Time-Differenced Carrier Phase

TDOP Time Dilution Of Precision

TOW Time Of Week

UQ Uncertainty Quantification

UTC Coordinated Universal Time

VDOP Vertical Dilution Of Precision

WLS Weighted Least Squares

ZTD Tropospheric Zenith Path Delay

Bibliography

[1] D. Orendorff, F. van Diggelen, J. Elliott, M. Fu, M. Khider, and S. Dane, "Google Smartphone Decimeter Challenge." `https://kaggle.com/competitions/google-smartphone-decimeter-challenge`, 2021.

[2] A. Howard, A. Chow, B. Julian, D. Orendorff, M. Fu, M. Khider, M. Khider, and S. Dane, "Google Smartphone Decimeter Challenge 2022." `https://kaggle.com/competitions/smartphone-decimeter-2022`, 2022.

[3] A. Chow, D. Orendorff, M. Fu, M. Khider, S. Dane, and V. Gulati, "Google Smartphone Decimeter Challenge 2023-2024." `https://kaggle.com/competitions/smartphone-decimeter-2023`, 2023.

[4] T. Suzuki, "First Place Award Winner of the Smartphone Decimeter Challenge: Global Optimization of Position and Velocity by Factor Graph Optimization," in *Proceedings of the 34th International Technical Meeting of the Satellite Division of The Institute of Navigation (ION GNSS+ 2021)*, (St. Louis, Missouri), pp. 2974–2985, Sept. 2021.

[5] T. Suzuki, "1st Place Winner of the Smartphone Decimeter Challenge: Two-Step Optimization of Velocity and Position Using Smartphone's Carrier Phase Observations," in *Proceedings of the 35th International Technical Meeting of the Satellite Division of The Institute of Navigation (ION GNSS+ 2022)*, (Denver, Colorado), pp. 2276–2286, Sept. 2022.

[6] T. Suzuki, "Precise Position Estimation Using Smartphone Raw GNSS Data Based on Two-Step Optimization," *Sensors*, vol. 23, no. 3, 2023.

[7] T. Suzuki, "Second Place Winner of the Smartphone Decimeter Challenge: An Open-Source Factor Graph Optimization Package for GNSS and IMU Integration in Smartphones," in *Proceedings of the 37th International Technical Meeting of the Satellite Division of The Institute of Navigation (ION GNSS+ 2024)*, (Baltimore, Maryland), pp. 2703–2713, Sept. 2024.

[8] H. Cherfi, J. Lesouple, J. Solà, and P. Thevenon, "Single Frequency GNSS Carrier Phase Cycle Slip Detection and Identification Using a Factor Graph Approach," in *Proc. ION Pacific PNT 2024*, (Honolulu, HI, USA), pp. 344 – 355, Apr. 2024.

[9] E. Kaplan and C. Hegarty, *Understanding GPS: Principles and Applications*. Artech House, 2006.

[10] P. Groves, *Principles of GNSS, Inertial, and Multisensor Integrated Navigation Systems, Second Edition*. Artech House, 2013.

[11] "Galileo Space Segment - Navipedia."

[12] P. Steigenberger, Z. Deng, J. Guo, L. Prange, S. Song, and O. Montenbruck, "BeiDou-3 orbit and clock quality of the IGS Multi-GNSS Pilot Project," *Advances in Space Research*, vol. 71, no. 1, pp. 355–368, 2023.

[13] P. J. Teunissen, O. Montenbruck, *et al.*, *Springer handbook of global navigation satellite systems*, vol. 10. Springer, 2017.

[14] J. Sanz Subirana, M. Hernández-Pajares, and J. M. Juan Zornoza, *GNSS data processing. Vol. 1, Fundamentals and Algorithms*. European Space Agency, 2013.

[15] A. Einstein, "Zur Elektrodynamik bewegter Körper," *Annalen der Physik*, vol. 17, pp. 891–921, 1905.

[16] A. Einstein, "Die Feldgleichungen der Gravitation," *Akademie der Wissenschaften zu Berli*, pp. 844–847, 1915.

[17] N. Ashby and J. J. Spilker, "Introduction to relativistic effects on the Global Positioning System," *Global Positioning System: Theory and applications.*, vol. 1, pp. 623–697, 1996.

[18] K. Davies, *Ionospheric Radio*. London, UK: The Institution of Engineering and Technology, 1990.

[19] B. Hofmann-Wellenhof, H. Lichtenegger, and J. Collins, *GPS Theory and Practice*. Springer-Verlag, 1993.

[20] J. A. Klobuchar, "Ionospheric Time-Delay Algorithm for Single-Frequency GPS Users," *IEEE Transactions on Aerospace and Electronic Systems*, vol. Aes-23, no. 3, pp. 325–331, 1987.

[21] G. Hochegger, B. Nava, S. Radicella, and R. Leitinger, "A family of ionospheric models for different uses," *Physics and Chemistry of the Earth, Part C: Solar, Terrestrial & Planetary Science*, vol. 25, no. 4, pp. 307–310, 2000.

[22] M. Hernández-Pajares, J. M. Juan, J. Sanz, and R. Orús, "Second-order ionospheric term in GPS: Implementation and impact on geodetic estimates," *Journal of Geophysical Research: Solid Earth*, vol. 112, no. B8, pp. 1–16, 2007.

[23] J. P. Collins, "Assessment and development of a tropospheric delay model for aircraft users of the global positioning system," *M. Sc. E. thesis, Department of Geodesy and Geomatics Engineering Technical Report*, no. 203, 1999.

[24] N. Ashby and M. Weiss, "Global Positioning System Receivers and Relativity," *National Institute of Standards and Technology (NIST) Technical Note*, vol. 1385, Mar. 1999.

[25] T. Murphy, P. Geren, and T. Pankaskie, "GPS Antenna Group Delay Variation Induced Errors in a GNSS Based Precision Approach and Landing Systems," in *Proceedings of the 20th International Technical Meeting of the Satellite Division of The Institute of Navigation (ION GNSS 2007)*, (Fort Worth, TX), pp. 2974–2989, Sept. 2007.

[26] N. Sunderhauf, M. Obst, G. Wanielik, and P. Protzel, "Multipath mitigation in GNSS-based localization using robust optimization," in *2012 IEEE Intelligent Vehicles Symposium*, (Alcal de Henares , Madrid, Spain), pp. 784–789, June 2012.

[27] P. D. Groves, Z. Jiang, M. Rudi, and P. Strode, "A portfolio approach to NLOS and multipath mitigation in dense urban areas," in *Proceedings of the 26th International Technical Meeting of The Satellite Division of the Institute of Navigation (ION GNSS 2013)*, (Manassas, USA), pp. 3231 – 3247, 2013.

[28] P. Xu, G. Zhang, B. Yang, and L.-T. Hsu, "Machine Learning in GNSS Multipath/NLOS Mitigation: Review and Benchmark," *IEEE Aerospace and Electronic Systems Magazine*, vol. 39, no. 9, pp. 26–44, 2024.

[29] P. J. G. Teunissen, P. J. de Jonge, and C. C. J. M. Tiberius, "The least-squares ambiguity decorrelation adjustment: its performance on short GPS baselines and short observation spans," *Journal of Geodesy*, vol. 71, pp. 589–602, Sept. 1997.

[30] K. Borre, D. M. Akos, N. Bertelsen, P. Rinder, and S. H. Jensen, *A Software-Defined GPS and Galileo Receiver: A Single-Frequency Approach*. Birkhäuser, 2007.

[31] F. Van Diggelen, *A-GPS: Assisted GPS, GNSS, and SBAS*. Artech House, 2009.

[32] R. Durrett, *Probability: theory and examples*, vol. 49. Cambridge university press, 2019.

[33] H.-A. Loeliger, "An introduction to factor graphs," *IEEE Signal Processing Magazine*, vol. 21, no. 1, pp. 28–41, 2004.

[34] M. Kaess, A. Ranganathan, and F. Dellaert, "iSAM: Incremental Smoothing and Mapping," *IEEE Transactions on Robotics*, vol. 24, no. 6, pp. 1365–1378, 2008.

[35] M. Kaess, H. Johannsson, R. Roberts, V. Ila, J. J. Leonard, and F. Dellaert, "iSAM2: Incremental smoothing and mapping using the Bayes tree," *The International Journal of Robotics Research*, vol. 31, no. 2, pp. 216–235, 2012.

This document may not be reproduced, modified, adapted, published, translated in any way, in whole or in part, nor disclosed to a third party without the prior written consent of ENAC. © 2025, ENAC

[36] P. Virtanen *et al.*, "SciPy 1.0: fundamental algorithms for scientific computing in Python," *Nature Methods*, vol. 17, pp. 261–272, Mar. 2020.

[37] F. Dellaert and M. Kaess, "Square Root SAM: Simultaneous Localization and Mapping via Square Root Information Smoothing," *The International Journal of Robotics Research*, vol. 25, no. 12, pp. 1181–1203, 2006.

[38] S. Thrun and M. Montemerlo, "The Graph SLAM Algorithm with Applications to Large-Scale Mapping of Urban Structures," *The International Journal of Robotics Research*, vol. 25, no. 5-6, pp. 403–429, 2006.

[39] F. Dellaert and M. Kaess, *Factor Graphs for Robot Perception*. Hanover, MA, USA and Delft, The Netherlands: now Publishers Inc., 2017.

[40] K. J. Doherty, Z. Lu, K. Singh, and J. J. Leonard, "Discrete-Continuous Smoothing and Mapping," *IEEE Robotics and Automation Letters*, vol. 7, no. 4, pp. 12395–12402, 2022.

[41] S. Yang, G. Chen, Y. Zhang, H. Choset, and F. Dellaert, "Equality Constrained Linear Optimal Control With Factor Graphs," in *2021 IEEE International Conference on Robotics and Automation (ICRA)*, pp. 9717–9723, 2021.

[42] R. Kümmerle, G. Grisetti, H. Strasdat, K. Konolige, and W. Burgard, "G2o: A general framework for graph optimization," in *2011 IEEE International Conference on Robotics and Automation*, pp. 3607–3613, 2011.

[43] S. Agarwal, K. Mierle, and T. C. S. Team, "Ceres Solver," 2023.

[44] F. Dellaert, "Factor Graphs and GTSAM: A Hands-on Introduction," Tech. Rep. Gt-rim-cp&r-2012-002, Georgia Institute of Technology, Sept. 2012.

[45] J. Dong and Z. Lv, "miniSAM: A Flexible Factor Graph Non-linear Least Squares Optimization Framework," *CoRR*, vol. abs/1909.00903, 2019.

[46] H. Jiang, T. Li, and C. Shi, "An Effective GNSS Fault Detection and Exclusion Algorithm for Tightly Coupled GNSS/INS/Vision Integration via Factor Graph Optimization," in *2022 International Conference on Automation, Robotics and Computer Engineering (ICARCE)*, pp. 1–5, 2022.

[47] J. Ortiz, M. Pupilli, S. Leutenegger, and A. J. Davison, "Bundle adjustment on a graph processor," in *Proceedings of the IEEE/CVF Conference on Computer Vision and Pattern Recognition*, pp. 2416–2425, 2020.

[48] D. Wisth, M. Camurri, and M. Fallon, "Robust Legged Robot State Estimation Using Factor Graph Optimization," *IEEE Robotics and Automation Letters*, vol. 4, no. 4, pp. 4507–4514, 2019.

[49] J. Dai, S. Liu, X. Hao, Z. Ren, and X. Yang, "UAV Localization Algorithm Based on Factor Graph Optimization in Complex Scenes," *Sensors*, vol. 22, no. 15, 2022.

[50] T. A. Davis, J. R. Gilbert, S. I. Larimore, and E. G. Ng, "Algorithm 836: COLAMD, a column approximate minimum degree ordering algorithm," *ACM Trans. Math. Softw.*, vol. 30, pp. 377–380, Sept. 2004.

[51] J. Nocedal and S. J. Wright, *Numerical Optimization*. Springer, 2006.

[52] W. H. Press, S. A. Teukolsky, W. T. Vetterling, and B. P. Flannery, *Numerical Recipes: The Art of Scientific Computing*. Cambridge University Press, 2007.

[53] M. Powell, "A New Algorithm for Unconstrained Optimization," in *Nonlinear Programming* (J. Rosen, O. Mangasarian, and K. Ritter, eds.), pp. 31–65, Academic Press, 1970.

[54] K. Madsen, H. B. Nielsen, and O. Tingleff, *Methods for Non-Linear Least Squares Problems (2nd ed.)*. Lyngby, Denmark: Informatics and Mathematical Modelling, Technical University of Denmark, 2004.

[55] R. E. Kalman, "A New Approach to Linear Filtering and Prediction Problems," *Journal of Basic Engineering*, vol. 82, pp. 35–45, Mar. 1960.

[56] C. Taylor and J. Gross, "Factor Graphs for Navigation Applications: A Tutorial," *NAVIGATION: Journal of the Institute of Navigation*, vol. 71, no. 3, 2024.

[57] S. Z. Farooq, D. Yang, T. Jin, and E. N. J. Ada, "Survey of Cycle Slip Detection & Correction Techniques for Single Frequency Receivers," in *2018 IEEE 18th International Conference on Communication Technology (ICCT)*, pp. 957–961, 2018.

[58] M. Kirkko-Jaakkola, J. Traugott, D. Odijk, J. Collin, G. Sachs, and F. Holzapfel, "A raim approach to GNSS outlier and cycle slip detection using L1 carrier phase time-differences," in *2009 IEEE Workshop on Signal Processing Systems*, pp. 273–278, 2009.

[59] S. Fujita, S. Saito, and T. Yoshihara, "Cycle slip detection and correction methods with time-differenced model for single frequency GNSS applications," *Transactions of the institute of systems, control and information engineers*, vol. 26, no. 1, pp. 8–15, 2013.

[60] S.-G. Lin and F. Yu, "Cycle slips detection algorithm for low cost single frequency GPS RTK positioning," *Survey Review*, vol. 45, no. 330, pp. 206–214, 2013.

[61] M. Joerger, F.-C. Chan, and B. Pervan, "Solution Separation Versus Residual-Based RAIM: Solution Separation Versus Residual-Based RAIM," *Navigation*, vol. 61, pp. 273–291, Dec. 2014.

This document may not be reproduced, modified, adapted, published, translated in any way, in whole or in part, nor disclosed to a third party without the prior written consent of ENAC. © 2025, ENAC

[62] S. Kay, *Fundamentals Of Statistical Processing, Volume 2: Detection Theory*. Prentice-Hall signal processing series, Pearson Education, 2009.

[63] S. Fortunati and L. Ortega, "On the efficiency of misspecified Gaussian inference in nonlinear regression: Application to time-delay and Doppler estimation," *Signal Processing*, vol. 225, p. 109614, Dec. 2024.

[64] A. Mennad, S. Fortunati, M. N. El Korso, A. Younsi, A. M. Zoubir, and A. Renaux, "Slepian-Bangs-type formulas and the related Misspecified Cramér-Rao Bounds for Complex Elliptically Symmetric distributions," *Signal Processing*, vol. 142, pp. 320–329, Jan. 2018.

[65] C. D. Richmond and L. L. Horowitz, "Parameter Bounds on Estimation Accuracy Under Model Misspecification," *IEEE Transactions on Signal Processing*, vol. 63, pp. 2263–2278, Mar. 2015.

[66] J. Neyman and E. S. Pearson, "IX. On the problem of the most efficient tests of statistical hypotheses," *Philosophical Transactions of the Royal Society of London. Series A, Containing Papers of a Mathematical or Physical Character*, vol. 231, pp. 289–337, Feb. 1933.

[67] L. Yang, N. L. Knight, Y. Li, and C. Rizos, "Optimal Fault Detection and Exclusion Applied in GNSS Positioning," *Journal of Navigation*, vol. 66, no. 5, pp. 683–700, 2013.

[68] T. Takasu and A. Yasuda, "Development of the low-cost RTK-GPS receiver with an open source program package RTKLIB," in *International symposium on GPS/GNSS*, vol. 1, pp. 1–6, 2009.

[69] K. Parvazi, S. Farzaneh, and A. Safari, "Role of the RLS-VCE-estimated stochastic model for improvement of accuracy and convergence time in multi-GNSS precise point positioning," *Measurement*, vol. 165, p. 108073, 2020.

[70] H. Cherfi, J. Lesouple, J. Solà, and P. Thevenon, "Uncertainty Quantification of First Fix in a Time-Differenced Carrier Phase Observation Model," *Sensors*, vol. 25, May 2025.

[71] B. Congram and T. D. Barfoot, "Experimental Comparison of Visual and Single-Receiver GPS Odometry." `https://arxiv.org/abs/2106.02122`, June 2021.

[72] J. Kim, M. Park, Y. Bae, O.-J. Kim, D. Kim, B. Kim, and C. Kee, "A Low-Cost, High-Precision Vehicle Navigation System for Deep Urban Multipath Environment Using TDCP Measurements," *Sensors*, vol. 20, p. 3254, June 2020.

[73] K. Chen, G. Chang, C. Chen, and T. Zhu, "An improved TDCP-GNSS/INS integration scheme considering small cycle slip for low-cost land vehicular applications," *Measurement Science and Technology*, vol. 32, p. 055006, Mar. 2021.

[74] L. Ji, R. Sun, Q. Cheng, and J. Wang, "Evaluation of the performance of GNSS-based velocity estimation algorithms," *Satellite Navigation*, vol. 3, p. 18, Sept. 2022.

[75] R. Sun, Q. Cheng, and J. Wang, "Precise vehicle dynamic heading and pitch angle estimation using time-differenced measurements from a single GNSS antenna," *GPS Solutions*, vol. 24, p. 84, June 2020.

[76] Z. Li, D. Wang, Y. Dong, and J. Wu, "An enhanced tightly-coupled integrated navigation approach using phase-derived position increment (PDPI) measurement," *Optik*, vol. 156, pp. 135–147, Mar. 2018.

[77] T. Suzuki, "GNSS Odometry: Precise Trajectory Estimation Based on Carrier Phase Cycle Slip Estimation," *IEEE Robotics and Automation Letters*, vol. 7, pp. 7319–7326, July 2022.

[78] P. Freda, A. Angrisano, S. Gaglione, and S. Troisi, "Time-differenced carrier phases technique for precise GNSS velocity estimation," *GPS Solutions*, vol. 19, pp. 335–341, Apr. 2015.

[79] P. Lyu, S. Bai, J. Lai, B. Wang, X. Sun, and K. Huang, "Optimal Time Difference-Based TDCP-GPS/IMU Navigation Using Graph Optimization," *IEEE Transactions on Instrumentation and Measurement*, vol. 70, pp. 1–10, Nov. 2021.

[80] K.-W. Chiang, Y.-H. Li, L.-T. Hsu, and F.-Y. Chu, "The Design a TDCP-Smoothed GNSS/Odometer Integration Scheme with Vehicular-Motion Constraint and Robust Regression," *Remote Sensing*, vol. 12, no. 16, 2020.

[81] T. Suzuki, "Time-relative RTK-GNSS: GNSS loop closure in pose graph optimization," *IEEE robotics and automation letters*, vol. 5, no. 3, pp. 4735–4742, 2020.

[82] X. Li, X. Li, X. Wang, H. Chang, Y. Tan, and Z. Shen, "Factor graph-based PPP-RTK for accurate and robust positioning in urban environments," *Journal of Geodesy*, vol. 98, p. 21, Mar. 2024.

[83] S. Bai, J. Lai, P. Lyu, Y. Cen, X. Sun, and B. Wang, "Performance enhancement of tightly coupled GNSS/IMU integration based on factor graph with robust TDCP loop closure," *IEEE Transactions on Intelligent Transportation Systems*, vol. 25, no. 3, pp. 2437–2449, 2023.

[84] A. Guillard, P. Thevenon, and C. Milner, "Using TDCP Measurements in a Low-Cost PPP-IMU Hybridized Filter for Real-Time Applications," in *ION GNSS+, The International Technical Meeting of the Satellite Division of The Institute of Navigation*, (Denver, Colorado), pp. 2090–2103, Institute of Navigation, Sept. 2022.

[85] J. Kim, Y. Kim, J. Song, D. Kim, M. Park, and C. Kee, "Performance Improvement of Time-Differenced Carrier Phase Measurement-Based Integrated GPS/INS Considering Noise Correlation," *Sensors*, vol. 19, p. 3084, Jul 2019.

This document may not be reproduced, modified, adapted, published, translated in any way, in whole or in part, nor disclosed to a third party without the prior written consent of ENAC. © 2025, ENAC

[86] X. Bai, W. Wen, and L.-T. Hsu, "Time-correlated window-carrier-phase-aided GNSS positioning using factor graph optimization for urban positioning," *IEEE Transactions on Aerospace and Electronic Systems*, vol. 58, no. 4, pp. 3370–3384, 2022.

[87] P. J. G. Teunissen, "GNSS Ambiguity Bootstrapping: Theory and Application," Jan. 2001.

[88] K. B. Petersen and M. S. Pedersen, *The Matrix Cookbook*. Technical University of Denmark, Nov. 2012.

Appendix A

Maximum Likelihood Estimation

This appendix introduces the definition of the Maximum Likelihood Estimator (MLE) for real-valued continuous random vectors. It is assumed that the reader is already familiar with the definition of a random vector (for further details, one may refer to [32], among many other standard references).

A.1 Definitions

Definition A.1.1 (Estimator)**.** *Let $\boldsymbol{x}$ be a real-valued random vector of dimension m, let $\boldsymbol{\theta} \in \Theta \subseteq \mathbb{R}^n$ and let $f : \mathbb{R}^m \to \Theta \subseteq \mathbb{R}^n$ be a measurable function. The random vector $\widehat{\boldsymbol{\theta}}_f \triangleq f(\boldsymbol{x})$ is an* estimator *of $\boldsymbol{\theta}$.*

In this thesis, very often a sample $\boldsymbol{x}(\omega)$ of the random vector $\boldsymbol{x}$ is passed to the function f. Indeed, $f(\boldsymbol{x}(\omega))$ is a vector, not a random vector. Although $f(\boldsymbol{x}(\omega))$ should be called an *estimate*, the word *estimator* is sometimes used anyway. The distinction should be clear from the context.

Definition A.1.2 (Density function)**.** *Let $\boldsymbol{x}$ be a continuous real-valued random vector of dimension m. The* density function *of $\boldsymbol{x}$ is the piecewise continuous function $f : \mathbb{R}^m \to \mathbb{R}^+$ such that for all measurable subset $\mathcal{O} \subseteq \mathbb{R}^m$, $\mathbb{P}(\boldsymbol{x} \in \mathcal{O}) = \displaystyle\int_{\mathcal{O}} f(\boldsymbol{t})\mathrm{d}\boldsymbol{t}$.*

Definition A.1.3 (Likelihood function and operator)**.** *Let $\boldsymbol{x}$ be a continuous real-valued random vector of dimension m and let $\boldsymbol{\theta} \in \Theta \subseteq \mathbb{R}^n$.*

Let $f : (\Theta \subseteq \mathbb{R}^n) \times \mathbb{R}^m \to \mathbb{R}^+$ and its restriction $f_{\boldsymbol{\theta}} : \mathbb{R}^m \to \mathbb{R}^+$, $\boldsymbol{t} \mapsto f_{\boldsymbol{\theta}}(\boldsymbol{t}) = f(\boldsymbol{\theta}, \boldsymbol{t})$ be such that $f_{\boldsymbol{\theta}}$ is the density function of $\boldsymbol{x}$.

Given a sample $\boldsymbol{x}(\omega) \in \mathbb{R}^m$ of $\boldsymbol{x}$, the likelihood function of $\boldsymbol{\theta}$ given $\boldsymbol{x}(\omega)$ *is defined as $\mathcal{L}_{\boldsymbol{x}(\omega)} : \Theta \subseteq \mathbb{R}^n \to \mathbb{R}^+$, $\boldsymbol{\theta} \mapsto \mathcal{L}_{\boldsymbol{x}(\omega)}(\boldsymbol{\theta}) = f(\boldsymbol{\theta}, \boldsymbol{x}(\omega))$.*

At a higher level, the likelihood function of $\boldsymbol{\theta}$ given $\boldsymbol{x}$ *is defined as $\mathcal{L}_{\boldsymbol{x}} : \Theta \subseteq \mathbb{R}^n \to \mathbb{R}^+$, $\boldsymbol{\theta} \mapsto \mathcal{L}_{\boldsymbol{x}}(\boldsymbol{\theta}) = f(\boldsymbol{\theta}, \boldsymbol{x})$.*

If E denotes the set of continuous real-valued random vectors of dimension m, the likelihood operator *(of $\boldsymbol{\theta}$) is defined as $\mathcal{L} : E \to \left(\Theta \subseteq \mathbb{R}^n \to \mathbb{R}^+\right)$, $\boldsymbol{x} \mapsto \mathcal{L}(\boldsymbol{x}) = \mathcal{L}_{\boldsymbol{x}}$.*

Definition A.1.4 (Maximum likelihood estimator)**.** *Let $\boldsymbol{x}$ be a continuous real-valued*

This document may not be reproduced, modified, adapted, published, translated in any way, in whole or in part, nor disclosed to a third party without the prior written consent of ENAC. © 2025, ENAC

random vector and let $\mathcal{L}$ *be the likelihood operator. The* maximum likelihood estimator *is the random variable* $\widehat{\boldsymbol{\theta}}_{MLE} \triangleq \arg\max \mathcal{L}(\boldsymbol{x})$.

Although not necessarily, this definition assumes that $\arg\max \mathcal{L}$ is a measurable function.

Other estimators, such as Bayesian estimators that incorporate prior knowledge, may differ in philosophical or epistemological interpretation (e.g., frequentist vs. Bayesian perspectives), and may involve functions of different dimensions or additional random variables. However, when such estimators are defined through the maximization of a specific objective function, they are treated equivalently in this thesis, regardless of their underlying interpretation. As such, they fit within the definitions provided in this appendix, and no further distinction is made in this thesis beyond the function they maximize. In particular, when the Factor Graph Optimization (FGO) framework is used to represent the MLE, it naturally encompasses these estimators as well, since they all share the same underlying mathematical structure.

Appendix B

Analytical Solution of the Linear Gaussian Factor Graph Optimization Problem

B.1 Definitions

Definition B.1.1 (Positive-definite matrix)**.** *Let* $\boldsymbol{M} \in \mathcal{M}_n(\mathbb{R})$*.* $\boldsymbol{M}$ *is* positive-definite *if* $\forall \boldsymbol{x} \in \mathbb{R}^n \setminus \{\boldsymbol{0}\}, \boldsymbol{x}^\mathsf{T}\boldsymbol{M}\boldsymbol{x} > 0$*.*

Definition B.1.2 (Injective application)**.** *Let* f *be an application.* f *is* injective *if* $\forall x, \forall y, x \neq y \Rightarrow f(x) \neq f(y)$ *(or equivalently,* $\forall x, \forall y, f(x) = f(y) \Rightarrow x = y$*).*

Definition B.1.3 (Cholesky decomposition)**.** *Let* $\boldsymbol{M} \in \mathcal{M}_n(\mathbb{R})$ *be a symmetric positive definite matrix. The* Cholesky decomposition *of* $\boldsymbol{M}$ *is given by* $\boldsymbol{M} = \boldsymbol{L}\boldsymbol{L}^\mathsf{T}$*, where* $\boldsymbol{L} \in \mathcal{M}_n(\mathbb{R})$ *is a lower triangular positive definite matrix.*

B.2 Generalized Inverse

In Appendix A is stated that if $\boldsymbol{x}$ is a real-valued random vector of dimension m, $\boldsymbol{H} \in \mathcal{M}_{m,n}(\mathbb{R})$ represents a linear application, $\boldsymbol{R}$ is a real symmetric positive-definite matrix, defining the application

$$q : \Theta \subseteq \mathbb{R}^n \to \mathbb{R}^+, \boldsymbol{\theta} \mapsto \|\boldsymbol{x} - \boldsymbol{H}\boldsymbol{\theta}\|^2_{\boldsymbol{R}}, \tag{B.1}$$

with $\|\boldsymbol{\mu}\|^2_{\boldsymbol{R}} \triangleq \boldsymbol{\mu}^\mathsf{T}\boldsymbol{R}^{-1}\boldsymbol{\mu}$, it can be shown that if and only if $\operatorname{rank}(\boldsymbol{H}) = n$ (which implies $m \geq n$)

$$\arg\min q = \left(\boldsymbol{H}^\mathsf{T}\boldsymbol{R}^{-1}\boldsymbol{H}\right)^{-1}\boldsymbol{H}^\mathsf{T}\boldsymbol{R}^{-1}\boldsymbol{x}. \tag{B.2}$$

The Cholesky decomposition $\boldsymbol{L}$ of $\boldsymbol{R}$ is introduced. From this decomposition are defined $\widetilde{\boldsymbol{H}} \triangleq \boldsymbol{L}^{-1}\boldsymbol{H}$ and $\widetilde{\boldsymbol{x}} \triangleq \boldsymbol{L}^{-1}\boldsymbol{x}$. It can be shown

$$q(\boldsymbol{\theta}) = \left\|\widetilde{\boldsymbol{x}} - \widetilde{\boldsymbol{H}}\boldsymbol{\theta}\right\|^2_{\boldsymbol{I}}. \tag{B.3}$$

This document may not be reproduced, modified, adapted, published, translated in any way, in whole or in part, nor disclosed to a third party without the prior written consent of ENAC. © 2025, ENAC

The application q is a quadratic form. Its Jacobian matrix at $\widehat{\boldsymbol{\theta}}$ exists and is

$$\boldsymbol{Q}_{\widehat{\boldsymbol{\theta}}} = 2\widehat{\boldsymbol{\theta}}^{\mathsf{T}}\widetilde{\boldsymbol{H}}^{\mathsf{T}}\widetilde{\boldsymbol{H}} - 2\widetilde{\boldsymbol{x}}^{\mathsf{T}}\widetilde{\boldsymbol{H}} \in \mathcal{M}_{1,n}(\mathbb{R}). \tag{B.4}$$

A necessary first order condition for $\widehat{\boldsymbol{\theta}}$ to be a minimum of q is that $\boldsymbol{Q}_{\widehat{\boldsymbol{\theta}}} = \boldsymbol{0}$, or equivalently:

$$\boldsymbol{Q}_{\widehat{\boldsymbol{\theta}}} = \boldsymbol{0} \Leftrightarrow \widetilde{\boldsymbol{H}}^{\mathsf{T}}\widetilde{\boldsymbol{H}}\widehat{\boldsymbol{\theta}} = \widetilde{\boldsymbol{H}}^{\mathsf{T}}\widetilde{\boldsymbol{x}}. \tag{B.5}$$

Recalling from the definition of an estimator in Appendix A, it is assumed that $\arg\min q$ is a function, meaning for a given random variable $\boldsymbol{x}$, there is a unique vector $\widehat{\boldsymbol{\theta}}$ that minimizes q. In that case, equation (B.5) has to admit a unique solution. This is equivalent to considering the matrix $\widetilde{\boldsymbol{H}}^{\mathsf{T}}\widetilde{\boldsymbol{H}}$ to be invertible.

Proposition B.2.1. *Let $\boldsymbol{M} \in \mathcal{M}_{m,n}(\mathbb{R})$. $\boldsymbol{x} \mapsto \boldsymbol{M}\boldsymbol{x}$ is injective if and only if $\boldsymbol{M}\boldsymbol{x} = \boldsymbol{0} \Rightarrow \boldsymbol{x} = \boldsymbol{0}$ (or equivalently $\operatorname{rank}(\boldsymbol{M}) = n$).*

Given $\boldsymbol{M} \in \mathcal{M}_{m,n}(\mathbb{R})$, saying that $\boldsymbol{M}$ is injective means that the application $\boldsymbol{x} \mapsto \boldsymbol{M}\boldsymbol{x}$ is injective.

Proposition B.2.2. *Let $\boldsymbol{M} \in \mathcal{M}_{n}(\mathbb{R})$. $\boldsymbol{x} \mapsto \boldsymbol{M}\boldsymbol{x}$ is invertible if and only if it is injective.*

From these propositions, the matrix $\widetilde{\boldsymbol{H}}^{\mathsf{T}}\widetilde{\boldsymbol{H}}$ is invertible if and only if it is injective.

Proposition B.2.3. *Let $\boldsymbol{M} \in \mathcal{M}_{m,n}(\mathbb{R})$. $\boldsymbol{M}^{\mathsf{T}}\boldsymbol{M}$ injective $\Leftrightarrow$ $\boldsymbol{M}$ injective.*

Proof. Let $\boldsymbol{x}$ be such that $\boldsymbol{M}\boldsymbol{x} = \boldsymbol{0}$. It comes $\boldsymbol{M}^{\mathsf{T}}\boldsymbol{M}\boldsymbol{x} = \boldsymbol{M}^{\mathsf{T}}\boldsymbol{0} = \boldsymbol{0}$. Since $\boldsymbol{M}^{\mathsf{T}}\boldsymbol{M}$ is injective, it comes $\boldsymbol{x} = \boldsymbol{0}$, so $\boldsymbol{M}$ is injective.

Reciprocally, let $\boldsymbol{x}$ be such that $\boldsymbol{M}^{\mathsf{T}}\boldsymbol{M}\boldsymbol{x} = \boldsymbol{0}$. It implies $\boldsymbol{x}^{\mathsf{T}}\boldsymbol{M}^{\mathsf{T}}\boldsymbol{M}\boldsymbol{x} = \boldsymbol{x}^{\mathsf{T}}\boldsymbol{0} = 0$. Defining $\boldsymbol{z} = \boldsymbol{M}\boldsymbol{x}$, it comes $\boldsymbol{z}^{\mathsf{T}}\boldsymbol{z} = \sum_{i=1}^{m} z_i^2 = 0$. This implies that $\boldsymbol{z} = \boldsymbol{0} = \boldsymbol{M}\boldsymbol{x} \Rightarrow \boldsymbol{x} = \boldsymbol{0}$ by injectivity of $\boldsymbol{M}$, so $\boldsymbol{M}^{\mathsf{T}}\boldsymbol{M}$ is injective. □

Therefore, the solution to equation (B.5) is unique and well defined if and only if $\widetilde{\boldsymbol{H}}$ is injective, and is given by:

$$\widehat{\boldsymbol{\theta}} = \left(\widetilde{\boldsymbol{H}}^{\mathsf{T}}\widetilde{\boldsymbol{H}}\right)^{-1}\widetilde{\boldsymbol{H}}^{\mathsf{T}}\widetilde{\boldsymbol{x}} = \left(\boldsymbol{H}^{\mathsf{T}}\boldsymbol{R}^{-1}\boldsymbol{H}\right)^{-1}\boldsymbol{H}^{\mathsf{T}}\boldsymbol{R}^{-1}\boldsymbol{x}. \tag{B.6}$$

Proposition B.2.4. *Let $\boldsymbol{M} \in \mathcal{M}_{m,n}(\mathbb{R})$, $\boldsymbol{P} \in \mathcal{M}_{m}(\mathbb{R})$ with $\boldsymbol{P}$ invertible. $\boldsymbol{P}\boldsymbol{M}$ injective $\Leftrightarrow$ $\boldsymbol{M}$ injective.*

From this proposition, since $\widetilde{\boldsymbol{H}} = \boldsymbol{L}^{-1}\boldsymbol{H}$ is injective, this is equivalent to $\boldsymbol{H}$ injective, or equivalent to $\operatorname{rank}(\boldsymbol{H}) = n$.

Necessary and sufficient conditions on $\boldsymbol{H}$ have been found in order to have q with a unique critical point. In order to be a minimum, if defined, the Hessian of q at that point has to be studied. For any vector, the Hessian matrix of q at that vector is:

$$\widetilde{\boldsymbol{H}}^{\mathsf{T}}\widetilde{\boldsymbol{H}}. \tag{B.7}$$

In particular, at the critical point, in order to be a minimum, the Hessian has to be positive definite.

Proposition B.2.5. *Let* $\boldsymbol{M} \in \mathcal{M}_{m,n}(\mathbb{R})$. $\boldsymbol{M}^\mathsf{T}\boldsymbol{M}$ *positive definite* $\Leftrightarrow$ $\boldsymbol{M}$ *injective.*

Proof. Let $\boldsymbol{x} \neq \boldsymbol{0}$. Defining $\boldsymbol{z} = \boldsymbol{M}\boldsymbol{x}$, it comes $\boldsymbol{z}^\mathsf{T}\boldsymbol{z} = \sum_{i=1}^{m} z_i^2 > 0 \Rightarrow \boldsymbol{z} \neq \boldsymbol{0} \Leftrightarrow \boldsymbol{M}\boldsymbol{x} \neq \boldsymbol{0}$ which shows the injectivity of $\boldsymbol{M}$.

Reciprocally, let $\boldsymbol{x} \neq \boldsymbol{0}$. $\boldsymbol{M}\boldsymbol{x} \neq \boldsymbol{0}$ since $\boldsymbol{M}$ is injective. Defining $\boldsymbol{z} = \boldsymbol{M}\boldsymbol{x} \neq \boldsymbol{0}$, it comes $\boldsymbol{x}^\mathsf{T}\boldsymbol{M}^\mathsf{T}\boldsymbol{M}\boldsymbol{x} = \boldsymbol{z}^\mathsf{T}\boldsymbol{z} = \sum_{i=1}^{m} z_i^2 > 0$, which shows that $\boldsymbol{M}^\mathsf{T}\boldsymbol{M}$ is positive definite. □

Since $\widetilde{\boldsymbol{H}}$ is injective, it comes that the Hessian matrix $\widetilde{\boldsymbol{H}}^\mathsf{T}\widetilde{\boldsymbol{H}}$ is positive definite, so the critical point $\widehat{\boldsymbol{\theta}}$ is a unique minimizer of q.

This document may not be reproduced, modified, adapted, published, translated in any way, in whole or in part, nor disclosed to a third party without the prior written consent of ENAC. © 2025, ENAC

Appendix C

Kalman Filter Update Equations

Recalling Equation (2.72) of Section 2.5.2

$$\boldsymbol{\mu}_{k+1|k+1} = \arg\min \left(\boldsymbol{\theta} \mapsto \left\| \boldsymbol{\mu}_{k+1|k} - \boldsymbol{\theta} \right\|^2_{\boldsymbol{\Sigma}_{k+1|k}} + \left\| \boldsymbol{y}_{k+1}(\omega) - \boldsymbol{H}_{k+1}\boldsymbol{\theta} \right\|^2_{\boldsymbol{R}_{k+1}} \right) \tag{C.1}$$

corresponding to the a posteriori estimate of $\boldsymbol{\theta}_{k+1}$, it is stated that

$$\boldsymbol{\mu}_{k+1|k+1} = \boldsymbol{\mu}_{k+1|k} + \boldsymbol{K}_{k+1} \left(\boldsymbol{y}_{k+1}(\omega) - \boldsymbol{H}_{k+1}\boldsymbol{\mu}_{k+1|k} \right) \tag{C.2}$$

where

$$\boldsymbol{K}_{k+1} \triangleq \widehat{\boldsymbol{\Sigma}}_{k+1|k}\boldsymbol{H}_{k+1}^{\mathsf{T}} \left(\boldsymbol{H}_{k+1}\boldsymbol{\Sigma}_{k+1|k}\boldsymbol{H}_{k+1}^{\mathsf{T}} + \boldsymbol{R}_{k+1} \right)^{-1} \tag{C.3}$$

defines the Kalman gain matrix.

These equations correspond to the a posteriori estimate of a Kalman Filter (KF).

To prove it, the problem can be written in a form similar to Equation (2.15), i.e., this problem can be written as

$$\boldsymbol{\mu}_{k+1|k+1} = \arg\min \left(\boldsymbol{\theta} \mapsto \left\| \boldsymbol{A}\boldsymbol{\theta} - \boldsymbol{b} \right\|^2_{\boldsymbol{\Omega}} \right) \tag{C.4}$$

where $\boldsymbol{A} \triangleq \begin{pmatrix} \boldsymbol{I}_n \\ \boldsymbol{H}_{k+1} \end{pmatrix}$, $\boldsymbol{b} = \begin{pmatrix} \boldsymbol{\mu}_{k+1|k} \\ \boldsymbol{y}_{k+1}(\omega) \end{pmatrix}$ and $\boldsymbol{\Omega} = \begin{pmatrix} \boldsymbol{\Sigma}_{k+1|k} & \boldsymbol{0} \\ \boldsymbol{0} & \boldsymbol{R}_{k+1} \end{pmatrix}$.

It can be noted that $\forall \boldsymbol{H}_{k+1}$, $\operatorname{rank}(\boldsymbol{A}) = \dim(\boldsymbol{\theta}_{k+1}) = n$, which indicates that no matter what the observation model $\boldsymbol{H}_{k+1}$ is, the update equations of a KF are always well defined.

Equation (2.64) defines the matrix

$$\boldsymbol{S}_{k+1} = \boldsymbol{H}_{k+1}\boldsymbol{\Sigma}_{k+1|k}\boldsymbol{H}_{k+1}^{\mathsf{T}} + \boldsymbol{R}_{k+1} \tag{C.5}$$

so the Kalman gain as in Equation (C.3) can be written

$$\boldsymbol{K}_{k+1} \triangleq \widehat{\boldsymbol{\Sigma}}_{k+1|k}\boldsymbol{H}_{k+1}^{\mathsf{T}}\boldsymbol{S}_{k+1}^{-1}. \tag{C.6}$$

This document may not be reproduced, modified, adapted, published, translated in any way, in whole or in part, nor disclosed to a third party without the prior written consent of ENAC. © 2025, ENAC

From Equation (2.15), assuming $\boldsymbol{\Omega}$ is a real symmetric positive-definite matrix, it comes

$$\begin{aligned}
\boldsymbol{\mu}_{k+1|k+1} &= \left(\boldsymbol{A}^{\mathsf{T}}\boldsymbol{\Omega}^{-1}\boldsymbol{A}\right)^{-1}\boldsymbol{A}^{\mathsf{T}}\boldsymbol{\Omega}^{-1}\boldsymbol{b} \\
&= \left(\boldsymbol{H}_{k+1}^{\mathsf{T}}\boldsymbol{R}_{k+1}^{-1}\boldsymbol{H}_{k+1} + \boldsymbol{\Sigma}_{k+1|k}^{-1}\right)^{-1}\left(\boldsymbol{\Sigma}_{k+1|k}^{-1}\boldsymbol{\mu}_{k+1|k} + \boldsymbol{H}_{k+1}^{\mathsf{T}}\boldsymbol{R}_{k+1}^{-1}\boldsymbol{y}_{k+1}\left(\omega\right)\right) \\
&= \left(\boldsymbol{\Sigma}_{k+1|k} - \boldsymbol{K}_{k+1}\boldsymbol{H}_{k+1}\boldsymbol{\Sigma}_{k+1|k}\right) \\
&\times \left(\boldsymbol{\Sigma}_{k+1|k}^{-1}\boldsymbol{\mu}_{k+1|k} + \boldsymbol{H}_{k+1}^{\mathsf{T}}\boldsymbol{R}_{k+1}^{-1}\boldsymbol{y}_{k+1}\left(\omega\right)\right) \text{ from [88, Equation 156]} \\
&= \left(\boldsymbol{I}_n - \boldsymbol{K}_{k+1}\boldsymbol{H}_{k+1}\right)\boldsymbol{\Sigma}_{k+1|k}\left(\boldsymbol{\Sigma}_{k+1|k}^{-1}\boldsymbol{\mu}_{k+1|k} + \boldsymbol{H}_{k+1}^{\mathsf{T}}\boldsymbol{R}_{k+1}^{-1}\boldsymbol{y}_{k+1}\left(\omega\right)\right) \\
&= \boldsymbol{\mu}_{k+1|k} - \boldsymbol{K}_{k+1}\boldsymbol{H}_{k+1}\boldsymbol{\mu}_{k+1|k} + \boldsymbol{\Sigma}_{k+1|k}\boldsymbol{H}_{k+1}^{\mathsf{T}}\boldsymbol{R}_{k+1}^{-1}\boldsymbol{y}_{k+1}\left(\omega\right) \\
&- \boldsymbol{K}_{k+1}\boldsymbol{H}_{k+1}\boldsymbol{\Sigma}_{k+1|k}\boldsymbol{H}_{k+1}^{\mathsf{T}}\boldsymbol{R}_{k+1}^{-1}\boldsymbol{y}_{k+1}\left(\omega\right) \\
&= \boldsymbol{\mu}_{k+1|k} - \boldsymbol{K}_{k+1}\boldsymbol{H}_{k+1}\boldsymbol{\mu}_{k+1|k} \\
&+ \boldsymbol{\Sigma}_{k+1|k}\boldsymbol{H}_{k+1}^{\mathsf{T}}\left(\boldsymbol{I}_n - \boldsymbol{S}_{k+1}^{-1}\boldsymbol{H}_{k+1}\boldsymbol{\Sigma}_{k+1|k}\boldsymbol{H}_{k+1}^{\mathsf{T}}\right)\boldsymbol{R}_{k+1}^{-1}\boldsymbol{y}_{k+1}\left(\omega\right) \\
&= \boldsymbol{\mu}_{k+1|k} - \boldsymbol{K}_{k+1}\boldsymbol{H}_{k+1}\boldsymbol{\mu}_{k+1|k} \\
&+ \boldsymbol{\Sigma}_{k+1|k}\boldsymbol{H}_{k+1}^{\mathsf{T}}\left(\boldsymbol{I}_n - \boldsymbol{S}_{k+1}^{-1}\left(\boldsymbol{S}_{k+1} - \boldsymbol{R}_{k+1}\right)\right)\boldsymbol{R}_{k+1}^{-1}\boldsymbol{y}_{k+1}\left(\omega\right) \\
&= \boldsymbol{\mu}_{k+1|k} - \boldsymbol{K}_{k+1}\boldsymbol{H}_{k+1}\boldsymbol{\mu}_{k+1|k} + \boldsymbol{\Sigma}_{k+1|k}\boldsymbol{H}_{k+1}^{\mathsf{T}}\boldsymbol{S}_{k+1}^{-1}\boldsymbol{R}_{k+1}\boldsymbol{R}_{k+1}^{-1}\boldsymbol{y}_{k+1}\left(\omega\right) \\
&= \boldsymbol{\mu}_{k+1|k} - \boldsymbol{K}_{k+1}\boldsymbol{H}_{k+1}\boldsymbol{\mu}_{k+1|k} + \boldsymbol{K}_{k+1}\boldsymbol{y}_{k+1}\left(\omega\right) \\
&= \boldsymbol{\mu}_{k+1|k} + \boldsymbol{K}_{k+1}\left(\boldsymbol{y}_{k+1}\left(\omega\right) - \boldsymbol{H}_{k+1}\boldsymbol{\mu}_{k+1|k}\right). \qquad \text{(C.7)}
\end{aligned}$$

It is also stated that the variance of the estimator associated to the estimate Equation (2.72) is

$$\boldsymbol{\Sigma}_{k+1|k+1} = \left(\boldsymbol{I} - \boldsymbol{K}_{k+1}\boldsymbol{H}_{k+1}\right)\boldsymbol{\Sigma}_{k+1|k}. \qquad \text{(C.8)}$$

To prove it, the problem can be written in the same form as in Equation (C.4), and from Equation (2.17), it comes

$$\begin{aligned}
\boldsymbol{\Sigma}_{k+1|k+1} &= \left(\boldsymbol{A}^{\mathsf{T}}\boldsymbol{\Omega}^{-1}\boldsymbol{A}\right)^{-1} \\
&= \left(\boldsymbol{H}_{k+1}^{\mathsf{T}}\boldsymbol{R}_{k+1}^{-1}\boldsymbol{H}_{k+1} + \boldsymbol{\Sigma}_{k+1|k}^{-1}\right)^{-1} \\
&= \left(\boldsymbol{\Sigma}_{k+1|k} - \boldsymbol{K}_{k+1}\boldsymbol{H}_{k+1}\boldsymbol{\Sigma}_{k+1|k}\right) \text{ from [88, Equation 156].} \qquad \text{(C.9)}
\end{aligned}$$

Appendix D

Geometry of the TDCP Model

D.1 Direction of Null and Extremum Model Error

Recalling that $\delta\boldsymbol{r}(t) = \widehat{\boldsymbol{r}}(t) - \boldsymbol{r}(t)$ and that equation (4.17) is the function δh_i that maps an error $\delta\boldsymbol{r}(t)$ to a model error as

$$\begin{aligned}\delta h_i(\delta\boldsymbol{r}(t)) = &\left\|\boldsymbol{r}(t) + \delta\boldsymbol{r}(t) + \Delta\boldsymbol{r} - \boldsymbol{s}_i(t')\right\| - \left\|\boldsymbol{r}(t) + \delta\boldsymbol{r}(t) - \boldsymbol{s}_i(t)\right\| \\ &- \left\|\boldsymbol{r}(t) + \Delta\boldsymbol{r} - \boldsymbol{s}_i(t')\right\| + \left\|\boldsymbol{r}(t) - \boldsymbol{s}_i(t)\right\|\end{aligned} \tag{D.1}$$

where $\|\boldsymbol{x}\| = \sqrt{\langle\boldsymbol{x},\boldsymbol{x}\rangle}$ and $\langle\boldsymbol{x},\boldsymbol{y}\rangle = \boldsymbol{x}^{\mathsf{T}}\boldsymbol{y}$ is the dot product on $\mathbb{R}^3$.
Defining $\boldsymbol{a} \triangleq \boldsymbol{r}(t) + \Delta\boldsymbol{r} - \boldsymbol{s}_i(t')$ and $\boldsymbol{b} \triangleq \boldsymbol{r}(t) - \boldsymbol{s}_i(t)$, Equation (D.1) becomes

$$\delta h_i(\delta\boldsymbol{r}(t)) = \|\boldsymbol{a} + \delta\boldsymbol{r}(t)\| - \|\boldsymbol{a}\| - (\|\boldsymbol{b} + \delta\boldsymbol{r}(t)\| - \|\boldsymbol{b}\|)\,. \tag{D.2}$$

Given that $\delta h_i(\mathbf{0}) = 0$, it comes $\forall\delta\boldsymbol{r}(t) \in \mathbb{R}^3 \setminus \{-\boldsymbol{a},\ -\boldsymbol{b}\}$

$$\begin{aligned}\delta h_i(\delta\boldsymbol{r}(t)) &= d\left(\delta h_i\right)_{\mathbf{0}}\left(\delta\boldsymbol{r}(t)\right) + o\left(\|\delta\boldsymbol{r}(t)\|\right) \\ &= \left\langle \frac{\boldsymbol{a}}{\|\boldsymbol{a}\|} - \frac{\boldsymbol{b}}{\|\boldsymbol{b}\|}, \delta\boldsymbol{r}(t) \right\rangle + o(\|\delta\boldsymbol{r}(t)\|)\end{aligned} \tag{D.3}$$

where $d\left(\delta h_i\right)_{\mathbf{0}}\left(\delta\boldsymbol{r}(t)\right)$ is the differential of δh_i at $\mathbf{0}$, evaluated at $\delta\boldsymbol{r}(t)$. If this term had to be expressed in the canonical bases of $\mathbb{R}^3$ and $\mathbb{R}$, this expression would be equal to the Jacobian matrix of δh_i at $\mathbf{0}$ multiplied by $\delta\boldsymbol{r}(t)$. Therefore, in a neighborhood of $\mathbf{0}$, the linear approximation of δh_i is given by:

$$\delta h_i(\delta\boldsymbol{r}(t)) \approx \left\langle \frac{\boldsymbol{a}}{\|\boldsymbol{a}\|} - \frac{\boldsymbol{b}}{\|\boldsymbol{b}\|}, \delta\boldsymbol{r}(t) \right\rangle. \tag{D.4}$$

Now, the vector $\dfrac{\boldsymbol{a}}{\|\boldsymbol{a}\|} - \dfrac{\boldsymbol{b}}{\|\boldsymbol{b}\|}$ has to be studied to give it a geometrical interpretation, other than being the difference between two very close unit vectors. The function

$$\gamma : \mathbb{R}^3 \to \mathbb{R}^3,\ \boldsymbol{x} \mapsto \frac{\boldsymbol{a}}{\|\boldsymbol{a}\|} - \frac{\boldsymbol{a}+\boldsymbol{x}}{\|\boldsymbol{a}+\boldsymbol{x}\|} \tag{D.5}$$

This document may not be reproduced, modified, adapted, published, translated in any way, in whole or in part, nor disclosed to a third party without the prior written consent of ENAC. © 2025, ENAC

is defined. Additionally, defining $\boldsymbol{v} \triangleq \boldsymbol{b} - \boldsymbol{a}$,

$$\gamma(\boldsymbol{v}) = \frac{\boldsymbol{a}}{\|\boldsymbol{a}\|} - \frac{\boldsymbol{a}+\boldsymbol{v}}{\|\boldsymbol{a}+\boldsymbol{v}\|} = \frac{\boldsymbol{a}}{\|\boldsymbol{a}\|} - \frac{\boldsymbol{b}}{\|\boldsymbol{b}\|}. \tag{D.6}$$

Now that the vector $\dfrac{\boldsymbol{a}}{\|\boldsymbol{a}\|} - \dfrac{\boldsymbol{b}}{\|\boldsymbol{b}\|}$ is expressed as the evaluation of the function γ at $\boldsymbol{v}$, the linear approximation of γ is given $\forall \boldsymbol{\alpha} \in \mathbb{R}^3 \setminus \{-\boldsymbol{a}\}, \forall \boldsymbol{x} \in \mathbb{R}^3$,

$$\gamma(\boldsymbol{\alpha}+\boldsymbol{x}) = \gamma(\boldsymbol{\alpha}) + d\gamma_{\boldsymbol{\alpha}}(\boldsymbol{x}) + o(\|\boldsymbol{x}\|) \tag{D.7}$$

where $d\gamma_{\boldsymbol{\alpha}}(\boldsymbol{x})$ is the differential of γ at $\boldsymbol{\alpha}$, evaluated at $\boldsymbol{x}$. If this term had to be expressed in the canonical basis of $\mathbb{R}^3$, it would be equal to the Jacobian matrix of γ at $\boldsymbol{\alpha}$ multiplied by $\boldsymbol{x}$. It can be shown that

$$d\gamma_{\boldsymbol{\alpha}}(\boldsymbol{x}) = -\frac{1}{\|\boldsymbol{a}+\boldsymbol{\alpha}\|}\left(\boldsymbol{x} - \frac{\boldsymbol{a}+\boldsymbol{\alpha}}{\|\boldsymbol{a}+\boldsymbol{\alpha}\|}\left\langle \frac{\boldsymbol{a}+\boldsymbol{\alpha}}{\|\boldsymbol{a}+\boldsymbol{\alpha}\|}, \boldsymbol{x}\right\rangle\right). \tag{D.8}$$

Since $\gamma(\boldsymbol{0}) = \boldsymbol{0}$, the linear approximation of the function γ around $\boldsymbol{0}$ is given by

$$\gamma(\boldsymbol{x}) \approx -\frac{1}{\|\boldsymbol{a}\|}\left(\boldsymbol{x} - \frac{\boldsymbol{a}}{\|\boldsymbol{a}\|}\left\langle \frac{\boldsymbol{a}}{\|\boldsymbol{a}\|}, \boldsymbol{x}\right\rangle\right). \tag{D.9}$$

As the vector $\boldsymbol{v}$ is infinitesimal and orthogonal to $\boldsymbol{a} = \boldsymbol{s}_i(t') - \boldsymbol{r}(t')$, the scalar product term $\left\langle \dfrac{\boldsymbol{a}}{\|\boldsymbol{a}\|}, \boldsymbol{v}\right\rangle$ is neglected, leading to

$$\frac{\boldsymbol{a}}{\|\boldsymbol{a}\|} - \frac{\boldsymbol{b}}{\|\boldsymbol{b}\|} = \gamma(\boldsymbol{v}) \approx -\frac{\boldsymbol{v}}{\|\boldsymbol{a}\|} = \frac{\boldsymbol{a}-\boldsymbol{b}}{\|\boldsymbol{a}\|}. \tag{D.10}$$

Finally, injecting Equation (D.10) into Equation (D.4) leads to

$$\delta h_i\left(\delta \boldsymbol{r}(t)\right) \approx 0 \Leftrightarrow \left\langle \frac{\boldsymbol{a}-\boldsymbol{b}}{\|\boldsymbol{a}\|}, \delta \boldsymbol{r}(t)\right\rangle \approx 0 \tag{D.11}$$

which indicates that the model error is null for any error $\delta\boldsymbol{r}(t)$ orthogonal to $\boldsymbol{b} - \boldsymbol{a} = \boldsymbol{s}_i(t') - \boldsymbol{s}_i(t) - \Delta\boldsymbol{r}$, and the directions of extremum error are given by this same vector.

D.2 TDCP Model Error Along the Worst Direction

In Section D.1, the vectors $\boldsymbol{a} = \boldsymbol{r}(t) + \Delta\boldsymbol{r} - \boldsymbol{s}_i(t')$ and $\boldsymbol{b} = \boldsymbol{r}(t) - \boldsymbol{s}_i(t)$ are defined, and the vector $\boldsymbol{v} = \boldsymbol{b} - \boldsymbol{a}$ is shown to be the vector that defines the direction of extremum error. Here, the model error δh_i of Equation (4.17) is studied along a one-dimensional subspace, i.e., for any unit vector $\boldsymbol{e}$, considering the application

$$\begin{aligned} \nu : \mathbb{R} &\to \mathbb{R} \\ \lambda &\mapsto \delta h_i\left(\lambda \boldsymbol{e}\right) \end{aligned} \tag{D.12}$$

with

$$\delta h_i\left(\lambda \boldsymbol{e}\right) = \|\boldsymbol{a} + \lambda \boldsymbol{e}\| - \|\boldsymbol{a}\| - \left(\|\boldsymbol{b} + \lambda \boldsymbol{e}\| - \|\boldsymbol{b}\|\right), \tag{D.13}$$

one finds out that the derivative of ν at λ is

$$\nu'(\lambda) = \frac{\langle \boldsymbol{a} + \lambda \boldsymbol{e}, \boldsymbol{e} \rangle}{\|\boldsymbol{a} + \lambda \boldsymbol{e}\|} - \frac{\langle \boldsymbol{b} + \lambda \boldsymbol{e}, \boldsymbol{e} \rangle}{\|\boldsymbol{b} + \lambda \boldsymbol{e}\|}. \tag{D.14}$$

Finally, if $\boldsymbol{e} = \dfrac{\boldsymbol{v}}{\|\boldsymbol{v}\|}$ and $\delta \boldsymbol{r}(t) = \lambda \boldsymbol{e}$ for some $\lambda \in \mathbb{R}$, then $\|\delta \boldsymbol{r}(t)\| = |\lambda|$ and the derivative of ν at $\|\delta \boldsymbol{r}(t)\|$ in the direction of $\boldsymbol{v}$ is obtained.

This document may not be reproduced, modified, adapted, published, translated in any way, in whole or in part, nor disclosed to a third party without the prior written consent of ENAC. © 2025, ENAC

Appendix E

Horizontal and Vertical Impact of TDCP Correlations

The results presented in this appendix correspond to an in-depth study of the experiments discussed in Chapter 5.

E.1 Horizontal Positioning Error

In Table E.1 and Table E.2 are visible the distribution of horizontal positioning errors, corresponding to the Euclidean norm of the East and North component errors, for synthetic and real observations, respectively. These distributions are shown for the three Factor Graph Optimization (FGO) architectures and for three temporal window lengths ($w = 2$, 10, and 60).

In Figure E.1 and Figure E.2 are visible the evolution of the mean horizontal positioning error as a function of the temporal window length w, for all three FGO architectures, for synthetic and real observations, respectively.

E.2 Vertical Positioning Error

In Table E.3 and Table E.4 are visible the distribution of vertical positioning errors, for synthetic and real observations, respectively. These distributions are shown for the three FGO architectures and for three temporal window lengths ($w = 2$, 10, and 60).

In Figure E.3 and Figure E.4 are visible the evolution of the mean vertical positioning error as a function of the temporal window length w, for all three FGO architectures, for synthetic and real observations, respectively.

This document may not be reproduced, modified, adapted, published, translated in any way, in whole or in part, nor disclosed to a third party without the prior written consent of ENAC. © 2025, ENAC

Table E.1: Distribution of the Euclidean norm of horizontal positioning errors obtained from **synthetic** observations. Each row corresponds to one of the three FGO architectures, and each column corresponds to a different temporal window size w.

Arch.	$w = 2$	$w = 10$	$w = 60$
1	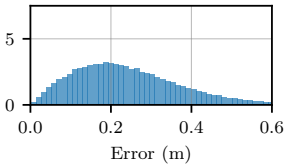	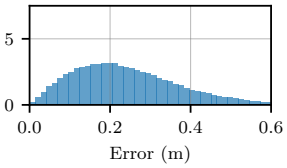	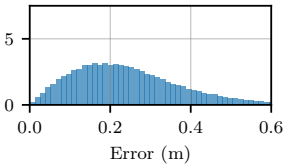
2	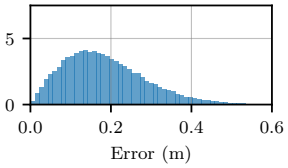	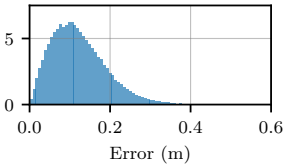	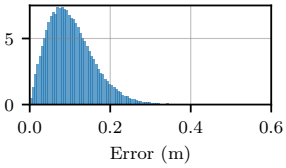
3	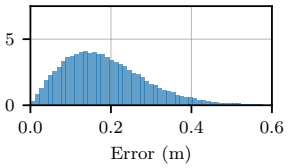	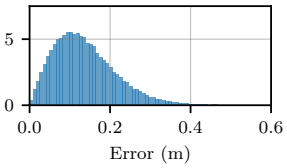	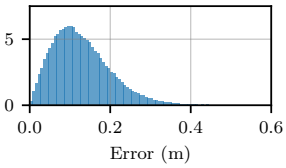

Table E.2: Distribution of the Euclidean norm of horizontal positioning errors obtained from **real** observations. Each row corresponds to one of the three FGO architectures, and each column corresponds to a different temporal window size w.

Arch.	$w = 2$	$w = 10$	$w = 60$
1	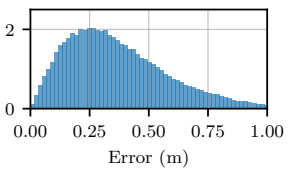	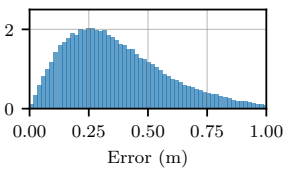	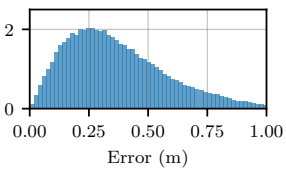
2	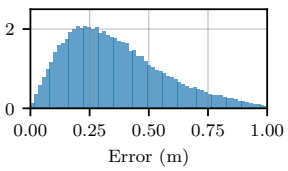	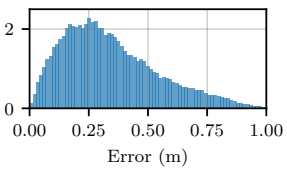	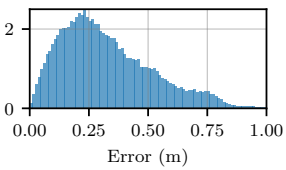
3	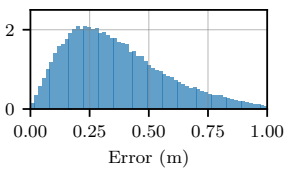	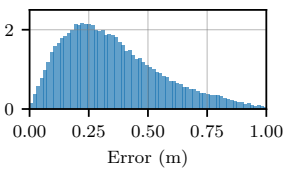	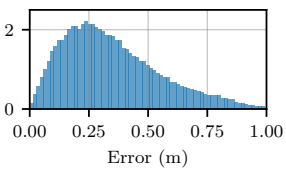

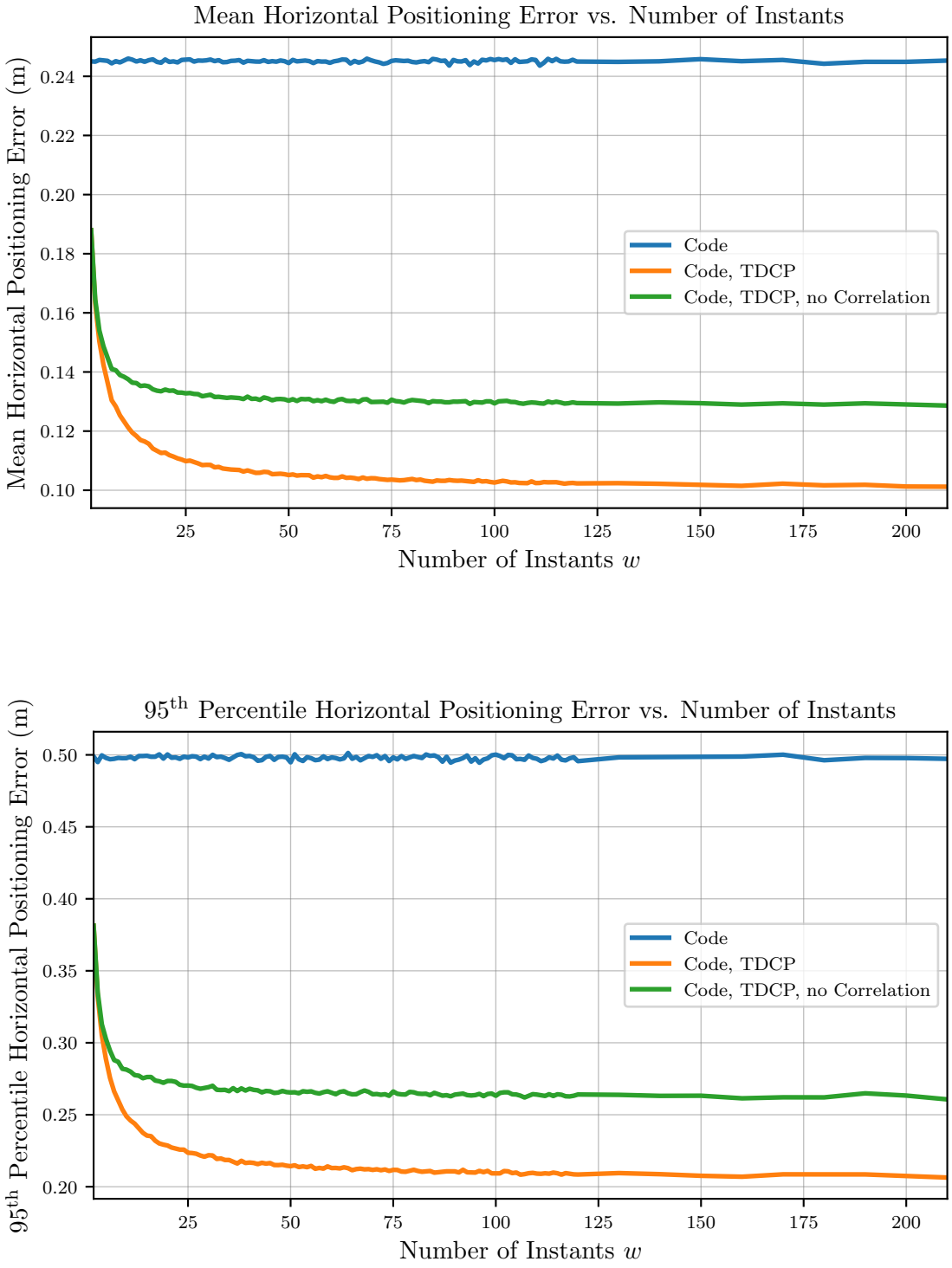

Figure E.1: Horizontal positioning error for **synthetic** observations, as a function of temporal window size w, for all three FGO architectures. Top: mean positioning error. Bottom: 95th percentile positioning error. The curve is plotted with points sampled every 1 unit from $w = 2$ to $w = 120$ and every 10 units from $w = 120$ to $w = 220$, resulting in slower variations in the second part.

This document may not be reproduced, modified, adapted, published, translated in any way, in whole or in part, nor disclosed to a third party without the prior written consent of ENAC. © 2025, ENAC

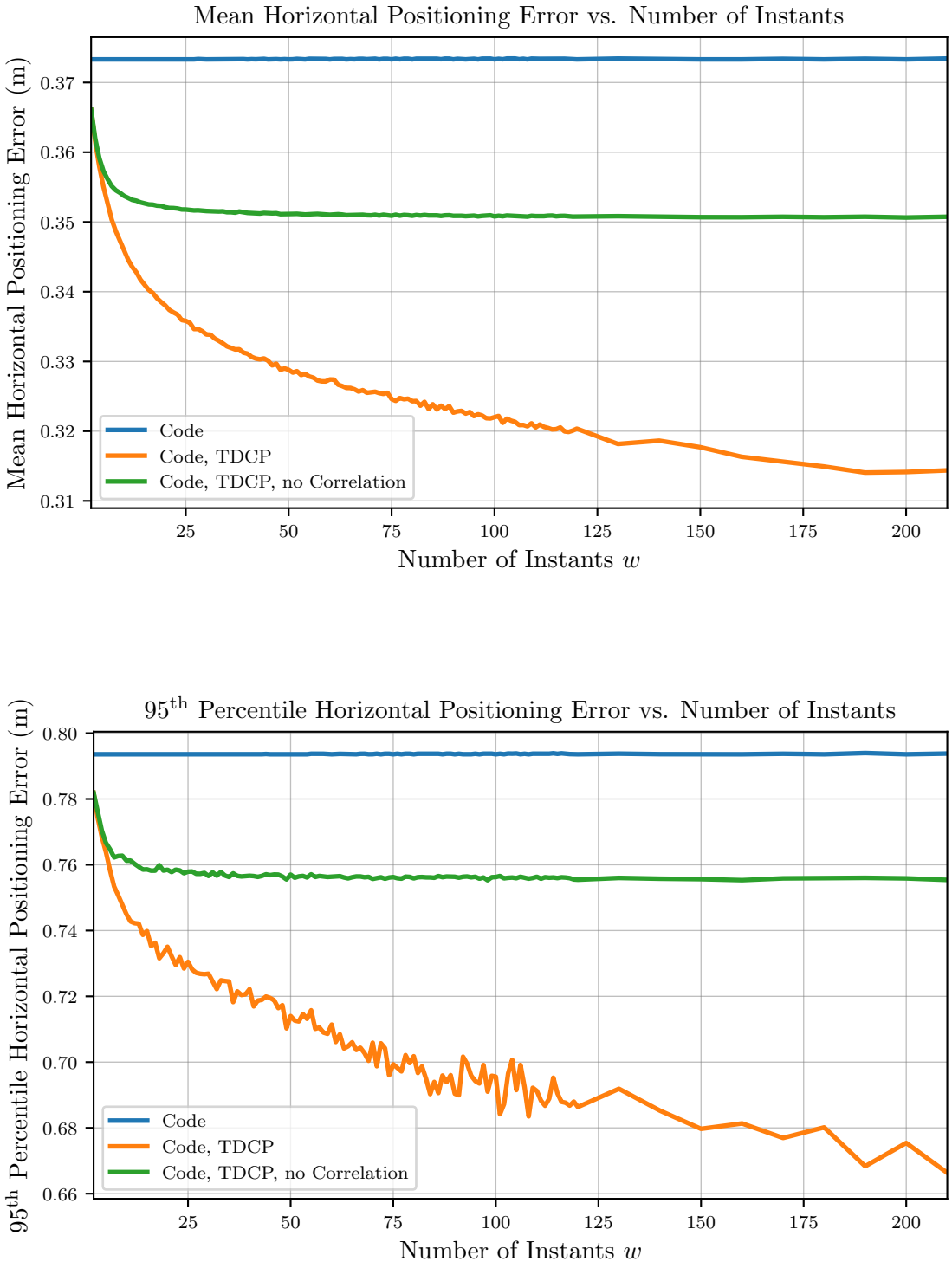

Figure E.2: Horizontal positioning error for **real** observations, as a function of temporal window size w, for all three FGO architectures. Top: mean positioning error. Bottom: 95th percentile positioning error. The curve is plotted with points sampled every 1 unit from $w = 2$ to $w = 120$ and every 10 units from $w = 120$ to $w = 220$, resulting in slower variations in the second part.

Table E.3: Distribution of the Euclidean norm of vertical positioning errors obtained from **synthetic** observations. Each row corresponds to one of the three FGO architectures, and each column corresponds to a different temporal window size w.

Arch.	$w = 2$	$w = 10$	$w = 60$
1	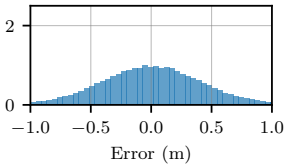	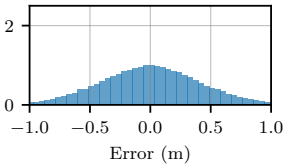	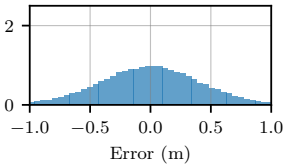
2	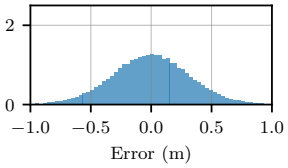	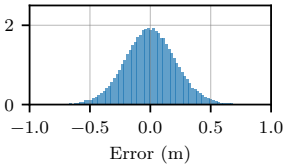	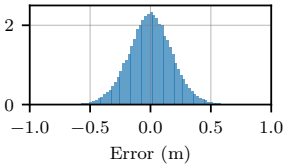
3	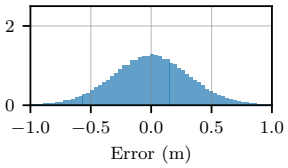	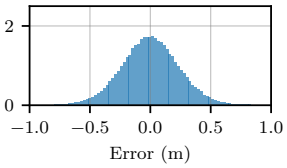	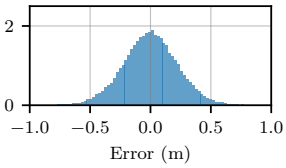

Table E.4: Distribution of the Euclidean norm of vertical positioning errors obtained from **real** observations. Each row corresponds to one of the three FGO architectures, and each column corresponds to a different temporal window size w.

Arch.	$w = 2$	$w = 10$	$w = 60$
1	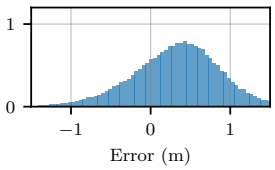	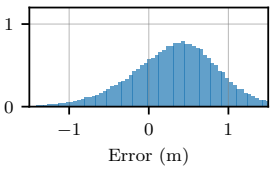	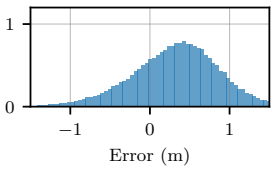
2	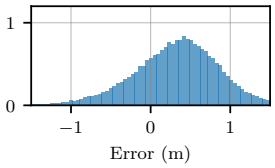	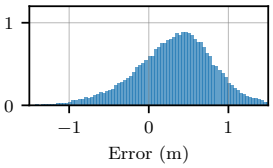	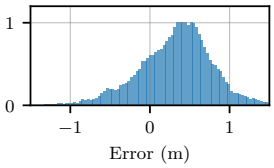
3	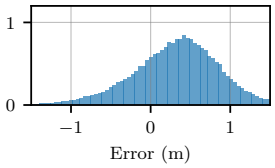	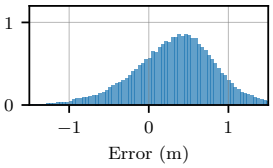	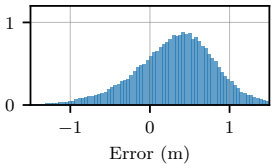

This document may not be reproduced, modified, adapted, published, translated in any way, in whole or in part, nor disclosed to a third party without the prior written consent of ENAC. © 2025, ENAC

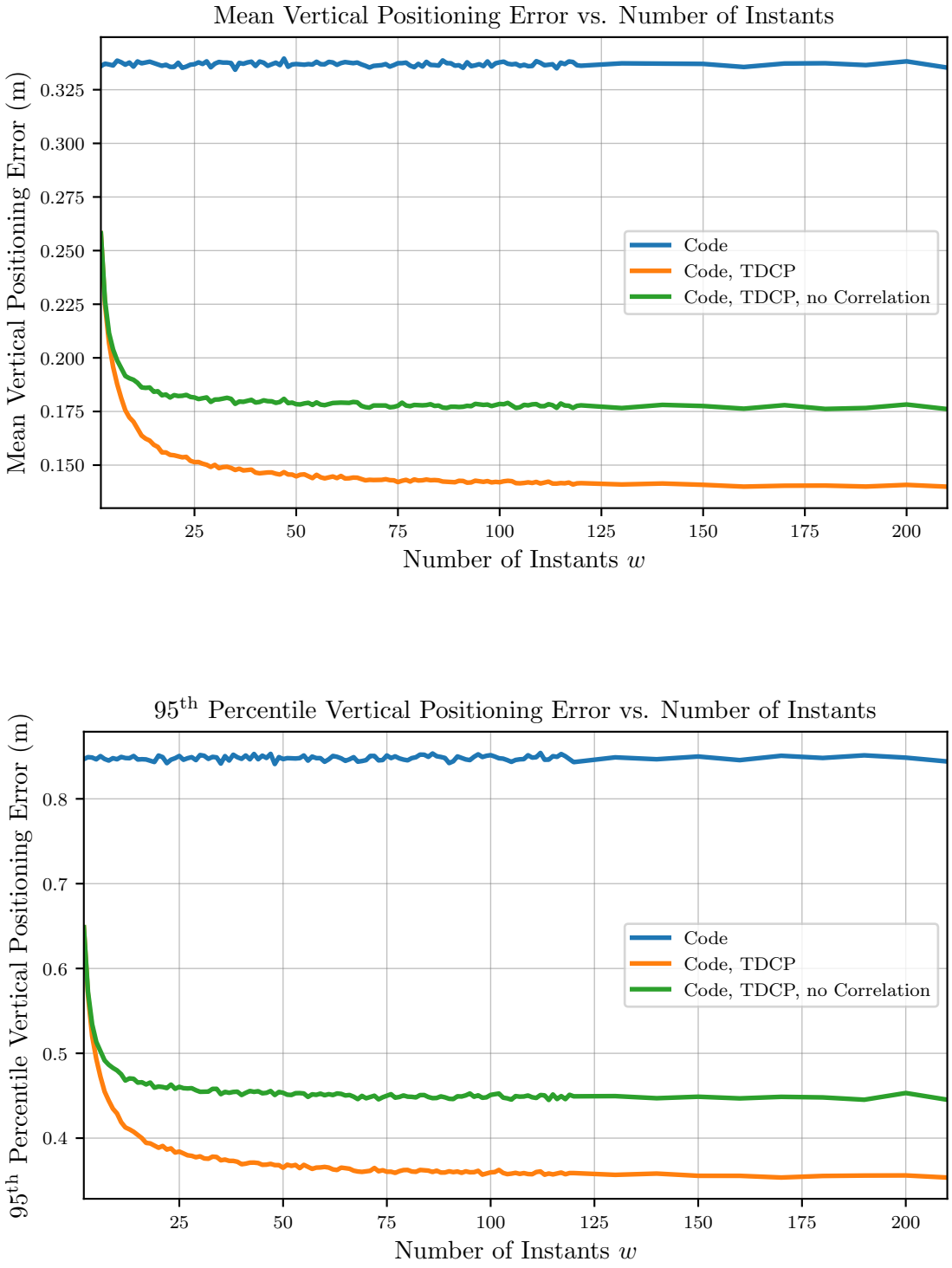

Figure E.3: Vertical positioning error for **synthetic** observations, as a function of temporal window size w, for all three FGO architectures. Top: mean positioning error. Bottom: 95th percentile positioning error. The curve is plotted with points sampled every 1 unit from $w = 2$ to $w = 120$ and every 10 units from $w = 120$ to $w = 220$, resulting in slower variations in the second part.

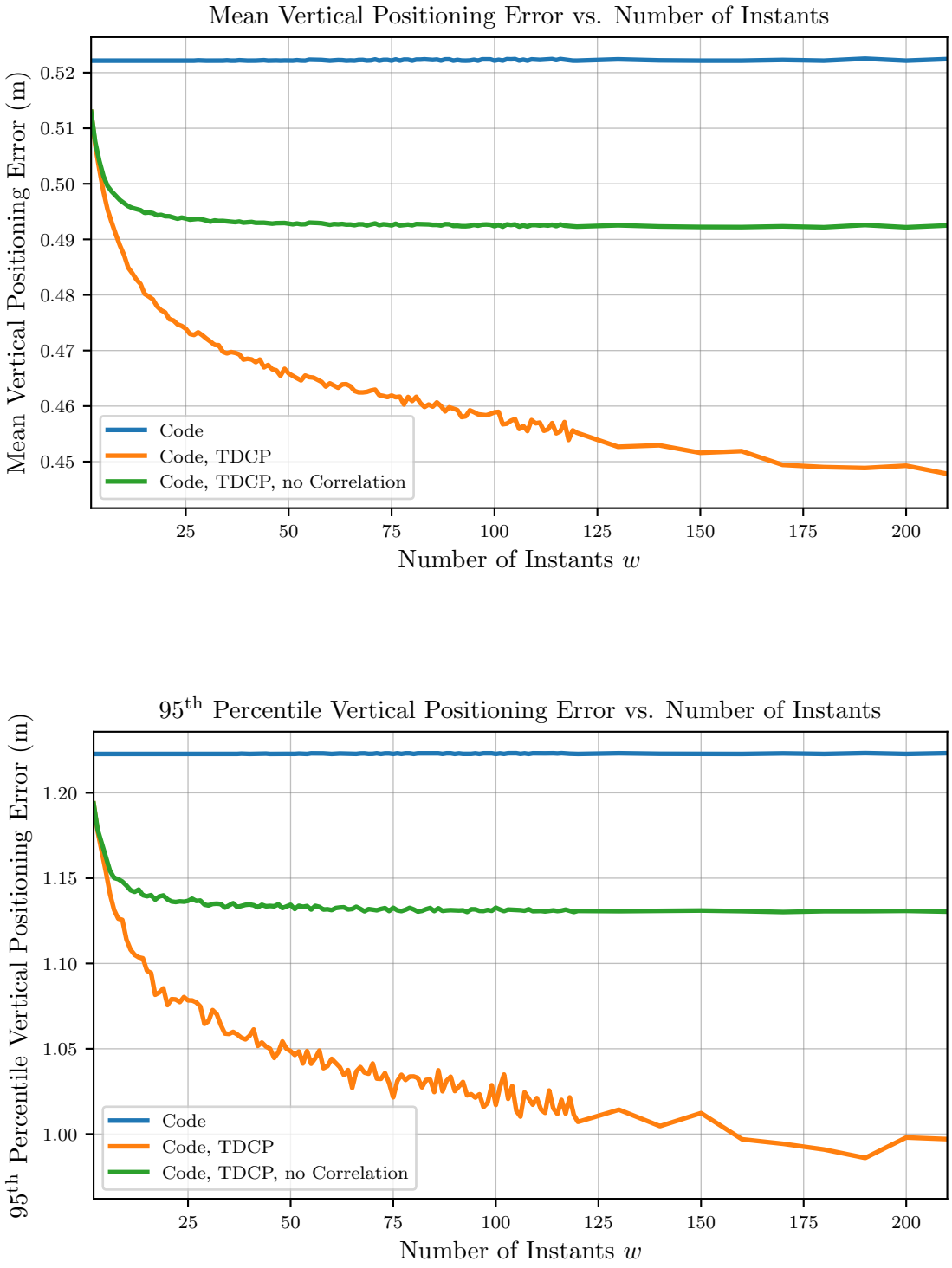

Figure E.4: Vertical positioning error for **real** observations, as a function of temporal window size w, for all three FGO architectures. Top: mean positioning error. Bottom: 95th percentile positioning error. The curve is plotted with points sampled every 1 unit from $w = 2$ to $w = 120$ and every 10 units from $w = 120$ to $w = 220$, resulting in slower variations in the second part.

This document may not be reproduced, modified, adapted, published, translated in any way, in whole or in part, nor disclosed to a third party without the prior written consent of ENAC. © 2025, ENAC